Extension of the Liège Intranuclear Cascade Model to the 2-15 GeV Incident Energy Range

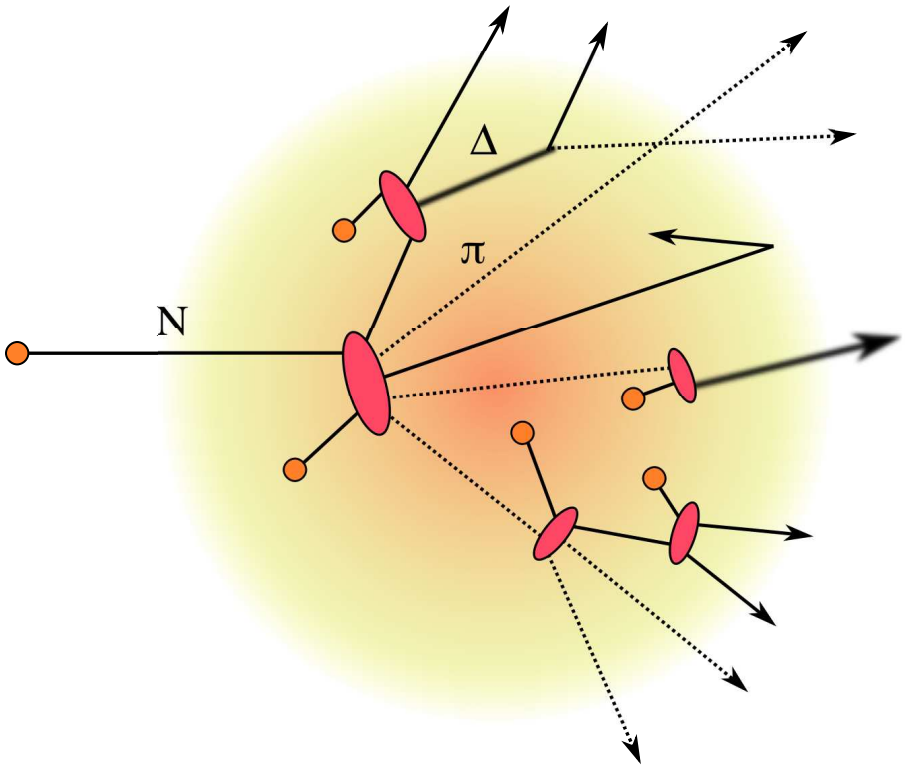

Thesis presented in fulfillment of the requirement for the Degree of Doctor in Science

Pedoux Sophie

University of Liège
Faculty of Sciences
Department of Astrophysics, Geophysics and Oceanography
Fundamental Interactions in Physics and Astrophysics
Academic year 2011-2012

Université de Liège

Acknowledgment

Tout d'abord, je voudrais remercier monsieur Cugnon sans qui ce travail n'aurait pas été possible. Travailler avec quelqu'un avec une telle expertise dans la physique nucléaire à été un véritable honneur. Je voudrais le remercier plus particulièrement pour l'aide qu'il m'a apportée au cours de ces derniers mois.

Ce travail a été soutenu financièrement par l'Institut Interuniversitaire des Sciences Nucléaires (I.I.S.N.). Je remercie monsieur Cugnon de m'avoir confié cette bourse au sortir de mes licences.

Il y a 10 ans, j'ai mis les pieds pour la première fois à l'université. J'étais intimidée par ce lieu qui a toujours été mystique pour moi. Grand-papa aurait été fier de me voir là, assise dans un amphithéâtre, prenant consciencieusement note. Après tout, c'est un peu grâce à lui si j'ai choisi de faire des études universitaires. Je lui en serai toujours reconnaissante. Je tiens également à remercier toute ma famille pour leur soutien. D'où que vous soyez, merci.

Je pense pouvoir dire que les étudiants en physique sont caractérisés par une ouverture d'esprit hors du commun. Au cours de mes études, j'ai eu l'occasion de me faire des amis avec qui j'espère ne jamais perdre contact, amis qui vous soutiennent et vous rendent confiance quand vous doutez. Des amis qui sont toujours là pour vous aider, que ce soit pour partager des tuyaux, débuguer un programme, boire un café, relire une thèse, discuter de physique (ou d'autres sujets), aller à un concert à Paris, jouer une partie de D&D ou, même, poncer un parquet...

Et puis, je n'ai pas que des amis physiciens.. A tous, donc, je vous dis merci !!! Sans vous, ça n'aurait pas été pareil.

En rejoignant le personnel de l'université en tant que doctorant, j'ai rencontré une deuxième fois mes professeurs, mais dans un climat bien différent. Au cours de ces années, j'ai également eu la chance de rencontrer des personnes qui viennent d'autres coins du globe, et d'ainsi découvrir des cultures très différentes de la nôtre... J'espère que ces contacts m'auront apporté plus qu'une meilleure maîtrise de l'anglais. Parmis eux, je voudrais surtout remercier Davide qui, travaillant aussi sur INCL, m'a beaucoup aidé et beaucoup appris. Grazie mille !

Les cours, les séminaires, les conférences, les "journal clubs", les proceedings, les articles et la thèse auront été pour moi autant d'occasions d'apprendre et de m'améliorer. Je remercie mes collègues de l'IFPA présents ou passés, et plus particulièrement Jean-René, pour les discussions intéressantes que j'ai eues avec eux et pour leurs conseils occasionnels.

Enfin, je voudrais remercier Benoit, pour ses encouragements et sa présence. Pour sa patience aussi, elle aura parfois été mise à rude épreuve. Une nouvelle vie m'attend, un nouveau travail, une nouvelle maison, mais tu resteras mon point de repère. Merci Touha.

Contents

1 Introduction

This PhD thesis is a new landmark in the steady development of the Liège intranuclear cascade model and of the associated code especially devoted to the description of spallation reactions. In general these reactions are defined as the ones which result from the interaction of a high energy hadron (or a light nucleus) with a nucleus. By tradition, this word is used when the incident energy lies between $\sim$ 200 MeV to $\sim$ 2 or 3 GeV (or rather the incident energy per nucleons for light nuclei). The main property of these reactions is the abundant emission of neutrons. Other particles (p, d, t, ^3He, α, pions...) can be emitted as well, but at much smaller rates.

This copious emission of neutrons has triggered a revived interest, in the last two decades, due to development of efficient neutron spallation sources. The latter are actually simple devices, basically a piece of heavy metal, bombarded by a high energy proton beams; an incident proton-induced spallation reaction producing several neutrons. These neutrons multiply by secondary reactions and diffuse out the spallation target. They can thus be used in special pipes for condensed matter studies or for producing isotopes for medical applications. The same idea is at the basis of the plans for futures "incinerators" of nuclear waste, the so-called Accelerator-Driven Systems (ADS). In such devices, the neutron spallation source is located at the core of a sub-critical nuclear reactor, partially loaded with nuclear waste (more details are given in Chapter 2). Neutrons issued from the spallation source can multiply in the reactor core and eventually transmute the radiotoxic isotopes in the waste into other stable or short-lived isotopes. These technological development imply careful design, which are generally based on simulations of the transport of particles inside the apparatus, at least in the spallation source. In turn, the improvement of the transport codes requires more and more accurate reaction models. On the other hand the production of neutrons in a spallation source is optimum technologically and economically for proton incident energy around one GeV. Therefore, a considerable effort has been made, especially in Europe, in the frame of the EU HINDAS [1] and EUROTRANS [2] projects, to improve the predictive capabilities of the reaction models in this energy range. In particular, the intranuclear cascade model developed in Liège (INCL4) has become, in the frame of these collaboration, one of the most successful models after several refinements.

Spallation reactions are also relevant in other scientific domain. In particular, they are induced by Galactic Cosmic Rays (GCR) either in the upper atmosphere or in space missions,

where they can pose serious problems concerning radiation protection for astronauts and electronic devices. The average energy of GCR is about 600 MeV, right in the domain where INCL4 is working well. However the energy spectrum of GCR is rather extended and it is generally considered that radiation protection studies need precise reaction models for proton energy up to $\sim$ 10 GeV, in a domain where INCL4 was not suited for reasons explained below. It was the purpose of this PhD to extend INCL4 in order to make it suitable in this energy range.

Spallation reactions are generally described as proceeding in two stages, as suggested by Serber [3] in 1947. These two stages are very different from each other. The first one is called intranuclear cascade, it is very fast and, at the end of it, the target nucleus is left in an excited equilibrated state. The de-excitation of the target is the second stage of the reaction. A more complete description of the spallation reactions is introduced in Chapter 2. Different models are used for the two stages: intranuclear cascade models for the first stage and evaporation models for the second stage. The intranuclear cascade model of Liège (INCL) is one of these intranuclear models. A recent intercomparison of the different model combinations to simulate spallation reactions [4] has showed that INCL4, when combined with the de-excitation code ABLA07, is one of the most efficient for the simulation of spallation reactions [5]. Nuclear reaction models are presented briefly in Chapter 3.

The standard version of the code, INCL4.2, presented in Chapter 4, is approximately limited to the energy range going from 100 MeV to 2 GeV and takes into account nucleons, pions and Δ_{1232} resonances produced in the reaction, which is largely sufficient in this energy domain. To extend the applicability of INCL toward the high energy side requires to take into account all the new channels opening in the new energy domain. In our case, these channels are mainly resonance production channels. As we explain in more details in Chapter 5, these resonances are numerous, they have large width, and short life-time. Furthermore, they are so much overlapping that one may wonder whether considering such objects with a well-defined identity is relevant. The interaction of resonances with nucleons and with other resonances is not well known. This description thus introduces uncertainties in the reaction mechanisms. It looks legitimate to consider alternative descriptions for the new channels to be added. These alternative descriptions should allow us to somehow short-cut or bypass the explicit resonance degrees of freedom. The strategy we have adopted in this work consists in replacing the production of resonances, in nucleon-nucleon collisions and pion-nucleon collisions, by the direct production of the particles they would have decayed in. The extension of INCL4.2 to the incident energy range going from $\sim$ 2 GeV to $\sim$ 10–15 GeV, and its implementation in the code, is the object of Chapter 5.

As we explain later, the selection of the outgoing channel in a collision, in INCL4.2, is based on Monte Carlo methods and elementary cross sections. We have limited ourselves to pion producing channels: up to four-pion production channels in nucleon-nucleon collisions and up to two and three pion production channels in pion-nucleon collisions [6, 7, 8, 9, 10]. Of course, such extension of the model raises questions about, for example, theoretical limitations to the INC models that have to be respected. At the beginning of this work, it was not obvious that quark degrees of freedom should not be taken into account at high energy. In fact, existing models devoted mainly to heavy ion reactions in the energy range under consideration in this work introduce a transition from the resonance dynamics to the string dynamics, some times abruptly, roughly when the c.m. energy of NN collisions exceeds a few GeV, *i.e.* in the middle of the energy range under consideration in this work. We show in Chapter 6 that the extended version of INCL4 that we have constructed is actually able to simulate spallation reactions up to 10–15 GeV with rather satisfactory agreement with experimental data.

We have performed tests with the extended version of INCL4.2 for neutron, proton and pion emissions. For pion emissions, extensive comparisons with the results from the HARP

experiment [11, 12, 13] have been performed concerning double-differential pion production for incident protons and charged pions over a large set of targets and for incident energies going up to 12 GeV/c. Tests on nuclear fragmentation have also been realized, but no comparison with experimental data at incident energies higher than 2 GeV has been made. The results may however shed some light on the possibility of the so-called limiting fragmentation of the target nucleus

Finally, we present conclusions and perspectives in Chapter 7.

Marty McFly: *Uh, does it run, like, on regular unleaded gasoline?*
Dr. Emmett Brown: *Unfortunately no, it requires something with a little more kick - plutonium.*
Marty McFly: *Uh, plutonium? Wait a minute. Are you telling me that this sucker is nuclear?*
Dr. Emmett Brown: *No, no, no, no, no. This sucker's electrical. But I need a nuclear reaction to generate the 1.21 gigawatts of electricity I need.*

Back to the future, Robert Zemeckis, Bob Gale, 1985

2

Motivating background

Our society has to face many challenges in the years to come. One of the most important of which is global warming, which is deeply related to the challenge for energy policy, supply and consumption. The energy needs of our civilization have been increasing almost continuously over the last century. We burn oil and gas, we need electricity, at work or at home, for lightning, for cooking, even our leisures increase our needs for energy. Our life style has grown dependent upon energy and we now realize that our unconsidered level of consumption will impact our planet and its climate. We have to search for new energy sources as well as we have to improve the efficiency of the exploitation of the sources we already have.

The acuteness of the world energy problem is revealed simply by some key numbers concerning the general trends. In 2008, the world energy consumption was of 12,369 Mtoe, out of which a little more than 80% was produced using oil, coal and gas[1]. The world energy consumption has doubled between 1960 and 2000, largely triggered by the rise of the world population, which has doubled between 1970 and 2000 [15]. The problem consists in meeting the ever growing energy needs while reducing CO_2 emissions, which are considered as the main source of global warning. Obviously, a considerable amount of our oil, coal and gas consumption should be replaced by CO_2-free energy sources. In view of this enormous shift, it is clear that all sources of CO_2-free energy should be considered. This has led to what is called "Nuclear Renaissance", i.e. plans (at the world level) to increase nuclear power and to make it as sustainable as possible. Presently, nuclear energy represents roughly 6% of the total produced energy, worldwide, but represents about 16% in European Union and 20% in Belgium. One of the key ideas in "Nuclear Renaissance" is to shift from the present available reactors, known as generation II reactors, in which only a small fraction of the fuel is used, to so-called generator IV reactors, based on fission induced by fast neutrons, which will be able to burn uranium much more efficiently. This change will be effective in some forty years from now. In between, the generation III reactors (basically the same as generation II plus additional safety features) will help to fill the gap.

The future of nuclear energy will depend upon the ability of the nuclear industry to solve three main problems: (1) no rapid exhaustion of resources (in this respect, the development of generation IV reactors is absolutely needed), (2) nuclear safety and security (3) the management of nuclear wastes from nuclear reactors.

[1] according to IEA [14]

We will elaborate a little bit on the third issue. Nuclear wastes contain highly radio-toxic long-lived isotopes. Two main strategies are envisaged. The first one rests on the storage of the wastes, after possible removal of U and Pu isotopes to ensure their non-proliferation, in deep underground repositories, until their radio-toxicity fades away. This solution assumes a monitoring of the storage sites over a large time-scale, at least ten thousand of years. The second considered solution implies the separation of highly radio-toxic long-lived isotopes, mainly actinides, from the rest and their transmutation. This transmutation (or rather incineration) will be realized in so-called accelerator driven systems (ADS). The latter will consist in high-energy (typically in the GeV range) and high-intensity accelerator, delivering a proton beam on a spallation target located in the core of sub-critical reactor. The neutrons issued from the spallation target multiply in the core and eventually transmute the waste isotopes. Projects of this kind have been developed to the point that the first prototype, known as MYRRHA, will be build in the years to come in Belgium [16]. It is briefly presented in Sec. 2.2.

For the optimization of such devices, numerical tools like MCNPX, particle transport codes, are used. They simulate a nuclear reactor in operation, giving precious information on, for example, what wastes to expect or damages to be found in the surrounding vessels at the end of operation. These tools provide valuable information to test ideas and hereby enhance conception of the new generation of nuclear reactors. It is thus very important for these tools to be as reliable as possible, which needs accurate reaction models. The Liège intranuclear cascade model INCL4.2 is used in those simulation codes to describe spallation nuclear reactions.

Spallation reactions are also of interest in projects of intense neutron spallation sources [17], the development of cancer hadron-therapy over the world [18] and radiation protection issues regarding cosmic rays in space missions [19, 20]. As a matter of fact, cosmic ray particles have the right characteristics to undergo spallation reactions with materials they encounter. They are at the source of high radiation hazard for human being during space missions. The application of INCL4+ABLA to this field, with its high predictive power and low time consumption, would be beneficial but, as we will show in section 2.3, it requires the possibility to accommodate particles with a kinetic energy higher than the upper energy limit of INCL4.2.

The extension of the INCL model to high energy, which is at the basis of the main motivation of this thesis, requires the introduction of all the possible inelastic channels, but the standard version of the model (INCL4.2) is limited to excitation of the Δ resonance in inelastic nucleon-nucleon collisions. This is largely sufficient for the energy domain relevant for ADS. However, for applications to space radiations (and others), this is not satisfactory. It is often considered that accurate simulations require to take account of the cosmic ray spectrum up to 10-15 GeV.

2.1 Spallation Reactions

The set of nuclear reactions between a projectile with a high kinetic energy (typically an energy between 100 MeV and a few GeV) and a target nucleus are called spallation reactions. The etymological root for "Spallation" is the English verb "to spall" which means "to produce fragments". Indeed, during these reactions, the target nucleus emits a lot of particles, mainly neutrons, that can interact with the surrounding nuclei. One can then distinguish the microscopic spallation, a single spallation reaction, and the macroscopic spallation, which takes into account secondary reactions caused by the emitted particles.

Serber was the first to suggest, in 1947, that these reactions proceed in two stages [3]:

1. A first stage, very fast (of the order of 10^{-22} s), called the intranuclear cascade. It can be regarded as a succession of collisions between the incident particle and the nucleons of the

target nucleus. As not only nucleons intervene during this stage, it is sometimes referred as "hadronic cascade".

2. The second stage, the evaporation, starts at the end of the cascade when the remnant of the target nucleus is left in an excited, more or less equilibrated, state. The de-excitation, which is much slower than the cascade (10^{-20} s), occurs either by emission of particles or, sometimes, by fission of the remnant.

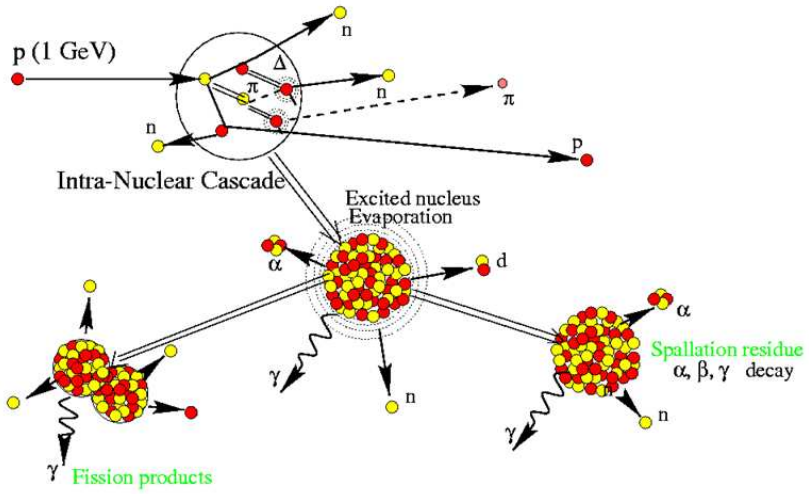

Figure 2.1: *Spallation reaction*

This two-stage description has to be taken into account in numerical simulations. In order to get a complete description, spallation reactions are usually simulated by two different codes, one for each stage, coupled together. The cascade can be simulated by codes such as Isabel [21] or INCL [22], which is at the heart of this work. The de-excitation is performed by codes such as ABLA [23, 24], GEMINI [25] or SMM [26].

Figure 2.1 shows a schematic representation of a spallation reaction. If the projectile, usually a proton, has an energy in the 100 MeV–10 GeV range, then its de Broglie wavelength $\lambda = h/\sqrt{2mE}$ is of the order of 1 fm at the most, which is much smaller than the radius of a heavy nuclei. The projectile doesn't feel the nucleus as a whole but instead penetrates it and triggers a cascade of collisions with the nucleons.

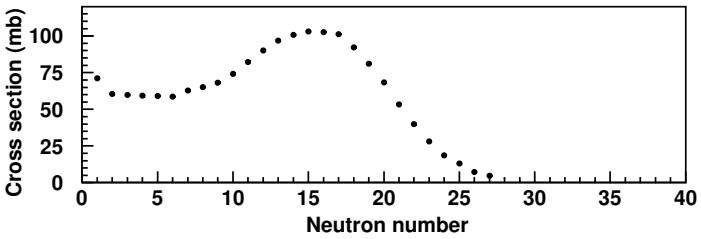

Figure 2.2: *Neutron multiplicity cross section with respect to the produced neutron number, data comes from [27]*

During the cascade, the energy of the incoming particle is transferred to a few nucleons of the target, and some of them are ejected from the nucleus. The neutron yield in spallation can

be very important. Figure 2.2 shows the neutron yield for a 1.2 GeV proton on lead. After the cascade, the remnant is left in an excited state. Because of the importance of neutron emission, the remnant is a neutron poor isotope, which will decay by further evaporation or fission.

2.2 A spallation based reactor (or ADS): MYRRHA

The principle of a spallation-based reactor, also called ADS, is the following: an accelerator delivers a proton beam which bombards a spallation target, located in the center of the reactor; in the vicinity of the target, there is the "fuel" of the ADS, the material that will be transmuted in the reactor, for instance minor actinides, and release energy at the same time. Minor actinides are the isotopes which combine a high radiotoxicity with a long life-time, and the disposal of these materials is a major issue in nuclear energy production.

The first experimental reactor of this type is the goal of the MYRRHA project (Multi-purpose hYbrid Research Reactor for High-tech Applications); it will be build at the SCK-CEN in Belgium [16]. An illustration of this reactor is shown in figure 2.3. On the figure, one can notice that the proton beam is accelerated to 600 MeV. This energy has been chosen as the best compromise between the quantity $\frac{n/p}{E_p}$ (which is the number of produced neutrons, per incident proton, divided by the energy E_p of the proton beam; this quantity is proportional to the "price" in energy of a neutron) and technical issues such as the evacuation of the heat at the surface between the proton beam and the spallation target or the capacity to build an accelerator able to operate for long periods.

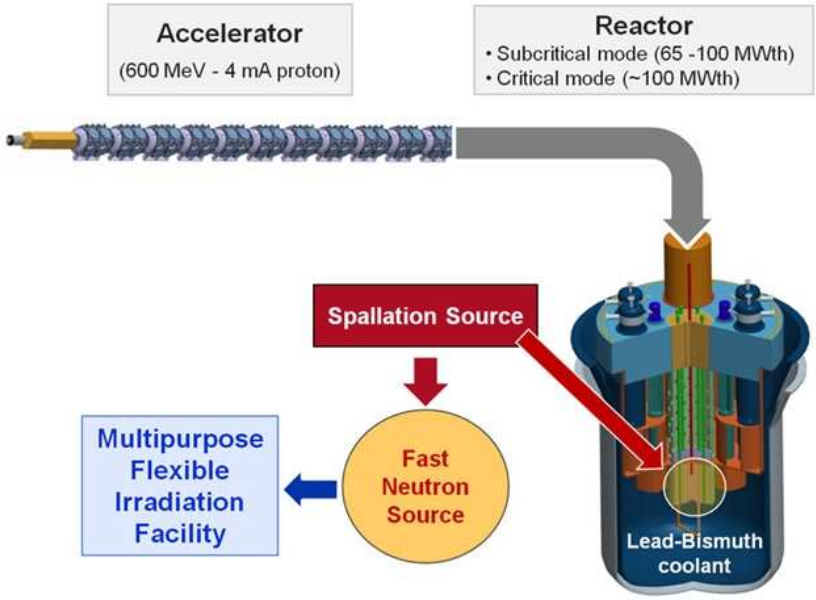

Figure 2.3: *Schematic representation of an ADS [28]*

Such reactors have an enhanced safety: they are sub-critical (the fuel cannot sustain by itself the chain reaction). If the proton beam is turned off, the neutron supply stops and the reactor is automatically shut down. The spallation target, liquid eutectic lead-bismuth, was chosen because it can produce a high quantity of neutrons and absorb and evacuate the energy from the proton beam at the same time while keeping the working temperature at a moderate level.

Furthermore, the spallation neutrons have a fast spectrum, hence such a reactor offers a

flexible research facility to develop the components for future fast reactors. Finally, the neutron fluxes can reach very high intensity, which is useful for the production of radio-isotopes for medicine.

Over the last decade, the need to improve the productivity and the safety of nuclear reactors led to a new generation of reactors. Numerical codes have been developed in order to simulate spallation reactions and to reproduce all the pertinent observables of these reactions in the context of the Nuclear Renaissance.

2.3 Space radiation

Cosmic ray particles can be split in two categories, the Galactic Cosmic Rays (GCR), which originate essentially from the Galaxy, and particles emitted during a burst in our Sun, which is called Solar Particle Event (SPE). These 2 types of cosmic rays have very different compositions, very different energy profile and contribute differently to the equivalent dose received by exposed people.

When cosmic rays reach the upper atmosphere or encounter matter, they can undergo spallation reactions. In manned missions in space, these reactions are the main source for the radiation received by the astronauts. Table 2.1 shows the composition (in %) of the two types of cosmic rays and their relative contribution (in %) to the equivalent dose.

	GCR		SPE	
	Composition	Equivalent dose	Composition	Equivalent dose
Proton	87	19	80–90	90
Helium	12	17	10–20	10
Ions	1	64	1	

Table 2.1: *Baryon components of GCR and SPE and their relative contributions to equivalent dose, evaluated at the skin, assuming exposure during the solar minimum behind a 5 g/cm^2 aluminium shield. Adapted from Ref. [20].*

Figure 2.4 shows the energy spectrum of protons in GCR; the flux is maximum in the energy range 0.5–1 GeV and then decreases rapidly with the increasing kinetic energy of the protons (nuclei in GCR have approximately the same maximum in their energy spectrum). It is already reduced by a factor of one thousand for protons with a kinetic energy of 10-15 GeV. In the case of SPE, the proton energy seldom reaches 1 GeV.

It is interesting to note that simulation codes that were developed for nuclear reactors could be applied to cosmic ray simulation, with a relatively small number of modifications. They would need to accommodate light ions as projectile and they would need to be extended to the appropriate energy range. The extension of the INCL4.2 model to high energy (up to about 15 GeV) is the purpose of this work. This extension requires to take into account the new inelastic channels in nucleon-nucleon and pion-nucleon collisions that open in the 2–15 GeV energy range, which are believed to mostly correspond to excitation of hadronic resonances. However, we propose here an alternative method to the one consisting in implementing all the resonances. We investigate the possibility to somehow short-cut the resonances degrees of freedom by directly considering the particles produced by their decay. We limit ourselves to produced nucleons and pions in this work. Such an approach was already used in Refs. [29, 30], in particular for the study of pion-induced reactions, but at low energy (less than 1 GeV). Finally, the comparison

of our model's predictions with an extensive and systematic set of data, to test our assumptions and see if this method is applicable in spallation reactions at high energy, is also one of our motivations.

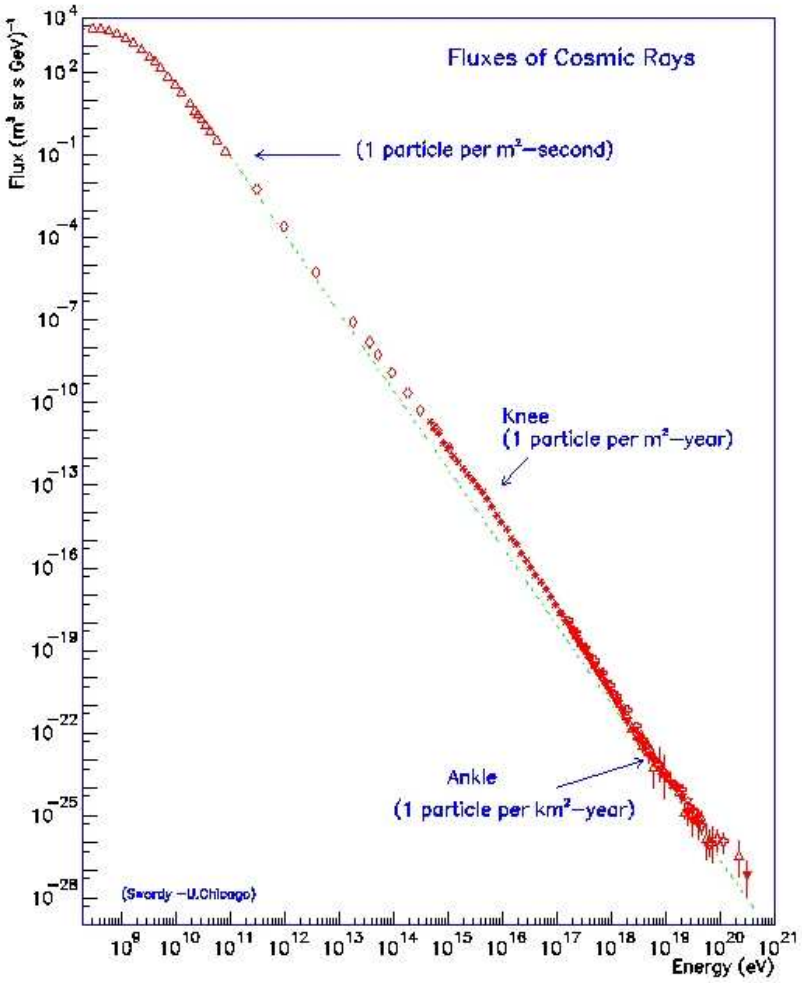

Figure 2.4: *Proton flux from GCR, given in* $(m^3 srsGeV)^{-1}$*, with respect to their kinetic energy (in eV). The figure comes from Ref. [31].*

3

Nuclear models for nucleon-nucleus reactions

3.1 Introduction

The theoretical study of nuclear reactions started more or less 80 years ago. It developed in two somehow opposite directions. On the one hand, this was more or less the first time reactions between microscopic objects were studied and theorists concentrated on the formal formulation of the reaction processes in general, inventing for instance the concept of the S-matrix (and also the R-matrix for the special cases of the resonant reactions). On the other hand, theorists designed a large number of specialized models corresponding partly to the many types of reactions showing apparently different facets. It is then not surprising that a theory allowing the ab initio calculation of a cross section is still not really existing (except for very simple cases). This, of course, is partly due to the complexity of the nuclear forces, but also to the fact that various types of reactions correspond mainly to differences in the number (and the nature) of involved degrees of freedom. The late developments present considerable progress along this line and allow for a clarification of the situation. We will say a few words about this aspect concerning the case of the spallation reactions.

Until a period which may be identified to the mid-1960s, nuclear reactions were usually described by considering two different processes:

The formation of a compound nucleus this concept was first introduced by Bohr [32], he made the hypothesis that a collision between a projectile and a heavy target would result in the formation of a compound nucleus by a complex process involving probably all the nucleons. This concept is efficient when the available energy has some specific values, this is reflected in the presence of narrow resonances in the cross sections. They correspond to quantum quasi-bound states of the compound nucleus, which have quantum numbers, like the bound states, but also a resonance width, corresponding, through the Heisenberg uncertainty principle, to a finite lifetime. Bohr also reached the conclusion that the possible later break up of this intermediate system has no connection with the first stage of the collision. In other words, he assumed the independence of the production channel and the evaporation of the compound nucleus (C. N.). The time span of these reactions depends on the projectile's energy and can last for 10^{-19} s to 10^{-15} s. The independence hypothesis made for the C. N. implies that all the outgoing channels are in competition

and are equiprobable. Thus it is usually considered that the C. N. state is reached when the residual nucleus has achieved a statistical equilibrium. The statistical fluctuations of energy can lead to further emission of particles with an angular distribution symmetric around 90°, in the center of mass.

The direct reactions for these reactions, the outgoing channel is directly linked to the incoming channel, and there is no formation of any intermediate system. The time span for direct reactions is shorter than for the C. N. and actually corresponds more or less to the transit time of the projectile across the nucleus (about 10^{-22} s). The emitted particles follow a narrow forward-peaked angular distribution. Typical direct reactions are the inelastic scattering leading to low-lying states of the target, or the charge-exchange reactions (the emitted particle has the same mass as the projectile, the net effect of the reaction is a transfer of electric charge). In these reactions, the number of involved degrees of freedom is very low, sometimes limited to those of only one target nucleon.

The formation of a C. N. is ubiquitous at low energy. It can coexist with direct reactions. When the incident energy increases, say above 10 MeV, the resonances start to overlap and the cross sections are slowly varying with energy. Furthermore the energy spectra of the emitted particles becomes more complicated. They are no more limited to evaporation spectrum, at very low energy, typical of C. N. reactions, and to high energy, close to the projectile velocity, typical of direct reactions. Sometimes, particles are ejected after the direct reactions and before statistical equilibrium is reached. These reactions are explained as taking place by series of nucleon-nucleon interactions, sometimes ejecting one of them, and leading progressively to a fully statistical excitation of the nucleus. They are called *pre-equilibrium emissions*.

Figures 3.1 shows the angle-integrated spectra $d\sigma/dE$ for neutron and, respectively, proton production, induced by protons with a kinetic energy of 10 MeV (left panel) and 100 MeV (right panel) on a ^{208}Pb target. These figures were generated with the nuclear reaction code TALYS [33]. They illustrate that each regime (direct reactions, the pre-equilibrium reactions and the compound nucleus reactions) has a different contribution to the spectra. The direct reactions describe the high energy part of the spectra, where the ejectile has nearly the same energy as the projectile. The compound nucleus can be used to describe the low energy part of the spectra, when the residual nucleus has reached statistical equilibrium and the emitted particle barely has enough energy to pass the Coulomb barrier. In between these two contributions, one can see the contribution of pre-equilibrium emission, which obviously increase with the energy of the projectile.

In this chapter, before considering a few models of nuclear reactions, we will introduce the Fermi gas model for the nucleus in Section 3.2. This model description of the nucleus is used by some models for nuclear reactions that we will explain further. We will then give an overview of models for the direct reactions, the compound nucleus formation and the pre-equilibrium emissions in Section 3.4, 3.5 and 3.6, respectively. Even though it shares some features with pre-equilibrium models, intranuclear cascade model will be presented separately, in section 3.6.3, first because this theoretical model is the basis for INCL, at the center of this work and second because the intranuclear cascade models can be considered as high energy nuclear reaction models as well.

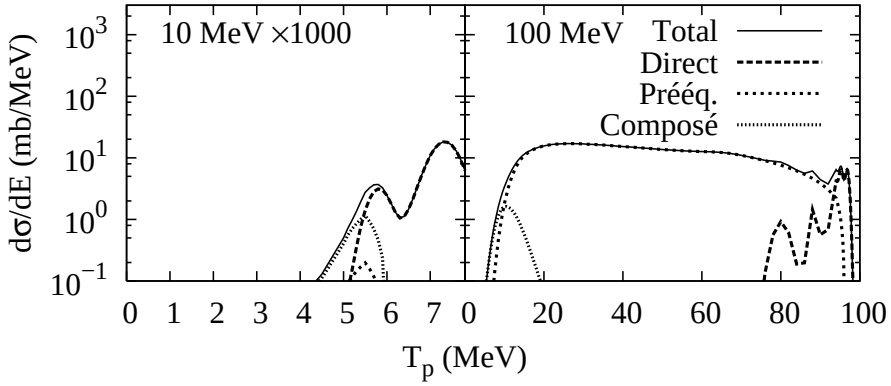

(a)

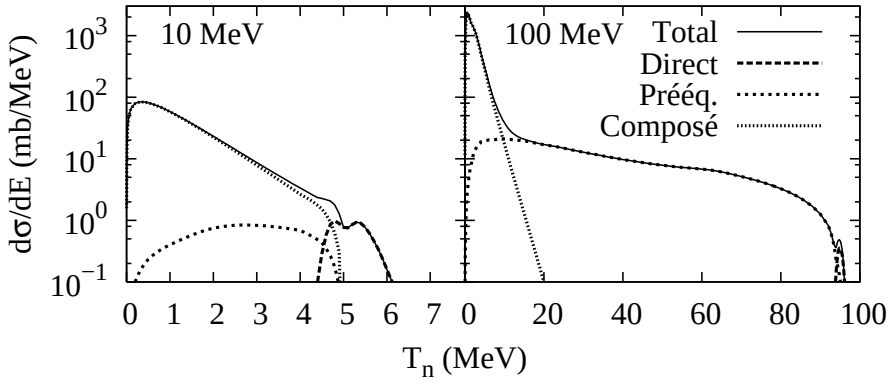

(b)

Figure 3.1: *Differential cross section for proton production 3.1(a) and neutron production 3.1(b) induced by protons on lead ^{208}Pb. The kinetic energy of the projectile are 10 MeV (left panel) and 100 MeV (right panel). The curves have been computed with the nuclear reaction code TALYS [33]. Taken from [34]*

3.2 The description of the nucleus

3.2.1 Introduction

In principle, the knowledge of the complete wave function of the nucleus gives us all of its properties, but the complexity of the wave function increases too rapidly with the number of nucleons. We are not able to determine it, except for the lightest nuclei, and even if we were, it would be too complicated to be useful. To describe the nucleus we use models instead. These models are, by essence, a simplification of the problem under consideration and one must chose carefully the model because each of them has its own successes and limitations. Nuclear models can be classified according to two categories (i) the semi-classical models (*e. g.* the liquid drop model or the Fermi gas model) or (ii) quantum models (*e. g.* the shell model).

We will limit ourselves to the description of the Fermi gas model, as this model is used in INCL to generate the nucleus at the beginning of each event.

3.2.2 Fermi gas model

In this model, the nucleus is considered as a collection of independent particles that are confined in a spherical region of radius R and a potential with a depth V_0. This potential has been introduced to account on the average for the interaction of a nucleon with all its partners.

The momentum distribution of the particles can be calculated [35, 36] and there is a Fermi momentum p_F defined by

$$p_F = \left(\frac{9\pi}{8}\right)^{1/3} \frac{\hbar}{r_0} \tag{3.1}$$

where $\hbar$ is the reduced Planck's constant and where r_0 is defined by the relation between the radius of the nucleus and its mass number A: $R = r_0 A^{1/3}$. This momentum corresponds to an energy, the Fermi energy $E_F = p_F^2/2M$, which is the maximum kinetic energy for a neutron bound in the nucleus. In the ground state, all particles have an energy $E < E_F$. They form the Fermi sea. The Fermi energy is different for protons because of Coulomb effects that should be taken into account. On figure 3.2 one can see an illustration of the nucleus as a finite square potential well. In this model, the excited states correspond to one or several particle-hole excitations.

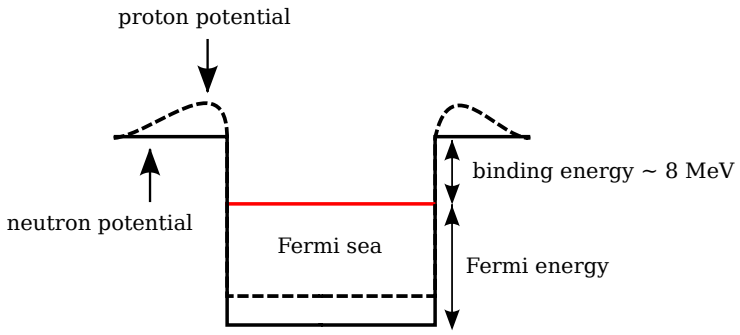

Figure 3.2: *Potential well for neutrons and protons in a heavy nucleus showing the Fermi level [35].*

3.3 Elastic scattering and total reaction cross section: The optical model

The optical model is based on the observation that the bulk features of the nucleus are determinant in the projectile-nucleus elastic scattering, contrary to the details of the nuclear structure. This observation leads to the assumption that, for this process, all nucleon-nucleon (NN) interactions between the projectile and the target can be replaced by a one-body interaction that can be represented by a potential V.

This potential, called the optical model potential, is a function of the relative position between the projectile and the target nucleus; general features of the potential can be deduced from the NN interaction [37]. The interaction between two nucleons is short-ranged and falls off exponentially with the distance; this indicates that (i) V(r) should also decrease exponentially and tend to zero outside the nucleus and (ii) it should be uniform inside the nucleus. The second point comes from the fact that the projectile only feels its nearest neighbors and is surrounded by nucleons; this leads to a null resultant force on the projectile inside the nucleus and, thus, to a constant potential.

If the potential was real, it would not be able to account for the flux diverted into other channels. In optics, scattering and absorption of light can be mathematically treated by a complex refractive index. It was then proposed to treat the absorption in nucleon-nucleus interaction by means of a complex potential. A simplified optical potential can thus be defined as

$$V(r) = -U(r) - iW(r), \tag{3.2}$$

with $U(r)$ and $W(r)$ both real and with $W(r)$ positive. The optical potential model enables to calculate simply [36] the elastic scattering cross section σ_E, the total reaction (or absorption) cross section σ_R and their sum σ_T, the total cross section:

$$\sigma_E = \frac{\pi}{k^2}\sum_L (2L+1)|1-S_L|^2, \tag{3.3}$$

$$\sigma_R = \frac{\pi}{k^2}\sum_L (2L+1)\left(1-|S_L|^2\right), \tag{3.4}$$

$$\sigma_T = \frac{2\pi}{k^2}\sum_L (2L+1)(1-\Re e S_L). \tag{3.5}$$

where k is the incident particle wave number and where S_L is the scattering amplitude of the Lth partial wave. An analysis performed with the optical model actually consists in the measurement of these cross sections and of the differential elastic cross sections. Then, through the scattering amplitude of partial waves, the form of the optical potential can be deduced and give, in turn, information about the nucleus.

In practice, the optical potential is more complicated than indicated in equation 3.2. The full optical model has two additional terms, an electrostatic term $V_C(r)$ for protons and other charged particles and a spin-orbit term $V_{so}(r)$. It is written as

$$V(r) = U f_U(r) + iW f_W(r) + V_C(r) + V_{so}(r). \tag{3.6}$$

the form factors $f_U(r)$ and $f_W(r)$ are chosen partly for mathematical convenience and partly on general physics arguments. A satisfactory choice for $f_U(r)$ is the Saxon-Woods function:

$$f_U(r) = \frac{1}{1+\exp\frac{r-R}{a}} \tag{3.7}$$

with the parameters R and a that can be linked to the radius and surface diffuseness of the nucleus, respectively. The imaginary part of the potential, as it describes the sum of the inelastic reactions, does not have the same profile: $f_W(r)$ may be different from f_U. The interested reader can find more information in [38, 36].

Systematic analysis of proton and neutron scattering have been performed with the optical model, to study the behavior of the potential with energy and from one nucleus to another. These studies have shown that the potential depth smoothly decreases with increasing energy. This feature of the potential has been introduced in the latest versions of INCL.

3.4 Direct reactions

Let us take the example of the inelastic scattering leading to the excitation of the target from its ground state Φ_0 to some low-lying excited state Φ_1. This is often successfully described by the so-called Distorted Wave Born Approximation (DWBA) model. The latter assumes that

there is one single interaction between the incoming particle and any nucleon of the target. The cross section thus assumes the following Born approximation form

$$\frac{d\sigma}{d\Omega} \propto |\langle \chi_{\vec{k}'}(\vec{r})\Phi_1| \sum_i v(\vec{r}-\vec{r}_i)|\chi_{\vec{k}}(\vec{r})\Phi_0\rangle|^2, \tag{3.8}$$

where v is the (effective) nucleon-nucleon interaction and where the χ's are the optical model scattering waves in the respective channels. To exhibit the fact that few degrees of freedom are involved, let us make the simplifying assumptions that the nucleon-nucleon interaction is zero-ranged ($v \propto \delta$) and that the incident particle wave functions in the entrance and exit channels (χ) are plane waves. Then the above expression reduces to

$$\frac{d\sigma}{d\Omega} \propto |\langle \Phi_1| \sum_i e^{-i\vec{q}.\vec{r}_i}|\Phi_0\rangle|^2, \tag{3.9}$$

where $\vec{q}$ is the momentum transfer. Finally, if Φ_0 is a Slater determinant and if Φ_1 is the same Slater determinant where a (hole) orbital is replaced by a (particle) orbital, the last expression becomes

$$\frac{d\sigma}{d\Omega} \propto |\int \psi_h^\star(\vec{r}) e^{-i\vec{q}.\vec{r}} \psi_p(\vec{r})|^2. \tag{3.10}$$

This expression is thus valid when the process reduces to the mere promotion of a target nucleon from the single-particle state h to the single-particle state p. The more general expression 3.8, when compared to the latter does give a "measure" of the probability for the state Φ_1 to be considered as a simple particle-hole excitation of the state Φ_0. In all generality, the functions χ in eq. 3.8 are taken as scattering states in the optical model potentials in the respective channels, in order to account for the loss of flux before and after the interaction, due to other competing channels. This complicates the analysis, but does not change the physical features outlined above.

3.5 The compound nucleus

At low energy, a few MeV, the compound nucleus mechanism (the capture of the projectile by the target to form an intermediate system which will de-excite by emission of ejectiles) is used to describe the reactions. This mechanism is suggested by the observation of narrow peaks in the cross sections, at those energies. These peaks are an indication that the reaction involves resonances, levels of the compound nucleus with rather precise excitation energies. When the C. N. does not have enough energy to emit more particles, it loses its excitation energy by gamma emission.

As we stated in the introduction, Bohr first introduced the concept of compound nucleus, along with the independence hypothesis: the decay channel of the C. N. is independent of its formation channel. We will present three models that can describe reaction cross sections, based on the compound nucleus assumption: the Breit-Wigner theory and the Weißkopf-Ewing and Hauser-Feshbach theories.

3.5.1 Breit-Wigner theory and resonances

A resonance corresponds to a state of given energy, spin and parity of the compound nucleus. The width Γ and the lifetime τ of resonances are connected to each other by the uncertainty principle $\Gamma\tau \approx \hbar$. As already mentioned above, the lifetime of C. N. states is of the order of

10^{-15} s. If we introduce the concept of reaction channel, defined by the interacting particles, their quantum numbers, their relative momentum and their spin, we can express Bohr's independence hypothesis by writing the cross section for a reaction leading from the channel α to the channel β, $\sigma_{\alpha,\beta}$, as the product of the cross section for formation of the compound nucleus through the channel α, $\sigma_{CN}(\alpha)$, times a branching ratio for the decay of the C. N. to channel β. This branching ratio can be expressed by the ratio of the decay rate in channel β, $\Gamma_\beta/\hbar$, and the total decay rate, $\Gamma/\hbar$. The cross section can thus be written as

$$\sigma_{\alpha,\beta} = \sigma_{CN}(\alpha)\frac{\Gamma_\beta}{\Gamma}. \tag{3.11}$$

The Breit-Wigner formula can describe the resonances of the cross sections. If the spin of the incident particle and the target nucleus are respectively i and I and the spin of the C. N. is J, α is the incident channel to form the resonance R, at energy E_R with a full width at half maximum equal to Γ_R, then the Breit-Wigner formula for the compound nucleus cross section σ_{CN}, in the vicinity of the resonance, is given by

$$\sigma_{CN} = \frac{\pi}{k^2}\frac{\Gamma_\alpha\Gamma_R}{(E-E_R)^2+\Gamma_R^2/4}\ \frac{2J+1}{(2i+1)(2I+1)}, \tag{3.12}$$

where E is the energy of the incident particle and $k = (2mE)^{1/2}/\hbar$ is the wave-number of the scattering wave-function.

It is practically impossible to make predictions of the resonances, their properties being related to fine details of the nuclear dynamics. As energy increases, the resonances get closer and closer and become wider. Eventually, they start to overlap and it becomes impossible to identify a single resonance and the cross section fluctuates. Its average value can be calculated using statistical models, such as the two models described just below.

3.5.2 The Weißkopf-Ewing and Hauser-Feshbach theories

Bohr's independence hypothesis was used by Weißkopf and Ewing to develop a theory of compound nucleus reactions that can be used to calculate the cross sections of reactions to the continuum [36].

If we consider a reaction that proceeds from an initial channel α to a final channel β with the intermediate formation of a compound nucleus, the reaction cross section is given by relation 3.11. We now consider the reciprocity theorem, that relates the cross section $\sigma_{\alpha,\beta}$ to the cross section for the time-reversed process $\beta\alpha$

$$g_\alpha k_\alpha^2\sigma_{\alpha,\beta} = g_\beta k_\beta^2\sigma_{\beta,\alpha}, \tag{3.13}$$

where $g_\alpha = 2i_\alpha + 1$ and $g_\beta = 2i_\beta + 1$ are the statistical weights of the initial and final channels, i_α and i_β the spin of the projectile and the ejectile, and k_α and k_β their wave-numbers. This gives

$$g_\alpha k_\alpha^2\sigma_{CN}(\alpha)\Gamma_\beta = g_\beta k_\beta^2\sigma_{CN}(\beta)\Gamma_\alpha \tag{3.14}$$

that can also be written as

$$\frac{\Gamma_\beta}{g_\beta k_\beta^2\sigma_{CN}(\beta)} = \frac{\Gamma_\alpha}{g_\alpha k_\alpha^2\sigma_{CN}(\alpha)}. \tag{3.15}$$

This relations should hold for all possible channels, thus

$$\Gamma_\alpha \propto g_\alpha k_\alpha^2\sigma_{CN}(\alpha). \tag{3.16}$$

As the total decay width can be defined as the sum over all the possible channels ($\Gamma = \sum_\alpha \Gamma_\alpha$), we obtain

$$\sigma_{\alpha,\beta} = \sigma_{CN}(\alpha)\frac{g_\beta k_\beta^2 \sigma_{CN}(\beta)}{\sum_\alpha g_\alpha k_\alpha^2 \sigma_{CN}(\alpha)}. \tag{3.17}$$

If we now consider the ejectiles with an energy comprised between ϵ_β and $\epsilon_\beta + d\epsilon_\beta$, the residual nucleus has an energy in the range U_β and $U_\beta = dU_\beta$ (U_β is the energy of the compound nucleus after the emission of the ejectile of energy ϵ_β, if the binding energy of the ejectile is taken into account). Introducing the level density of the residual nucleus $\omega(U_\beta)$, and since $k^2 = 2m\epsilon$, equation 3.17 becomes the Weißkopf-Ewing formula [39] for angle-integrated cross sections:

$$\sigma_{\alpha,\beta}(\epsilon_\beta)d\epsilon_\beta = \sigma_{CN}(\alpha)\frac{g_\beta \mu_\beta \epsilon_\beta \sigma_{CN}(\beta)\omega(U_\beta)dU_\beta}{\sum_\alpha \int_0^{E_\alpha^{max}} g_\alpha \mu_\alpha \epsilon_\alpha \sigma_{CN}(\alpha)\omega(U_\alpha)dU_\alpha}, \tag{3.18}$$

where μ_α is the reduced mass of the ejectile α. This theory is usually used to describe the de-excitation of a C. N. . Then the values of the partial widths Γ_β, given by the fraction in Eq. 3.17, are sufficient: this theory is simple to use but has the inconvenience that it does not consider explicitly the conservation of angular momentum and that it does not provide the angular distribution of the emitted particles, contrary to the Hauser-Feshbach theory. If the compound nucleus is in the state with angular momentum J, and the projectile and target angular momentum are, respectively, i_α and I_α, the Hauser-Feshbach expression for the energy-averaged angle-integrated cross section is [40]:

$$\sigma_{\alpha,\beta} = \frac{\pi}{k_\alpha^2}\sum_J \frac{(2J+1)}{(2i_\alpha+1)(2I_\alpha+1)}\,\frac{\sum_{s,l} T_l(\alpha)\sum_{s',l'} T_{l'}(\beta)}{\sum_\alpha \sum_l T_l(\alpha)} \tag{3.19}$$

where $T_l = 1 - |\bar{S}_l|^2$ is the transmission coefficient that can be defined from the optical model and relations 3.3. The quantities l and s are the angular momentum and the spin of the incident (emitted for the primed symbols) particle, respectively. Of course, the sums are limited by the possible couplings of the various angular momenta and spins. The angular distribution of emitted particles in a particular channel can be derived from equation 3.19, as shown in Ref [36].

3.6 Pre-equilibrium emission

3.6.1 General ideas

The angle-integrated spectra $d\sigma/dE$ presented in Figure 3.1 can be separated in three different energy regimes for the ejectiles. The high energy regime can be explained with the direct reactions models, which take into account the structure of the target, leading to the resonance structure particularly visible for the emission of protons with 100 MeV projectiles. The low energy regime, which has the shape of a Maxwellian shape is described with the compound nucleus model. The intermediate regime corresponds to the emission of particles before the statistical equilibrium is reached, they are called pre-equilibrium particles. It is particularly visible on the nucleon spectra (right panels) that the contribution of pre-equilibrium emissions increases with the projectile energy.

These emissions can be interpreted in the following way: a projectile enters the target and triggers a sequence of particle-hole excitations sharing its energy among a number of nucleons increasing at each interaction. Sometimes one of the nucleons has sufficient energy to escape from the nucleus. We will present here one of the models based on these ideas, introduced by Griffin [41], the exciton model. We will also discuss briefly the improvements that can be considered for this model.

3.6.2 The exciton model

In this model, the projectile can excite a particle located in the Fermi sea, by interaction with the nucleons of the target nucleus, and create a "particle-hole" pair. Both the excited particle and the hole are indiscriminately called excitons. The exciton model will essentially study the evolution of the number n of the excitons with time.

If p is the number of particles and h is the number of holes, the two-body interaction assumption induces some selection rules, and the number of excitons $n = p + h$ can only vary in one interaction as

$$\Delta p = 0, \pm 1, \qquad \Delta h = 0, \pm 1, \qquad \Delta n = 0, \pm 2, \tag{3.20}$$

Figure 3.3 shows the evolution of the number of excitons for the first interactions.

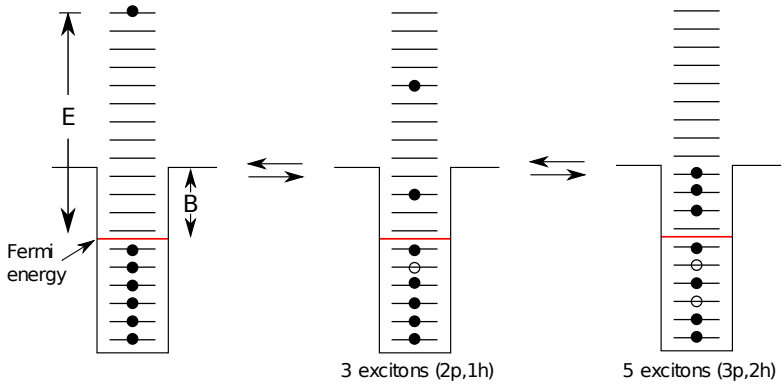

Figure 3.3: *Schematic representation of the first few stages of a nucleon-induced reaction in the exciton model. The horizontal lines indicate equally spaced single particle states in the potential well, the particles are represented by solid circles, the holes are represented by empty circles. E is the incident particle energy measured from the Fermi energy and coincides with the initial excitation energy; B is the nucleon binding energy. Figure adapted from [42]*

Assuming equally spaced single-nucleon states with density g, as in Fig. 3.3, the density of nuclear states, made of n excitons, of excitation energy E is given by

$$\rho_n(E) = \frac{g(gE)^{n-1}}{n!(n-1)!}. \tag{3.21}$$

The decay rate $\lambda^n_{n'}$ in which a compound nucleus in a n-exciton state evolves toward a state with $n' = n$ or $n \pm 2$ exciton can be written using Fermi's Golden rule as

$$\lambda^n_{n'}(E) = \frac{2\pi}{\hbar}\overline{|M|^2}\rho_{n'}(E), \tag{3.22}$$

where $\overline{|M|^2}$ is the mean value of the transition matrix element and $\rho_{n'}(E)$ is the density defined above (Eq. 3.21). As the density of states ρ_n increases with the number of excitons, one can easily see that we have

$$\lambda^n_{n'=n+2} \gg \lambda^n_{n'=n} \gg \lambda^n_{n'=n-2}$$

The probability $\mathcal{P}(p, h, E, \epsilon)$ to emit a particle with an energy between ϵ and $\epsilon + d\epsilon$ when the composite nucleus has a total energy E and is in a p-particle and h-hole configuration (the density ρ_n is then written as $\rho_{p,h}$) can be defined as

$$\mathcal{P}(p, h, E, \epsilon)d\epsilon = \frac{\rho_{p-1,h}(E - \epsilon)g(\epsilon)d\epsilon}{\rho_{p,h}(E)}, \tag{3.23}$$

where $g(\epsilon)$ is the free single particle state density. The decay rate for emission in the continuum of an unbound particle with energy $\epsilon_c = \epsilon - B$ (B is the binding energy), through the channel c, $\lambda_c(E, \epsilon_c)$ can be defined as the product of the probability defined above and a decay rate evaluated by the detailed balance principle [42]:

$$\lambda_c^n(E, \epsilon_c)d\epsilon_c = \mathcal{P}(p, h, E, \epsilon)d\epsilon \left(\frac{\sigma_{inv}(\epsilon_c) v \rho_c(\epsilon_c)}{g(\epsilon)V} \right). \tag{3.24}$$

where $\sigma_{inv}(\epsilon_c)$ is the particle inverse cross section, $\rho_c(\epsilon_c)$ is the density of the particle continuum states, v and $g(\epsilon)$ are the particle velocity outside the nucleus and its single-state density within the nucleus and V is the volume of the laboratory frame.

The probability $P(n, E, t)$ of finding the composite nucleus with excitation energy E at time t in a configuration with $n = p + h$ excitons can then be computed, using the decay rates defined by equations 3.22 and 3.24. One can obtain this so-called occupation probability by solving a set of Boltzmann master equations [43, 44]:

$$\begin{aligned} \frac{dP(n, E, t)}{dt} &= P(n-2, E, t)\lambda_n^{n-2}(E) + P(n+2, E, t)\lambda_n^{n+2}(E) \\ &\quad - P(n, E, t)\left(\lambda_{n+2}^n(E) + \lambda_{n-2}^n(E) + \lambda_c^n(E)\right). \end{aligned} \tag{3.25}$$

With the total decay rate for emission to the continuum of any particle with any energy $\lambda_c^n(E)$ defined by

$$\lambda_c^n(E) = \sum_{c'} \int_0^{E_{c',max}} \lambda_{c'}^n(E, \epsilon_{c'})d\epsilon_{c'}, \tag{3.26}$$

where $\lambda_{p,h,c}^n(E, \epsilon_c)$ is the decay rate given by Eq. 3.24.

If one defines the mean lifetime t_n of an n-exciton state with energy E as

$$t_n(E) = \int_0^{t_{eq}} P(n, E, t)dt \tag{3.27}$$

where t_{eq} is the equilibration time necessary to reach a state of statistical equilibrium. One can then integrate equation 3.25 over time to obtain

$$\begin{aligned} -P(n, E, 0) &= t_{n-1}(E)\lambda_n^{n-2}(E) + t_{n+2}(E)\lambda_n^{n+2}(E) \\ &\quad - t_n(E)\left(\lambda_{n+2}^n(E) + \lambda_{n-2}^n(E) + \lambda_c^n(E)\right). \end{aligned} \tag{3.28}$$

And once the value of $P(n, E, 0)$ is obtained, one can easily calculate the cross section for emission of particles in channel c:

$$\begin{aligned} \sigma_c(E, \epsilon_c)d\epsilon_c &= \sigma_R \int_0^{t_{eq}} \sum_{n, \Delta n=2} P(n, E, t)\lambda_c^n(E, \epsilon_c)d\epsilon_c \\ &= \sigma_R \sum_{n, \Delta n=2} t_n \lambda_c^n(E, \epsilon_c)d\epsilon_c. \end{aligned} \tag{3.29}$$

where σ_R is the reaction cross section for the incident channel and the sum runs over the number of excitons n, which is incremented by 2 for each term ($n = 1, 3, 5, \ldots$).

To solve the set of master equations 3.25 and 3.28, numerical, iterative or analytical methods can be used. One of the problems encountered is the determination of t_{eq}. In practice, one can easily find a time after which pre-equilibrium emission becomes negligible and thus assume that time to be t_{eq}.

The exciton model presented here can account for the shape of the energy spectra of the ejectiles, and for the energy differential cross sections when the reaction cross sections values are known (Eq. 3.29).

To take geometrical effects into account, one can introduce in this model a dependence on the impact parameter and sum over all the impact parameters, this has been realized in the "Geometry Dependent Hybrid model". The information about the ejectile or about the angular distribution of the ejectiles can also be included in the model. For instance, the two component exciton model makes the difference between protons and neutrons and the angular direction of the emitted particle can also be taken into account in the definition (3.23) of the emission probability. More details about these evolutions of the exciton model can be found in Ref. [42].

3.6.3 Intranuclear cascade model

General features

The intranuclear cascade proposed by Serber [3] in 1947 considers that the reaction induced by a high-energy particle (∼180 MeV in the original paper) can be viewed as proceeding in two stages, a sequence of two-body collisions that spreads progressively the energy of the projectile over an increasing number of nucleons, this stage is referred as the intranuclear cascade (INC) and is very fast; the second stage, slower than the cascade, takes place at the end of it and the residual nucleus de-excites by the usual evaporation processes.

The basic idea of this model is the following: when the energy of the projectile is high enough for its de Broglie wavelength λ to be of the order of the size of the nucleons, the projectile does not interact with the target nucleus as a whole but triggers an intranuclear cascade of two-body reactions. This is very different from the compound nucleus, as the degrees of freedom of the nucleons are explicitly taken into account here in these models.

The assumption of independent binary collisions implies that the nucleons involved in a collision have time to reach their asymptotical state before they get involved in another collision. We assume that this happens at a distance equal to the range of the nuclear interaction r_s. This leads to a double limitation for the domain of application of the intranuclear cascade:

$$\lambda \ll r_s \ll d, \tag{3.30}$$

where d is the mean distance between two nucleons. The nuclear interaction range, $r_s \approx 1$–1.5 fm, yields a low-energy bound for the projectile of $\sim$ 250 MeV to be in the cascade regime. The distance between the nucleons is evaluated to be $d \approx 2$–2.5 fm, so the second inequality is only partially respected. But an incident energy higher than this bound doesn't automatically respect the conditions 3.30, and if it does for the first collision, there is no guaranty that it will be respected for the subsequent collisions.

Serber also suggested that, if the nucleus is represented as a Fermi gas, the collisions with low-momentum transfer would be discouraged since these tend to lead from an occupied state to another occupied state; as a result of this suggestion the mean free path of the high energy particles is increased, as the duration of the cascade.

The INC models are valid for kinetic energies of the projectile ranging from a few hundreds MeV to a few GeV, which encompass the threshold for pions and the Δ resonance production. A Monte Carlo approach can easily be implemented to simulate such reactions. Usually, such simulations are semi-classical, because the particles are considered as point-like and follow classical trajectories. The uncertainty principle is not accounted for but some quantum features are included: the Pauli blocking, the introduction of a mean nuclear potential and the stochastic

nature of the final states. The particles are usually considered as moving according to straight classical trajectories, in a nucleus described with the Fermi gas model. If one of them reaches the surface of the nucleus with enough energy, it can be emitted.

One can consider that there are two approaches to simulate INC:

- **Space-like approach:** The nucleus is considered as a continuous medium and each participating nucleon (only the projectile at the beginning of the cascade) are given a mean free path[1]. When they have travelled that distance, they are supposed to collide with a nucleon from the continuum. The characteristics of the latter nucleon depend on the location of the collision inside the nucleus. This approach is used, for example, by the INC model ISABEL [21]
- **Time-like approach:** Each nucleon of the target and each particle of the projectile are considered in this approach. They are all given a position and a momentum. They are all propagated until two of them get close enough[2] to interact with each other.

The latter approach is used in the INCL model. At the end of the cascade, the residual nucleus de-excites through evaporation. The simulation models should be used with a separate model for de-excitation. Sometimes, a pre-equilibrium model is used after the cascade and before the evaporation, as for example in CEM [45]. The criterion used to stop the cascade in INCL makes this additional step unnecessary. More generally, both INC and pre-equilibrium models describe the evolution of an excited Fermi gas towards equilibration under the influence of binary collisions. There is thus a redundancy in using a pre-equilibrium model between the cascade and the evaporation. This point is discussed in Refs. [46]

Intranuclear cascade model and transport equations

The INC simulation model appears as a reasonable and empirical model embodying basic features of nuclei and nucleon-nucleon cross sections. However, it is partially substantiated by the efforts made in the nineties towards a theoretical derivation of a nuclear (intranuclear) transport theory. Derivations start with either the Green-function formalism or with the Liouville-von Neumann hierarchy for reduced density matrices, but yield basically the same result [47]. The Wigner-transformed one-body density $f(\vec{r},\vec{p})$ (which can be viewed as the phase-space distribution function) obeys a nuclear Boltzmann-like equation, under the following assumptions: (i) collisions are independent, (ii) ladder diagrams should be summed up (in the G-matrix), due to strong nuclear interactions (iii) other correlations than the two-body correlations entering the G-matrix are neglected (iv) only the leading terms of the small gradient expansions are retained. Condition (i) is equivalent to the condition $\lambda\!\!\!^{-} \ll r_S <\sim d$ mentioned in relation 3.30 above. The transport equation writes:

$$\begin{aligned}\frac{\partial f}{\partial t} + \frac{\vec{p}}{m}.\vec{\nabla} f - \vec{\nabla} U.\vec{\nabla}_p f + \vec{\nabla}_p U.\vec{\nabla} f = \\ \pi\hbar^2 \int \frac{d^3p_2}{(2\pi)^3}\int \frac{d^3p_3}{(2\pi)^3}\int \frac{d^3p_4}{(2\pi)^3}|G(12\rightarrow 34)|^2 \\ \times\{f_3 f_4 \overline{f}\ \overline{f}_2 - f f_2 \overline{f}_3 \overline{f}_4\}\delta^3(\vec{p})\delta(e(p)),\end{aligned} \tag{3.31}$$

[1]The mean free path is defined as $\lambda = 1/\rho\sigma$, where ρ stands for the density of the nucleus and σ is the elementary NN reaction cross section.

[2]Their relative distance should be inferior to a certain interaction distance $d_{int} = \sqrt{\sigma_{NN,tot}/\pi}$, where $\sigma_{NN,tot}$ is the total NN interaction cross section.

where $f_i = f(\vec{r}, \vec{p}_i, t)$ and $\overline{f}_i = 1 - f_i$. The delta functions stand symbolically for momentum and energy conservation in collisions. In addition,

$$e(p_i) = \frac{p_i^2}{2m} + U(p_i), U(p_i) = \int \frac{d^3p'}{(2\pi)^2} f' \langle \vec{p}_i \vec{p}' | G(\rho(\vec{r})) | \vec{p}_i \vec{p}' \rangle, \tag{3.32}$$

and G is the Brueckner matrix, solution of

$$G = V + V \frac{Q}{E - H_{12}} G, \tag{3.33}$$

where Q is the Pauli operator forbidding occupied intermediate states. Equation 3.31 without the rhs is just a drift equation (when the potential is constant) and can be solved by the test-particle (simulation) technique, as it is well known. It has been shown that INC simulation of collisions properly accounts of the collision term. In fact, summing over the runs amounts to a Monte-Carlo approximation of the collisional integral [48]. Therefore, the INC model is sometimes considered as a way to solve Eq.3.31 numerically for the average distribution f, when the mean field is kept constant and when the G-matrix (which represents the scattering matrix inside the nuclear medium) is taken as the free scattering matrix. One has to realize however that the INC model takes account of more correlations than the nuclear Boltzmann equation does [49]. Indeed, collisions depend upon the actual (in the same event) two-body distribution, which is correlated by previous collisions, at least in time-like INC models. The latter take account of all correlations, built by collisions, in all reduced distribution functions, not only in f. Whether these correlations are properly taken into account remains an open question.

Medium effects enter the nuclear Boltzmann equation at several places (the replacement of the free collision T-matrix by the G-matrix, the mean field which is self-consistently constructed from the G-matrix and the energy of the particles which includes this mean field effects). Whether these medium effects are important or not in practice remains an open question. The success of the INC models argues in favor of the smallness of these medium effects. An interesting discussion is contained in Ref.[50].

4

The Liège Intranuclear Cascade model

The Liège Intra Nuclear Cascade model was created in 1980 to study the collisions between heavy ions [51]. Five years later, the model has been adapted to $\bar{p}$–nucleus reactions. Soon after, a version of the model has been adapted and specialized to high energy proton-nucleus collisions. Over the last decade, an effort has been made to develop the code to make it suitable for simulations of particle therapy and radiological protection. The presentation of the successive versions of the code can be found in [22, 52, 53, 54, 55, 56, 57].

At the beginning of this PhD thesis, the standard version of the INCL code for nucleon-nucleus collisions was the INCL4.2 version, described in [58]. Since the present work has been based on an extension of this standard version, we will present the latter in section 4.1 by detailing each step of the simulation. In section 4.2, we will describe extensively the way INCL4.2 manages a collision between two particles; the extension to high energy of the code is performed mainly by modifying the collision process and by adding new inelastic channels that open in the 2–15 GeV range. Other extensions of the code have been developed in parallel with the extension to high energy presented here. They have been implemented in versions posterior to INCL4.2 and will shortly be presented in Section 4.4.

4.1 The INCL4.2 code

INCL4.2 is a Monte Carlo simulation code for the cascade stage of spallation reactions, written in fortran. It has been developed and tested in the 200 MeV–2 GeV incident kinetic energy range. INCL4.2 has proven to be one of the best codes for the simulation of spallation [58], when coupled with the evaporation code ABLA [23, 59]. It can reproduce a lot of relevant observables such as total reaction cross section, particle multiplicities, double differential cross sections, residue mass spectra, isotopic distributions and recoil energy spectra.

At the beginning of the simulation, the incoming particle (or projectile) and the target nucleus are randomly generated. Then, the projectile triggers a cascade of collisions, which are always binary in INCL4.2 and treated separately one from another. The cascade lasts until the stopping time, that is self determined by the model [58], is reached; then the remaining Δ resonances are forced to decay and the evaporation routine is called. One of the salient features of INCL4.2 is that it does not require any free parameter to be used.

Preparation of the projectile

The INCL4.2 model can accommodate nucleons and pions p, n, π^-, π^0 , π^+) as projectiles. The following quantities can be calculated from the incident kinetic energy T_{inc}:

$$\beta_{inc} = \sqrt{T_{inc}^2 + 2T_{inc}m_{inc}c^2}/(T_{inc} + m_{inc}c^2), \quad (4.1)$$

$$\gamma_{inc} = (1 - \beta_{inc}^2)^{-1/2}, \quad (4.2)$$

$$E_{inc} = m_{inc}c^2\gamma_{inc}, \quad (4.3)$$

$$p_{inc} = m_{inc}\beta_{inc}\gamma_{inc} \quad (4.4)$$

where m_{inc} is the mass of the projectile. The impact parameter vector of the projectile on the target nucleus is randomly determined in a circle of radius R_{max} centered on the incident direction passing by the center of the target. The maximum value of the impact parameter R_{max} is defined below.

The INCL4.2 model can also accommodate light clusters (d, t, ^3He, ^4He) as projectiles. Since we will not use this possibility in the present work, we refer to Ref [58] for details.

Generation of the target nucleus

Each of the A_T nucleons of the target is given a momentum and a position according to a uniform Fermi sphere and a Saxon-Woods distribution, respectively. The nucleon density distribution can be written

$$\rho(r) = \begin{cases} \frac{\rho_0}{1+\exp\frac{r-R_0}{a}} & \text{for } r < R_{max}, \\ 0 & \text{for } r > R_{max}, \end{cases} \quad (4.5)$$

where $R_{max} = R_0 + 8a$ and R_0 and a have been parametrized as functions of the target mass number A_T [58], the density ρ_0 is such that the distribution is normalized to A_T.

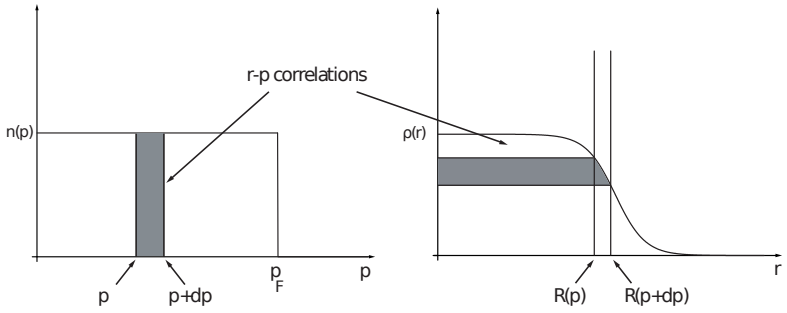

Figure 4.1: *Correlations in momentum–radial positions*

The momentum of the nucleons is generated according to a Fermi sphere distribution with a Fermi momentum p_F, as shown on Figure 4.1. A nucleon with a large momentum is expected to reach a larger radial distance than a nucleon with a small momentum. Therefore it is considered that a nucleon with a momentum p is to reach a maximum radial distance $R(p)$. Because of these $r - p$ correlations, a nucleon with a momentum between p and $p + dp$ should be located, with a constant uniform probability, in a sphere of radius $R(p)$. This radius can be deduced by assuming that the number of nucleons populating the layer of density profile $\rho\,(R(p))$ and $\rho\,(R(p + dp))$ is the same as the number of nucleon with a momentum between p and $p + dp$:

$$A_T \frac{4\pi p^2 dp}{\frac{4}{3}\pi p_F^3} = \frac{4}{3}\pi R^3(p) d\rho. \quad (4.6)$$

where $d\rho$ is the thickness of the density layer.

The limit conditions are naturally set to $R(0) = 0$ and $R(p_F) = R_{max}$, and the integration of equation 4.6 yields [58]

$$\left(\frac{p}{p_F}\right)^3 = \frac{4\pi}{3A_T}\int_0^{R(p)} \frac{d\rho(r)}{dr} r^3 dr, \tag{4.7}$$

from which $R(p)$ can be deduced.

This procedure is equivalent as choosing the initial position and momentum of any nucleon at random in the joint probability distribution:

$$\frac{dn}{d^3\vec{r}d^3\vec{p}} = f(\vec{r},\vec{p}) = A_T \frac{\theta(R(p)-r)\theta(p_F-p)}{\left(\frac{4\pi}{3}\right)^2 R^3(p)p_F^3}. \tag{4.8}$$

where $\theta(x)$ is the Heavyside function. In practice, the value of p can be generated from the uniform Fermi sphere distribution and the position is generated uniformingly in a sphere of radius $R(p)$.

Mean field of the nucleus

Nucleons are supposed to experience a nuclear mean field, which describes the smooth effect of the interaction with the other nucleons (in contrast with the collisions which correspond to rapid changes). In INCL4.2 this mean field is described by an attractive square well potential of the same depth V_0 for all baryons (nucleons as well as Δ 's). However, to be consistent with the description of the initial state of the target, the range of the potential depends upon the momentum of the baryons: it is taken equal to $R(p)$ for a target nucleon of momentum p. The combination of such a potential with the distribution 4.8 presents the advantage that this distribution is perfectly invariant on the average, under the propagation of the nucleons in absence of collisions. In other words, the average distribution of the nucleons is stable.

For particles with a momentum p larger than p_F it is assumed that the range of the average potential is equal to $R(p_F) = R_{max}$. In INCL4.2, there is no potential for pions.

Finally, the total energy of a particle is conserved when it enters or leaves the nucleus. As a consequence, the incident particle acquires a total kinetic energy $T_{inc} + V_0$, when it enters the nucleus (at $r = R_{max}$).

Propagation of the particles: the cascade

Once the target and the projectile are initialized, the particles are propagated using relativistic kinematics and following straight trajectories. In INCL4.2, there is a distinction between "participants" and "spectators". At the beginning of the event, the projectile is the only participant and afterward, each particle that has collided with a participant (or is created during an inelastic interaction) is promoted as a participant; every other particle is a spectator. The purpose for this distinction is to forbid collisions between spectators. This interdiction prevents the spectator nucleons near the surface of the Fermi sea to gain energy at the expense of another spectator and leave the nucleus, even if the latter was left alone.

When two particles, with at least one participant among them, reach their minimum distance of approach $\vec{d}_{min}$, INCL4.2 computes the impact parameter b_{min} of the system of the two particles in the center of mass frame using

$$b_{min}^2 = d_{min}^2 + \frac{(\vec{d}_{min}.\vec{\beta}_{cm})^2}{1-\beta_{cm}^2}, \tag{4.9}$$

where $\vec{\beta}_{cm}$ is the center of mass velocity in the laboratory frame.

The test to decide whether there will be an interaction or not is the following: the quantity πb_{min}^2 is compared to the total cross section for the center of mass energy $\sqrt{s}$ of the 2 particles $\sigma(\sqrt{s})$ and the decision is:

- if $\pi b_{min}^2 > \sigma(\sqrt{s})$, the motion of the particles is not perturbed and the particles can be propagated until the next collision check.
- if $\pi b_{min}^2 < \sigma(\sqrt{s})$, and provided that the Pauli blocking procedure does not forbid it, a collision happens. Afterwards, the next possible collision can be considered.

The Pauli blocking procedure will be explained hereafter. The collision mechanisms in INCL4.2 and the procedure to select the outgoing channel are explained in section 4.2. The possible outgoing channels for a collision of two nucleons are elastic and inelastic. In the latter case, a Δ_{1232} resonance is produced, with a life-time, and then decays in a pion and a nucleon.

Another peculiarity of INCL4.2 is that the time steps are determined in advance. The straight trajectories, the relativistic kinematics and the use of the minimum distance of approach as a criterion to test collisions are the features that allows INCL4.2 to generate a chronological table with the times for the possible avatars (collision, reflections or transmissions, and decays). When a collision is rejected, the particles are propagated until the next time in the table, the next time at which a participant and another particle reach their minimum distance of approach. If a collision happens, the table is updated to take into account the new trajectories of the outgoing particles or, if necessary, to add the entries for a particle produced during the collision. At the beginning of the cascade, INCL4.2 computes its stopping time t_{stop} (explained later on), this time is important because no interaction that would occur after that time is recorded in the table of times.

The dynamical Pauli blocking

The dynamical Pauli blocking in INCL4.2 operates in phase space and is implemented as follows: if there is a collision between two nucleons i and j at position $\vec{r}_{i(j)}$ that leads to a final state with momenta $\vec{p}_{i(j)}$, the phase space occupation probabilities f_i are evaluated by counting nearby nucleons in a small phase space volume,

$$f_i \;=\; \frac{1}{2}\,\frac{(2\pi\hbar)^3}{\frac{4\pi}{3}r_{PB}^3\;\frac{4\pi}{3}p_{PB}^3}\;\sum_{k\neq i}\;\theta\left(r_{PB}-|\vec{r}_k-\vec{r}_i|\right)\;\theta\left(p_{PB}-|\vec{p}_k-\vec{p}_i|\right), \tag{4.10}$$

where the sum is limited to particles k with the same isospin component as particle i (or j). The factor $1/2$ is introduced because spin components are ignored. The parameters r_{PB} and p_{PB} have been fixed to $r_{PB} = 3.18$ fm and $p_{PB} = 200$ MeV/c [58]. The decision test to allow or forbid the collision compares a random number with the product $(1 - f_i)(1 - f_j)$. In collisions that produce a Δ_{1232} resonance (see 4.2), the Pauli blocking is not applied to the Δ, because their density is very small. Pauli blocking is applied to the nucleon produced in the decay of the Δ. Finally, unphysical results can arise from the interplay between this implementation of the Pauli blocking and the fluctuations of the phase space occupation in the initial state, as the latter is randomly generated. Indeed, the Fermi sphere is filled on the average, but, in some events it may have holes and allow collisions to fill these holes unduly. This has been remedied by forbidding reactions with a final energy in the Fermi sphere lower than the minimum energy of a Fermi gas. The simultaneous use of these two constraints is referred as the Consistent Dynamical Pauli Principle (CDPP). See Ref [58] for more details.

Transmission and reflection on the surface

If the propagation of a particle would lead it through the nuclear surface, there is a possibility that the particle is reflected. Inside the nucleus, all the particles are submitted to a potential V_0. When a participant reaches the nuclear surface at $r = R(p)$, it can be reflected if its kinetic energy T_i is below the emission threshold ($T_i < V_0$), or otherwise transmitted with a probability[60]

$$T = \frac{4\sqrt{T_i(T_i - V_0)}}{2T_i - V_0 + 2\sqrt{T_i(T_i - V_0)}} e^{-2G}, \tag{4.11}$$

where G is the Gamow factor. If the test for the transmission is positive, the particle is ejected with a final kinetic energy $T_{fin} = T_i - V_0$, without change of direction. In other words, refraction is discarded.

One of the enhancements that have been implemented in INCL since the 4.2 version, described here, is the possibility for the nucleus to emit a cluster rather than a single particle; this new feature is presented in section 4.4.

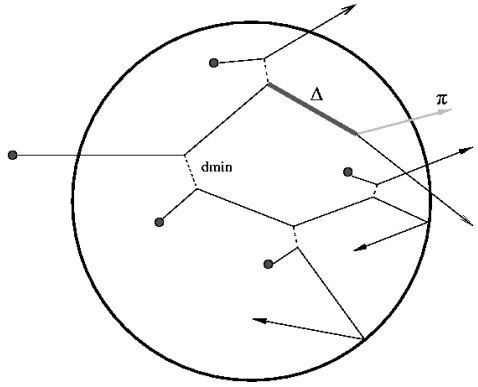

Figure 4.2: *Representation of an intranuclear cascade.*

Figure 4.2 represents an intranuclear cascade event; an incoming nucleon reaches the minimum distance of approach with another nucleon and undergoes an elastic collision; it moves towards a second interaction, inelastic, and a Δ resonance is produced; the Δ decays and the pion and nucleon are both transmitted through the nuclear surface; the second participant from the first collision has also caused secondary collisions and one of the participant nucleons is reflected on the surface.

Stopping time of the cascade

The cascade keeps going until the code reaches the bottom of the table of times. As we already stated, INCL4.2 computes a stopping time t_{stop} for the cascade. This time is evaluated in an self-consistent way [58] and was deduced from the monitoring and averaging over many simulations of some characteristic observables of the reaction such as the excitation energy E^*, its time derivative, the mean kinetic energy of the ejected particles (the ratio between the kinetic energy of the ejectiles T_{ej} and their mass number A_{ej}: T_{ej}/A_{ej}) and the anisotropy of the momentum content of the participant baryons inside the target volume ξ_{zz} defined as

$$\xi_{zz} = \frac{\sigma_z^2 - \frac{1}{2}(\sigma_x^2 + \sigma_y^2)}{\sigma_x^2 + \sigma_y^2 + \sigma_z^2}, \tag{4.12}$$

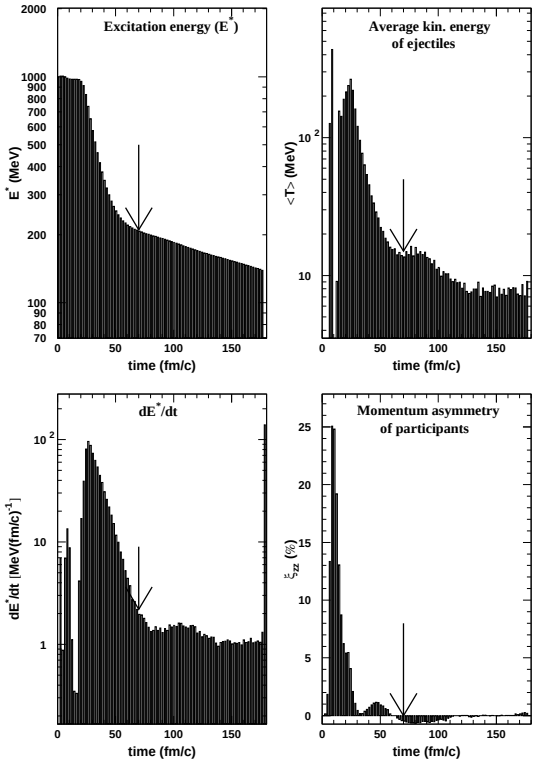

Figure 4.3: *Time variation of the value of the excitation energy E^* averaged over runs (upper left panel), the average kinetic energy of the ejectiles $\langle T \rangle$ (upper right panel), the time derivative of the excitation energy dE^*/dt (lower left panel) and the asymmetry of the participant momentum distribution ξ_{zz} within INCL4.2 (lower right panel). The results correspond to collisions of 1 GeV protons with Pb nuclei, at an impact parameter of 4 fm. The arrows indicate the chosen stopping time. Figure reproduced from [58].*

where z is the incident direction and the quantities σ_k^2 $(k = x,\ y,\ z)$ are defined by

$$\begin{aligned} \sigma_k^2 &= \sum_{i \in A_{rem}} (p_{i,k} - \langle p_{i,k} \rangle)^2, \\ \langle p_{i,k} \rangle &= \frac{1}{A_{rem}} \sum_{i \in A_{rem}} p_{i,k}, \end{aligned}$$

with the mass number of the remnant A_{rem}.

The obtained results (see figure 4.3) show that there is a more or less well-defined time that separates a phase with rapid variations and another phase with slow variations, typical from evaporation processes. It is then natural to choose this time as the stopping time of the cascade; it has been parametrized in INCL4.2 as

$$t_{stop} = f_{stop} t_0 \left(\frac{A_T}{208} \right)^{0.16}, \tag{4.13}$$

where $t_0 = 70$ fm/c and $f_{stop} = 1$ by default, the user can change this factor to modify t_{stop}. Note that, evaluated in this way, the stopping time is independent of the incident energy and of the impact parameter of the projectile.

End of the cascade

At the end of the cascade, surviving Δ resonances from inelastic collisions are forced to decay. Before INCL4.2 transmits to the evaporation routine the complete description of the remnant and the ejected particles, the conservation of baryon number, charge, energy, momentum and angular momentum is verified. If the subscripts P, T, ej, rem and π denote respectively the projectile, the target, the ejectiles, the remnant and the pions created trough resonances, we can write the conservation laws as

- *Baryon number conservation:* $A_P + A_T = A_{ej} + A_{rem}$,
- *Charge conservation:* $Z_P + Z_T = Z_{ej} + Z_\pi + Z_{rem}$,
- *Energy conservation:* $T_{lab} = K_{ej} + W_\pi + E_{rec} + E^* + S$
  where K_{ej} is the kinetic energy of the ejectiles, W_π is the total energy of the pions, E_{rec} is the recoil energy of the remnant and E^* its excitation energy, and finally S is the separation energy. It corresponds to the minimum necessary energy to remove all ejectiles and pions from the target nucleus ground state.
- *Momentum conservation:* $\vec{p}_{lab} = \vec{p}_{ej} + \vec{p}_\pi + \vec{p}_{rem}$,
- *Angular momentum conservation:* $\vec{l} = \vec{l}_{ej} + \vec{l}_\pi + \vec{l}_{rem} + \vec{l}^*$,
  where $\vec{l}$ is the angular momentum of the incident particle, $\vec{l}_{rem}$ the angular momentum corresponding to a c. m. motion of the remnant, and $\vec{l}^*$ is the intrinsic angular momentum of the remnant.

The first three laws are, in principle, automatically satisfied by INCL4.2. The last two laws allow to calculate the momentum and angular momentum of the remnant. INCL4.2 transmits to the evaporation routine all the information about the remnant (composition, momentum, excitation energy, angular moment). After de-excitation, all the properties of the cascade and evaporation particles and of the residue are recorded.

4.2 Elementary collisions

We are now going to explain in further details the treatment of collisions in INCL4.2.

Monte Carlo methods are used to select the outgoing channel by comparing a random number and the elementary cross sections of the various accessible channels. The parametrization of the cross sections that are used in INCL4.2 are presented in appendix A.

4.2.1 Baryon-Baryon (B-B) collisions

A subroutine named `COLLIS` is in charge of the B-B collisions. The center of mass frame is used in this subroutine, the rest of the cascade uses the laboratory frame. Another subroutine `LOREN` allows to switch from the laboratory frame to the center of mass frame and vice versa. The possible reactions are:

$$NN \Leftrightarrow NN, \tag{4.14}$$

$$NN \Leftrightarrow N\Delta, \tag{4.15}$$

where N stands for a nucleon and Δ stands for a resonance Δ_{1232}. There is always two outgoing particles, the use of the c.m. frame makes the splitting of energy and momentum over them simple.

The test for inelasticity compares a random number `rndm`, comprised between 0 and 1, and the ratio between the elastic and the total cross sections σ_{el}/σ_{tot} and yields:

- if $rndm < \sigma_{el}/\sigma_{tot}$ the elastic channel is selected,
- if $rndm > \sigma_{el}/\sigma_{tot}$ the inelastic channel is selected.

Elastic Baryon–Baryon collision

In an elastic collision between two baryons (nucleon–nucleon or nucleon–Δ), the differential cross sections are used to generate the final state in the center of mass of the system. We will develop here the proton-proton case, other cases can be found in [54]. The p-p differential cross section can be written

$$\frac{d\sigma}{dt} \propto e^{B_{pp}t}, \tag{4.16}$$

where t is the usual Mandelstam variable $t = (p_1 - p_3)^2 = (p_2 - p_4)^2$ and B_{pp} is a function defined by:

$$B_{pp} = \frac{5.5 p_{lab}^8}{7.7 + p_{lab}^8}, \qquad p_{lab} < 2, \tag{4.17}$$

$$= 5.334 + 0.67(p_{lab} - 2), \qquad 2 < p_{lab}. \tag{4.18}$$

In this formula, B_{pp} is expressed in $(\mathrm{GeV}/c)^2$ and p_{lab} in GeV/c. A symmetrized version of the differential cross section should be needed, but because the collision is considered in the center of mass frame, Equation 4.16 is sufficient to completely determine the system since the two protons are emitted back to back.

Inelastic collision and Δ production

The inelastic cross section is taken as the difference between the total and the elastic cross section. Below 2 GeV, the inelasticity is dominated by one pion production channel and observations indicate that the pion production should mainly proceed through the Δ resonance. This picture has been used in INCL4.2: if the collision is inelastic, a Δ_{1232} resonance is given randomly a mass that follows the distribution

$$f(M) \propto \frac{1}{(M - M_0)^2 + \frac{\Gamma_0^2}{4}}\, \theta(M - M_n - m_\pi)\, \theta(\sqrt{s} - M_n - M), \tag{4.19}$$

where θ is the Heavyside function, and where $M_0 = 1.232$ GeV and $\Gamma_0 = 0.130$ GeV are the fundamental parameter of the Δ resonance, M_n and m_π are respectively the nucleon and the pion mass, and $\sqrt{s}$ is the center of mass energy. This corresponds to a truncated lorentzian distribution centered on the mean mass of the resonance (1232 MeV) and with a width of 130 MeV. The lifetime of the Δ is randomly determined according to the exponential law

$$\rho(\tau) = \exp\left(\frac{-q^3}{q^3 + 180^3}\frac{\Gamma}{\hbar}\tau\right), \tag{4.20}$$

$\Gamma = 115$ MeV and q has the dimension of a momentum and is expressed by

$$q = \frac{\sqrt{\left[m_\Delta^2 - (m_N + m_\pi)^2)\right]\left[m_\Delta^2 - (m_N - m_\pi)^2\right]}}{2m_\Delta} \tag{4.21}$$

The description used for the angular distribution of the Δ production is:

$$\frac{d\sigma}{dt}(NN \to N\Delta) \propto e^{B'_{pp}t} \tag{4.22}$$

in this equation, t is the momentum transfer in from the incident nucleon to the Δ resonance and B'_{pp} is numerically close to the B_{pp} parameter.

4.2.2 The decay of the delta resonance

After its lifetime has elapsed, a Δ resonance decays in a pion and a nucleon. This decay is assumed to be anisotropic and the angular distribution of the produced pion is given in the Δ resonance c. m. frame by [22]:

$$\frac{d\sigma}{d\Omega} = 1 + 3\lambda \cos^2\theta_\pi, \tag{4.23}$$

where θ_π is the angle between the direction of the pion momentum in the rest frame of the Δ resonance and the direction of the momentum of the Δ resonance; λ is the helicity of the resonance and is a relic of the production of the Δ . If the resonance was produced in a $N-N$ collision with a polar angle ϑ in the center of mass frame, then the helicity λ of the resonance is given by $\cos^2\vartheta$.

The produced nucleon is submitted to Pauli blocking; if the phase space for the nucleon is already occupied, the decay is rejected and the lifetime of the Δ is increased. The decay rate $\Gamma(\Delta \to \pi N)$ of the resonance can be written using Fermi's golden rule as

$$\Gamma(\Delta \to \pi N) = \frac{2\pi}{\bar{h}} |\langle \pi N|\mathcal{M}|\Delta\rangle|^2 \rho \tag{4.24}$$

where $\langle \pi N|\mathcal{M}|\Delta\rangle$ is the transition matrix element of the reaction and ρ is the final state density. Assuming the isobar model, and subsequently the conservation of isospin, the previous equation yields:

$$\Gamma(\Delta_i \to \pi_j N_k) = \frac{2\pi}{\bar{h}} \left| \left(1j, \frac{1}{2}k|\frac{3}{2}i\right)\right|^2 |\langle \pi N|\mathcal{O}|\Delta\rangle|^2 \rho, \tag{4.25}$$

where the subscripts i, j, k represents the third component of isospin of the particles, $\left(1j, \frac{1}{2}k|\frac{3}{2}i\right)$ is a Clebsch Gordan coefficient and $\langle \pi N|\mathcal{O}|\Delta\rangle$ is the reduced matrix element, which does not depend upon i, j, or k.

The branching ratio for the decay of a given resonance, Δ^+ for example, gives the probability for a given final state to be produced. These probabilities are used in INCL4.2 to set the type of the particles produced in the decay. If we consider the Δ^+ decay, we obtain

$$\frac{\Gamma(\Delta^+ \to \pi^+ n)}{\Gamma(\Delta^+ \to \pi^0 p)} = \frac{|\left(11, \frac{1}{2}-\frac{1}{2}|\frac{3}{2}\frac{1}{2}\right)|^2}{|\left(10, \frac{1}{2}\frac{1}{2}|\frac{3}{2}\frac{1}{2}\right)|^2} = \frac{1/3}{2/3} = \frac{1}{2}, \tag{4.26}$$

the final state densities and the reduced matrix element disappeared because of the isobar model, the Clebsch-Gordan coefficients are the only remaining factors. We can also compute

$$\frac{\Gamma(\Delta^0 \to \pi^- p)}{\Gamma(\Delta^0 \to \pi^0 n)} = \frac{|\left(1\,-1, \frac{1}{2}\frac{1}{2}|\frac{3}{2}\,-\frac{1}{2}\right)|^2}{|\left(10, \frac{1}{2}\,-\frac{1}{2}|\frac{3}{2}\,-\frac{1}{2}\right)|^2} = \frac{1/3}{2/3} = \frac{1}{2}, \tag{4.27}$$

$$\frac{\Gamma(\Delta^{++} \to \pi^+ p)}{\Gamma(\Delta^0 \to \pi^- p)} = \frac{|\left(11, \frac{1}{2}\frac{1}{2}|\frac{3}{2}\frac{3}{2}\right)|^2}{|\left(1\,-1, \frac{1}{2}\frac{1}{2}|\frac{3}{2}\,-\frac{1}{2}\right)|^2} = \frac{1}{1/3} = 3, \tag{4.28}$$

The same procedure can be applied to the production of Δ resonances and yield

$$\begin{aligned} \frac{\sigma(pp \to p\Delta^+)}{\sigma(pp \to n\Delta^{++})} &= \frac{1}{3}, \\ \frac{\sigma(np \to n\Delta^+)}{\sigma(np \to p\Delta^0)} &= 1, \\ \frac{\sigma(nn \to n\Delta^0)}{\sigma(nn \to p\Delta^-)} &= \frac{1}{3}, \end{aligned} \tag{4.29}$$

4.2.3 Pion-Nucleon collisions

In INCL4.2, pions can only be produced through Δ resonances, but once they have been produced they can, in turn, interact with the nucleons. The total reaction cross sections used in INCL4.2 are presented in appendix A.

Inelastic channels in $\pi - N$ collision are partly neglected by INCL4.2: In the energy range up to a few GeV, elastic scattering dominates. It is treated, up to $\sqrt{s} = 3$ GeV, as proceeding through the formation of a Δ with a shorter lifetime for $\sqrt{s} > 1.5$ GeV. The cross section is given by Eq. A.8. For $\sqrt{s} > 3$ there is no interaction.

The figure A.2, in appendix A, represents the experimental total $\pi^+ - p$ and $\pi^- - p$ cross sections. It is possible to use the isobar model, as we did in the previous section, to find the ratio between the various possible $\pi - N$ reactions. As an example the ratio between the $\pi^+ p$ and $\pi^- p$ reactions is given by

$$\frac{\sigma(\pi^+ p \to \Delta^{++})}{\sigma(\pi^- p \to \Delta^0)} = \frac{|\frac{3}{2}\frac{3}{2}|\left(11, \frac{1}{2}\frac{1}{2}\right)|^2}{|\left(\frac{3}{2}\ -\frac{1}{2}|1\ -1, \frac{1}{2}\frac{1}{2}\right)|^2} = \frac{1}{1/3} = 3, \tag{4.30}$$

which is in agreement with the experimental data shown on figure A.2 in the appendix A. On this figure, one can see that the maximum for the Δ resonance peak is around 210 mb and 70 mb for the $\pi^+ p$ and $\pi^- p$ reactions, respectively. The other resonances visible in Fig. A.2 are not pure $T = \frac{3}{2}$ resonances.

4.3 The evaporation code ABLA07

At the end of the cascade stage, the information on the remnant are transmitted to a de-excitation model. All the simulations presented in this work have been performed using the INCL + ABLA07 combination of models. We will shortly introduce here the salient features of ABLA07, a complete description of the model can be found in [24].

ABLA is the evaporation model of the abrasion-ablation code, initially developed by Bowman *et al.* [61], and have since been improved at GSI [62]. This dynamical code can be used to describe the de-excitation of a thermalized system using a comparison of the partial width of the various processes that are in competition:

Fission: this process plays an important role in the decay of heavy nuclei. At each de-excitation step, a competition between fission and other decay channels is realized using an analytical approximation of the one-dimensional Fokker-Planck equation for the time-dependent fission-decay width. An improved version of the semi-empirical fission model PROFI [62, 63] is called to compute the characteristics of the fragments formed in fission over a large range of energies.

Particle evaporation: the Weißkopf-Ewing formalism is used to compute the decay width Γ_ν of a specific initial nucleus by emission of a particle ν. The particles that can be emitted are p, n, d, t, ^3He, α or intermediate mass fragments (IMF). The kinetic-energy spectra of the emitted particles are directly calculated from the inverse cross sections.

Simultaneous break-up of the system: in the previous versions of ABLA, the IMF production was underestimated. To remedy this situation the range of emitted fragments has been extended to above $Z = 2$ either by evaporation or by the simultaneous break-up, which happens if the excitation energy per nucleon exceeds a limiting value.

Gamma emission: in the last de-excitation step of the evaporation cascade, the emission of photons becomes competitive with particle decay for heavy compound nuclei and are taken in account in ABLA07.

The probabilities associated with each channel $P_j = \Gamma_j / \sum \Gamma_i$ are used and compared in order to select the outgoing channel.

4.4 Parallel developments of INCL

Several improvements have been implemented in the INCL model since the 4.2 version was released. Even though our work is based on that version, it seems appropriate to complete the presentation of the model with the latest features included in it. We refer to Ref. [5, 64] for a detailed description of the latest version of INCL.

Among the improvements that have been added to the code, we will present here the cluster emission, the inclusion of known phenomenology, an enhanced Pauli blocking procedure, an improvement of the treatment of the soft collisions and finally the possibility for the participants to have their status changed under certain conditions.

Cluster emission

The emission of light clusters was one of the first developments implemented in the model, actually the only difference between INCL4.2 and INCL4.3 is the possibility to emit light clusters. It is realized through a dynamical coalescence mechanism [65], that has been further improved in the 4.5 version, but the main idea remains the same: a particle transmitted through the surface of the nucleus is able to drag along other nucleons to form a cluster, provided they are sufficiently close (in phase space).

In practice, when a particle reaches the surface with an energy higher than the threshold energy (see 4.1), it becomes the leading nucleon of a possible cluster. Potential clusters containing the leading nucleon are considered by the code (up to $A_{cl} = 12$ for the INCL4.5 version). The cluster which is basically the most bound cluster per nucleon is then selected and emitted if (i) its energy (in the target system) is above the threshold for emission (ii) the test for transmission through the Coulomb barrier is positive and (iii) the emission direction is not too tangential (the idea behind this criterion that a cluster has a high probability to get dissolved when it spends too much time in the nuclear surface). If all these tests are positive, the cluster will be emitted, otherwise the test for transmission or reflection, as explained in the description of INCL4.2, will performed for the leading nucleon only. At the end of the cascade, short lived clusters that could have been produced (e.g. ^5Li) are forced to decay. For more details and comparison with extensive experimental data, see Ref. [64].

Inclusion of known phenomenology

Phenomenology has always played an important role in the model as efforts have always been made to take it into account. In INCL4.5, it has been further enhanced without the introduction of user-based parameters with three mandatory modifications:

1. *Isospin and energy-dependent potential well* for nucleons have now replaced the sole constant potential that was in INCL4.2. This potential was inspired by phenomenology of the real part of the optical model potential [66].

2. *Average potential* for pions as well as a pion transmission to the Coulomb barrier have been added to the code. This potential is isospin-dependent too and is based on the phenomenology of the pion optical model [67].

3. *Deflection of charged particles in the Coulomb field* The Coulomb interaction between the charged particles and the nucleus is now taken into account in the calculation of the trajectories of the projectile and the emitted particles.

Pauli blocking

The way to construct the target nucleus in INCL4.2 may lead to a non uniform Fermi sea in a given event. The dynamical Pauli blocking, even though it has the advantage to account for the depletion of the Fermi sea, may then sometimes accept a collision that shouldn't be accepted. The compromise that has been followed in INCL4.5 to prevent this to happen, is the application of a strict Pauli blocking (the rejection of an event if the outgoing particles are not outside the Fermi sea) to the first collision. The Pauli blocking has been further hardened by the additional interdiction to consider collisions between two nucleons below the Fermi level, and not only between two spectators, as it was the case before.

Modification of the status of the participants

This feature allows participant nucleons that have an energy too close to the Fermi level to have their status changed back to spectators. The low limit has been fixed to the Fermi energy plus a small quantity fixed to 18 MeV. This procedure was inspired from the Isabel code[1][64, 5].

Soft collisions

Collisions in which the c. m. energy $\sqrt{s_0}$ doesn't exceed 1925 MeV are defined as *soft collisions*. They were neglected in INCL4.2 because they are expected to contribute more to the mean field rather than to affect the energy-momentum flow. Soft collisions usually occur when the nucleons are close to the Fermi energy and are expected to be forbidden by the Pauli blocking. The exception to this argument is the collision between a low-energy nucleon in the nuclear periphery. In INCL4.5, the treatment of soft collisions has changed as follows: (i) the energy threshold is not applied to the first collision, because neglecting the first collision at low energy may come to neglecting the entire event and (ii) the threshold value has now been lowered to $\sqrt{s_0} = 1910\ MeV$.

[1]The Isabel code is another intranuclear cascade model, its description can be found in Ref. [21]

5

Extension of INCL4.2 to high energy

To extend INCL4.2 to incident energies, up to about 15 GeV, we at least have to add the channels that open in the 2–15 GeV energy range in the nucleon-nucleon and pion-nucleon collisions; those are inelastic channels involving intermediate production of resonances. As already mentioned, the resonances that should be implemented are numerous, they have large width and a short lifetime (see Fig. 5.1). Moreover, their interactions with nucleons or with other resonances are not well known. Hence, one can formulate serious doubts about the usual modeling of collisions as forming resonances with a well-defined averaged lifetime, like it is usually done, for example, in QMD or other models. Indeed, the mass of a given resonance is, in general, taken at random in a distribution extending over an interval equal to the specific width, and it may very well be close to the average mass of another resonance with the same quantum numbers. One may really doubt about the appropriateness of treating such a resonance individually. Furthermore, as these resonances have a very small lifetime, they likely decay before interacting. Therefore, it is legitimate to raise the question of the relevance of taking account of the formation of resonances in elementary collision and to ask whether it is not more appropriate to model elementary resonances as giving directly the asymptotic states. This question is at the basis of this thesis.

Of course, modeling the elementary collisions as giving directly final particles can be a reasonable option only if the lifetimes of the various resonances are smaller than the time separating collisions. This time is actually roughly $d/\langle v\rangle$, where d is the average distance between two nucleons in the target and where $\langle v\rangle$ is the average relative velocity. Of course, the maximum value of $\langle v\rangle$ is limited by the velocity of the projectile $\langle v_{inc}\rangle$ and its minimum value is 0. So a conservative value is $\langle v\rangle \approx 1/2c$, $d \approx 2$ fm and $d/\langle v\rangle \approx 4fm/c$. This should be compared with the resonance lifetime which is $\tau\,[\mathrm{fm}/c] = 200/\Gamma\,[\mathrm{MeV}]$. This value ranges between 2 fm/c to 0.5 fm/c for the resonances in Fig. 5.1. Therefore, the modeling of the elementary collisions by direct production of the final states seems rather justified for the baryonic resonances. This is not completely true for strange resonances, their lifetime being very large compared to $d/\langle v\rangle$. However, the overall strangeness production remains quite small in the energy range under consideration compared to pion production which will be our main topic.

The situation is rather similar for mesonic resonances, although it is less favorable than for baryonic resonances. Production of narrow non-strange resonances, like η and ω, is more dis-

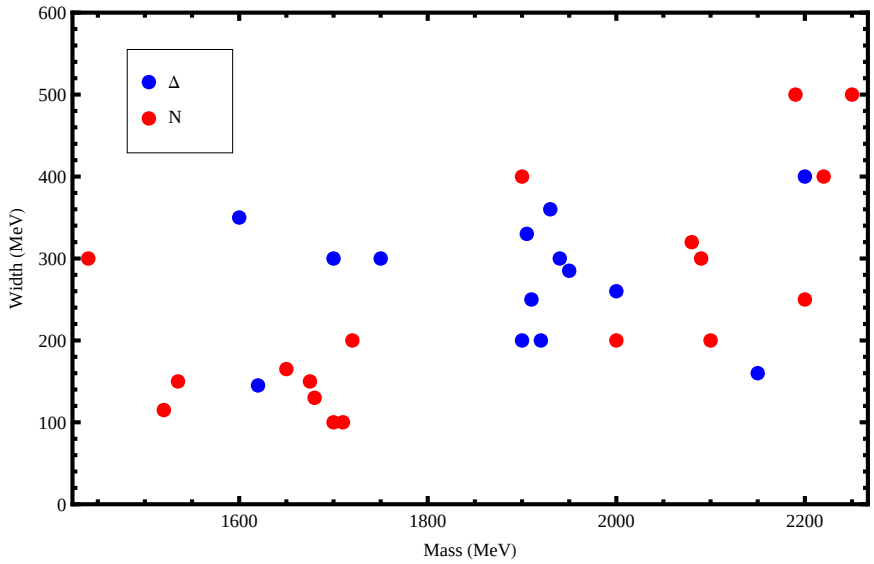

Figure 5.1: *Width of* Δ *-resonances (blue) and N resonances (red) as a function of their masses.*

turbing, as their lifetime clearly exceeds $d/\langle v \rangle$. However, their production is in general less important than pion production. Following these arguments, we decided to test the direct production picture in the extension of INCL4.2: instead of producing resonances in the high energy interactions, the decay products of the resonances are directly produced. Most of the resonances decay into nucleons, pions and, to a lesser extent, into strange particles. Strangeness is not included in INCL4.2. We recall that the contribution of strange-particle production cross sections to inelastic cross section is very low[1]. The extension to the production of strange particles remains a project for future work.

The decay of the resonances may produce more than one pion at a time. We have implemented in INCL4.2 the direct multiple pion production (also referred as the multipion production) up to four produced pions in NN collisions and up to three produced pions in πN collisions (four pions in the final state).

In Sec. 4.2, we explained that INCL4.2 uses the total NN cross section to test whether there is collision or not, and the corresponding elastic cross sections for determining whether the scattering is elastic or inelastic. This philosophy, to use cross sections as criterion to select the outgoing channel by means of Monte Carlo methods, has been kept in the extended version of INCL4.2. To take the multipion production channels into account, we thus have to parametrize their cross sections and use them to select the outgoing channels using Monte Carlo methods. But, as incident energy increases, the number of inelastic channels is increasing very much and it is hard to gather all the necessary information to determine all final inelastic channels. For a few of them, there is enough experimental data to allow a parametrization of the cross section but, for most of them (especially when the number of pions increases) the data is too scarce to have such parametrization. We have solved this problem by constructing "generic multiple pion production" cross section, exploiting available data and isospin symmetry as efficiently as possible. These generic cross sections can be used to select the number of produced pions. The determination of the outgoing channel being completed by a charge repartition model which attributes to each outgoing particle an electric charge.

[1] e.g. $\sigma(pp \to \text{strange particle})/\sigma(pp \to \text{inel}) \approx 7.5\%$ at 12 GeV/c

The generic multipion production cross sections $\sigma(NNa\pi)$ and $\sigma(\pi Na\pi)$[2], where a is the number of produced pions[3], are constructed by summing known cross sections for specific channels with the adequate value of a, or their parametrized forms. However, measurements are sometimes too scarce to give any indication on a possible parametrization of the specific cross sections, sometimes they simply do not exist, making impossible to construct directly the generic multipion production cross sections. In such cases, isospin conservation and isospin symmetry is used to palliate this lack of information. It is indeed possible to construct the cross sections $\sigma(NNa\pi)$ and $\sigma(\pi Na\pi)$ for definite isospin states of the initial state. For $a = 1, 2$, this turns out to yield unambiguous results; however, this is not the case for larger a. Other arguments, based on available experimental data give indications for the modeling of those cross sections; details are given in Sections 5.1.4 and 5.2.

The number of particles in the final state in a NN or πN collision being selected with the generic multipion production cross sections, the complete determination of the collision requires to attribute to each of the outgoing particles an electric charge. The model responsible for the charge repartition among the outgoing particles is described in Section 5.3. The idea is to associate a weight, a probability, to each possible outgoing channel with a given number of nucleons and pions and than to use Monte Carlo to select the charge repartition. For one produced pion in the final states, the probability for a given charge repartition is uniquely determined by isospin conservation and isospin symmetry. When there are two pions in the final states, a simplifying assumption have to be introduced to fully exploit isospin conservation and symmetry: the two pions are emitted in the lowest possible angular momentum state. For more than two pions in the final states, a specific model is needed. It is based on charge equilibration arguments.

Finally, once the outgoing particles are determined, the energy available in the collision must be shared among them, in agreement with conservation laws. We introduced an independent model for the repartition of energy and momentum. In agreement with what is said in [10], we adopted a uniform phase space model for repartition of the momenta. Comparison with experiment showed that this model was too simple and led us to further improve our approach by shifting from the uniform phase space model to a forward peaked biased model. This is described in Section 5.4. The various phases of the elaboration of the extension of the INCL4.2 model have been reported on in Refs. [6, 7, 8, 9].

5.1 Parametrization of the multipion production cross sections in NN collisions

We have parametrized the $a = 1, 2$ direct pion production using a procedure presented by Bystricky *et al.* [68]. In this article, the authors provide a procedure to parametrize the one- and two-pion production cross sections ($\sigma_I(NN\pi)$ and $\sigma_I(NN\pi\pi)$) in a given isospin state I, from the experimental data. This procedure does not require the knowledge of all possible channels with specific charged states; it is presented in section 5.1.1.

This procedure cannot be applied to parametrize isospin-dependent multipion production cross section when the number of produced pions is higher than two. We have thus constructed the isospin-dependent three-pion production cross section based on considerations made from experimental data available. It is presented in section 5.1.4. The four-pion production cross sections have been associated to the difference between the reaction cross section and the other

[2] This is a short-hand notation for $\sigma(NN \to NNa\pi)$ and $\sigma(\pi N \to \pi Na\pi)$.

[3] $a = 1,\ 2,\ 3,\ 4$ in NN collisions and $a = 1,\ 2,\ 3$ in πN

parametrized cross sections:

$$\sigma_I(NN4\pi) = \sigma_I^R - \sum_{a=1}^{3} \sigma_I(NNa\pi). \tag{5.1}$$

The limitation to $a = 4$ seems to be justified in the energy range under consideration. The generalization to higher values of a is however straightforward, even if the construction of the σ_I's rapidly becomes tedious.

5.1.1 The procedure of Bystricky et al.

The procedure presented by Bystricky *et al.* [68] for direct one- and two-pion production cross sections is based on isospin decomposition. Writing the elastic scattering amplitudes for two nucleons as

$$\begin{aligned} \langle pp|M|pp\rangle &= \langle nn|M|nn\rangle = M_1^{el}; \\ \langle np|M|np\rangle &= (M_1^{el} + M_0^{el})/2; \\ \langle pn|M|np\rangle &= (M_1^{el} - M_0^{el})/2. \end{aligned} \tag{5.2}$$

where one has for the isospin component

$$|pn\rangle = \frac{1}{\sqrt{2}}\left(|10\rangle + |00\rangle\right), \qquad |np\rangle = \frac{1}{\sqrt{2}}\left(|10\rangle - |00\rangle\right), \tag{5.3}$$

and, using the optical theorem, one gets

$$\begin{aligned} \sigma_{tot}(pp) &= \sigma_1, \\ \sigma_{tot}(np) &= (\sigma_1 + \sigma_0)/2, \end{aligned} \tag{5.4}$$

where σ_1 and σ_0 are the total NN cross sections in the isospin state $I = 1$ and $I = 0$, respectively. It follows from equations 5.2 that the relations 5.4 also hold for elastic cross sections and, therefore, also for reaction cross sections. One can thus write

$$\begin{aligned} \sigma_1^R &= \sigma^R(pp), \\ \sigma_0^R &= 2\sigma^R(np) - \sigma^R(pp). \end{aligned} \tag{5.5}$$

Assuming the dominance of pion emitting channels, one can relate the cross sections σ_I^R to the cross sections $\sigma_I(NNa\pi)$ as

$$\sigma_I^R = \sum_a \sigma_I(NNa\pi) \tag{5.6}$$

The $\sigma_I(NNa\pi)$ can be evaluated, in principle, by exhaustively summing the reaction cross sections for all compatible channels. For the simplest example ($a = 1$ and $I = 1$), one has

$$\sigma_1(NN\pi) = \sigma(pp \to pp\pi^0\,) + \sigma(pp \to np\pi^+). \tag{5.7}$$

A similar relation hold for $\sigma_0(NN\pi)$. This is also true for the two-pion production cross sections. Nevertheless, this way to compute the cross sections implies the knowledge of all the possible channels and, as the number of terms increases rapidly with the number of outgoing particles, it becomes difficult to apply, in practice, because of the incompleteness of the data.

Isospin symmetry can be used to reduce the number of cross sections needed. If we consider a reaction $NN \to NN\pi$, the idea is then to introduce the amplitudes

$$\left\langle I_f I_{3f} I_f^\pi I_{3f}^\pi | M | I_i I_{3i} \right\rangle , \tag{5.8}$$

where I_i and I_{3i} are the isospin and its projection of the initial nucleon system[4], I_f and I_{3f} are the isospin and its projection of the final nucleon system, I_f^π and I_{3f}^π are the isospin and its projection of the final pion. In the case of two incoming protons, whose isospin states can be found in B.1, we have:

$$\begin{aligned}
\left\langle pp\pi^0 \, | M | pp \right\rangle &= \langle 1110 | M | 11 \rangle = \frac{1}{\sqrt{2}} M_{11}, \\
\left\langle pn\pi^+ | M | pp \right\rangle &= \frac{1}{\sqrt{2}} \langle 0011 | M | 11 \rangle + \frac{1}{\sqrt{2}} \langle 1011 | M | 11 \rangle = \frac{1}{\sqrt{2}} M_{01} - \frac{1}{2} M_{11}, \\
\left\langle np\pi^+ | M | pp \right\rangle &= -\frac{1}{\sqrt{2}} \langle 0011 | M | 11 \rangle + \frac{1}{\sqrt{2}} \langle 1011 | M | 11 \rangle = -\frac{1}{\sqrt{2}} M_{01} - \frac{1}{2} M_{11},
\end{aligned} \tag{5.9}$$

where the coefficients appearing are Clebsch-Gordan coefficients and the reduced matrix elements follow the notation $M_{I_i I_f}$. Relations similar to 5.9 can be found for neutron-proton collisions in the initial state, they are presented in [68]. Using the definition $\sigma_{I_i I_f} = \int \left| M_{I_i I_f} \right|^2 d\Omega$, corresponding to an integration over all the final-state kinematic variables, we can write

$$\begin{aligned}
\sigma(pp \to pp\pi^0) &= \frac{1}{2} \sigma_{11}, \\
\sigma_\varphi(pp \to np\pi^+) &= \sigma_{01} + \frac{1}{2} \sigma_{11}.
\end{aligned} \tag{5.10}$$

The two relations in Eqs. 5.9, that respectively lead to the two cross sections $\sigma(pp \to pn\pi^+)$ and $\sigma(pp \to np\pi^+)$, have been summed to give the experimentally measured cross section indicated by the subscript φ. As a matter of fact, measured cross sections do not make the distinction between the two different possible isospin state for the pair of nucleons. More generally, each time a channel contains a pair of particles that can be interchanged (a pair of nucleons np, as in Eq. 5.10, or a pair of pions with different charges), all the relevant contributions to the amplitudes have to be taken into account and summed to obtain the experimentally measured cross section. In the following, the summation over the relevant contributions to the amplitudes will always be implied and the cross sections will always refer to the experimentally measurable ones, even if the subscript φ is not indicated.

In proton-neutron and neutron-neutron collisions, the same calculations can be performed to express the cross sections of particular channels as functions of $\sigma_{I_i I_f}$. It yields

$$\begin{aligned}
\sigma(nn \to nn\pi^0) &= \sigma(pp \to pp\pi^0) = \frac{1}{2} \sigma_{11} \\
\sigma(nn \to np\pi^-) &= \sigma(pp \to np\pi^+) = \sigma_{01} + \frac{1}{2} \sigma_{11} \\
\sigma(np \to pp\pi^-) &= \sigma(np \to nn\pi^+) = \frac{1}{3} \sigma_{10} + \frac{1}{2} \sigma_{11} \\
\sigma(np \to np\pi^0) &= \frac{1}{3} \sigma_{10} + \sigma_{01}
\end{aligned} \tag{5.11}$$

[4] A system composed of two nucleons can access the isospin states $I = 1$ or $I = 0$, we refer to appendix B for a complete description of the isospin states of systems of particles.

The one-pion production cross section in the isospin state I, $\sigma_I(NN\pi)$, can be decomposed as the sum of all the reactions leading to a final state with an isospin I. This gives

$$\begin{aligned} \sigma_1(NN\pi) &= \sigma_{01} + \sigma_{11}, \\ \sigma_0(NN\pi) &= \sigma_{10}. \end{aligned} \tag{5.12}$$

It is then possible to use the relations obtained in 5.10 and 5.11 to replace the $\sigma_{I_i I_f}$ in Eqs. 5.12, thus expressing $\sigma_1(NN\pi)$ and $\sigma_0(NN\pi)$ as linear functions of particular channel cross sections:

$$\begin{aligned} \sigma_1(NN\pi) &= \sigma(pp \to pp\pi^0\,) + \sigma(pp \to np\pi^+), \\ \sigma_0(NN\pi) &= 2\left[\sigma(np \to np\pi^0\,) + 2\sigma(np \to pp\pi^-)\right] \\ &\quad - \left[\sigma(pp \to pp\pi^0\,) + \sigma(pp \to np\pi^+)\right]. \end{aligned} \tag{5.13}$$

One can see the benefit of this procedure: the knowledge of all the possible cross sections is no longer necessary to compute $\sigma_I(NN\pi)$. For instance, $\sigma(np \to nn\pi^+)$ does not appear in the calculation of σ_0. Thus, to have a parametrization for this cross section is not necessary.

The same procedure can be applied to compute the isospin-dependent two pion production cross sections. In this case, the amplitudes are defined as

$$\left\langle I_f I_{3f} I_f^{2\pi} I_{3f}^{2\pi} | M | I_i I_{3i} \right\rangle, \tag{5.14}$$

where I_i, I_{3i}, I_f and I_{3f} have the same meaning as before and $I_f^{2\pi}$ and $I_{3f}^{2\pi}$ are the isospin and its projection of the final pion system. The reduced matrix elements will be noted as $M_{I_f I_f^{2\pi} I_i}$. In this case, we can have a pair of pions with different charges that can be interchanged, like we explained for the pn and np pairs. As an example, if we consider a pp collision, leading to a final state with two protons, one positive pion and one negative pion, we have to consider the amplitudes

$$\begin{aligned} \left\langle pp\pi^+\pi^- | M | pp \right\rangle &= \frac{1}{\sqrt{3}} M_{101} + \frac{1}{2} M_{111} + \frac{1}{\sqrt{60}} M_{121}, \\ \left\langle pp\pi^-\pi^+ | M | pp \right\rangle &= \frac{1}{\sqrt{3}} M_{101} - \frac{1}{2} M_{111} + \frac{1}{\sqrt{60}} M_{121}. \end{aligned} \tag{5.15}$$

To obtain the cross section $\sigma(pp \to pp\pi^+\pi^-)$, we have to sum the contributions of the cross sections computed from the amplitudes $\langle pp\pi^+\pi^- | M | pp \rangle$ and $\langle pp\pi^-\pi^+ | M | pp \rangle$, like we did in Eq. 5.10. Using the definition $\sigma_{I_i I_{2\pi} I_f} = \int \left| M_{I_i I_{2\pi} I_f} \right|^2 d\Omega$, we finally have

$$\begin{aligned} \sigma(pp \to pp\pi^+\pi^-) &= \frac{2}{3}\sigma_{101} + \frac{1}{2}\sigma_{111} + \frac{1}{30}\sigma_{121} \\ &\quad + \frac{1}{3\sqrt{5}} \int \left[M_{101}^* M_{121} + M_{121}^* M_{101} \right] d\Omega, \end{aligned} \tag{5.16}$$

where an interference term appears. The details of all possible amplitudes can be found in [68]. The cross sections obtained from these amplitudes are defined as:

$$
\begin{aligned}
\sigma(pp \to pp\pi^+\pi^-) &= \sigma(nn \to nn\pi^+\pi^-) = \frac{2}{3}\sigma_{101} + \frac{1}{2}\sigma_{111} + \frac{1}{30}\sigma_{121} \\
&\quad + \frac{1}{3\sqrt{5}} \int [M^*_{121} M_{101} + M^*_{101} M_{121}]\, d\Omega \\
\sigma(pp \to pp\pi^0\,\pi^0\,) &= \sigma(nn \to nn\pi^0\,\pi^0\,) = \frac{1}{3}\sigma_{101} + \frac{1}{15}\sigma_{121} \\
&\quad - \frac{1}{3\sqrt{5}} \int [M^*_{121} M_{101} + M^*_{101} M_{121}]\, d\Omega \\
\sigma(pp \to np\pi^+\pi^0\,) &= \sigma(nn \to np\pi^0\,\pi^-) = \sigma_{011} + \frac{1}{2}\sigma_{111} + \frac{3}{10}\sigma_{121} \\
\sigma(pp \to nn\pi^+\pi^+) &= \sigma(nn \to pp\pi^-\pi^-) = \frac{3}{5}\sigma_{121} \\
\sigma(np \to pp\pi^0\,\pi^-) &= \sigma(np \to nn\pi^+\pi^0\,) = \frac{1}{3}\sigma_{110} + \frac{1}{2}\sigma_{111} + \frac{3}{10}\sigma_{121} \\
\sigma(np \to np\pi^0\,\pi^0\,) &= \frac{1}{3}\sigma_{000} + \frac{1}{3}\sigma_{101} + \frac{4}{15}\sigma_{121} \\
&\quad + \frac{2}{3\sqrt{5}} \int [M^*_{121} M_{101} + M^*_{101} M_{121}]\, d\Omega \\
\sigma(np \to np\pi^+\pi^-) &= \frac{2}{3}\sigma_{000} + \frac{1}{3}\sigma_{110} + \sigma_{011} + \frac{2}{3}\sigma_{101} + \frac{2}{15}\sigma_{121} \\
&\quad - \frac{2}{3\sqrt{5}} \int [M^*_{121} M_{101} - M^*_{101} M_{121}]\, d\Omega
\end{aligned}
\tag{5.17}
$$

The two-pion production cross section in a given isospin state I, $\sigma_I(NN\pi\pi)$, are decomposed as the sum of all contributions that lead to the final state I; this gives:

$$
\begin{aligned}
\sigma_1(NN\pi\pi) &= \sigma_{011} + \sigma_{101} + \sigma_{111} + \sigma_{121}, \\
\sigma_0(NN\pi\pi) &= \sigma_{000} + \sigma_{110}.
\end{aligned}
\tag{5.18}
$$

We can use the relations 5.17 to replace the $\sigma_{I_i I_{2\pi} I_f}$, like we did in the one-pion production case (Eq.5.13). It yields

$$
\begin{aligned}
\sigma_1(NN\pi\pi) &= \sigma(pp \to pp\pi^+\pi^-) + \sigma(pp \to pp\pi^0\,\pi^0\,), \\
&\quad + \sigma(pp \to np\pi^+\pi^0\,) + \sigma(pp \to nn\pi^+\pi^+), \\
\sigma_0(NN\pi\pi) &= \frac{3}{2}\left[\sigma(np \to np\pi^+\pi^-) + \sigma(np \to pp\pi^0\,\pi^-)\right. \\
&\quad \left. - \sigma(pp \to np\pi^+\pi^0\,) - 2\sigma(pp \to pp\pi^0\,\pi^0\,)\,\right],
\end{aligned}
\tag{5.19}
$$

where all the interference terms have disappeared. These expressions show that we need to know (and parametrize) only six specific cross sections out of twelve possible different two-pion production cross sections.

5.1.2 Parametrizations of the reaction cross sections in the isospin state 0 and 1

It is possible to define σ_1^R and σ_0^R using the total inelastic pp and np cross sections, as shown in relations 5.5. Parametrizations of σ_1^R and σ_0^R used in INCL4.2 were limited to energies up to ∼3 GeV. We extended up to 15 GeV the parametrizations of $\sigma_{tot}(pp)$, $\sigma_{tot}(np)$, $\sigma_{el}(pp)$ and

$\sigma_{el}(np)$, coming from [34], with the fits proposed in [69]. These parametrizations depend on p_{lab}, the momentum in the laboratory frame[5]. They are given, with p_{lab} in GeV/c and σ in mb, by

$$\begin{aligned}
\sigma_{tot,pp} &= 34\left(\frac{p_{lab}}{0.4}\right)^{-2.104}, && p_{lab} < 0.44\\
&= 23.5 + 1000\ (p_{lab} - 0.7)^4, && 0.44 < p_{lab} < 0.87\\
&= 23.5 + \frac{24.6}{1+\exp\left(-\frac{p_{lab}-1.2}{0.10}\right)}, && 0.8 < p_{lab} < 1.5\\
&= 41 + 60\ (p_{lab} - 0.9)\exp\left(-1.2\ p_{lab}\right), && 1.5 < p_{lab} < 3.\\
&= 45.6 + 219\ p_{lab}^{-4.23} + 0.41\log^2(p_{lab}) - 3.41\log(p_{lab}). && 3. < p_{lab}
\end{aligned} \tag{5.20}$$

$$\begin{aligned}
\sigma_{tot,np} &= 6.3555\exp\left(-3.2481\log(p_{lab}) - 0.377\ \log^2(p_{lab})\right), && p_{lab} < 0.446\\
&= 33 + 196\ \left|p_{lab} - 0.95\right|^{2.5}, && 0.446 < p_{lab} < 1.\\
&= 24.2 + 8.9\ p_{lab}, && 1. < p_{lab} < 1.924\\
&= 48.9 - 33.7\ p_{lab}^{-3.08} + 0.619\log^2(p_{lab}) - 5.12\log(p_{lab}), && 1.924 < p_{lab}.
\end{aligned} \tag{5.21}$$

$$\begin{aligned}
\sigma_{el,pp} &= \sigma_{tot,pp}, && p_{lab} < 0.8\\
&= \frac{1250}{p_{lab}+50} - 4\ (p_{lab} - 1.3)^2, && 0.8 < p_{lab} < 2.\\
&= \frac{77}{p_{lab}+1.5}, && 2. < p_{lab} < 3.096\\
&= 11.2 + 25.5\ p_{lab}^{-1.12} + 0.151\log^2(p_{lab}) - 1.62\log(p_{lab}), && 3.096 < p_{lab}.
\end{aligned} \tag{5.22}$$

$$\begin{aligned}
\sigma_{el,np} &= \sigma_{tot,np}, && p_{lab} < 0.85\\
&= \frac{31}{\sqrt{p_{lab}}}, && 0.85 < p_{lab} < 2\\
&= \frac{77}{p_{lab}+1.5}. && 2 < p_{lab}.
\end{aligned} \tag{5.23}$$

As in INCL4.2, the inelastic cross sections are then defined by

$$\sigma_{inel,pp} = \sigma^R(pp) = \sigma_{tot,pp} - \sigma_{el,pp}$$
$$\sigma_{inel,np} = \sigma^R(np) = \sigma_{tot,np} - \sigma_{el,np}$$

And we can compute σ_1^R and σ_0^R using relations 5.5.

5.1.3 The one- and two-pion production cross sections $\sigma_I(NN\pi)$ and $\sigma_I(NN\pi\pi)$ parametrizations

Bystricky *et al.* also provide parametrizations for the experimental cross sections used in relations 5.13 and 5.19 (*e. g.* $\sigma(pp \to pp\pi^0)$, $\sigma(pp \to np\pi^+)$, etc.). If T_k is the threshold energy

[5]The momentum of a projectile in the laboratory frame depends on the center of mass energy following the relation

$$p_1^{lab}(s) = \frac{1}{2}\sqrt{\frac{m_2^4 + (m_1^2 - s)^2 - 2m_1^2(m_1^2 + s)}{m_2^2}}$$

where the subscript 1 relates to the projectile and the subscript 2 relates to the target. If the two interacting particles have the same mass $m_1 = m_2 = m$ then it can be simplified as $p_{lab} = \frac{1}{2}\sqrt{-4s + s^2/m^2}$

for the considered reaction k, Bystricky *et al.* parametrize the cross sections as

$$\sigma_k(x) = \begin{cases} 0 & \text{for } T \leq T_k \\ \left|F^k(x)\right|^2 & \text{for } T > T_k. \end{cases} \tag{5.24}$$

where x has been defined as $x = \ln(T/T_k)$. The effective amplitudes $F^k(x)$ are expanded into a series

$$F^k(x) = \sum_{n=0}^{\infty} a_n^k L_n^\alpha(x), \tag{5.25}$$

the parameters a_n^k having to be adjusted on experimental data [68] and $L_n^\alpha(x)$ being orthonormal functions:

$$L_n^\alpha(x) = e^{-x/2} x^{\alpha/2} \mathcal{L}_n^\alpha(x)$$

where the quantities $\mathcal{L}_n^\alpha(x)$ are the generalized Laguerre polynomials; the order α has to be positive to ensure proper threshold behavior. Best fits were obtained by setting $\alpha = 2$, therefore we will use this value as well.

We used the set of parameters $(T_k; a_n^k)$ from Ref.[68] and summarized in Tables 5.2 to 5.4. Table 5.2 gives the parameters used to compute the one-pion production cross sections, Tables 5.3 and 5.4 gives the parameters for the parametrization of the two-pion production cross sections, for incident pp and np interaction, respectively.

In Table 5.3, one can see that the number of neutral pions that is produced is not set. This is due to the fact that the data used by Bystricky *et al.* to perform these parametrizations were very scarce and imprecise. Nevertheless, the fits they proposed are in reasonable agreement with the data from [69] and we retained them. In general, their fits give satisfactory results in the energy range of interest here, namely from a few GeV to approximately 15 GeV. But, for a few cases the upper energy limit for the validity of the fit is very low. Above that value, the functions they provide diverge (see Fig5.2 for an example). Therefore, we extended their parametrizations, using fits at "high energy" of the form

$$\sigma = \frac{A}{(Bp_{lab} + 1)^2} \tag{5.26}$$

where A and B are parameters. The continuity of the cross section and its derivative allowed us to determine their values. They are summarized in Table 5.1.

Reaction	A (mb)	B $((\mathrm{GeV}/c)^{-1})$
$np \to np\pi^0$	611.576	2.3146
$pp \to pp\pi^0\,\pi^0\,(+m\pi^0\,)$	3.8942	0.23158
$pp \to np\pi^+(+m\pi^0\,)$	7.1233	0.04028
$pp \to nn\pi^+\pi^+(+m\pi^0\,)$	2.8878	0.01451

Table 5.1: *Parameters of the fit at high energy (see Eq.5.26.)*

On Figure 5.2 we show the parametrizations from Bystricky [68] for $\sigma(pp \to pp\pi^0\,\pi^0\,)$ (blue line) and its extension to higher energy (red line).

In summary, we used the parametrizations given by Bystricky [68] for $\sigma_I(NN\pi)$, and $\sigma_I(NN\pi\pi)$, where the isospin I can have the values 1 or 0. However, special care has to be exercised in two cases:

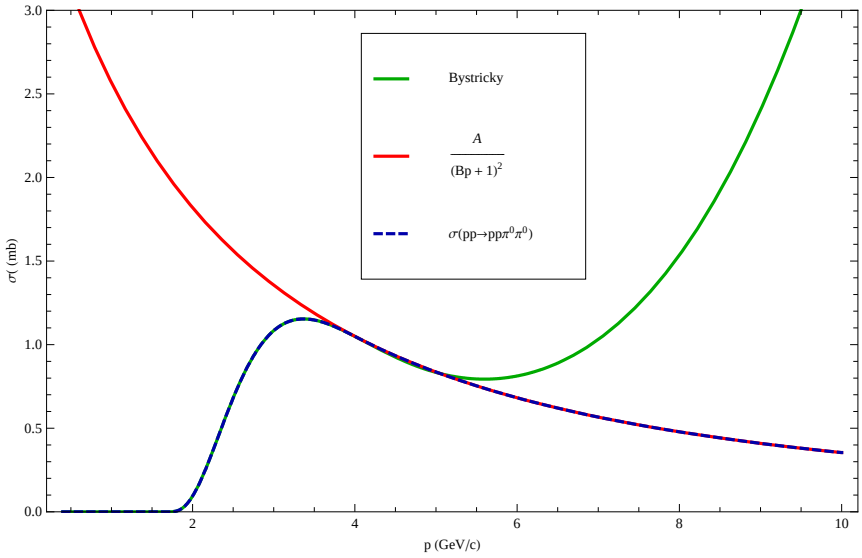

Figure 5.2: *Parametrization of $\sigma(pp \to pp\pi^0)$. At low energy, we follow the parametrization 5.24, connected at high energy with a power law of the form 5.26. The parameters are given in Tables 5.2 and 5.1.*

- when $\sigma_I(NN\pi)$, calculated by Eqs. 5.5 and 5.6, is larger than σ_I^R (due to numerical uncertainties in the parametrization, this may occur close to threshold, the excess being anyway limited to a few percent), the quantity $\sigma_I(NN\pi)$ is put equal to σ_I^R. Similarly, the value of $\sigma_I(NN\pi\pi)$, is bounded by $\sigma_I^R - \sigma_I(NN\pi)$, whenever necessary. This correction is however of minor importance, in practice.

- the functions 5.24 used in [68] diverge above energies around 15 GeV; however, in some cases the divergence already appears at 2 GeV. Because of this, we forced the functions to decrease, using parametrization 5.26. The value of the parameters are given in Table 5.1.

These parametrizations allow us to compute $\sigma_I(NN\pi)$ according to the relations computed in 5.13, and $\sigma_I(NN\pi\pi)$ according to the relations computed in 5.18.

The particular case of the delta resonance

In the standard version of INCL4.2, pion production was only possible through the creation and decay of Δ_{1232} resonances:

$$NN \to N\Delta, \qquad \Delta \to N\pi,$$

and the cross section for the first reaction is taken equal to the experimental inelastic cross section. This picture is based on the observation that this resonance is the dominant channel, below $E_{lab} \approx 2$ GeV. The results obtained with INCL4.2 are competitive with other models [5, 4, 58, 54]. Indeed, the mechanism described above is presumably correct at low energy. One should notice that this mechanism is inadequate in half of the np channel, namely the $I = 0$ component (a $I = 3/2$ resonance cannot be produced in a $I = 0$ channel). Since the dynamics of the Δ -resonance is already implemented in INCL4.2, since this dynamics is rather well understood and since the Δ -resonance has a relatively small width and is well isolated from other resonances, we decided to keep it where it is predominant. Specifically, we considered that

Coeff.	One-pion production channel			
	$pp \to pp\pi^0$	$pp \to np\pi^+$	$np \to np\pi^0$	$np \to pp\pi^+$
T_k	279.63	292.31	279.8	286.9
E_{max}	15	28	4.5	15
a_0	203.19	1200.3	8.4438	3.2048
a_1	-538.55	3738.9	-8.7429	-2.0695
a_2	906.90	-7498.0	8.5462	2.2426
a_3	-980.89	-10084.0	-3.3312	-1.0246
a_4	665.17	-9097.5		
a_5	-258.19	5311.7		
a_6	43.649	1822.6		
a_7		280.04		

Table 5.2: *Parameters of the fit for one-pion production exclusive inelastic reactions. The threshold energy for the considered reaction T_k is expressed in MeV. The value E_{max} is the upper energy limit of the fit, expressed in GeV. Adapted from [68].*

Coeff.	Two-pion production channel in $pp \to$			
	$pp\pi^+\pi^-$	$pp\pi^0\,\pi^0$ $(+m\pi^0)$	$np\pi^+$ $(+m\pi^0)$	$nn\pi^+\pi^+$ $(+m\pi^0)$
T_k	599.80	900	800	605.78
E_{max}	28	2	3.2	10
a_0	0.87175	50.553	50.282	0.95935
a_1	2.7436	-64.103	-63.216	0.94904
a_2	-3.7286	42.320	43.103	-0.76062
a_3	2.7880	-11.306	-12.031	
a_4	-1.0430			

Table 5.3: *Parameters of the fit for two-pion production exclusive inelastic reactions. The threshold energy for the considered reaction T_k is expressed in MeV. The value E_{max} is the upper energy limit of the fit, expressed in GeV. Adapted from [68].*

Coeff.	Two-pion production channel	
	$np \to np\pi^+\pi^-$	$np \to pp\pi^-\pi^0$
T_k	600.2	586.6
E_{max}	18	18
a_0	2.5273	0.057113
a_1	2.1099	2.2850
a_2	-5.5603	-1.4654
a_3	6.2285	0.16617
a_4	-4.3318	
a_5	1.3471	

Table 5.4: *Parameters of the fit for two-pion production exclusive inelastic reactions. The threshold energy for the considered reaction T_k is expressed in MeV. The value E_{max} is the upper energy limit of the fit, expressed in GeV. Adapted from [68].*

the one-pion production in the $I = 1$ channel proceeds through the Δ -resonance production mechanism. We however consider direct pion production in the $I = 0$ channel.

In our extended version of INCL4.2, when a collision between a proton and a neutron occurs, the initial state of the nucleons is given an isospin state $|10\rangle$ or $|00\rangle$, with a probability 1/2.

5.1.4 The three-pion production cross section $\sigma(NN\pi\pi\pi)$ parametrization

It is not possible to extend the procedure of Bystricky *et al.* to three-pion production cross sections. The quantities introduced in Eqs. 5.12 and 5.18 now have four indices. They are not related simply to physical cross sections, and the relations we search become very complicated and too many terms (corresponding to parametrizations of cross sections of particular channels) were involved. Furthermore, there are 16 different reactions to consider and all these reactions haven't been measured and even less been parametrized.

Nevertheless, there are a few observations that can be made from experimental data [69] in order to gather information on 3 pion production cross sections:

- We have data on three cross sections ($\sigma(pp \to pp\pi^+\pi^0\pi^-)$, $\sigma(pp \to np2\pi^+\pi^-)$ and $\sigma(pp \to np\pi^+2\pi^0)$). Their threshold values are estimated to be around 1.6 GeV/c (this corresponds to an incident kinetic energy around 0.9 GeV); but the available data starts only at 2.81 GeV/c and the cross section remains negligible at that energy. If we consider the one- and two-pion production cross sections that we have already parametrized, their sum starts to be smaller than the inelastic reaction cross section at a momentum of 2.2 GeV/c, in isospin state 1 and at a momentum of 3.84 GeV/c, in isospin state 0. In both cases, this corresponds roughly to the maximum of the two-pion production cross sections. We have set these momentum values as the start of the three-pion production cross section.

- The few data at our disposal show that the maximum for the three-pion production channels is located at a momentum of more or less 6 GeV/c. It seems reasonable to assume that below this maximum:

$$\sigma_I(NN\pi\pi\pi) = \sigma_I^R - \sigma_I(NN\pi\pi) - \sigma_I(NN\pi)$$

- Finally, we have to assume that the cross section $\sigma_I(NN\pi\pi\pi)$ will decrease after the maximum and we used parametrization of the same form as for one-pion production: $A/(B\ p_{lab} + 1)^2$. We solved the system of equations using the values at our disposal for the maximum at $p_{lab} = 6$ GeV/c and the experimental data at high energy to estimate the parameters A and B.

The cross sections $\sigma_I(NN3\pi)$ we have obtained, expressed as functions of the laboratory momentum p_{lab}, are parametrized by:

$$\begin{aligned}
\sigma_1(NN\pi\pi\pi) &= 0, && p_{lab} < 2.2 \\
&= \sigma_1^R - \sigma_1(NN\pi) - \sigma_1(NN\pi\pi), && 2.2 < p_{lab} < 6. \\
&= \frac{16778}{(p_{lab} + 37.061)^2}, && 6. < p_{lab}
\end{aligned} \tag{5.27}$$

$$\begin{aligned}
\sigma_0(NN\pi\pi\pi) &= 0, && p_{lab} < 3.84 \\
&= \sigma_0^R - \sigma_0(NN\pi) - \sigma_0(NN\pi\pi), && 3.81 < p_{lab} < 6. \\
&= \frac{5469.82}{(p_{lab} + 10.864)^2}, && 6. < p_{lab}
\end{aligned} \tag{5.28}$$

where p_{lab} is always given in GeV/c. Above 6 GeV/c, the four-pion production is assumed to open. Its cross section is assumed to be given by

$$\sigma_I(NN\pi\pi\pi\pi) = \sigma_I^R - \sigma_I(NN\pi) - \sigma_I(NN\pi\pi) - \sigma_I(NN\pi\pi\pi). \tag{5.29}$$

In the few experimental data that we found concerning the 4 pion production cross sections [69], it seems that even if the absolute threshold is around 2 GeV/c, the cross section stays negligible until 5.5–6.5 GeV/c with a maximum around 10–12 GeV/c. This is in agreement with the parametrizations we proposed. In principle, we should have constructed as well cross sections for n>4. However, for our purpose here, *i.e.* the extension of INCL4.2 to $\sim$ 10–12 GeV, this is not really necessary. First of all, as we have just mentioned, it seems to be consistent with the few available experimental data. Second, in the energy range under consideration, the number of NN collisions in the 8–12 GeV range (where n>4 processes might not be negligible) is very small compared to the whole number of NN collisions.

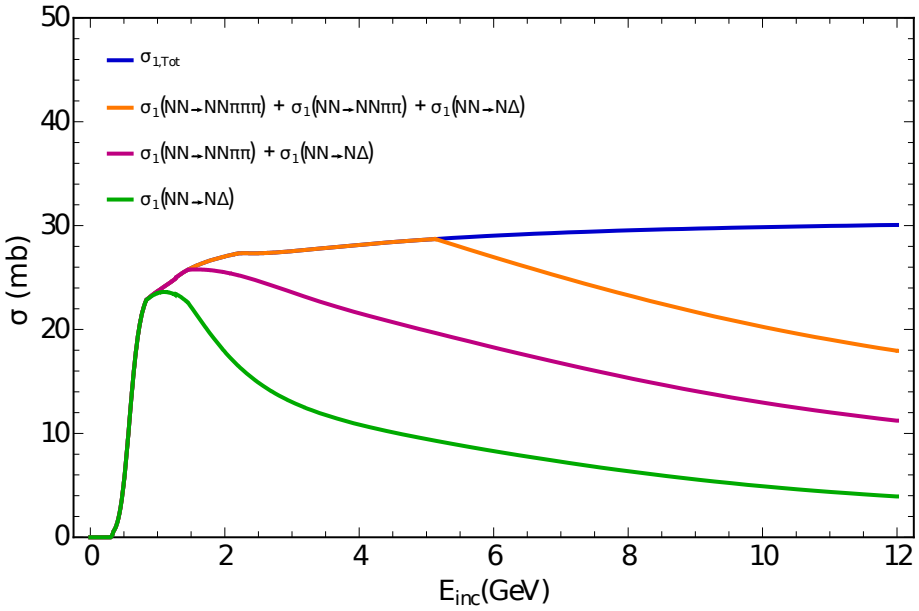

Figure 5.3: *The reaction cross section in the isospin state $I = 1$ σ_1^R (blue) and its decomposition (see Eq. 5.6) in $\sigma_1(N\Delta)$ (green), $\sigma_1(NN2\pi)$ (orange),$\sigma_1(NN3\pi)$ (purple).*

Figures 5.3 and 5.4 show the parametrizations for σ_1^R and σ_0^R, respectively, along with their decomposition in the one-, two-, three-, and four-pion production channels.

5.2 Parametrizations of the multipion production cross sections in nucleon-pion collisions

In INCL4.2, only the elastic channel in pion-nucleon collisions is considered and is assumed to correspond to the formation of a delta resonance, which is sufficient below 2 GeV. In this thesis, we have added the following pion producing inelastic channels:

$$N\pi \to N\pi\pi,$$
$$N\pi \to N\pi\pi\pi,$$
$$N\pi \to N\pi\pi\pi\pi.$$

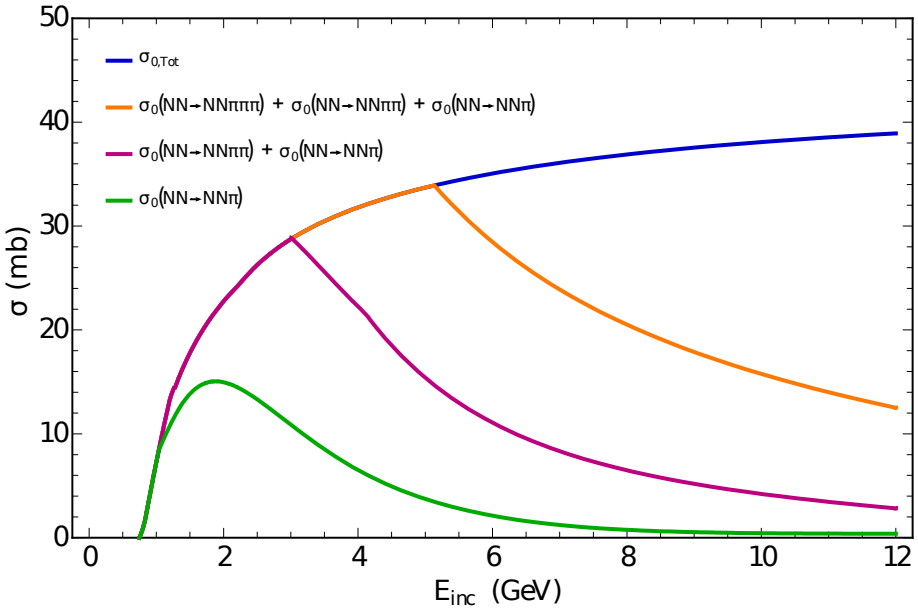

Figure 5.4: *The reaction cross section in the isospin state $I = 0$ σ_0^R (blue) and its decomposition (see Eq. 5.6) in $\sigma_0(NN\pi)$ (green), $\sigma_0(NN2\pi)$ (orange),$\sigma_0(NN3\pi)$ (purple).*

If we extend the procedure developed in Section 5.1.1 to the pion-nucleon system, we obtain a decomposition of the cross section in the isospin states $I = 3/2$ and $I = 1/2$ [34]:

$$\begin{aligned}
\sigma(p\pi^+) &= \sigma(n\pi^-) = \sigma_{3/2}, \\
\sigma(p\pi^-) &= \sigma(n\pi^+) = \frac{1}{3}\sigma_{3/2} + \frac{2}{3}\sigma_{1/2}, \\
\sigma(p\pi^0) &= \sigma(n\pi^0) = \frac{2}{3}\sigma_{3/2} + \frac{1}{3}\sigma_{1/2}, \\
&= \frac{\sigma(p\pi^+) + \sigma(p\pi^-)}{2}.
\end{aligned} \tag{5.30}$$

The relations 5.30 show that the total reaction cross section between a proton and a positive pion $\sigma(p\pi^+)$ and between a proton and a negative pion $\sigma(p\pi^-)$ are sufficient to define all the cross sections for collisions between a nucleon and a pion.

The parametrizations of the total and the total inelastic cross sections are presented in A.2. For the elastic channel, the fit of the delta resonance peak introduced in INCL4.2 has also been retained. Above the Δ resonance peak, the pion and the nucleon are assumed to form a hadronic system with a mass equal to $\sqrt{s}$ and a short lifetime, thus simulating an elastic scattering. For the inelastic channels, we used the parametrizations proposed in [69] for the inelastic cross sections $\sigma^R(N\pi)$. The function proposed in the $p\pi^+$ case was not valid at low laboratory momentum, its threshold behavior was wrong. To correct this defect, we have adjusted a low momentum component using a simple power law of the same form as suggested by [54]; assuming p_{lab} is expressed in GeV/c, this yields

$$\begin{aligned}
\sigma^R(p\pi^+) &= 17.965(p_{lab})^{5.4606}, && p_{lab} < 0.75 \\
&= 24.3 - 12.3(p_{lab})^{-1.91} + 0.324\log^2(p_{lab}) && \\
&\quad - 2.44\log(p_{lab}), && 0.75 < p_{lab}
\end{aligned} \tag{5.31}$$

$$\begin{aligned}\sigma^R(p\pi^-) &= 0, && p_{lab} < 0.473 \\ &= 26.6 - 7.18(p_{lab})^{-1.86} + 0.327\log^2(p_{lab}) && \\ &\quad - 2.81\log(p_{lab}), && 0.473 < p_{lab}\end{aligned} \tag{5.32}$$

The shape of $\sigma^R(p\pi^+)$ and $\sigma^R(p\pi^-)$ are given in Figs. 5.6 and 5.7. The cross section $\sigma^R(p\pi^0)$ can be derived easily, using 5.30, it is represented on Fig. 5.8.

5.2.1 One-pion production cross section $\sigma(N2\pi)$ parametrization

Experimental data and parametrizations can be found in [69] for the one-pion production inelastic channels in $p\pi^+$ collisions for the two possible outgoing channels:

$$p\pi^+ \begin{cases} \to & p\pi^+\pi^0\,, \\ \to & n\pi^+\pi^+. \end{cases} \tag{5.33}$$

In $p\pi^-$ collisions, there are three possible outgoing one pion production channels:

$$p\pi^- \begin{cases} \to & p\pi^-\pi^0\,, \\ \to & n\pi^+\pi^-, \\ \to & n\pi^0\,\pi^0\,. \end{cases} \tag{5.34}$$

In [69], experimental data for all these channels exist but they are very scarce for the last channel. There are suggested parametrizations only for the first two channels.

The $\sigma(N\pi\pi)$ cross sections all present the following shape: they first increase to a maximum value, generally a few mb for a center of mass energy around 2 GeV, depending on the channel. Above that energy, the cross sections start decreasing, parametrizations for all the channels are proposed in [69], as illustrated for the $p\pi^+ \to p\pi^+\pi^0$ channel on Fig. 5.5.

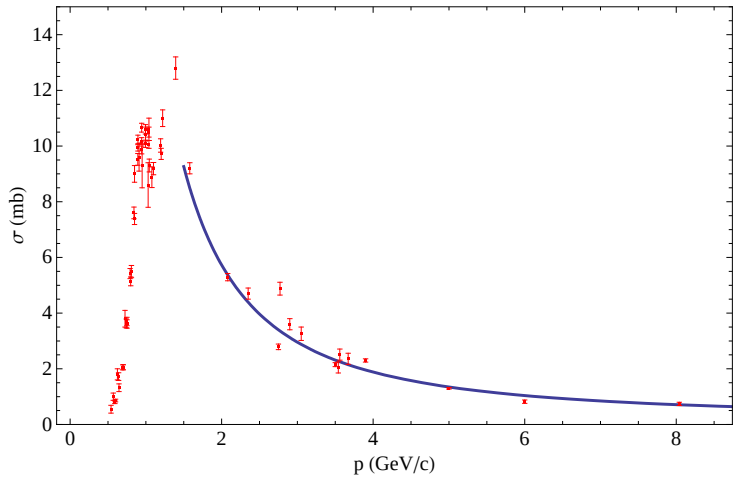

Figure 5.5: *Comparison between the experimental measures of $\sigma(p\pi^+ \to p\pi^+\pi^0)$ (red symbols) and the fit proposed in [69] (blue line), given in Eq. 5.35. The fit is only valid between 2 and 16 GeV/c incident momentum, we show here the fit extended down to 1.5 GeV/c incident momentum.*

If we consider a $p\pi^+$ collision, the possible final states with one produced pion are $p\pi^+ \rightarrow p\pi^+\pi^0$ and $p\pi^+ \rightarrow n\pi^+\pi^+$. The parametrizations mentioned above are given by:

$$\begin{aligned} \sigma\left(p\pi^+ \rightarrow p\pi^+\pi^0\right) &= 0.204 + 18.2\ p_{lab}^{-1.72} \\ \sigma\left(p\pi^+ \rightarrow n\pi^+\pi^+\right) &= 6.33\ p_{lab}^{-1.13} \end{aligned} \tag{5.35}$$

the limit of validity of these parametrizations are $2 < p_{lab} < 16$ GeV/c for both channels. One can notice that the lower limit of validity of the fit is slightly larger than the maximum observed in the cross sections. It appeared that the sum of these two parametrizations becomes smaller than the inelastic reaction cross section for a momentum $p_k = 1.55$ GeV/c, which is close to the momentum at which the cross section is maximum.

We have thus parametrized the one-pion production cross section in $p\pi^+$ collisions as:

$$\sigma(p\pi^+ \rightarrow N2\pi) \begin{cases} = \sigma^R(p\pi^+) & \text{for } p_{lab} < p_k, \\ = \sigma\left(p\pi^+ \rightarrow p\pi^+\pi^0\right) + \sigma\left(p\pi^+ \rightarrow n\pi^+\pi^+\right) & \text{for } p_k < p_{lab}. \end{cases} \tag{5.36}$$

The momentum range between 1.55 and 2 GeV/c is out of the domain of validity for the fit, but the cross sections parametrized this way have a maximum value around 17.9 mb, which is in agreement with the experimental data in [69]. If one sums the maximum values of the experimental cross sections, the maximum is 17.6 ± 0.7 mb at an incident momentum of 1.4 GeV/c. The agreement is good and we have kept the parametrized cross section as in Eq.5.36.

The one-pion production cross section in $p\pi^-$ collisions has been parametrized almost the same way. The existing fits proposed in [69] are:

$$\begin{aligned} \sigma\left(p\pi^- \rightarrow p\pi^0\,\pi^-\right) &= 9.04\ p_{lab}^{-1.17}, \\ \sigma\left(p\pi^- \rightarrow n\pi^+\pi^-\right) &= 13.5\ p_{lab}^{-1.21}, \end{aligned} \tag{5.37}$$

The measures of $\sigma\left(p\pi^- \rightarrow n\pi^0\,\pi^0\right)$ are to scarce to perform a fit. The shape of this cross section is similar to $\sigma\left(p\pi^- \rightarrow n\pi^+\pi^-\right)$ but with a value corresponding approximately to one third of the latter[6]. Thus we have parametrized it as

$$\sigma\left(p\pi^- \rightarrow n\pi^0\,\pi^0\right) = \frac{\sigma\left(p\pi^- \rightarrow n\pi^+\pi^-\right)}{3}.$$

Finally, the one-pion production cross section in $p\pi^-$ (and $n\pi^+$) collisions has been parametrized as

$$\sigma(p\pi^- \rightarrow N2\pi) \begin{cases} = \sigma^R(p\pi^-) & \text{for } p_{lab} < p_k, \\ = \sigma\left(p\pi^- \rightarrow p\pi^0\,\pi^-\right) + \sigma\left(p\pi^- \rightarrow n\pi^+\pi^-\right) \times \frac{4}{3} & \text{for } p_k < p_{lab}. \end{cases} \tag{5.38}$$

The threshold p_k has been determined to be 1.24 GeV/c. The maximum value of the parametrized cross section is $\sim$21 mb, to be compared with the sum of experimental data which has maximum with a value of 23 ± 2.05 mb at a momentum of 1 GeV/c. The agreement is satisfactory and we have kept the parametrization 5.38.

5.2.2 Two- and three-pion production cross section parametrizations

The experimental data for the particular channels producing two pions are very scarce. We have enough experimental data to parametrize only one channel in $p\pi^+$ (leading to the final state $p\ 2\pi^+\pi^-$) and one channel in $p\pi^-$ (leading to the final state $p\ \pi^+2\pi^-$).

[6]This is in agreement with our electric charge repartition model, presented in 5.3

As previously explained, the outgoing channel is selected according to a two-step procedure, first, we select the number of produced particles, using parametrizations of cross sections and, second, the charge repartition is selected by Monte Carlo methods and probabilities associated to each particular channels. These probabilities are presented in Sec. 5.3 and Tables 5.5(a) to 5.5(b) show all the probabilities associated with each channel in $N\pi$ collisions. As we have parametrizations for only one channel in $p\pi^+$ and in $p\pi^-$, the cross sections $\sigma(N\pi \to N\pi\pi\pi)$ have been modeled by somehow using these probabilities backward.

According to our extended version of INCL4.2, the cross sections $\sigma(p\pi^+ \to p\ 2\pi^+\pi^-)$ and $\sigma(p\pi^+ \to p\ 2\pi^+\pi^-)$ are obtained by the relation:

$$\begin{aligned} \sigma(p\pi^+ \to p\ 2\pi^+\pi^-) &= \frac{6}{15}\sigma(p\pi^+ \to N\ 3\pi), \\ \sigma(p\pi^- \to p\pi^+\ 2\pi^-) &= \frac{34}{135}\sigma(p\pi^- \to N\ 3\pi), \end{aligned} \tag{5.39}$$

where the factors 6/15 and 34/135 come from Tables 5.5(a) and 5.5(c), respectively. We have modeled the two-pion production cross sections by inverting the relations 5.39:

$$\begin{aligned} \sigma(p\pi^+ \to N\ 3\pi) &= \frac{15}{6}\sigma(p\pi^+ \to p\ 2\pi^+\pi^-), \\ \sigma(p\pi^- \to N\ 3\pi) &= \frac{135}{34}\sigma(p\pi^- \to p\pi^+\ 2\pi^-), \end{aligned} \tag{5.40}$$

In both cases, the obtained cross sections have been limited to prevent the sum of pion producing channels to be greater than the total inelastic cross section.

The three-pion production cross sections are obtained using

$$\sigma(N4\pi) = \sigma^R(N\pi) - \sigma(N2\pi) - \sigma(N3\pi). \tag{5.41}$$

Figures 5.6, 5.7 and 5.8 show the parametrizations of the $N\pi$ cross sections we have described above:

These figures indicate that the presence of $n > 4$ processes are probably not negligible for $E_{cm} \gtrsim 5$ GeV. Their neglect is not however a real concern for the general purpose of this thesis. In the nuclear reaction studied here, most of $N\pi$ collisions occur at energy which are safely below the value mentioned above.

5.3 Charge repartition model

The cross sections computed in the previous section allow to determine the number of pions produced in NN and $N\pi$ collisions, to completely determine the reaction, the electric charges of the outgoing particles must be determined. To do so, we have computed a probability to associate with each possible charge repartition over the outgoing particles, for a given number of produced pions, and for given incoming particle system.

For one- and two-pion production in NN collisions, the probabilities for reaching a final state with definite charges is almost uniquely determined by isospin conservation and isospin symmetry (only a simple reasonable assumption is needed). In the case of three- and four- pion production, the states of the produced particles cannot be uniquely determined by the same arguments, because a definite final charge state may correspond to different re-couplings of isospin states of the particles. Thus a charge repartition model is needed. We developed such a model, based on the probabilities obtained in the two pion production case, to associate as well a probability to each possible outgoing channel when more than 2 pions are produced. This model is presented in Section 5.3.1.

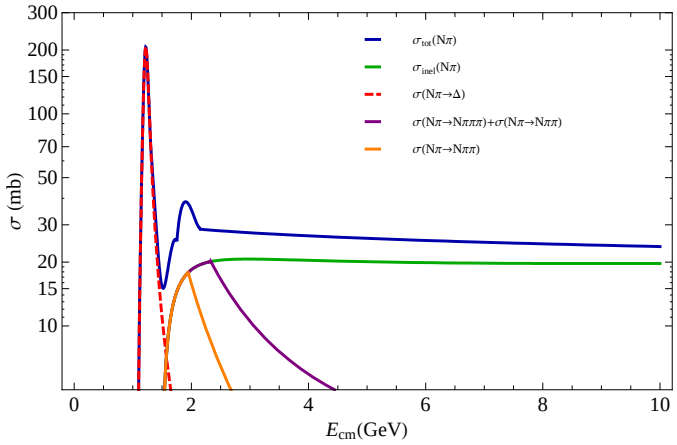

Figure 5.6: *Parametrizations of the cross sections in $p\pi^+$ and $n\pi^-$ collisions; the total reaction cross section (in blue) and the delta resonance production (red-dashed line) are parametrized as in INCL4.2 [34]. The inelastic cross section (in green) parametrized in Eq. 5.31, is decomposed in two-pion production channel (orange line) parametrized by Eq. 5.36 and three-pion production channel (purple line) as parametrized in 5.2.2 and the four-pion production channel, determined according to Eq. 5.41*

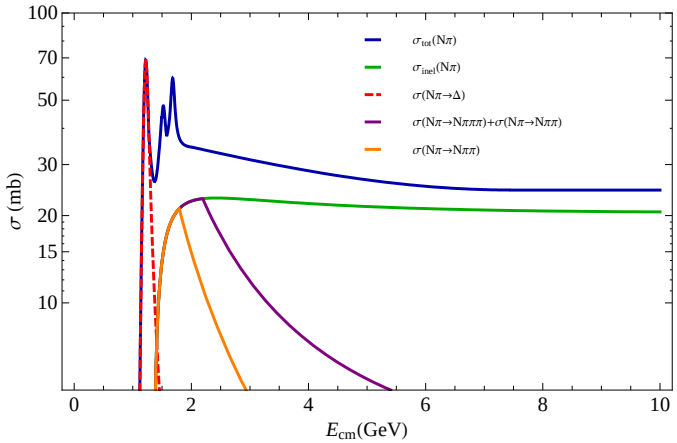

Figure 5.7: *Parametrizations of the cross sections in $p\pi^-$ and $n\pi^+$ collisions; the total reaction cross section (in blue) and the delta resonance production (in red) are parametrized as in INCL4.2 [34]. The inelastic cross section (in green) parametrized in Eq. 5.32, is decomposed in two-pion production channel (orange line) parametrized by Eq. 5.38 and three-pion production channel (purple line) as parametrized in 5.2.2 and the four-pion production channel, determined according to Eq. 5.41*

5.3.1 Nucleon–Nucleon collisions

Repartition of the charges in $NN \to N\pi$ channels

If the isospin state of the nucleons in the incoming channel is $|T_i m_i\rangle$, the one of the nucleons in the outgoing channel is $|T_f m_f\rangle$ and the one of the produced pion is $|T_\pi m_\pi\rangle$ (with $m_\pi = m_i - m_f$),

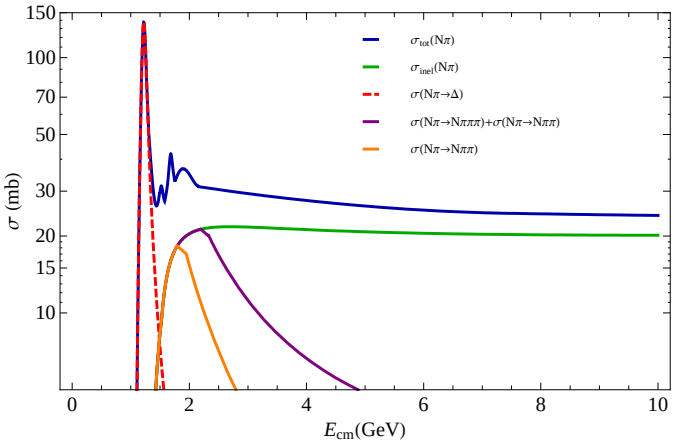

Figure 5.8: *Parametrizations of the cross sections in $p\pi^0$ and $n\pi^0$ collisions; each cross sections have been computed according to Eq.5.30 (the total reaction cross section in blue; the delta resonance production in red, the inelastic cross section in green, the two-pion production channel in orange, the three-pion production channel in purple)*

the probability P to associate with this channel can be written as:

$$P \ = C \left|(T_f \ m_f \ T_\pi \ m_\pi | \ T_i \ m_i)\right|^2 , \tag{5.42}$$

where C is a normalization factor. For fixed T_i and m_i, it is given by the relation

$$C \sum_{T_\pi, m_\pi} \left|(T_f \ m_f \ T_\pi \ m_\pi | \ T_i \ m_i)\right|^2 = C \sum_{T_\pi} 1 = 1.$$

which yields $C = 1$ as there is only one pion.

The one-pion production has been maintained to proceed through the delta resonance if the nucleons are in the isospin state $T = 1$; thus the direct one-pion production can only occur in the collision of a neutron and a proton, in the isospin state $T = 0$. The probabilities are then given by

$$\begin{aligned} np \to pp\pi^- \quad & P = |(111 \ -1|00)|^2 = 1/3, \\ np \to np\pi^0 \quad & P = |(1010|00)|^2 = 1/3, \\ np \to nn\pi^+ \quad & P = |(1 \ -111|00)|^2 = 1/3. \end{aligned}$$

Repartition of the charges in $NN \to N\pi\pi$ channels

The probability P associated with each channel in a collision producing two pions can be written

$$P \ = C \left|(T_f \ m_f \ T_\pi \ m_\pi | \ T_i \ m_i)\right|^2 , \tag{5.43}$$

where $|T_i m_i\rangle$ and $|T_f m_f\rangle$ are respectively the isospin states of the incoming and outgoing pair of nucleons and $|T_\pi m_\pi\rangle$ is, in this case, the isospin state of the two produced pions; C is defined as previously.

The calculation of the probabilities to associate with a pp reaction gives

$$pp \to pp\pi^+\pi^- \quad P = C\left(\frac{1}{3}\left|(1120|11)\right|^2 + \frac{2}{3}\left|(1100|11)\right|^2\right) \tag{5.44}$$

$$= C\left(\frac{1}{3}\frac{1}{10} + \frac{2}{3}1\right) = C\frac{21}{30} \tag{5.45}$$

$$pp \to pp\pi^0\,\pi^0 \quad P = C\left(\frac{2}{3}\left|(1120|11)\right|^2 + \frac{1}{3}\left|(1100|11)\right|^2\right) \tag{5.46}$$

$$= C\left(\frac{2}{3}\frac{1}{10} + \frac{1}{3}1\right) = C\frac{12}{30} \tag{5.47}$$

$$pp \to np\pi^+\pi^0 \quad P = C\left(\left|(1021|11)\right|^2\right) = C\frac{3}{10} \tag{5.48}$$

$$pp \to nn\pi^+\pi^+ \quad P = C\left(\left|(1\,-122|11)\right|^2\right) = C\frac{3}{5} \tag{5.49}$$

To compute these, we have used the symmetry properties of the two pion states under permutations which implies that $L+T$ should be even, where L is the angular momentum. Assuming that the 2 pions are produced in the lowest angular momentum state ($L = 0$), which seems reasonable, the two pion isospin states are limited to $T =$ even states. Hence, for instance, the produced $|\pi^+\pi^0\,\rangle$ state is a considered to have an isospin state $I = 2$ only. The renormalization factor $C = 1/2$, yielding:

$$pp \to \begin{cases} pp\pi^+\pi^- & \text{with } P = 7/20 \\ pp\pi^0\,\pi^0 & \text{with } P = 4/20 \\ np\pi^+\pi^0 & \text{with } P = 3/20 \\ nn\pi^+\pi^+ & \text{with } P = 6/20 \end{cases} \tag{5.50}$$

We can apply the same development to the nn and np reactions, the probabilities are given explicitly in the Tables 5.4(a) to 5.4(c).

Repartition of the charges in three- and four-pion production channels

As we already mentioned, for the $NN \to NN\pi\pi\pi$ reactions, we cannot compute uniquely the isospin states of the pion system (the recoupling of the individual isospins into the total isospin depends upon the order of the operation). Thus we have to adapt the definition of the probability 5.43 when there are more than 2 produced pions.

The probabilities we used have been computed under the assumption that the total electric charge does not depend on the number of produced pions. If ξ is the total electric charge of the pions and if we consider the probabilities computed above for the two-pion production in a pp collision, then we can write the probabilities P_ξ to associate with the production of a system of a pions ($a \geq 2$) as

$$\begin{aligned} P_0\left(pp \to pp(a\pi)^0\right) &= \frac{7}{20} + \frac{4}{20} = \frac{11}{20}, \\ P_{+1}\left(pp \to np(a\pi)^{+1}\right) &= \frac{3}{20}, \\ P_{+2}\left(pp \to nn(a\pi)^{+2}\right) &= \frac{6}{20}, \end{aligned} \tag{5.51}$$

where the notation $(a\pi)^\xi$ represents a system of a pions with a total electric charge ξ. If the total electric charge is not neutral, we separate the system of produced pions in the following way:

- the electric charge is given to $|\xi|$ pions,
- a system formed with the $(a-\xi)$ pions, if $a > \xi$, this system has a neutral global charge.

If we keep the example of a pp collision, this gives:

$$\begin{aligned} pp \to np(a\pi)^{+1} \quad &\Rightarrow \quad pp \to np\pi^+ \left((a-1)\pi\right)^0 \quad \text{given that } a > 1; \\ pp \to nn(a\pi)^{+2} \quad &\Rightarrow \quad pp \to nn\pi^+\pi^+ \left((a-2)\pi\right)^0 \quad \text{given that } a > 2. \end{aligned} \tag{5.52}$$

The remaining system of pions with a neutral electric charge (say b pions for simplicity) can be separated in a number of either $\pi^0\,\pi^0$ pair(s) or $\pi^+\pi^-$ pair(s) plus one π^0 if b is odd. Once the electric charge on the pions is known (probabilities given by relations 5.51) these pairs are the only element that can separate one final state from the other. Thus the probability to associate to one particular final state P, for a given number of produced pions is computed as

$$P = P_\xi \ \times \ (P(\pi^0\,\pi^0\,))^j \ \times \ (P(\pi^+\pi^-))^k, \tag{5.53}$$

where j and k are respectively the number of $\pi^0\,\pi^0$ and $\pi^+\pi^-$ pairs. Both isospin states of $\pi^0\pi^0$ and $\pi^+\pi^-$ are a mix between the states $|20\rangle$ and $|00\rangle$. We have computed the probabilities $P(\pi^0\,\pi^0\,)$ and $P(\pi^+\pi^-)$ assuming the pions are produced in the lowest isospin state $|00\rangle$:

$$\begin{aligned} P(\pi^0\,\pi^0\,) &= |(1010|00)|^2 = 1/3, \\ P(\pi^+\pi^-) &= |(111\ -1|00)|^2 + |(1\ -111|00)|^2 = 2/3, \end{aligned} \tag{5.54}$$

which actually correspond to a uniform production of supplementary pions (because of the multiplicity of $\pi^-\pi^+$).

Finally, if we consider the production of 3 pions in a pp collisions, we obtain the probabilities

$$pp \to \begin{cases} pp\pi^0\,\pi^+\pi^- & \text{with } P = 11/20 \times 2/3 = 22/60 \\ pp\pi^0\,\pi^0\,\pi^0 & \text{with } P = 11/20 \times 1/3 = 11/60 \\ np\pi^+\pi^+\pi^- & \text{with } P = 3/20 \times 2/3 = 6/60 \\ np\pi^+\pi^0\,\pi^0 & \text{with } P = 3/20 \times 1/3 = 3/60 \\ nn\pi^+\pi^+\pi^0 & \text{with } P = 6/20 = 18/60 \end{cases} \tag{5.55}$$

In Tables 5.5, we present the probabilities associated with three-pion production channels in np and nn collisions, along with the probabilities associated with four-pion production channels, computed according to the same method.

In np collisions, for both isospin states $|10\rangle$ and $|10\rangle$ of the system of nucleons, to compute probabilities to associate with channels with more than two produced pions, we have used the probabilities P_ξ given by the np collisions in the isospin state $|10\rangle$.

5.3.2 Charge repartition probabilities in nucleon-pion collisions

The same method as in NN collisions is applied. We just give a few details.

Repartition of the charges in one-pion production channels

The probabilities for a given final state is given by

$$P \ = C\,|(T_f\ m_f\ T_\pi\ m_\pi|\ T_i\ m_i)|^2\,, \tag{5.56}$$

(a)

pp →					
pp $\pi^+\pi^-$	7/20	pp $\pi^+\pi^-\pi^0$	22/60	pp $\pi^+\pi^-\pi^+\pi^-$	14/60
				pp $\pi^+\pi^-\pi^0\,\pi^0$	15/60
pp $\pi^0\,\pi^0$	4/20	pp $\pi^0\,\pi^0\,\pi^0$	11/20	pp $\pi^0\,\pi^0\,\pi^0\,\pi^0$	4/60
np $\pi^+\pi^0$	3/20	np $\pi^+\pi^+\pi^-$	6/60	np $\pi^+\pi^+\pi^-\pi^0$	6/60
		np $\pi^+\pi^0\,\pi^0$	3/60	np $\pi^+\pi^0\,\pi^0\,\pi^0$	3/60
nn $\pi^+\pi^+$	6/20	nn $\pi^+\pi^+\pi^0$	18/20	nn $\pi^+\pi^+\pi^+\pi^-$	12/60
				nn $\pi^+\pi^+\pi^0\,\pi^0$	6/60

(b)

nn →					
nn $\pi^+\pi^-$	7/20	nn $\pi^+\pi^-\pi^0$	22/20	nn $\pi^+\pi^-\pi^+\pi^-$	14/60
				nn $\pi^+\pi^-\pi^0\,\pi^0$	15/60
nn $\pi^0\,\pi^0$	4/20	nn $\pi^0\,\pi^0\,\pi^0$	11/60	nn $\pi^0\,\pi^0\,\pi^0\,\pi^0$	4/60
np $\pi^-\pi^0$	3/20	np $\pi^-\pi^+\pi^-$	6/60	np $\pi^-\pi^0\,\pi^+\pi^-$	6/60
		np $\pi^-\pi^0\,\pi^0$	3/60	np $\pi^-\pi^0\,\pi^0\,\pi^0$	3/60
pp $\pi^-\pi^-$	6/20	pp $\pi^-\pi^-\pi^0$	18/60	pp $\pi^-\pi^-\pi^+\pi^-$	12/60
				pp $\pi^-\pi^-\pi^0\,\pi^0$	6/60

(c)

np (T=1) →					
pp $\pi^-\pi^0$	3/20	pp $\pi^-\pi^+\pi^-$	6/60	pp $\pi^-\pi^0\,\pi^+\pi^-$	18/180
		pp $\pi^-\pi^0\,\pi^0$	3/60	pp $\pi^-\pi^0\,\pi^0\,\pi^0$	9/180
np $\pi^+\pi^-$	8/20	np $\pi^0\,\pi^+\pi^-$	28/60	np $\pi^+\pi^-\pi^+\pi^-$	56/180
				np $\pi^+\pi^-\pi^0\,\pi^0$	56/180
np $\pi^0\,\pi^0$	6/20	np $\pi^0\,\pi^0\,\pi^0$	14/60	np $\pi^0\,\pi^0\,\pi^0\,\pi^0$	14/180
nn $\pi^+\pi^0$	3/20	nn $\pi^+\pi^+\pi^-$	6/60	nn $\pi^+\pi^0\,\pi^+\pi^-$	18/180
		nn $\pi^+\pi^0\,\pi^0$	3/60	nn $\pi^+\pi^0\,\pi^0\,\pi^0$	9/180

(d)

np (T=0) →					
pp $\pi^-\pi^0$	0	pp $\pi^-\pi^+\pi^-$	6/60	pp $\pi^-\pi^0\,\pi^+\pi^-$	18/180
		pp $\pi^-\pi^0\,\pi^0$	3/60	pp $\pi^-\pi^0\,\pi^0\,\pi^0$	9/180
np $\pi^+\pi^-$	2/3	np $\pi^0\,\pi^+\pi^-$	28/60	np $\pi^+\pi^-\pi^+\pi^-$	56/180
				np $\pi^+\pi^-\pi^0\,\pi^0$	56/180
np $\pi^0\,\pi^0$	1/3	np $\pi^0\,\pi^0\,\pi^0$	14/60	np $\pi^0\,\pi^0\,\pi^0\,\pi^0$	14/180
nn $\pi^+\pi^0$	0	nn $\pi^+\pi^+\pi^-$	6/60	nn $\pi^+\pi^0\,\pi^+\pi^-$	18/180
		nn $\pi^+\pi^0\,\pi^0$	3/60	nn $\pi^+\pi^0\,\pi^0\,\pi^0$	9/180

Table 5.5: *Probabilities associated with each possible charge repartition for the one-, two-, three- and four-pion production channels in N–N collisions. On Table (d), in the case of a np collision with the system of nucleons in the isospin state $|00\rangle$, the final states $pp\pi^-\pi^0$ and $nn\pi^+\pi^0$ are forbidden by isospin symmetry.*

where $|T_i m_i\rangle$ and $|T_f m_f\rangle$ are respectively the isospin states of the incoming and outgoing system composed of one pion and one nucleon, $|T_\pi m_\pi\rangle$ is the isospin state of the produced pion(s); C is the normalization factor.

If we consider in details the case of a $\pi^+ p$ collision, the probabilities are computed as:

$$\begin{aligned}
p\pi^+ \to (p\pi^+)\pi^0 \quad & P = C\left|\left(10\frac{3}{2}\frac{3}{2}|\frac{3}{2}\frac{3}{2}\right)\right|^2 = C\frac{3}{5},\\
p\pi^+ \to (p\pi^0)\pi^+ \quad & P = C\left(\sqrt{\frac{2}{3}}\left|\left(11\frac{3}{2}\frac{1}{2}|\frac{3}{2}\frac{3}{2}\right)\right|^2 + \frac{1}{\sqrt{3}}\left|\left(11\frac{1}{2}\frac{1}{2}|\frac{3}{2}\frac{3}{2}\right)\right|^2\right)\\
& \quad = C\left(\frac{2}{3}\frac{2}{5} + \frac{1}{3}1\right) = C\frac{3}{5},\\
p\pi^+ \to n\pi^+\pi^+ \quad & P = C\left(\frac{1}{\sqrt{3}}\left|\left(11\frac{3}{2}\frac{1}{2}|\frac{3}{2}\frac{3}{2}\right)\right|^2 + \sqrt{\frac{2}{3}}\left|\left(11\frac{1}{2}\frac{1}{2}|\frac{3}{2}\frac{3}{2}\right)\right|^2\right)\\
& \quad = C\left(\frac{1}{3}\frac{2}{5} + \frac{2}{3}1\right) = C\frac{4}{5}.
\end{aligned}$$

We have to consider the two contributions for $(p\pi^+)\pi^0$ and $(p\pi^0)\pi^+$ together, because their final states cannot be set apart experimentally. The normalization factor C should be fixed to 1/2. Finally, we obtain:

$$p\pi^+ \to \begin{cases} p\pi^+\pi^0 & \text{with } P = \frac{1}{2}\left(\frac{3}{5} + \frac{3}{5}\right) = \frac{3}{5} \\ n\pi^+\pi^+ & \text{with } P = \frac{1}{2}\frac{4}{5} = \frac{2}{5} \end{cases} \tag{5.57}$$

Repartition of the charges in two- and three-pion production channels

As for NN collisions, the isospin states of the final particles cannot be computed uniquely. The probabilities to associate with each reaction in $N\pi$ producing more than one pion ($N\pi \to N\pi\pi\pi$ and $N\pi \to N\pi\pi\pi\pi$ channels) are thus computed using a similar assumption as in Section 5.3.1.

We use the same notation as in Section 5.3.1: a system composed with a pions ($a > 2$), that has a total electric charge ξ is noted $(a\pi)^\xi$. We then use the probabilities computed in the one-pion production case for a given charge ξ over the pions P_ξ (and a certain nucleon) to compute the probabilities with $a > 2$. For example, in a $p\pi^+$ collision we have:

- $P_{\xi=1} = P(p\pi^+ \to p\pi^+\pi^0) = \frac{3}{5}$,
- $P_{\xi=2} = P(p\pi^+ \to n\pi^+\pi^+) = \frac{2}{5}$.

The probabilities to associate with the two-pion production reactions are then

$$\begin{aligned}
p\pi^+ \to p\pi^+\pi^0\,\pi^0 \quad & P = CP_{\xi=1} \times P(\pi^0\,\pi^0) = C\frac{3}{5} \times \frac{1}{3} = C\frac{3}{15},\\
p\pi^+ \to p\pi^+\pi^+\pi^- \quad & P = CP_{\xi=1} \times P(\pi^+\pi^-) = C\frac{3}{5} \times \frac{2}{3} = C\frac{6}{15},\\
p\pi^+ \to n\pi^+\pi^+\pi^0 \quad & P = CP_{\xi=2} = C\frac{2}{5}
\end{aligned}$$

The probabilities for each possible reaction and for production of one, two or three produced pions are presented in the Tables 5.6 (a) to (f).

(a)

π^+ p →					
p $\pi^+\pi^0$	3/5	p $\pi^+\pi^+\pi^-$	6/15	p $\pi^+\pi^+\pi^0\,\pi^-$	6/15
		p $\pi^+\pi^0\,\pi^0$	3/15	p $\pi^+\pi^0\,\pi^0\,\pi^0$	3/15
n $\pi^+\pi^+$	2/5	n $\pi^+\pi^+\pi^0$	6/15	n $\pi^+\pi^+\pi^+\pi^-$	4/15
				n $\pi^+\pi^+\pi^0\,\pi^0$	2/15

(b)

π^- n →					
p $\pi^-\pi^-$	2/5	p $\pi^0\,\pi^-\pi^-$	6/15	p $\pi^+\pi^-\pi^-\pi^-$	4/15
				p $\pi^0\,\pi^0\,\pi^-\pi^-$	2/15
n $\pi^-\pi^0$	3/5	p $\pi^+\pi^-\pi^-$	6/15	n $\pi^+\pi^0\,\pi^-\pi^-$	6/15
		n $\pi^0\,\pi^0\,\pi^-$	3/15	n $\pi^0\,\pi^0\,\pi^0\,\pi^-$	3/15

(c)

π^- p →					
p $\pi^0\,\pi^-$	17/45	p $\pi^+\pi^-\pi^-$	34/135	p $\pi^+\pi^0\,\pi^-\pi^-$	34/135
		p $\pi^0\,\pi^0\,\pi^-$	17/135	p $\pi^0\,\pi^0\,\pi^0\,\pi^-$	17/135
n $\pi^+\pi^-$	21/45	n $\pi^+\pi^0\,\pi^-$	56/135	n $\pi^+\pi^+\pi^-\pi^-$	42/135
				n $\pi^+\pi^0\,\pi^0\,\pi^-$	35/135
n $\pi^0\,\pi^0$	7/45	n $\pi^0\,\pi^0\,\pi^0$	28/135	n $\pi^0\,\pi^0\,\pi^0\,\pi^0$	7/135

(d)

π^+ n →					
p $\pi^+\pi^-$	21/45	p $\pi^+\pi^0\,\pi^-$	56/135	p $\pi^+\pi^+\pi^-\pi^-$	42/135
				p $\pi^+\pi^0\,\pi^0\,\pi^-$	35/135
p $\pi^0\,\pi^0$	7/45	p $\pi^0\,\pi^0\,\pi^0$	28/135	p $\pi^0\,\pi^0\,\pi^0\,\pi^0$	7/135
n $\pi^+\pi^0$	17/45	n $\pi^+\pi^+\pi^-$	34/135	n $\pi^0\,\pi^0\,\pi^+\pi^-$	34/135
		n $\pi^+\pi^0\,\pi^0$	17/135	n $\pi^0\,\pi^0\,\pi^0\,\pi^0$	17/135

(e)

π^0 p →					
p $\pi^+\pi^-$	39/90	p $\pi^+\pi^0\,\pi^-$	117/270	p $\pi^+\pi^+\pi^-\pi^-$	78/270
				p $\pi^+\pi^0\,\pi^0\,\pi^-$	65/270
p $\pi^0\,\pi^0$	13/90	p $\pi^0\,\pi^0\,\pi^0$	39/270	p $\pi^0\,\pi^0\,\pi^0\,\pi^0$	13/270
n $\pi^+\pi^0$	38/90	n $\pi^+\pi^+\pi^-$	76/270	n $\pi^+\pi^+\pi^0\,\pi^-$	76/270
		n $\pi^+\pi^0\,\pi^0$	38/270	n $\pi^+\pi^0\,\pi^0\,\pi^0$	38/270

(f)

π^0 n →					
p $\pi^0\,\pi^-$	38/90	p $\pi^+\pi^-\pi^-$	76/270	p $\pi^+\pi^0\,\pi^-\pi^-$	76/270
		p $\pi^0\,\pi^0\,\pi^-$	38/270	p $\pi^0\,\pi^0\,\pi^0\,\pi^-$	38/270
n $\pi^+\pi^-$	39/90	n $\pi^+\pi^0\,\pi^-$	117/270	n $\pi^+\pi^+\pi^-\pi^-$	78/270
				n $\pi^+\pi^0\,\pi^0\,\pi^-$	65/270
n $\pi^0\,\pi^0$	13/90	n $\pi^0\,\pi^0\,\pi^0$	39/270	n $\pi^0\,\pi^0\,\pi^0\,\pi^0$	13/270

Table 5.6: *Probabilities associated with each possible charge repartition for the one-, two- and three-pion production channels in π–N collisions*

Discussion on the model

From Table 5.4(c), one can compute the average multiplicities of positive, neutral and negative pion. They are summarized in the following table for the two and four-pion production cases, for pp and np collisions. The model has a tendency to produce as many positive pions as neutral

	$\langle\pi^+\rangle$	$\langle\pi^0\rangle$	$\langle\pi^-\rangle$	Total
$pn \to NN\ 2\ \pi$	11/20	18/20	11/20	2
$pp \to NN\ 2\ \pi$	22/20	11/20	7/20	2
$pn \to NN\ 4\ \pi$	231/180	258/180	231/180	4
$pp \to NN\ 4\ \pi$	318/180	219/180	183/180	4

Table 5.7: *Average multiplicities of positive, neutral and negative pion, computed from the charge repartition model presented in Sec. 5.3 in the two- and four-pion production pp and np reactions.*

and negative ones as the number of pions increases.

We have tested the validity of this model for two-pion production reactions in pp collisions, as we have a parametrization for each of the possible outgoing channels in these reactions. Figure 5.9 shows a comparison between the probability associated for a channel and the quantity

$$\frac{\sigma(\text{channel})}{\sigma_1(NN\pi\pi)}.$$

These two quantities are expected to be close to each other but one can see on Fig. 5.9 that, as far as particular channels are concerned, the model used in our extended version of INCL4.2 does not give satisfactory results.

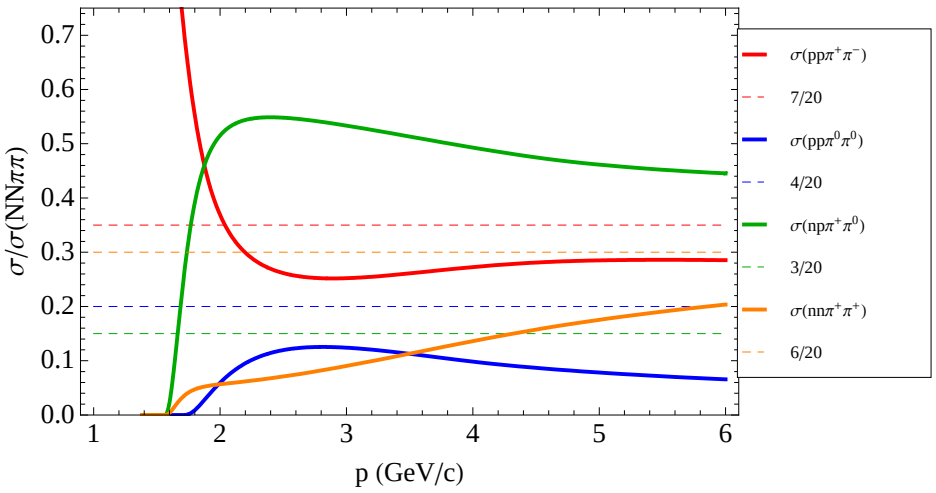

Figure 5.9: *Comparison of the ratio between the parametrization of particular channels in pp collisions and $\sigma_1(NN\pi\pi)$ (plain lines) and the quantity $\sigma_1(NN\pi\pi) \times P(\text{channel})$ (dashed lines), where $P(\text{channel})$ is the probability associated with each channel given in Table 5.4(a). The channels considered are $pp \to pp\pi^+\pi^-$ (red), $pp \to pp\pi^0\,\pi^0$ (blue), $pp \to np\pi^+\pi^0$ (green) and $pp \to nn\pi^+\pi^+$ (orange).*

All the channels are underestimated of at least 25%, except for the $pp \to pn\pi^+\pi^0$ channel (green line) which is largely overestimated. This overestimation is such that it relatively decreases

all other contributions. Nevertheless, if one considers the three underestimated channels, one can see that, as momentum increases, they tend to behave with as predicted by the probabilities and isospin symmetry.

Nevertheless, an evaluation of the multiplicities given by the experimental cross sections gives:

$$\begin{aligned}\langle\pi^+\rangle &\approx 28\% + 52\% + 2\times 14\% = 21.6/20,\\ \langle\pi^0\,\rangle &\approx 2\times 6\% + 52\% = 12.8/20,\\ \langle\pi^-\rangle &\approx 28\% = 5.6/20.\end{aligned}$$

These values are to be compared with the multiplicities generated by the extended version of INCL4.2 (given in Tab. 5.7), which are very close to the one computed from experiments.

If we had not made the assumption that the produced pions were in the lowest angular momentum state, the system composed of pions can access to the isospin state $I = 1$ and the probabilities associated with each channel in pp collisions would have been:

- $pp \to pp\pi^+\pi^-$ (in red): 27% (instead of 35%),
- $pp \to pp\pi^0\,\pi^0$ (in blue): 15% (instead of 20%),
- $pp \to np\pi^+\pi^0$ (in green): 35% (instead of 15%),
- $pp \to nn\pi^+\pi^+$ (in orange): 23% (instead of 30%).

These values are closer to what is observed but the discrepancies remain very large.

One should also be aware that the error on the parametrization proposed for the $pp \to np\pi^+\pi^0$ channel (the green line) is very large. The data for this channel is very scarce and the error on the amplitude of the cross sections is of the order of 30%. This error probably accounts for the discrepancies observed on figure 5.9. Moreover the same test can be realized on the pion-nucleon collisions, this is showed in Fig. 5.10. In the $N\pi$ collisions, the charge repartition model gives good results, especially for the $p\pi^-$ channels.

Our charge repartition model, even though it is not adapted to simulate one particular channel, can reproduce the multiplicities of the pions quite well. In an intranuclear cascade model as INCL, the cascade is simulated as a series of collisions and, in this multiple scattering picture, the model for the repartition of the charges we have adopted is expected to be sufficient.

5.4 The energy-momentum repartition model

The selection of the outgoing channel in NN and πN collisions is realized using the multipion cross sections, parametrized in Section 5.1, and the charge repartition probabilities, computed in Section 5.3. The last step of the determination of the final state of the particles amounts to sharing the available energy and momentum between the outgoing particles, respecting the conservation laws. In the standard INCL4.2, there is never more than two outgoing particles; thus it is very straightforward to distribute energy and momentum over them, in center of mass frame. The inelastic channels we have added to INCL4.2 can have up to 6 outgoing particles, which was not supported by INCL4.2. The code thus needed to be given the possibility to share energy and momentum in multipion production collisions, where the number of particles in the outgoing channel can be more than two. This has been realized assuming, at first, that the produced particles would uniformly populate the phase space, using a method inspired from the Raubold–Lynch method, presented by James in Ref [70].

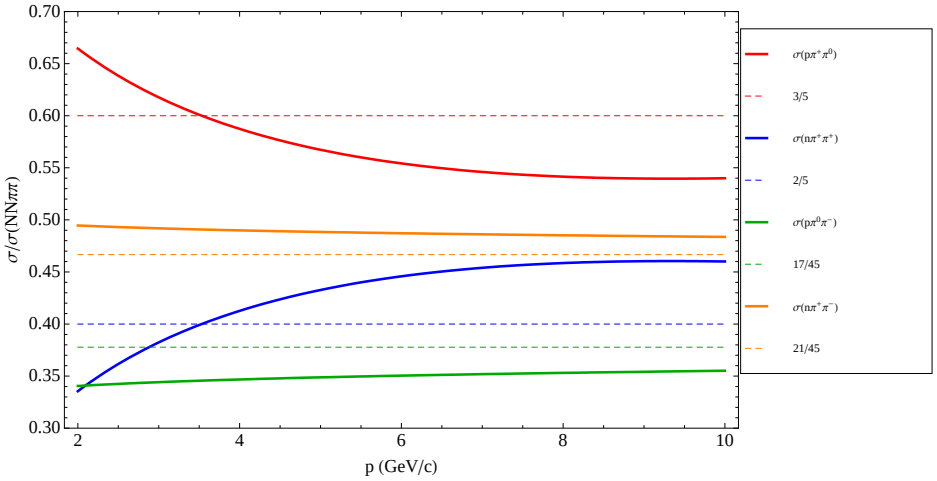

Figure 5.10: *Comparison of the ratio between the parametrization of particular channels in $p\pi^+$ and $p\pi^-$ collisions and $\sigma(N\pi\pi)$ (plain lines) and the quantity $\sigma(N\pi\pi) \times P(\text{channel})$ (dashed lines), where $P(\text{channel})$ is the probability associated with each channel given in Table 5.5(a) and 5.5(c). The channels considered are $p\pi^+ \to p\pi^+\pi^0$ (red), $p\pi^+ \to n\pi^+\pi^+$ (blue), $p\pi^- \to p\pi^-\pi^0$ (green) and $p\pi^- \to n\pi^+\pi^-$ (orange).*

Generating energy and momentum for each particle is equivalent to populate a phase space with a certain density, which has been, at first, assumed to be uniform (which corresponds to the simplest model possible). In Section 5.4.1, we will explain how the generator of events, which is based on the phase space integral R_n, generates the energy and momentum of a system of particles, when the phase space is supposed to have a uniform density. The "phase space integral" R_n (presented in Appendix C.1) contains all the information about the kinematics of a reaction [71]. The hypothesis of a uniform phase space, even though it gave reasonable results has been replaced with a biased uniform phase space model, presented in Section 5.4.2.

5.4.1 Generating events with uniform phase space density

The phase space integral R_n, defined by Relation C.1, can be re-written in terms of the invariant masses M_i, according to Relation C.10 (as demonstrated in Appendix C). Since the integrals C.1 and C.10 are equal for any domain of integration, actually determined by P, the total 4-vector of the system, the integrands are equivalent. This means that generating final states with a constant density in phase space is equivalent to generating final states in the angular variables (or rather directions) of the momenta of the outgoing particles at random and in the M_i variables with a density given by

$$\varpi \propto p^*(M_2, m_1, m_2)\; p^*(M_3, M_2, m_3)\; \ldots\; p^*(\sqrt{s}, M_{n-1}, m_n), \tag{5.58}$$

where the M_i are the invariant masses of the subsystems composed with the i first particles. As demonstrated in Appendix C.1, the invariant masses are limited by

$$\begin{aligned}
m_1 + m_2 \leq \quad & M_2 \quad && \leq (\sqrt{s} - \sum_{j=1}^{n} m_j) + m_1 + m_2. \\
m_3 + M_2 \leq \quad & M_3 \quad && \leq (\sqrt{s} - \sum_{j=1}^{n} m_j) + m_1 + m_2 + m_3 \\
& \ldots && \\
m_{n-1} + M_{n-2} \leq \quad & M_{n-1} \quad && \leq (\sqrt{s} - \sum_{j=1}^{n} m_j) + m_1 + m_2 + m_3 + \ldots + m_{n-1} \\
& && = \sqrt{s} - m_n.
\end{aligned} \tag{5.59}$$

The first step for generating a final state is thus to take $M_2, M_3, ..M_{n-1}$, in the limits given in Eqs. 5.59, with the probability density given by Eq. 5.58. It is easy to see from Eqs. 5.59 that it is always possible to choose the values of the invariant masses in the indicated limits when the M_i's are generated from the smallest sub-system to the system composed with n particles.

The next step is to go from these variables to the momenta of the particles. This can be done using the Raubold-Lynch method [70], which can be formulated as follows:

1. From M_2, calculate $p^*(M_2, m_1, m_2)$ and generate two opposite vectors of this length along a given axis (the z-axis has been arbitrarily chosen). Rotate the two vectors to a direction taken at random (equivalent to two rotations: one around the y-axis with a uniform distribution of the cosine of the angle between -1 and +1 and one around the z-axis with a uniform distribution of the angle between 0 and 2π). Let us call the vectors $\vec{p}_1$ and $\vec{p}_2$.

2. From M_3, calculate $p^*(M_3, M_2, m_3)$, take $\vec{p}_3 = p^*(M_3, M_2, m_3)\vec{e}_z$ and make a Lorentz boost of $\vec{p}_1$ and $\vec{p}_2$ (i.e. for $i = 1, 3$) corresponding to a velocity

$$\beta = -\frac{\vec{p}_3}{\sqrt{\vec{p}_3^2 + M_2^2}}.$$

   It is easy to see that the resulting total momentum is zero[7]. Make a double rotation (of all vectors) as indicated in 1.

3. Repeat the same process for all M_i, $i = 4, \ldots, n-2$.

4. From M_{n-1}, calculate $p^*(\sqrt{s}, M_{n-1}, m_n)$, take $\vec{p}_n = p^*(\sqrt{s}, M_{n-1}, m_n)\vec{e}_z$ and make a Lorentz boost of all $\vec{p}_i$ for $i = 1, n-1$ corresponding to a velocity

$$\beta = -\frac{\vec{p}_n}{\sqrt{\vec{p}_n^2 + M_{n-1}^2}}.$$

   The total momentum is still zero. Make a double rotation (of all vectors) as above.

This procedure, illustrated in Figure 5.11, can be used to generate energy spectra in collisions with n outgoing particles. Figure 5.12 show such spectra for emitted pions in πN collision with

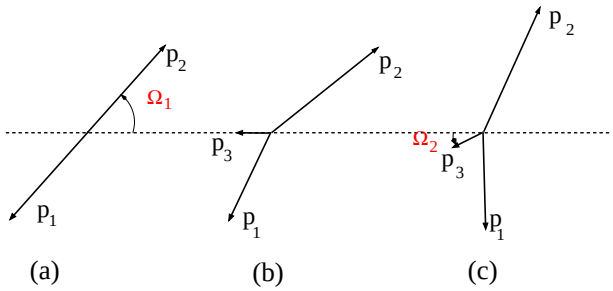

Figure 5.11: *Illustration of the generation of the momenta in the c. m. Ω_1 and Ω_2 stand symbolically for indicating directions in three dimensions. Part (a) corresponds to step 1 of the procedure outlined in the text. Parts (b) and (c) correspond to step 2.*

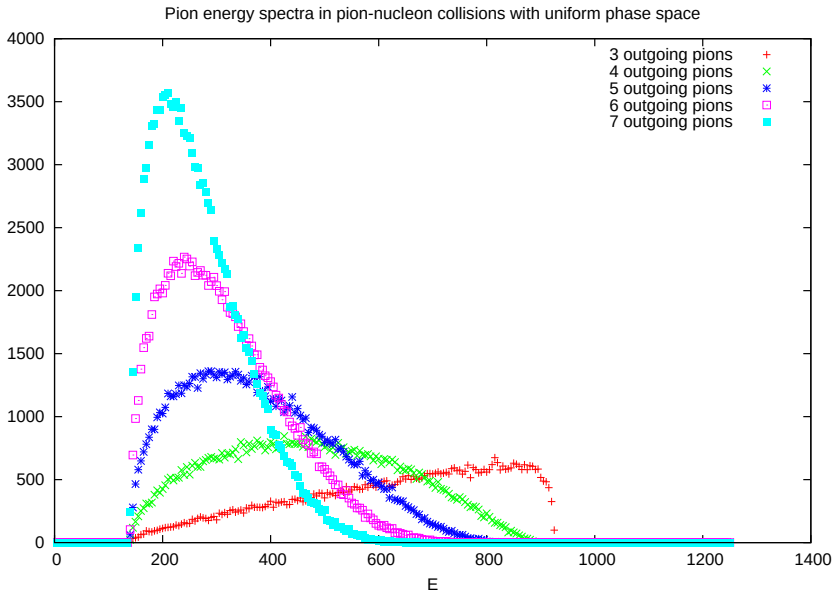

Figure 5.12: *Pion energy spectra (in MeV) corresponding to uniform phase space emission with $\sqrt{s}$ equal to twice the nucleon rest mass. The curves correspond to n= 3 (red), 4 (green), 5 (dark blue), 6 (purple) and 7 (light blue).*

$\sqrt{s}$ equal to twice the nucleon mass. This corresponds more or less to the conditions in nucleon-antinucleon annihilation at rest or at low energy.

One can see that the maximum energy for n=3 is equal approximately to 1/2 $\sqrt{s}$, corresponding to the emission of two pions with equal momentum and of the third one with twice this momentum in the opposite direction. The maximum energy is in fact given by

$$\varepsilon_{max} = \frac{1}{2}(\sqrt{s} - \frac{3m^2}{\sqrt{s}}), \tag{5.60}$$

which is close to $\sqrt{s}/2$ in the illustrated case. As the number n of pions increases, the pion

[7] Taking an advantage of the property: *If a collection of n particles with $\sum_i \vec{p}_i = 0$ and a total c. m. energy $\sqrt{s}$ are Lorentz-boosted with a velocity $\vec{\beta} = \frac{\vec{p}}{\sqrt{p^2+s}}$, where $\vec{p}$ is an arbitrary vector, their total momentum is equal to $\vec{p}$.*

spectrum resembles more and more to a (relativistic) Maxwellian distribution. This tendency persists when pions are emitted with nucleons, as shown in Fig.5.13.

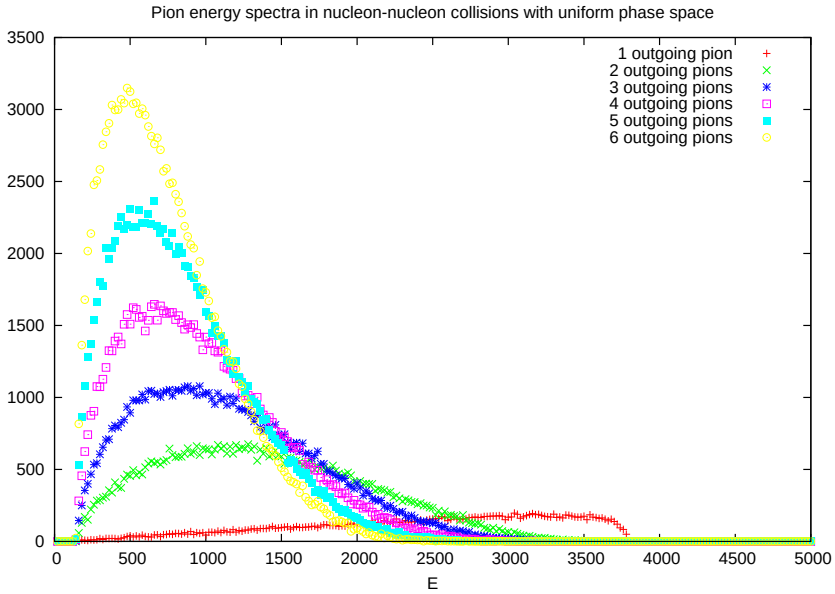

Figure 5.13: *Pion energy spectra (in MeV) corresponding to uniform phase space emission of two nucleons and n pions, with $\sqrt{s}$ equal to 8 GeV. The curves correspond to n= 1 (red), 2 (green), 3 (dark blue), 4 (purple), 5 (light blue) and 6 (yellow).*

We just mention that in that case, the maximum energy for a single emitted pion occurs when the pion is emitted in opposition with two parallel nucleons with the same velocity. It is easy to verify that the maximum energy is then given by

$$\varepsilon_{max} = \frac{1}{2}(\sqrt{s} - \frac{4M_N^2 - m^2}{\sqrt{s}}), \tag{5.61}$$

which approximately equal to $\sqrt{s}/2$ minus 250 MeV. The nucleon spectrum shows also the same tendency, although less pronounced, as illustrated in Fig.5.14.

It is obvious that the generation of final states described above yields isotropic distributions of pions and nucleons. This does not forbid to have correlations between particles.

5.4.2 Generating final states with biased phase space density

The use of a uniform phase space was our first assumption, and the results given by this model were reasonably good. Nevertheless we changed to a forward peaked phase space distribution.

The biased distributions can be obtained by introducing departures from the distributions for the M_i's and the angles described above. The simplest case, which is very helpful, consists in favoring emission of one of the particles in one direction.

Suppose that we consider a collision between two nucleons along the z-axis and suppose the dynamics is such that one of the nucleons is emitted close the incident direction, with some distribution, assumed to be of the form e^{Bt}, where B is a constant and t is the squared momentum transfer. Then it suffices, after the Raubold-Lynch procedure, to rotate the final state in such a

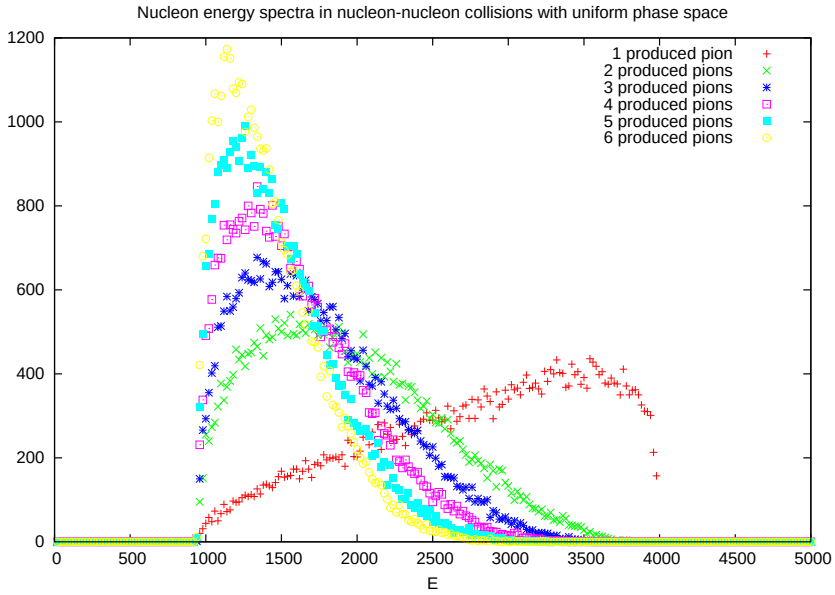

Figure 5.14: *Nucleon energy spectra (in MeV) corresponding to uniform phase space emission of two nucleons and n pions, with $\sqrt{s}$ equal to 8 GeV. The curves correspond to n= 1 (red), 2 (green), 3 (dark blue), 4 (purple), 5 (light blue) and 6 (yellow).*

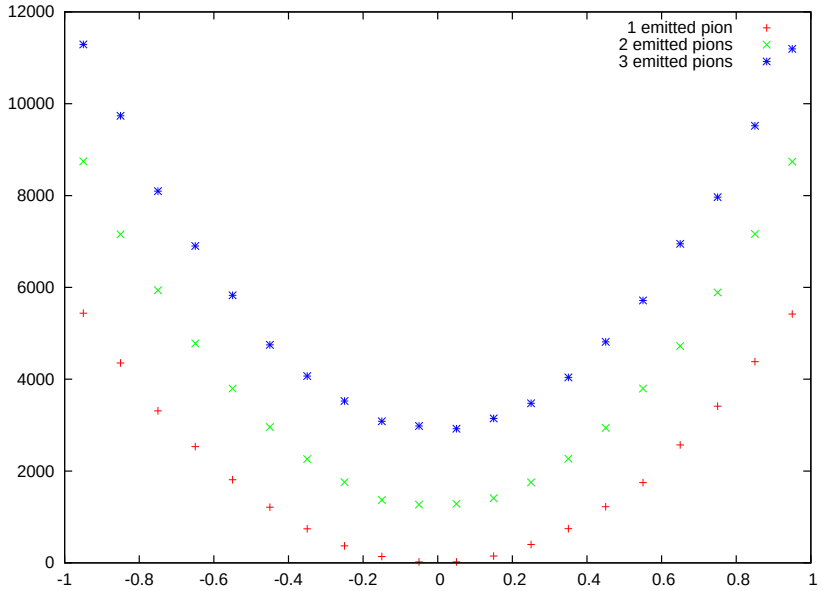

Figure 5.15: *Distribution of the cosine of the angle between the direction of the emitted nucleons and the incident collision direction when n= 1 (red), 2 (green) or 3 (blue) pions are emitted with the nucleons. The emission pattern corresponds to uniform phase space except for the direction of the nucleons, which is chosen according to a symmetrized e^{Bt} law. $\sqrt{s} = 4GeV$.*

way that the angle between the emitted particle and the incident direction has a value consistent with the above distribution. This is illustrated by Fig.5.15.

It should be noticed that this is the only controllable departure from uniform phase space model in the Raubold-Lynch procedure. If another angle is changed during the construction of the final state according some desired stochastic law, the final distribution of this angle will be deformed by the subsequent rotations.

It is worth to notice that in the case of nucleon-nucleon collisions producing pions, the "alignment" of the first nucleon with the incident direction (by using a biased distribution for the second direction) leads to a similar "alignment" of the second nucleon. This is due to the large difference of mass between the nucleons and the pions which helps to put momentum on the nucleons when sharing energy and momentum. That is at least what we observed in the simulations. This is not so true for pion-nucleon collisions: if the incident nucleon is emitted preferentially close the incident direction, this is not automatically the case for the incident pion, especially if the number of produced pions is large.

It is interesting to note that, in collisions at a few GeV, even if the distribution of the cosine of the angles indicate a strong forward and backward enhancement, the rapidity distribution is nevertheless much more uniform or centered about zero rapidity. This is illustrated in Fig. 5.16 below. This seems to indicate that forward and backward particles are rather "soft" particles.

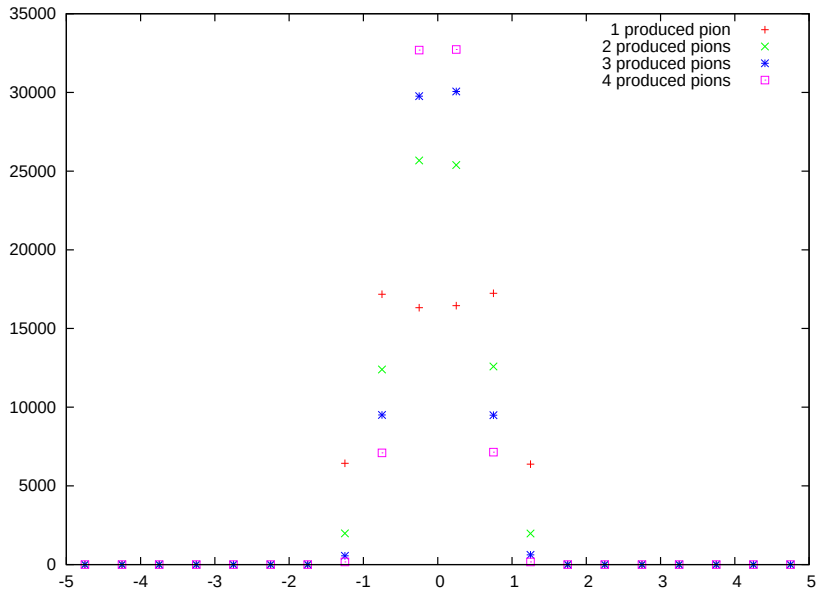

Figure 5.16: *Distribution of the nucleon rapidity in nucleon-nucleon collisions producing n= 1 (red), 2 (green), 3 (blue) or 4 (purple) pions. The emission pattern corresponds to uniform phase space except for the direction of the nucleons, which is chosen according to a symmetrized* e^{Bt} *law.* $\sqrt{s} = 4GeV$.

Similar results occur for the pion produced in the same collisions, as shown in Figs. 5.17 and 5.18.

5.4.3 Generating final states with a forward-peaked distribution

When we first implemented the Raubold-Lynch procedure in our extension to high energy of INCL4.2, we assumed a uniform phase space distribution generated as described above.

Although uniform phase space model already gave reasonable results, it does not reflect the

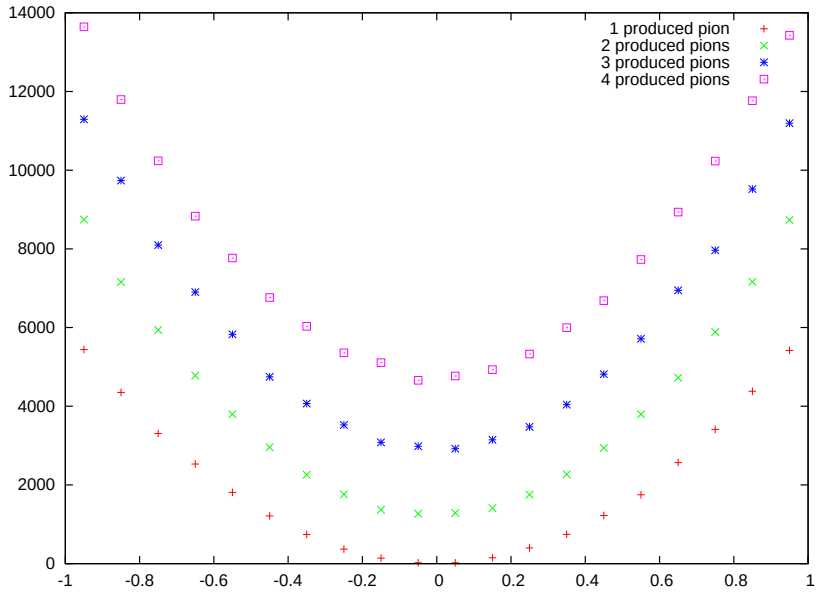

Figure 5.17: *Distribution of the cosine of the angle between a pion direction with the incident axis in nucleon-nucleon collisions producing n= 1 (red), 2 (green), 3 (blue) or 4 (purple) pions. The emission pattern corresponds to uniform phase space except for the direction of the nucleons, which is chosen according to a symmetrized e^{Bt} law. $\sqrt{s} = 4GeV$.*

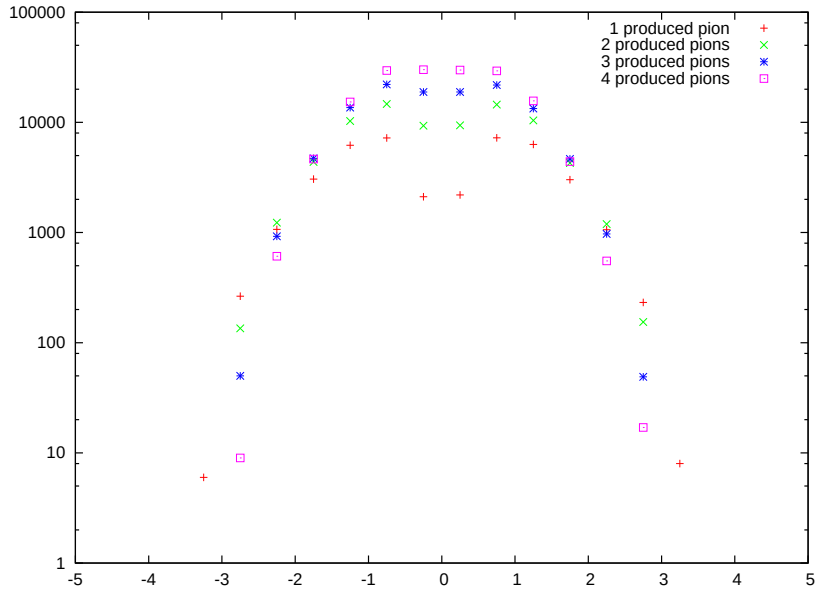

Figure 5.18: *Distribution of the pion rapidity in nucleon-nucleon collisions producing n= 1 (red), 2 (green), 3 (blue) or 4 (purple) pions. The emission pattern corresponds to uniform phase space except for the direction of the nucleons, which is chosen according to a symmetrized e^{Bt} law. $\sqrt{s} = 4GeV$.*

so-called peripheralism that characterizes cross sections in this energy regime (the emission of the nucleons should be rather forward peaked around the incident direction [69]). Therefore we used a biased phase space distribution, which also presents the advantage of improving our results:

- the final momenta are generated as described above, in accordance with uniform phase space;
- the momenta of the particles are rotated in such a way that the outgoing direction of a "tagged" particle (the nucleons in NN collisions and the incident nucleon in πN collisions) makes an angle θ with the incident direction of the collision with a suitable distribution:

  NN **collisions:** if θ is the angle between the incident direction of a nucleon and its emission angle in the c.m. frame, the distribution of θ is generated according to the probability law

  $$dP/dt \propto e^{Bt} \tag{5.62}$$

  where t is the squared momentum transfer of the nucleon and B is a constant. The value of B has been taken as equal to the slope parameter of elastic scattering and Δ production angular distributions, which assume a form similar to Eq. 5.62. Typically, in the energy range under consideration, $B = 6$ GeV^{-2} [72, 54].

  Nπ collisions: we used the same probability distribution as in NN collisions (Eq. 5.62). Nevertheless, the values for B are not as well documented and we chose $B = 15$ GeV^{-2}, following indications of [72].

5.5 Implementation in INCL4.2

5.5.1 Introduction of new channels

The new inelastic channels in NN collisions were introduced directly in the subroutine in charge of these collisions. All the parametrizations, presented in Sections 5.1 and 5.2, have been implemented in independent subroutines. They are used to determine the outgoing channel in the following way:

- when two particles are close enough to undergo a collision, according to the criterion introduced in Section 4.2 which compares the squared impact parameter to the total reaction cross section, the code tests the elasticity of the collision.
- Let E be center of mass energy for the collision. A number is randomly generated between zero and one; this number is compared to the ratio $\sigma_{el}(E)/\sigma_{tot}(E)$. The reaction is considered to be elastic if the random number is smaller than the ratio.
- If the collision is inelastic, the code will compute the cross section $\sigma_I^R(E)$, where I is the isospin state of the nucleons, it is 1 in the pp case (and nn case by isospin symmetry) and, in the np collisions case, it is either 1 or 0 with a 50% chance.
- A test similar to the test for the elasticity is performed to decide how many pions will be produced in the reaction (or if a Δ resonance is produced, if the incoming nucleons are in the isospin state $I = 1$). A random number, obviously different from the previous one, is generated and compared to the successive ratio $\left(\sum_{a=1}^{b} \sigma_I(NNa\pi)\right)/\sigma_I^R$ for b increasing

from 1 to 4. When the test becomes positive[8], the value of b indicates the number of produced pions.

The Figure 5.19(a) shows an illustration of the successive decisions leading to the determination of the final state in NN collisions.

The scheme we have followed to implement multipion production channels in pion-nucleon collisions, showed in Figure 5.19(b), is similar to the one in NN collisions:

- The total reaction cross sections are used to determined if the reaction occurs or not.
- If a reaction occurs, INCL4.2 test its "elasticity" by comparing a randomly generated number to the ratio $\sigma_{el}(E)/\sigma_{tot}(E)$, where the cross sections depends on the particles in the entrance channel (cf. Section 5.2).
- If the reaction is inelastic, a test is performed to determine the outgoing channel. As previously, a random number is generated and compared to the successive sums of the various possible channels, when the test will become positive, the channel is selected.

The number and the type (pion, nucleon, delta resonance) of the outgoing particles are determined following these decision chains. Once it is done, the subroutine which attributes an electric charge to each particle is called and a charge combination is selected, using the probabilities in Table 5.5 in NN collisions and in Table 5.6 in πN collisions. The charges of the nucleons are randomly distributed over the nucleons and the charges of the pions are randomly distributed over the pions. Everything was already in place in INCL4.2 to manage the creation and the decay of the Δ -resonances.

The generator of energy-momentum splitting is then called to attribute each particle a momentum and an energy following the biased distribution we introduced in Section 5.4. The biased distributions we used are exponentially peaked around the z-axis, while the produced particles should be peaked around the direction of the collision. We thus had to add rotations such that the axis around which the distribution is centered corresponds to the direction of the incoming nucleon (or pion in a pion-collision). These rotations are presented in Subsection 5.5.2.

The subroutine in charge of NN collisions was not programmed to transfer the characteristics of more that two particles to the main program, the parameters were such that these particles could only be baryons (nucleon or Δ -resonance). We added the transfer of the characteristics of the possibly produced pions: their number, their momentum, their third component of isospin (and thus their charges). We set their original positions as the center of mass of the incoming particles.

5.5.2 Rotations for the energy-momentum repartition routine

The introduction of a biased phase space in the subroutine in charge of the energy-momentum distribution over the outgoing particles introduced some compatibility problems. The biased distribution we have finally implemented in our extended version of INCL4.2 is an exponentially forward peaked distribution centered on a chosen direction, the axis of the collision in the center of mass frame. In the energy-momentum repartition routine, this direction corresponds to one axis, assume it is the z-axis. We thus have to perform a rotation such that the z-axis used in the final state generator routine corresponds to the direction of the collision in the center of mass frame.

[8]By "positive test" we always mean that the random number is smaller than the considered quantity, in this case the ratio of the b produced pions cross section and σ_I^R.

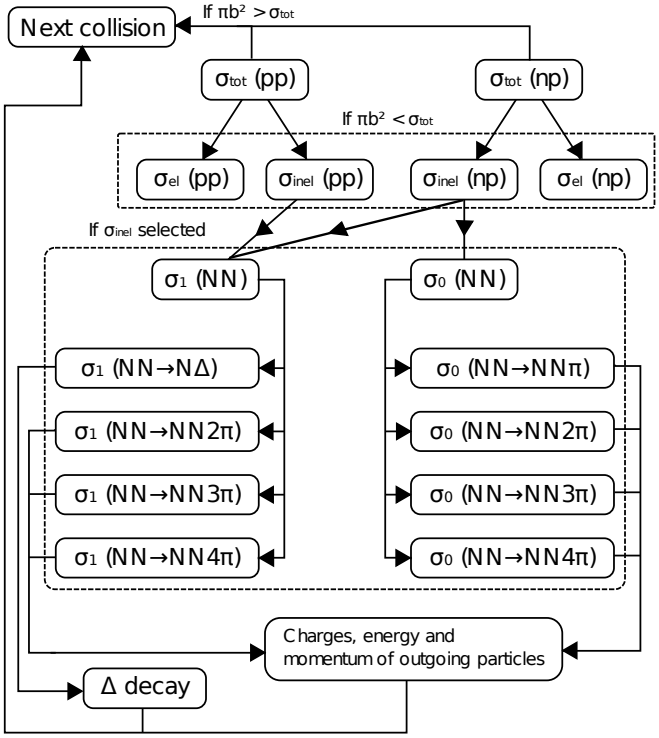

(a)

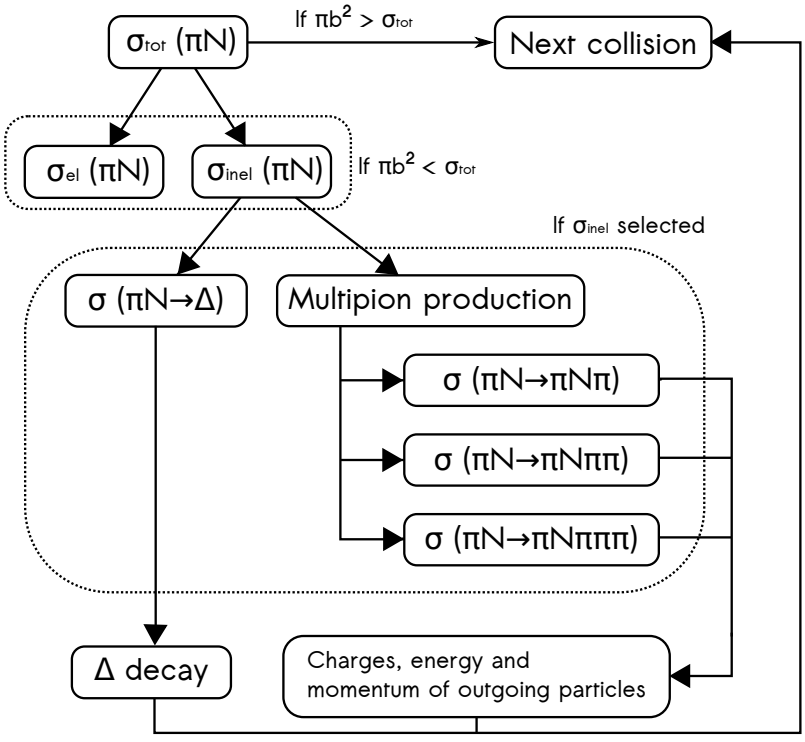

(b)

Figure 5.19: *Scheme of the decisions taken by INCL4 to select the final state in NN collisions (a) and in πN collisions (b). See the text for more details.*

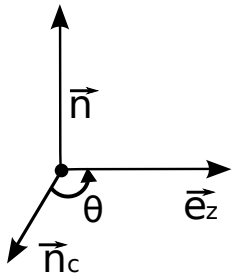

Figure 5.20: *Rotation of the z-axis direction $\vec{e}_z$ to the incident direction of the collision in the center of mass frame $\vec{n}_c$*

Figure 5.20 shows a general rotation of the vector $\vec{r}$ onto the vector $\vec{r'}$. This is realized by means of a rotation of an angle θ around an axis $\vec{n}$, in the direct sense given by $\vec{n}$. The vector $\vec{r'}$ can be written as

$$\vec{r'} = \vec{r}\cos\theta - \vec{r}\times\vec{n}\sin\theta + \vec{n}\,(\vec{n}.\vec{r})\,(1-\cos\theta)\,. \tag{5.63}$$

In our case, we want to perform a rotation of the incident direction $\vec{n_c} = (n_{c,x}, n_{c,y},\ n_{c,z})$ onto the z-axis $\vec{e_Z} = (0,0,1)$. The first step is to find $\vec{n}$, the normal vector to the plane defined by the two vectors $\vec{e_Z}$ and $\vec{n_c}$, around which the rotation will take place. It is defined by

$$\begin{aligned}\vec{n} &= \frac{\vec{e_Z}\times\vec{n_c}}{|\vec{e_Z}\times\vec{n_c}|} \\ &= \frac{(-n_{c,y}, n_{c,x}, 0)}{\sqrt{n_{c,y}^2 + n_{c,x}^2}}.\end{aligned} \tag{5.64}$$

From the definition, we also see that if the two vectors $\vec{e_Z}$ and $\vec{n_c}$ are parallel, $\vec{n}$ should be zero, this has been taken into account in the code with an additional criterion:

$$\text{If } \sqrt{n_{c,y}^2 + n_{c,x}^2} < n_{c,z}\times 10^{-8} \quad \text{then } \begin{cases}\vec{n} &= (0,0,1), \\ \theta &= 0.\end{cases} \tag{5.65}$$

When the vectors are not parallel, as shown on Figure 5.20, the angle θ between them is defined by

$$\theta = \arccos\left(\frac{\vec{e_Z}.\vec{n_c}}{|\vec{e_Z}||\vec{n_c}|}\right) = \arccos\left(n_{c,z}\right) \tag{5.66}$$

To obtain the forward peaked distribution of the produced particles, we apply formula 5.63 to the momentum vectors given by the energy-momentum repartition routine to obtain their momentum in the laboratory frame $\vec{p'}$, written as

$$\begin{aligned}\vec{p'_x} &= p_x\cos\theta + p_z n_y\sin\theta + n_x(\vec{n}.\vec{p})(1-\cos\theta) \\ \vec{p'_y} &= p_y\cos\theta + p_z n_x\sin\theta + n_y(\vec{n}.\vec{p})(1-\cos\theta) \\ \vec{p'_z} &= p_z\cos\theta - (p_x n_y - p_y n_x)\sin\theta + n_z(\vec{n}.\vec{p})(1-\cos\theta)\end{aligned}$$

where we have used the normal vector $\vec{n}$ and the rotation angle θ defined above.

5.5.3 Stopping time

The stopping time of the cascade is an important feature of the intranuclear cascade models. In particular, in INCL4.2, it has been parametrized in such way that it is independent of the incident energy and the impact parameter of the projectile (see Eq. 4.13) and that its value is 70 fm/c for an incident proton on lead. We have performed tests to check that the definition of t_{stop} was still valid after the extension of the domain of validity of INCL4.2 to incident kinetic energies up to 10 GeV.

It appeared that the value of the stopping time should be reduced at higher energy, as expected. We have chosen to multiply the stopping time by a scale factor such that it would decrease linearly from 70 fm/c at 2 GeV to 60 fm/c at 10 GeV.

5.6 Other tested enhancements of INCL4.2 for its extension to high energy

5.6.1 Hadronization time

One of the assumptions at the basis of the intranuclear cascade models is that the collisions are independent from each other (see Section 3.6.3). The nucleons involved in a collision thus should have time to reach their asymptotic state before getting involved in another collision. This feature of the intranuclear cascade has been translated in the code by the introduction of a variable called the hadronization time. The idea is that the participants in a collision are assigned an hadronization time and they cannot interact with any other particle as long as this time has not elapsed. It is defined as

$$t_{LG} = t_H \frac{E}{\sqrt{E^2 - p^2}}$$

where the energy E and the momentum p are related to the considered particles. We have used the same notations as in INCL4.2. In that version of the code, the hadronization time has been suppressed by setting $t_H = 0$.

We have performed an analysis with incident proton on tantalum to see whether or not this hadronization time should be introduced at high energy. Figure 5.21 shows the evolution of three pion production cross section at different incident momentum for the proton (1, 5 and 12 GeV/c) as the factor t_H was progressively increased from $t_H = 0$ to $t_H = 1.5$ by steps of 0.5.

The introduction of a hadronization time should forbid some collisions to happen to a nucleon which has had a collision a short time before. Thus, naively, one expects that as t_{LG} increases, the number of collisions in an event should decrease leading to a smaller pion production; this can be achieved by increasing either the energy of the particle or by increasing the factor t_H.

On the Figure 5.21, one can see that the cross section with an incident momentum of 1 GeV/c increases, reaches a maximum around $t_H = 0.5$ fm/c and then decreases. This is in contradiction with what was expected. In fact, it can be interpreted as follow: at that energy, the channels discussed in this work are not opened and thus the pion production can only occur through the Δ -resonance production and decay. The pion production thus mainly comes from the very first collision of the event because, in the secondary collisions, the chances to produce a pion decrease rapidly. But, if the introduction of t_H leads to an increased cross section, it is because the collisions that are prevented to happen are the recombination process $N\Delta \rightarrow NN$ which act like pion absorption in INCL.

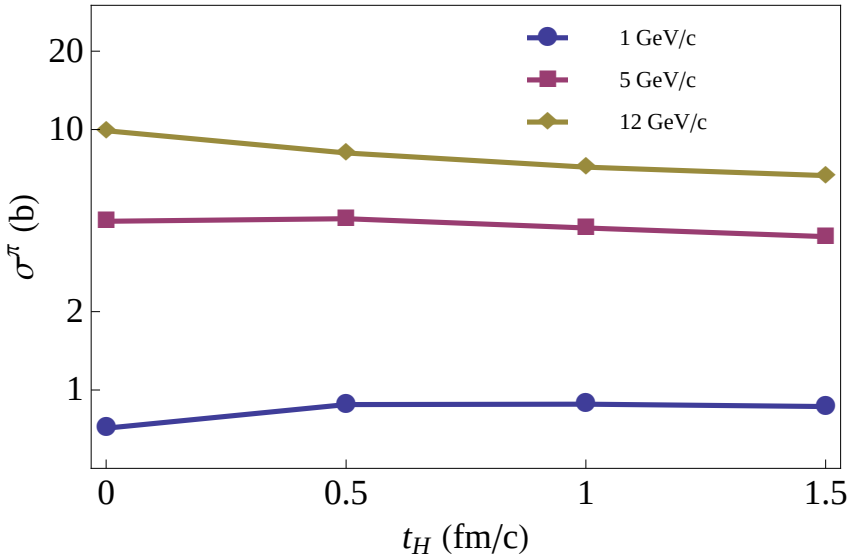

Figure 5.21: *Evolution of three-pion production cross section at different incident momentum for the proton (1 GeV/c in blue, 5 GeV/c in green and 12 GeV/c in yellow) as the factor t_H was progressively increased from $t_H = 0$ fm/c to $t_H = 1.5$ fm/c by steps of 0.5 fm/c.*

When the incident momentum increases, the secondary collisions become more and more important, this is why the increase of the cross section due to the introduction of t_H is somehow obliterated by the decrease in the pion production cross section due to the forbidden secondary collisions.

Finally, we have decided to put the hadronization time equal to zero because, as we will show in Sections 6.1.3 and 6.2.1, the total pion yields obtained with our version of the code is in rather good agreement with experimental data.

5.6.2 Forward emission of the pion in pion-nucleon elastic collisions

When a pion and a nucleon undergo an elastic collision, the reaction is implemented in INCL4.2 as the production of a Δ -resonance with a lifetime very short, in such way that the Δ decays almost immediately to produce the final pion and nucleon. The distributions of the particles produced in the Δ decay could be used for the elastic interaction of pion and nucleon and this has been exploited in INCL4.2.

The distribution implemented in the decay of the Δ -resonance favors the forward and backward emissions of the particles. Nevertheless, if one examines the data for elastic scattering [72], the pion is preferentially emitted in the forward directions. Thus we have introduced a separate distribution for the decay of a delta that is produced in an elastic collision, in which the pion is emitted in the forward direction. Figure 5.22 shows a comparison of positive pion spectra, for an incident proton with an energy of 730 MeV on a ^{63}Cu target, the simulations have been performed with the same version of INCL4.2 but with the addition of the forward emission for the pions in πN collisions for the right panel.

The results given by the introduction of this discrimination are unsatisfactory, they tend to destroy the results given by INCL4.2. The pions are emitted in the forward region, the number of secondary collisions decreases, leading to a reduced pion production. This reduced pion production doesn't appear in the low-angle-high energy emission region, in which the pion

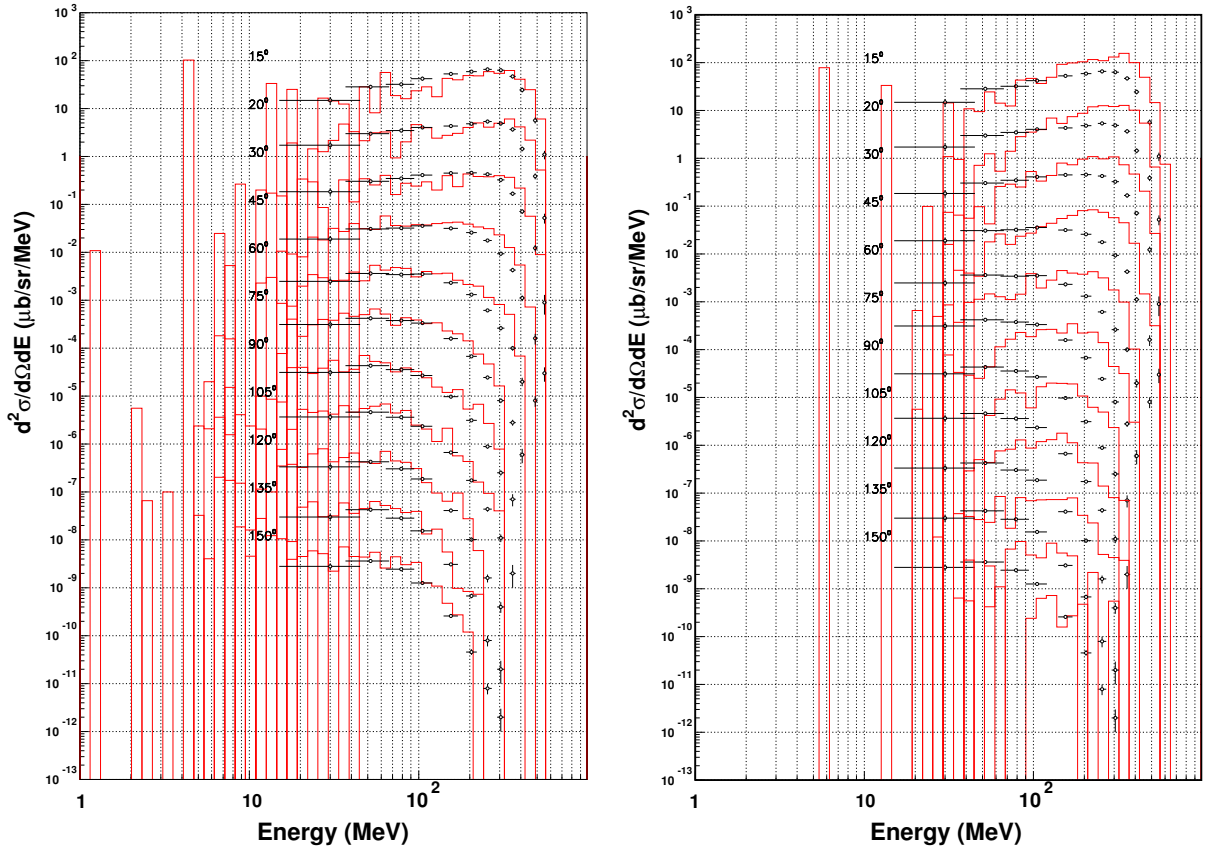

(a) INCL4.2

(b) INCL4.2 + Forward emission

Figure 5.22: *Positive pion spectra produced in a $p + {}^{63}Cu$ at an incident energy of 730 MeV. The simulations have been realized with INCL4.2 on the left panel, and with INCL4.2 plus the forward emission subroutine for elastic collisions in πN on the right.*

production is too important, but in the low energy region for the produced pion and in the large angle region.

In view of the results given by the forward emission of pions in elastic πN collisions, we removed it from our extension of the code.

6

Numerical results and comparison with experiment

The extension of INCL4.2 to the energy range between ∼2 and ∼15 GeV has been realized by the introduction of multipion production channels in inelastic NN and πN collisions. It is necessary to benchmark this new model against well chosen data. For pion production, the HARP experiment, described in Appendix D, provides golden plate data, since this experiment measured pion production in a systematic way, between 3 and 12 GeV/c and for an extended set of targets. Of course, even if pion production is the most important aspect of our work, it is also necessary to benchmark for other kind of data: particle production and residue cross sections. Unfortunately, these data are rather scarce in the momentum range under consideration.

In the following, we compare simulations given by the extended version of INCL4.2, referred as "INCL HE" from now on and on the figures, with experimental data. This version of the code corresponds to the standard version of INCL4.2 with additional multipion production channels, up to four produced pions in NN and up to four outgoing pions in πN collisions; the phase space distribution used to determine the energy and momenta of the emitted particles is biased according to an exponentially forward peaked emission, as described in 5.4.

For proton-induced reactions, we compare the simulations given by our version of INCL4.2 with experimental data and simulations calculated by the standard version of INCL4.2 as well. The standard version of INCL4.2 is always in red and the extended version is presented in blue (unless indicated otherwise). For all of our calculations, with both versions of INCL, the de-excitation code is the version ABLA07 [24] of the ABLA code. The choice of the evaporation code is however of no importance for pion production, since the latter occurs in the cascade stage only. For incident protons, the comparison also implies neutron and proton emissions (respectively in Secs. 6.1.1 and 6.1.2), on various targets.

In Section 6.1.3, we will focus on pion production cross sections and pion yields, which are the most direct observables linked to our extension of INCL4.2. First we present comparisons concerning total pion yield on various targets for incident energies ranging up to ∼12 GeV. Second, in the following sections, we will present comparisons of double-differential cross sections for positive and negative pion production in a reaction between a proton and a light target (carbon), a medium target (copper) and on a heavy target (lead). These comparisons have been realized with incident momenta of the proton corresponding to 3, 5, 8 and 12 GeV/c. Experimental data for these comparisons come from the HARP experiment [11, 12]. In this

experiment, two sets of data were measured separately, one in the 0.35–2.15 rad domain, and one for forward angles in a 0.05–0.25 rad domain. Section 6.1.4 shows the comparison with the data at large angle and comparison with the forward angle region are presented in Section 6.1.5. In order to clarify the discussion, we present only in this section the comparison for three chosen targets: carbon as a light target, copper as a medium target and lead as a heavy target. This is sufficient to exhibit the general trend of the dependence with the target mass numbers. Comparison with other targets is therefore postponed to Appendix D.

The HARP experiment has also performed experiments with incident charged-pions. Comparison between the results of our extended version of INCL4 and these data are presented in Section 6.2. We will end this chapter with a discussion on the numerical results in Section 6.3.

A preliminary account of the results presented here have been included in Ref. [10]. Let us note that there are slight differences between the results presented here and in Ref. [10]. The explanation is that a bug in the numerical code has been discovered since the acceptance of the paper [10] and has been fixed in the meantime. Results may differ by up to a factor two here and there but the bulk of the results are essentially the same.

A short study on residue production is presented in Section 6.4. The last section of this chapter is devoted to a short summary of our results.

6.1 Proton-induced reactions

Except for the comparisons with the HARP experimental data, the data for these reactions concern mainly protons with incident energy remaining under 3 GeV, many of them are even at the limit of validity of INCL4.2, ∼2 GeV. It is indeed important to check that our modified version does not bring significant changes where the standard version is working well.

6.1.1 Neutron emission

On Figs. 6.1 and 6.2, one can see double-differential cross sections for the production of neutrons in proton-induced reactions. Two different targets are studied: lead and iron; at two different energies: one at 1200 MeV, and the other at 3 GeV, which slightly is above the admitted upper limit of INCL4.2.

There are almost no differences between the two models at this energy, which was expected. At this energy, only the lowest multipion production channels intervene. Nevertheless, the extension to high energy of INCL4.2 seems to have improved the tail of the spectra for the most energetic neutrons at all angles. If one looks more carefully at the forward angle (see Fig. 6.1(b)), in the quasi-inelastic peak region, one can see that the quasi-inelastic peak is considerably improved for the spectrum at 10°, even though the one at 0°is less well described. The reduction of the importance of the quasi-inelastic peak comes from the fact that a proton-neutron collision has now 50% chances to not produce a Δ resonance (if the system of the nucleons are in the $I = 0$ isospin state).

Figs. 6.2 shows two sets of experimental data for a 3 GeV incident energy proton on iron (Fig. 6.2(a)) and lead (Fig. 6.2(b)). The results of the extended version of INCL4.2 are also better, especially for the 100–3000 MeV energy region. An interesting feature that appears on these figures is that the quasi-inelastic peak almost disappears in INCL HE; if this improves considerably the results for the iron target, this effect is more subject to discussions for the lead target. At 3 GeV, the two pion production channels in NN collisions are open, diminishing the importance of the Δ formation and reducing the quasi-inelastic peak. The shape of the double-differential cross sections at forward angle, for the extended version of INCL4.2, thus suggests

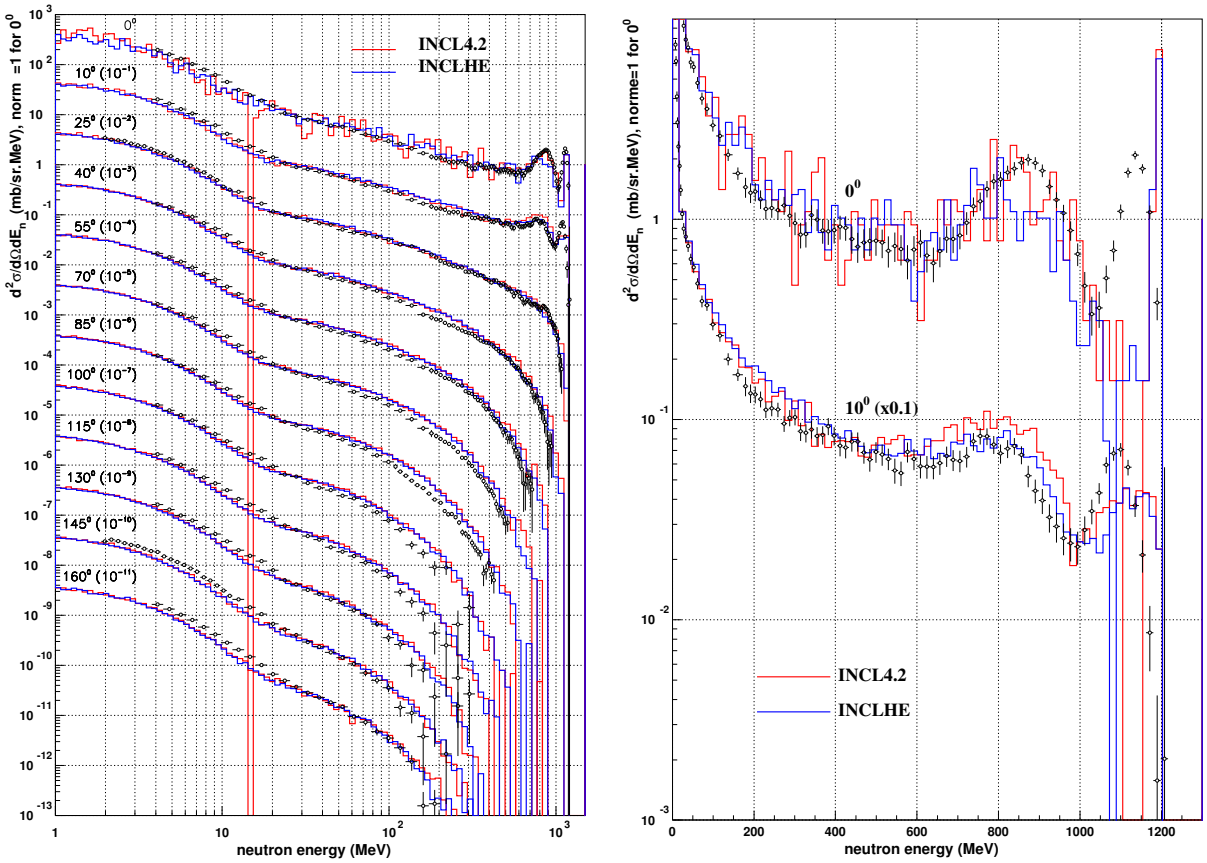

(a) (b)

Figure 6.1: *Double-differential cross sections for the production of neutrons in proton-induced reactions on Pb at 1.2 GeV incident energy at angles ranging from 0 to 160° in panel (a) and at forward angle (0° and 10°) in panel (b). The angles are indicated on the Figure. Data (symbols) from Refs. [73] are compared with the standard version (red lines) and the improved version (blue lines) of the INCL4 model. See text for detail.*

that we may have overestimated the effect of the multipion production channels in this region.

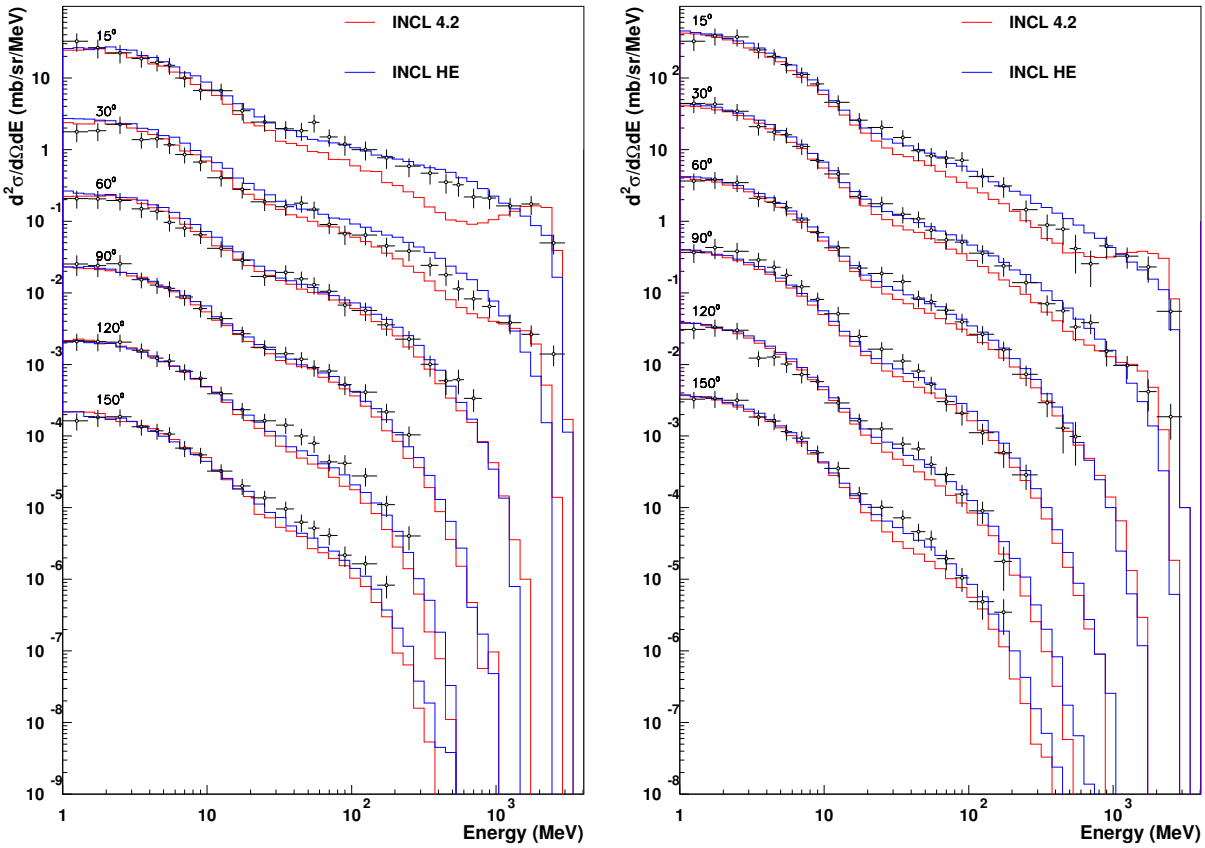

Figure 6.2: *Double-differential cross sections for the production of neutrons in proton-induced reactions on Fe (a) and on Pb (b) at 3 GeV incident energy at angles ranging from 15 to 150° as indicated on the Figure. Data (symbols) from Ref. [74] are compared with the standard version (red lines) and the improved version (blue lines) of the INCL4 model. See text for detail.*

6.1.2 Proton emission

Fig 6.3 shows double-differential cross sections for proton production in proton-induced reactions, with a kinetic energy of 2.6 GeV, on a gold target. The two panels compare simulations realized with extended version of INCL4.2 (in blue), the standard INCL4.2 (in red) and two different sets of data [75, 76].

One can see on these figures that the behavior of the simulations from both versions of the model is very similar for angles larger than 50°. For lower angles, the same difference between the models as for neutron emission appears: the quasi-inelastic peak disappears in the simulation with INCL HE.

The difference in shape between the simulations and the experimental data, for simulations from both versions of INCL4.2, is quite surprising. Previous comparisons did not suggest such a difference in the slope of the double-differential cross sections at forward angle. This is particularly visible in the comparison with the data from Bubak *et al.* at angles of 16° and 30° (right panel), for protons emitted with an energy around 100 MeV. Actually, these sets of data have

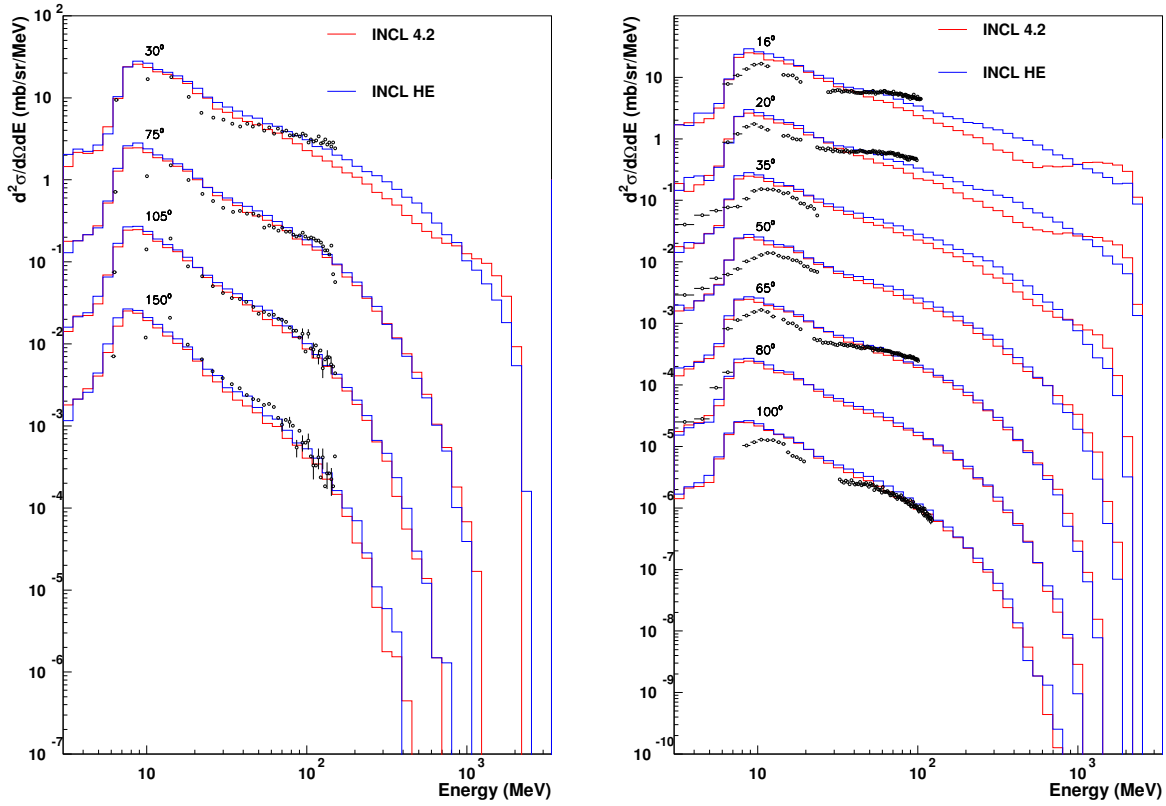

(a) (b)

Figure 6.3: *Proton spectra for $p - Au$ reaction at 2.6 GeV incident energy, the angles are indicated on the figures. Data (symbols) from Letourneau et al. [75] (a) and from Bubak et al. [76] (b) are compared with the standard version of INCL4 (red) and its extended version (blue) at different angles, indicated on the panels.*

been used in the inter-comparison of the IAEA between the intranuclear cascade + evaporation models [4] and none of the tested models could reproduce the flattened behavior of the proton emitted with an energy around 100 MeV, visible in the data. Note, however that the two sets of data do not seem to be totally compatible. The slope of the spectra around 100 MeV seems to be steeper in the Letourneau data (left panel).

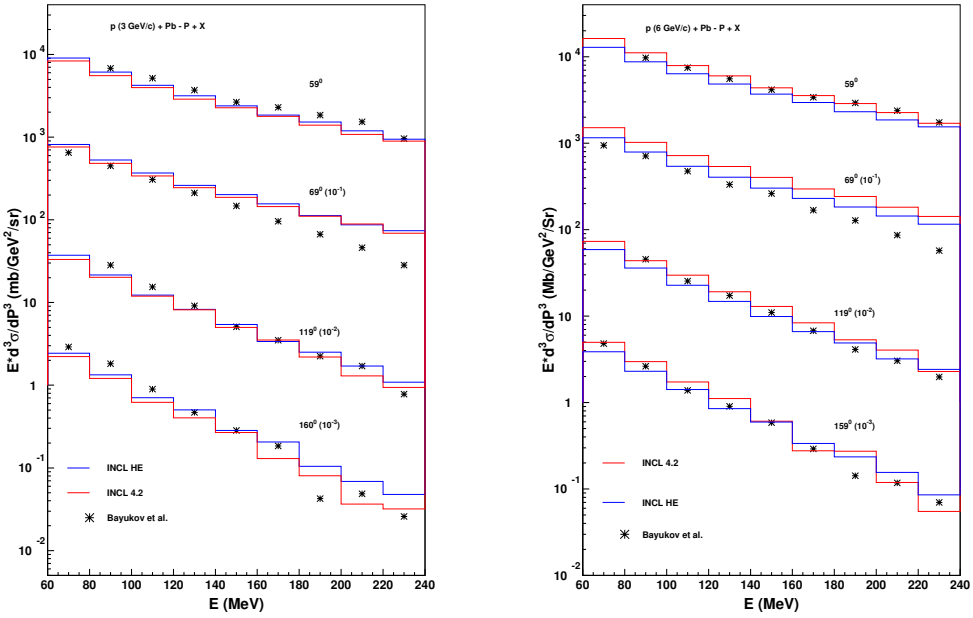

(a) p (3 GeV/c) + Pb $\rightarrow$ p (b) p (6 GeV/c) + Pb $\rightarrow$ p

Figure 6.4: *Invariant cross section for production of protons as a function of their kinetic energy in a proton-induced reaction on Pb at 3 GeV/c (a) and 6 GeV/c (b). Data (symbols), from Ref. [77], are compared with the standard version of INCL4.2 (red line) and the extended version of INCL4.2 (blue lines).*

Other set of data for proton emission with high energy projectile have been measured by Bayukov *et al.* [77]. We have compared the results of INCL4.2 and its extended version with these data. Fig. 6.4 shows invariant cross sections $Ed^3\sigma/dp^3$ for proton emission in a proton-induced reaction on a lead target, the momenta of the projectiles are 3 GeV/c (Fig. 6.4(a)) and 6 GeV/c (Fig. 6.4(b)). The data corresponds to 4 angles: 59°, 69°, 119°and 160°, and cover protons emitted with a kinetic energy comprised between 60 and 240 MeV, which is a very small region of the available phase space, given the incident energy.

One can see that for incident protons with momentum 3 GeV/c (Fig. 6.4(a)), both simulations are very similar to each other except for the largest angle. Both are in satisfactory agreement with the data. The simulations tend to underestimate slightly the proton emission for all angles except for 69°. For incident protons with 6 GeV/c momentum, the predictions of the extended version of INCL4.2 are slightly better than the ones from the standard version of INCL4.2, except for the 69°data.

A similar comparison with data also measured by Bayukov *et al.* [78] is shown on Fig. 6.5 for proton-induced reactions on carbon and uranium targets with incident proton momenta of 6 GeV/c and 7.5 GeV/c, respectively. In the case of the carbon target, the simulations are different from one other. At the largest angle, 160°, INCL HE is clearly better than the standard version, while it is more difficult to judge in the case of 119°, and INCL4.2 is better at 59°. And once

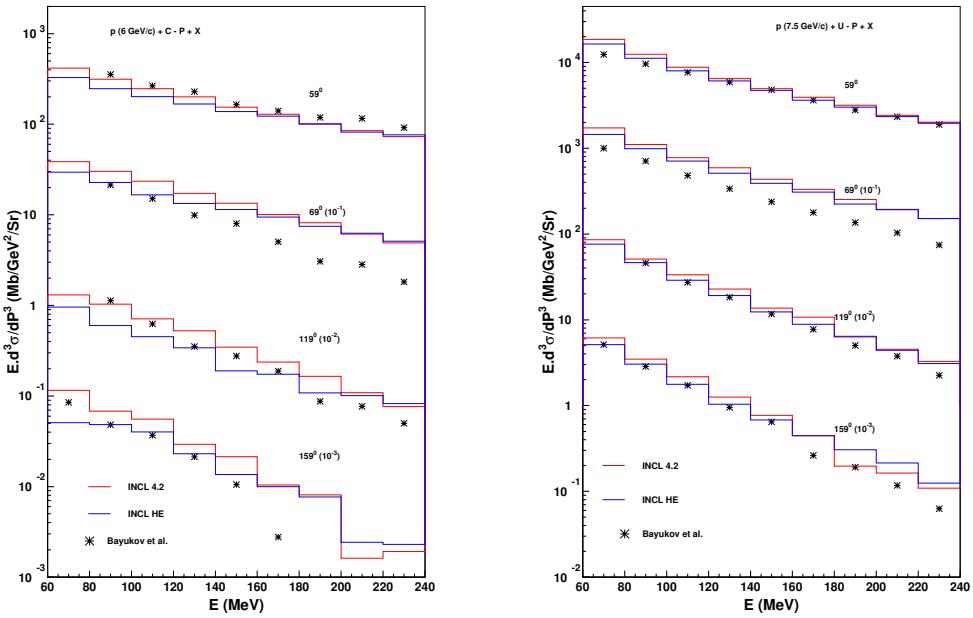

(a) p (6 GeV/c) + C $\rightarrow$ p (b) p (7 GeV/c) + U $\rightarrow$ p

Figure 6.5: *Invariant cross section for production of protons as a function of their kinetic energy in a proton-induced reaction on C at 6 GeV/c (a) and on U at 7.5 GeV/c (b). Data (symbols) from Ref. [77] are compared with the standard version of INCL4.2 (red line) and the extended version of INCL4.2 (blue lines).*

again, the situation is particular for the data at 69°. For the uranium target, the two models both give similar simulations, even though INCL HE seems to be slightly better. For this data, one can see that both models have the right order of magnitude for the cross section for all data except at 69°, where the cross section is systematically overestimated. The previous comparison realized with the data on the gold target doesn't suggest that the simulations overestimate systematically the proton production around this angle at energies between 60 and 240 MeV (there is data for 65°angle on Fig. 6.3(a) and for 75°in Fig. 6.3(b)). Thus we think that the systematic overprediction encountered for that particular angle might indicate a problem in the data.

6.1.3 Total π^+ and π^- yields and integrated pion production cross sections

The pion yield is the most direct variable to test our extension of INCL4.2 to high energy. The π^+ and π^- yields presented in Ref. [79] are compared with our results on Fig. 6.6. Globally, the behavior of the π^- yields are reproduced by the calculations, even if there is some local discrepancy. The comparison with π^+ yield is more delicate as the data is too scarce to draw definite conclusions, nevertheless it seems that the general trend is also well reproduced: at low incident energy, the π^+ yield is larger than the π^- one and the difference decreases with increasing incident energy as well as with increasing target mass. Both situations correspond to reactions in which secondary collisions become more and more important. One can also see a comparison with calculations using the MARS/CEM model (Refs. [80, 81, 82]) on Fig. 6.6. Our predictions are very close to the results of this model for energies up to more or less 4 GeV. At higher energies, the yields predicted by our model are larger than the ones from the MARS/CEM

model, but this difference between the predictions of the two models tends to decrease as the energy keeps increasing.

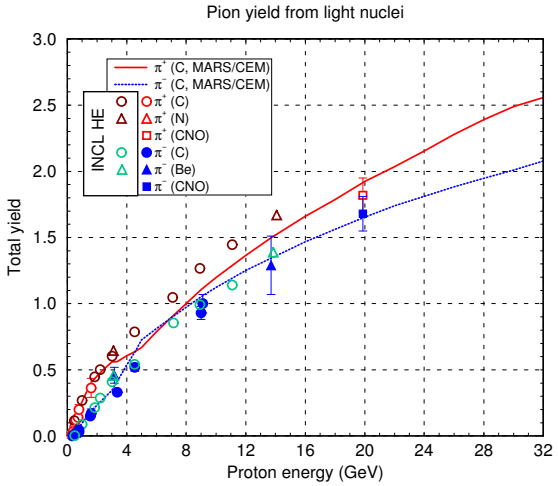

(a) C and N targets

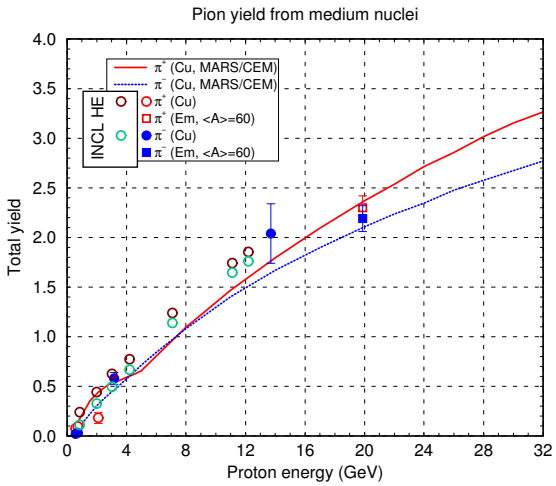

(b) Cu target

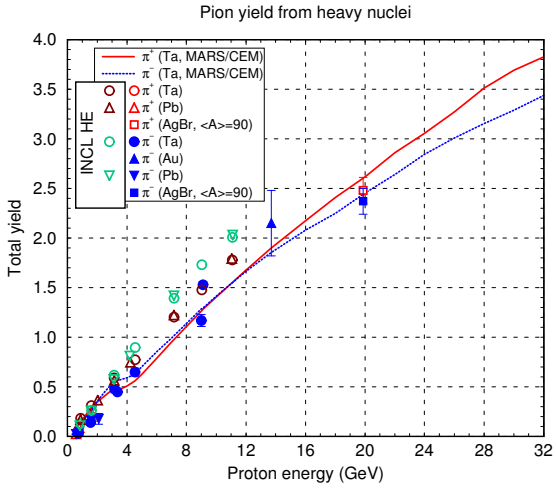

(c) Ta and Pb targets

Figure 6.6: *Total π^+ and π^- yields as functions of the incident energy in proton-induced reactions on light (a), medium-weight (b) and heavy (c) targets. Experimental data are represented by blue (π^-) and red (π^+) symbols. Our predictions are in green (π^-) and dark red (π^+) symbols. The meaning of the various symbols can be read from the panels. Data are taken from Ref. [79] and are also compared with the calculations based on the MARS/CEM model [80, 81, 45, 82], indicated by the full curves in the same colors as the experimental data.*

Fig. 6.7 shows integrated π^+ and π^- cross sections, measured by the HARP collaboration [11] for different targets[1] and different incident energies[2]. The integration of the double-differential cross sections were realized over the acceptance of the HARP experimental set-up. It corresponds to a domain extending from 350 to 2150 mrad for the polar angle and from 100-150 to 400-750 MeV/c (depending upon the angles as presented in Table D.1) for the emitted pion momentum.

[1]The targets used in the HARP experiment are, from the lightest to the heaviest: Be, C, Al, Cu, Sn, Ta and Pb.

[2]The momenta of the incident protons are 3, 5, 8 and 12 GeV/c.

This acceptance roughly corresponds to 25% of the total production cross section.

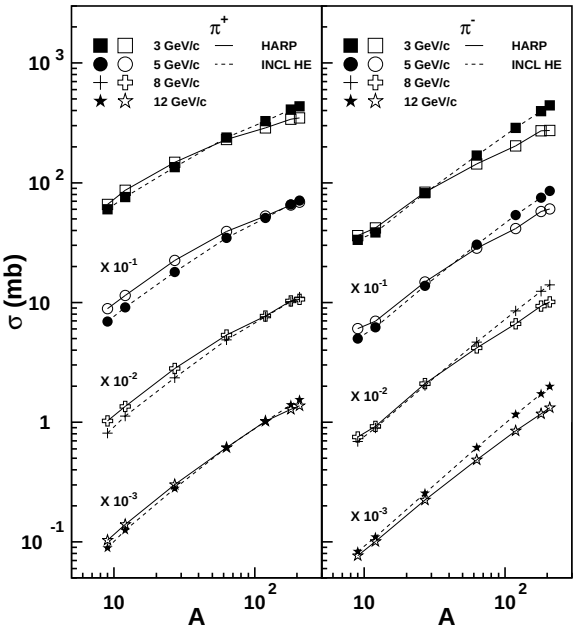

Figure 6.7: *π^+ (left panel) and π^- (right panel) production cross sections in proton-induced reactions on several targets and at different incident momenta. The data are obtained by integrating double-differential cross sections on the acceptance (in angle and momentum) of the HARP experiment, given in Tab. D.1. The experimental data correspond to the open symbols and our predictions correspond to the black symbols (lines are just to guide the eye). Data are from Ref. [83, 84, 85, 11] and refer to Be, C, Al, Cu, Sn, Ta and Pb targets.*

One can see that, on the average, the general trends are reproduced: the pion production cross sections are increasing with the target mass roughly according to a power law $\sigma = \sigma_0 A^\alpha$. The exponent α is close to unity for π^- production. For π^+ production, it goes from ~ 0.7 for the lowest incident energy to ~ 0.9 for the highest one. A value of α of $2/3$ would correspond to a black disk situation, but α is greater than this value, indicating that the pion production results from many collisions. The comparison with our results shows that the model slightly underestimates the π^+ production cross section for light targets and slightly overestimates the π^- production for heavy targets.

The dependence of the cross sections upon the incident energy, presented on Fig. 6.8, is slightly lower than linear and is roughly reproduced by our calculations. However, the cross sections do not increase very much over the incident energy range for light targets, whereas they increase by a factor 4 for heavy targets (both for π^+ and π^-). The behavior for light targets contrasts with the one indicated on Fig. 6.6: in that case, the total production cross section (equal to the yield multiplied by the total reaction cross section, which does not change much above 2 GeV/c) is increasing with energy, by a factor 2-3, in the energy range under interest here. The difference likely comes from the rather restricted acceptance for the data collected in Fig. 6.7, especially in momentum space: energetic pions produced in light targets, which are more numerous as the incident energy increases, are missing in these data.

One can see on Fig. 6.8 that the π^+/π^- ratio is close to unity for the light targets and decreases as the mass of the target increases, in the domain of acceptance of the HARP experiment.

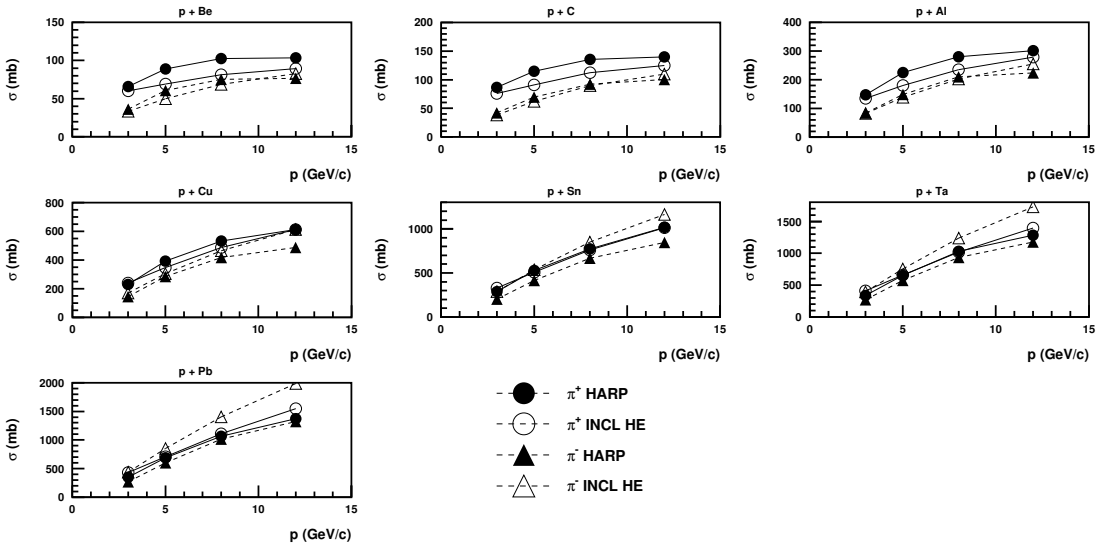

Figure 6.8: *Dependence of the π^+ (circle) and π^- (triangle) production cross sections in proton-induced reactions on several targets with the incident momentum p. The data are obtained by integrating double-differential cross sections on the acceptance (in angle and momentum) of the HARP experiment, given in Tab. D.1. The experimental data correspond to the black symbols and our predictions correspond to the open symbols (lines are just to guide the eye). Data are from Ref. [83, 84, 85, 11].*

Table 6.1 is a summary of the total π^+/π^- ratio (not limited to the acceptance of the HARP experiment), for the same targets but only for proton with incident momentum of 5 and 12 GeV/c.

Target	π^+/π^-	
	5 GeV/c	12 GeV/c
Be	1.37	1.19
C	1.47	1.23
Al	1.31	1.15
Cu	1.16	1.05
Sn	0.98	0.92
Ta	0.90	0.85
Pb	0.86	0.82

Table 6.1: *Ratio between the total π^+ and π^- production, calculated by the extended version of INCL4.2, for proton-induced reactions on different targets specified in the table, for incident momentum of protons of 5 and 12 GeV/c.*

Table 6.1 shows that, when the number of secondary collisions increases (when the available energy increases and when the target is heavier), the ratio between π^+ and π^- production cross section decreases. Indeed, it is expected that an incident proton has a higher chance to produce a π^+ than a π^- in a single collision on a nucleon, taken as a neutron or a proton with equal probability, because it brings an extra positive charge. This effect is slightly weakened for heavy nuclei, which are neutron rich. This tendency of producing preferentially positive pions

is attenuated by multiple collisions, i.e. when the incident energy and/or the target mass are increasing. In secondary πN collisions, the situation is a bit complicated by the fact that the nucleon can only have positive or neutral charges, thus favoring emission of negatively charged pions A quick review of Table 5.6, confirms that the charge repartition model, in πN collisions favors the production of negative pions. The fact that we have such an increase of the π^- yield confirms the importance of secondary collisions in the simulations.

6.1.4 Double-differential cross sections for large-angle pion production

Figure 6.9 shows negative pion spectra for a $p - Al$ reaction at 3 GeV/c and 4 GeV/c. Data comes from [79], the emitted pions have been measured at 4 different angles (45°, 59,8°, 72.5°and 84°) and with kinetic energy ranging from 100 MeV to 850 MeV.

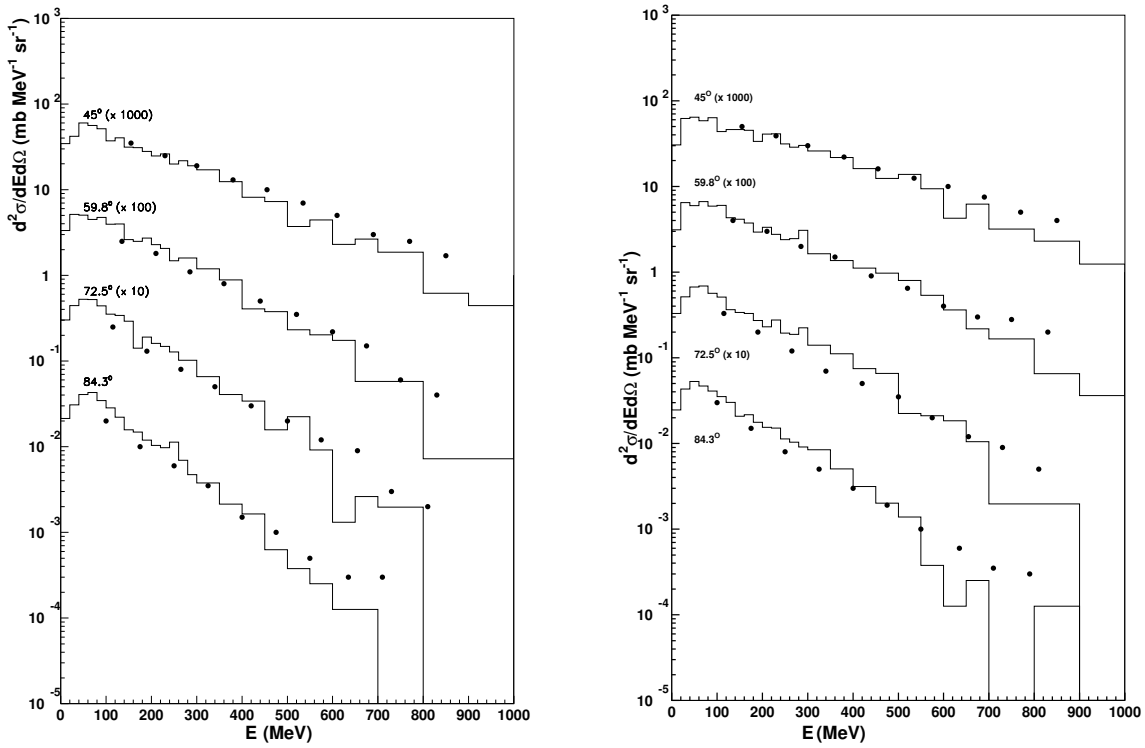

(a) p (3 GeV/c) + $Al \rightarrow \pi^-$ (b) p (4 GeV/c) + $Al \rightarrow \pi^-$

Figure 6.9: *Negative pion spectra for $p - Al$ reaction at 3 GeV/c (left panel) and 4 GeV/c (right panel) incident momenta. Data (symbols) from Ref. [79] are compared with the extended version of INCL4 (lines) at different angles, indicated on the panels.*

The overall agreement between the simulations and the data is quite good at all angles, especially for pions emitted with a kinetic energy below 600 MeV. In the article, the authors compare the data with the CEM model [82] (not shown here). Below the energy of 600 MeV, INCL HE gives slightly better results than CEM.

Double-differential cross sections for π^+ production in proton-induced reactions on three targets (C, Cu, and Pb) at incident momenta (3, 5, 8 and 12 GeV/c), measured by the HARP collaboration, are presented and compared with our calculations in Figs. 6.10 to 6.12. In order

to exhibit the effect of the implementation of direct multipion production, we show the results with both the standard version INCL4.2 and the extended version of our model (INCL HE). Of course, calculations have been done for all targets, but the results shown here are sufficient for illustrating the general trends of our results. The figures for the other targets can be found in Appendix D.

Each panel is divided in nine parts, each of them corresponding to a different angular bin in the experiments. The values of these angular bins are always the same and are arranged as follows:

350–550 mrad	550–750 mrad	750–950 mrad
950–1150 mrad	1150–1350 mrad	1350–1550 mrad
1550–1750 mrad	1750–1950 mrad	1950–2150 mrad

Table 6.2: *Angular bins of each panels on figures showing comparison between simulations and double-differential cross section data from HARP experiment.*

One can see on Figs. 6.10 to 6.12 that the agreement between the simulations and the data is quite remarkable. The introduction of multipion production channels has improved considerably the simulations if one compares the results given by the INCL4.2 version to the ones given by the extended version and the data from the HARP experiment. As the energy of the projectile increases, the results given by the standard version of INCL at forward angles become very poor, which was expected as we are far from the domain of validity of the model.

Figs. 6.13 to 6.15 display the same comparison for double-differential cross sections but for the negative pion production. In this case, our predictions are even slightly better. Another relatively small shortcoming appears for Pb target: the yield for low energy pions at small angles is overestimated.

The integrated cross sections showed on Fig. 6.7 showed that our extended version of INCL4.2 tends to underestimate pion production in reactions with light targets. This underestimation is turned into an overestimation as the mass of the target increases.

The comparison of the profile of the measured and simulated double-differential cross sections shows a systematic underestimation of the spectra for the 3-4 lowest angles, depending on the target. This underestimation concerns mainly emitted pions with a momentum comprised between 200 and 600 MeV. On the contrary, INCL HE tends to overestimate emitted pions with large momenta (larger than 600–700 MeV) for the other angular bins. Both of these systematic problems are attenuated for heavy targets. This can be explained by the secondary collisions which are favored in heavy targets. As the mass of the target increases, the underestimation of pion production at small angles disappears and even, in the case of the Pb target (and also in the Ta, showed in the appendix) starts to be overestimated. The pion production for heavy target tends to be too high.

The shapes of the pion momentum spectra do not change very much over the whole set displayed on Figs. 6.10 to 6.15. They show a maximum at small angles for all cases and smoothly change to a basically exponentially decreasing curve at large angles. The maximum is less and less pronounced with increasing incident momentum and with increasing target mass. This is basically in agreement with a multiple scattering picture. Indeed, this scenario is expected to produce more and more pions in the forward direction as the incident energy increases and, to some extent, when the target size increases.

It is interesting that our model, even if it does not perfectly reproduce the data, has nevertheless caught the general trends of the shape and intensity of the pion spectra. This presumably

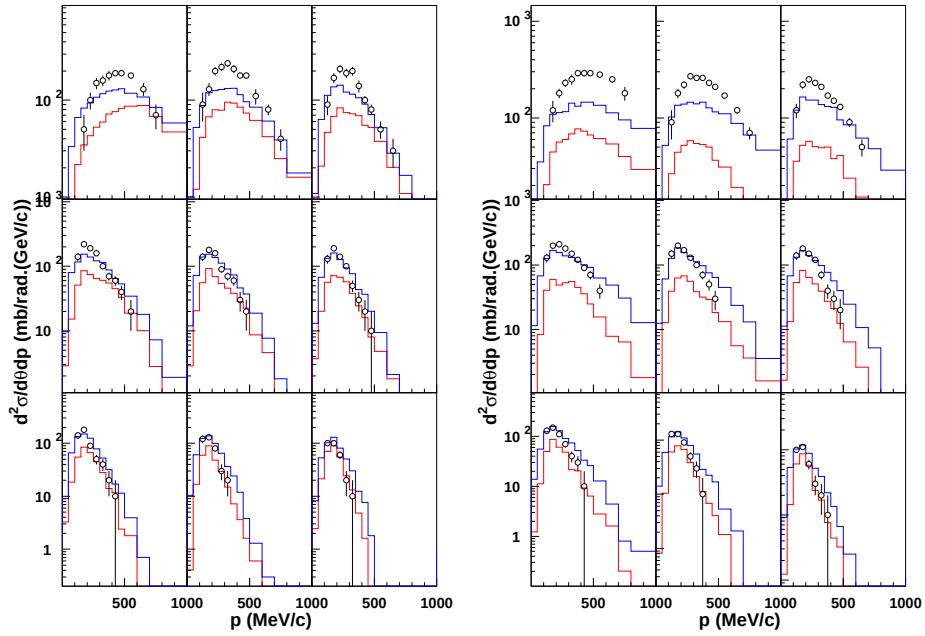

(a) p (3 GeV/c) + C → π^+ (b) p (5 GeV/c) + C → π^+

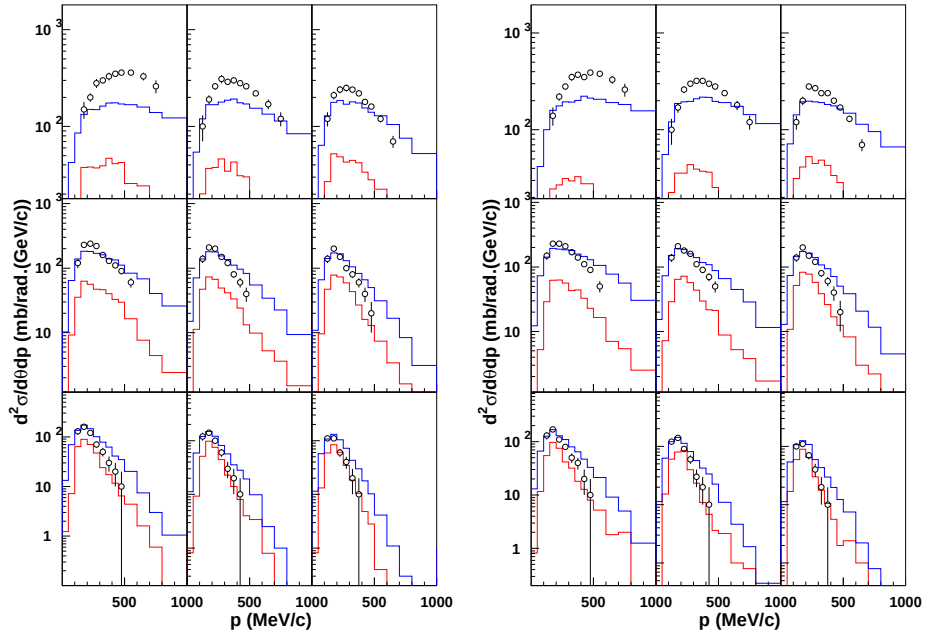

(c) p (8 GeV/c) + C → π^+ (d) p (12 GeV/c) + C → π^+

Figure 6.10: *Double-differential cross sections for π^+ production in proton-induced reactions on C at 3 GeV/c (a), 5 GeV/c (b), 8 GeV/c (c) and 12 GeV/c (d) incident momentum. Data (symbols) from Refs. [11, 85] are compared with the standard version (red lines) and the improved version (blue lines) of the INCL4 model (standard INCL4.2 version plus implementation of direct multipion production). See text for detail.*

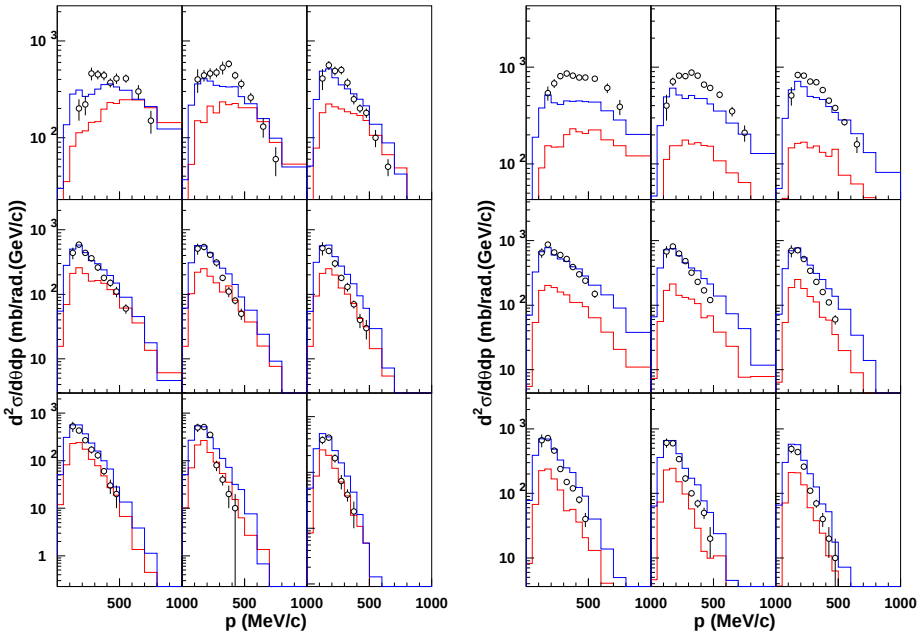

(a) p (3 GeV/c) + Cu $\rightarrow$ π^+

(b) p (5 GeV/c) + Cu $\rightarrow$ π^+

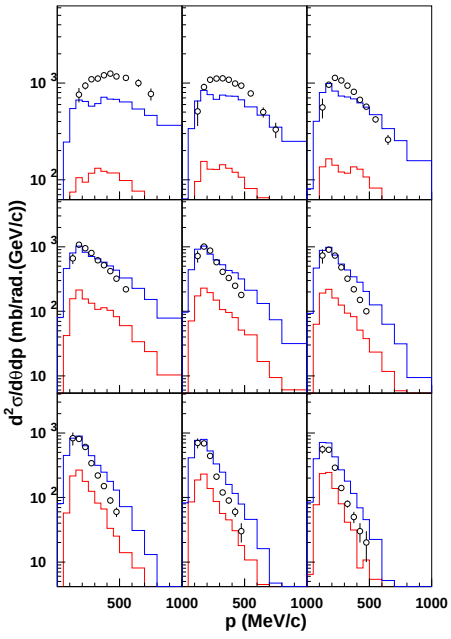

(c) p (8 GeV/c) + Cu $\rightarrow$ π^+

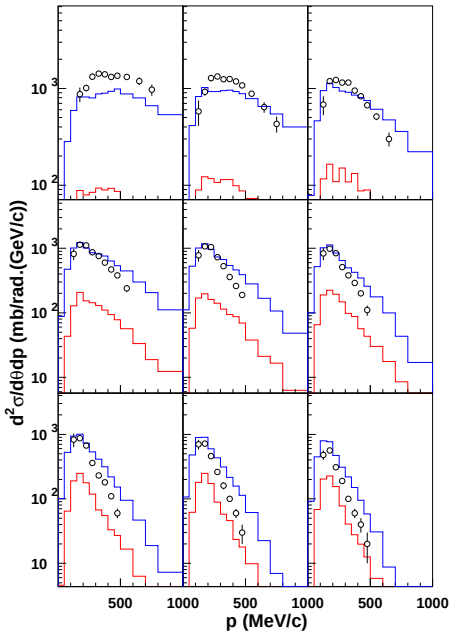

(d) p (12 GeV/c) + Cu $\rightarrow$ π^+

Figure 6.11: *Same as Figure 6.10, for a Cu target. Data come from Refs. [11, 85].*

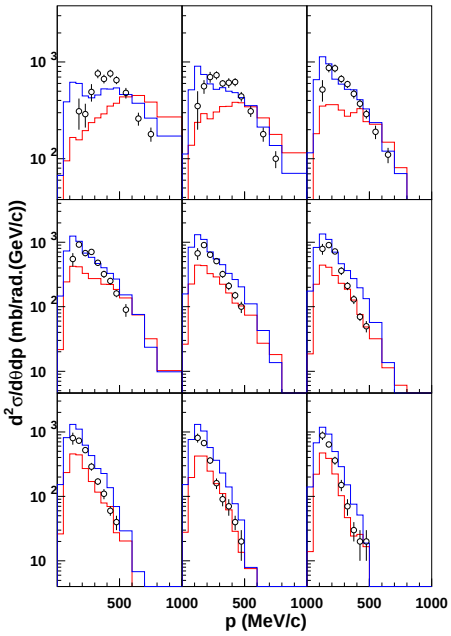

(a) p (3 GeV/c) + Pb $\rightarrow$ π^+

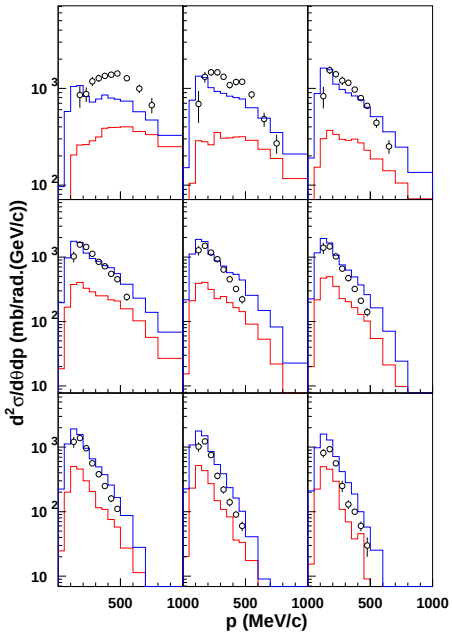

(b) p (5 GeV/c) + Pb $\rightarrow$ π^+

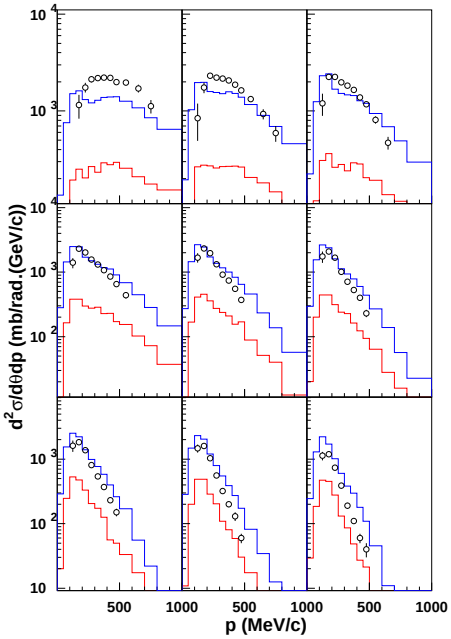

(c) p (8 GeV/c) + Pb $\rightarrow$ π^+

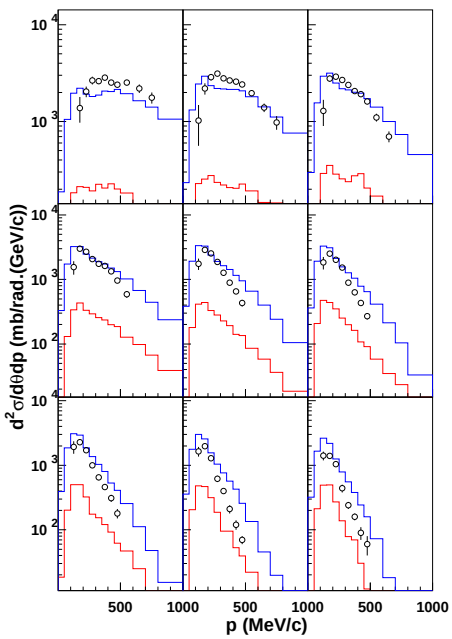

(d) p (12 GeV/c) + Pb $\rightarrow$ π^+

Figure 6.12: *Same as Figure 6.10, for a Pb target. Data come from Refs. [11, 84].*

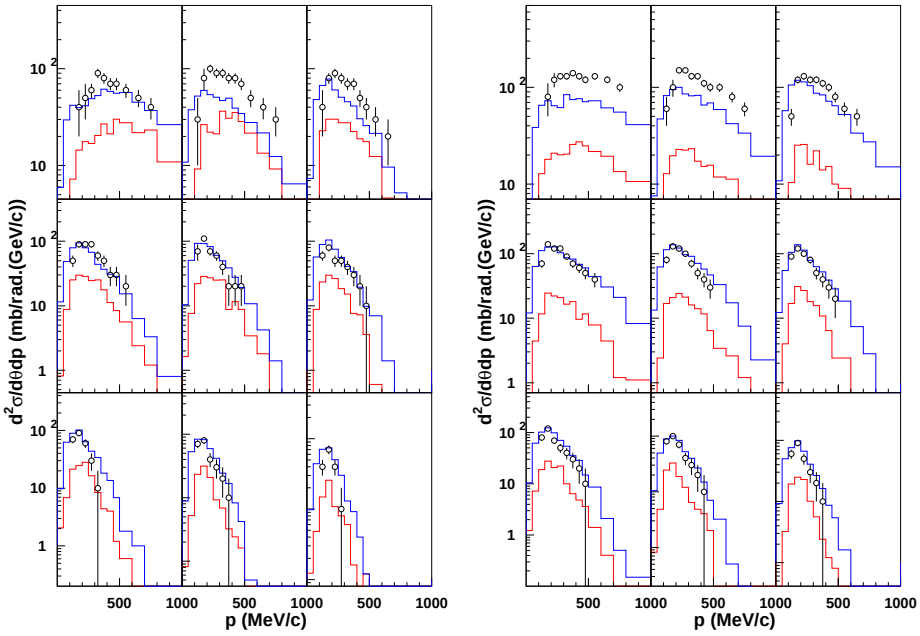

(a) p (3 GeV/c) + C $\rightarrow$ π^- (b) p (5 GeV/c) + C $\rightarrow$ π^-

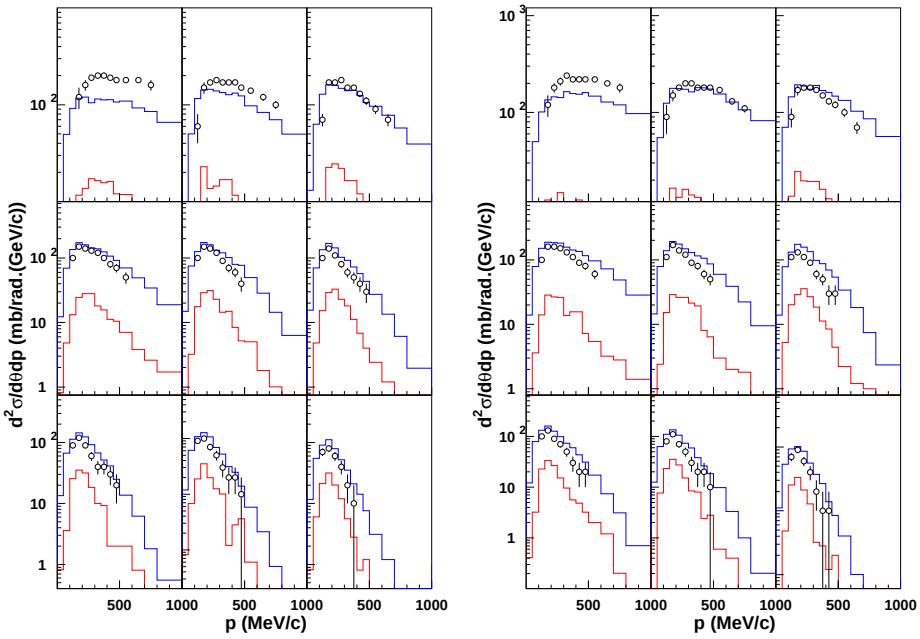

(c) p (8 GeV/c) + C $\rightarrow$ π^- (d) p (12 GeV/c) + C $\rightarrow$ π^-

Figure 6.13: *Double-differential cross sections for π^- production in proton-induced reactions on C at 3 GeV/c (a), 5 GeV/c (b), 8 GeV/c (c) and 12 GeV/c (d) incident momentum. Data (symbols) from Refs. [11, 85] are compared with the standard version (red lines) and the improved version (blue lines) of the INCL4 model (standard INCL4.2 version plus implementation of direct multipion production). See text for detail.*

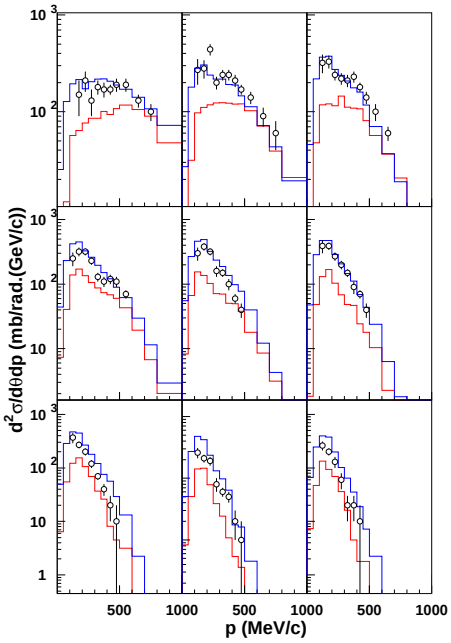

(a) p (3 GeV/c) + Cu $\rightarrow$ π^-

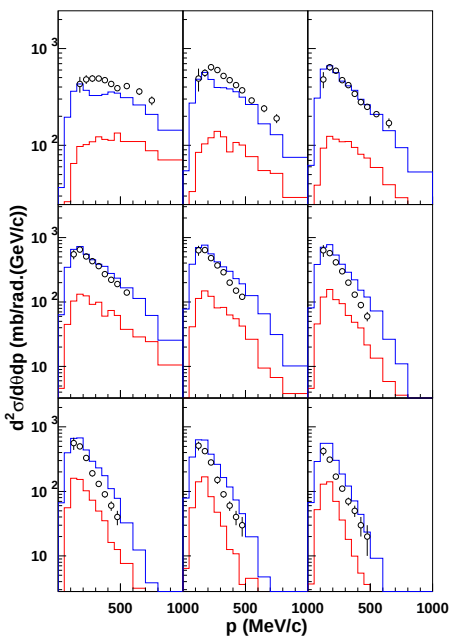

(b) p (5 GeV/c) + Cu $\rightarrow$ π^-

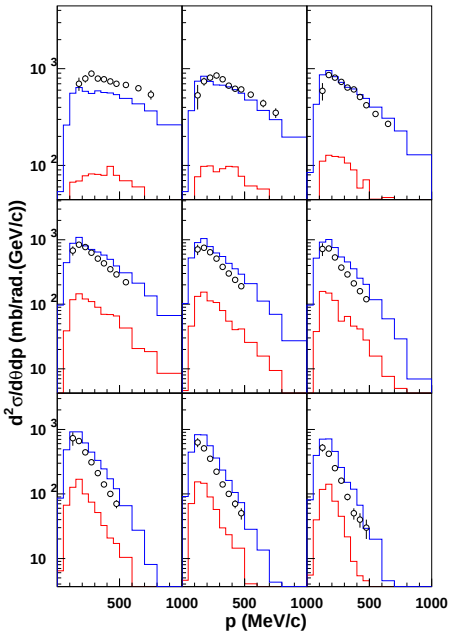

(c) p (8 GeV/c) + Cu $\rightarrow$ π^-

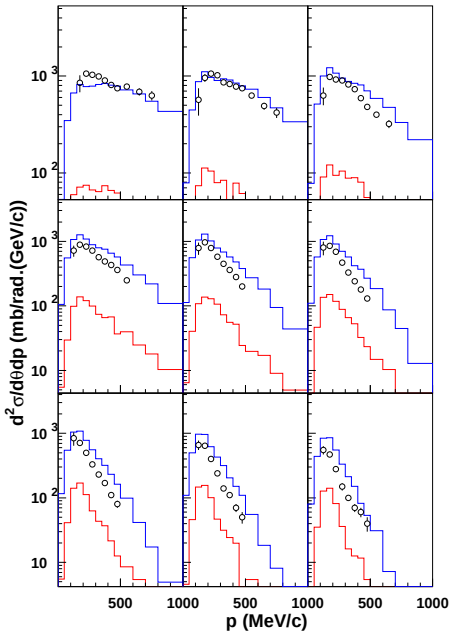

(d) p (12 GeV/c) + Cu $\rightarrow$ π^-

Figure 6.14: *Same as Figure 6.13, for a Cu target. Data come from Refs. [11, 85].*

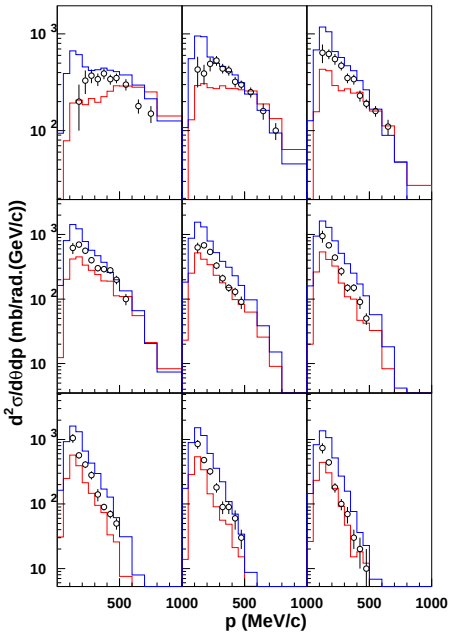

(a) p (3 GeV/c) + Pb $\rightarrow$ π^-

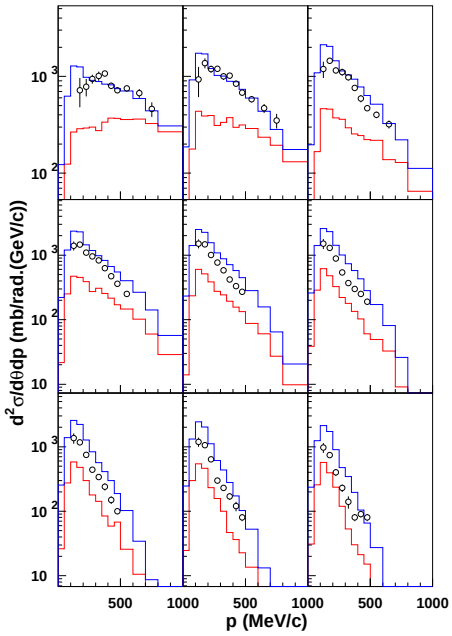

(b) p (5 GeV/c) + Pb $\rightarrow$ π^-

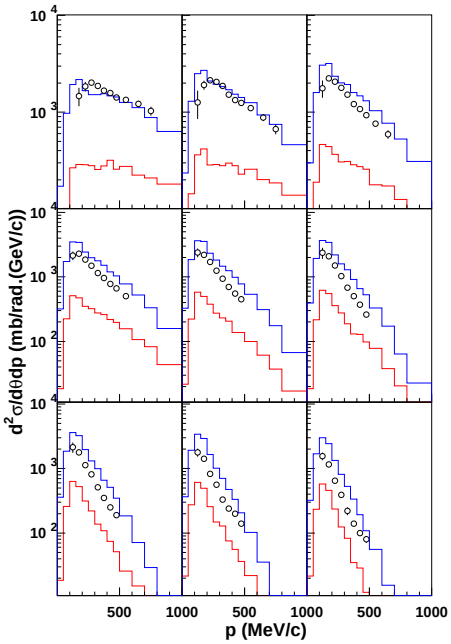

(c) p (8 GeV/c) + Pb $\rightarrow$ π^-

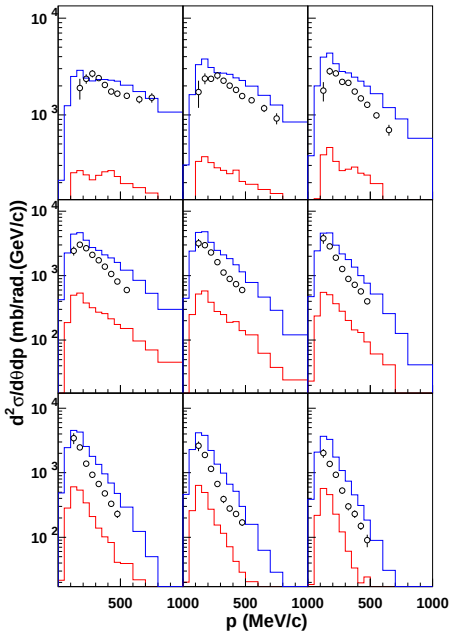

(d) p (12 GeV/c) + Pb $\rightarrow$ π^-

Figure 6.15: *Same as Figure 6.13, for a Pb target. Data come from Refs. [11, 84].*

means that it properly describes the multiple scattering in detail and that the latter, in reality, is dictated by the free elementary cross sections, as this is the basic premise of our INCL4 model.

On Figs. 6.10 to 6.15, we have included the predictions of the standard INCL4.2 model. First of all, one can see that the modifications described above have tremendously improved the predictive power of the model. It is interesting to note that the predictions of the modified model and those of the standard model are rather close to each other at large angles and for 3 GeV/c incident momentum. We recall that in the standard model, the main source of pions is coming from $NN \to N\Delta$, $\Delta \to \pi N$ processes. Of course, pions may be absorbed and re-emitted, but without changing very much the yield [34]. Therefore, this strongly suggests that, at large angles and low incident energy, pions are basically produced by a small number of collisions, in agreement with the discussion above.

The integration of the double-differential cross sections presented in Figs. 6.10-6.15 over the angular domain and over the momentum domain of the emitted pions (presented in Tab. D.1) confirms the previous observations: the implementation of multipion production channels has improved the simulations in the considered domain of energy. Figs. 6.16(a) to 6.18(d) show these integrated cross sections.

The comparison between the measured and simulated simple-differential cross sections shows interesting features:

- The predictions for π^- emission are, most of the time, slightly better than for π^+ emission.
- The angular profile of the emission of pions are not "sharp" enough, in the sense that simulations systematically underestimate predictions for the lower angles and overestimate large angle emissions. The profile should decrease more rapidly, for all targets and at all incident energies.
- The momentum profile is in very good agreement with experimental data, the model reproduces well the shape, for all targets. The energy-momentum repartition model, presented in the previous chapter, thus gives good results, but the angular profile could be further improved. The only problem that appears is an overestimation of produced pions with a momentum smaller than 250–300 MeV/c for heavy targets.

This might indicate that our phase space should be biased more in the direction of a forward peaked angular distribution.

6.1.5 Forward-angle pion production double-differential cross sections

The HARP collaboration has also published data on pion production at forward angles [12], in the 50–250 mrad region and for a larger range of pion momentum than in their previous work. We show in Figs. 6.19 to 6.21, their experimental data along with our predictions. Predictions from the standard INCL4.2 are not present on these figures.

One can see that the agreement is satisfactory and that our model for multipion production is able to generate high momentum pions. Actually, the calculated spectra do not fall off sufficiently fast at high pion momentum, compared to the experimental data. This may indicate that our modified uniform phase space model is still a little bit too crude. It seems that the configurations producing pions with the highest momentum should have a somehow reduced weight. Nevertheless, these results show at least that the production of pions by approximately uniform phase space does not produce results in sharp disagreement with experimental data.

Globally, the results for the negative pion production are better than for the positive pion production. The spectra are underestimated for low emitted pions with momenta lower than 2–3

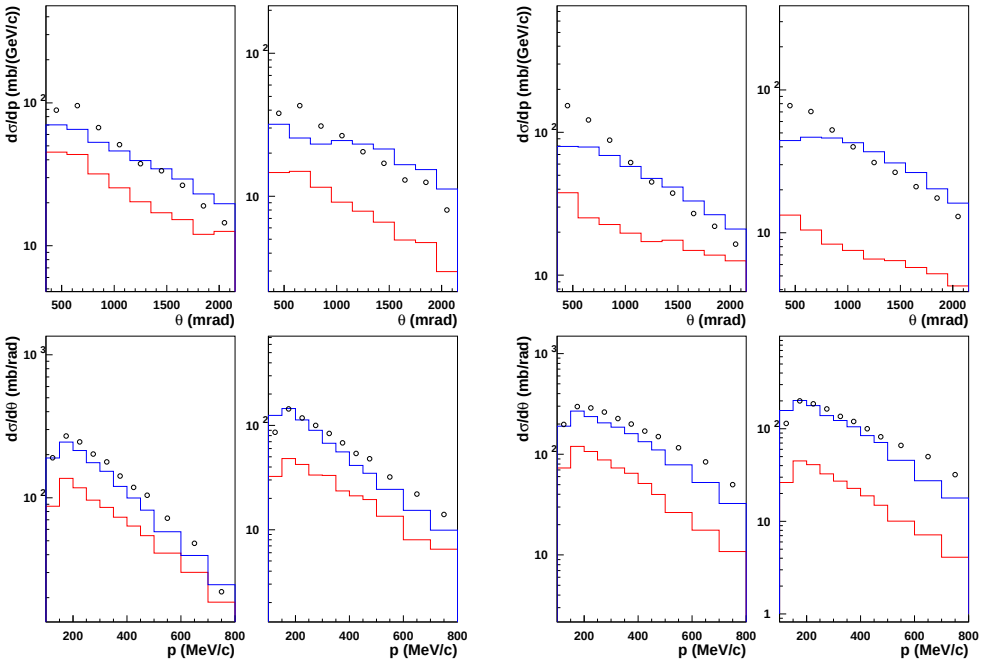

(a) p (3 GeV/c) + C

(b) p (5 GeV/c) + C

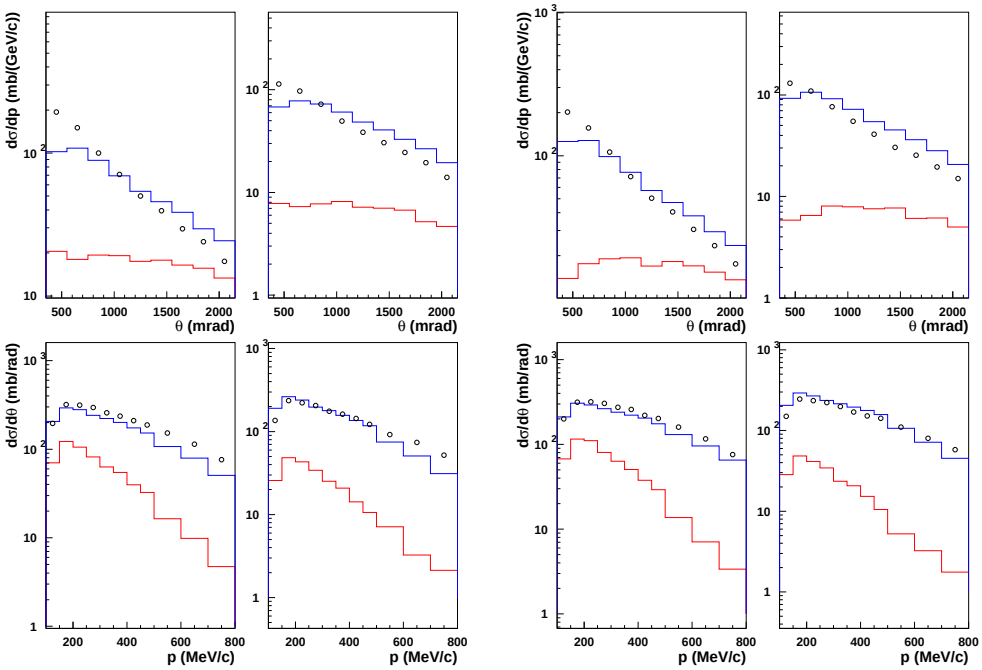

(c) p (8 GeV/c) + C

(d) p (12 GeV/c) + C

Figure 6.16: *Simple-differential cross section in proton-induced reactions on C target at 3 GeV/c (a), 5 GeV/c (b), 8 GeV/c (c) and 12 GeV/c (d) incident momentum. Each panel is divided in four, corresponding to the integration of the π^+ production (left column of the panel) double-differential cross sections or the π^- production (right column of the panel) double-differential cross sections of the HARP experiment Refs. [11, 85] over the momentum domain (upper part of the panel) or over the angular domain (lower part of the panel) presented in Tab. D.1. The date are represented by the circles and are compared with INCL HE (blue line).*

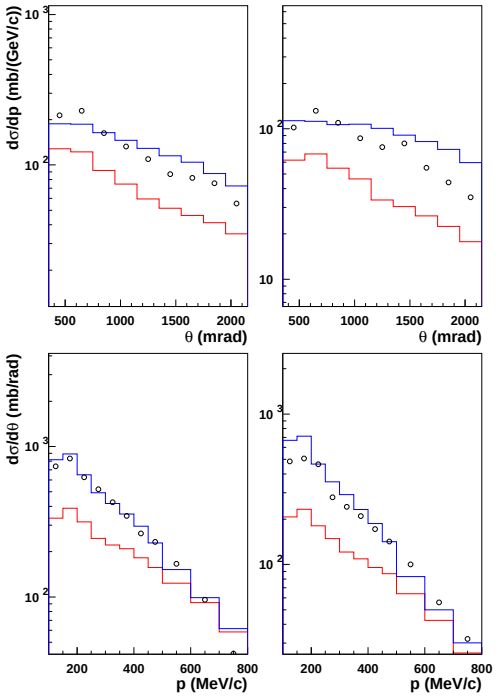

(a) p (3 GeV/c) + Cu

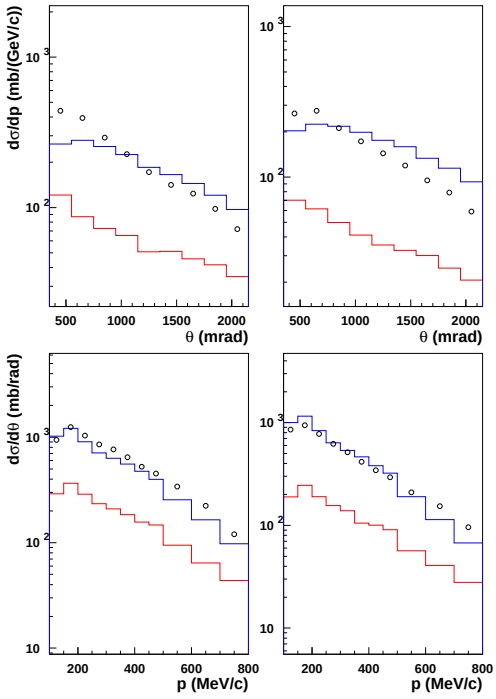

(b) p (5 GeV/c) + Cu

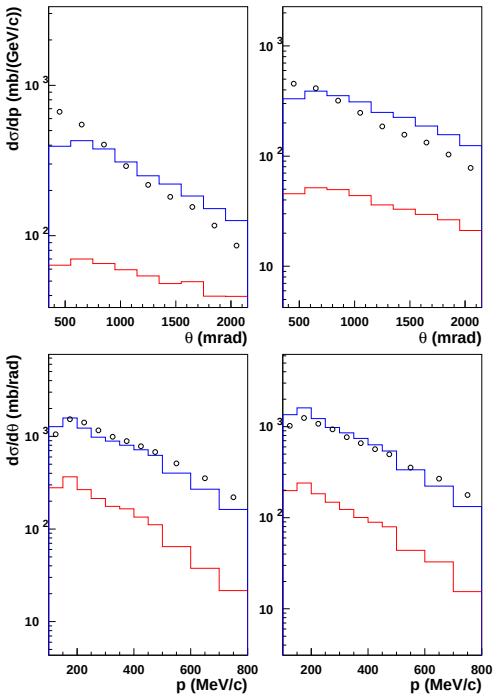

(c) p (8 GeV/c) + Cu

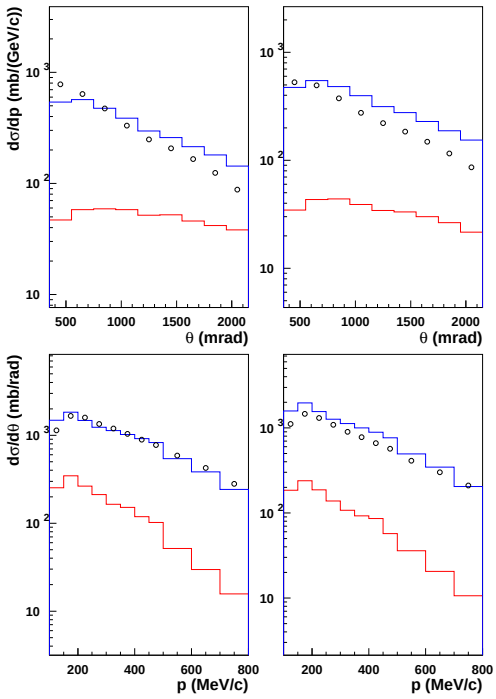

(d) p (12 GeV/c) + Cu

Figure 6.17: *Same as Figure 6.16, for a Cu target. Data are from Refs. [11, 85].*

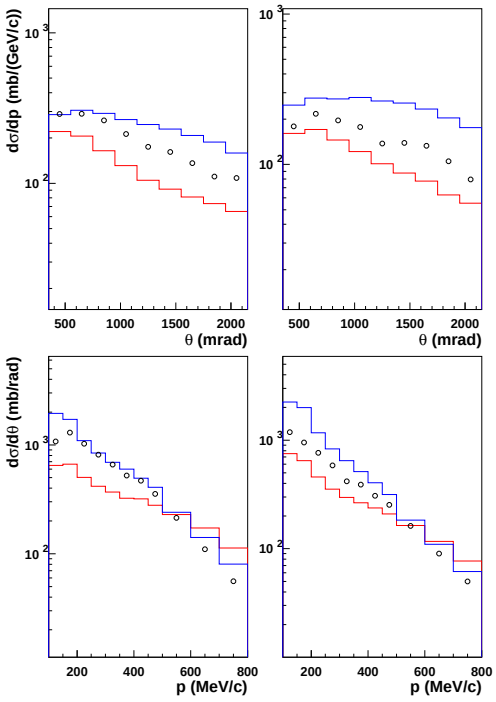

(a) p (3 GeV/c) + Pb

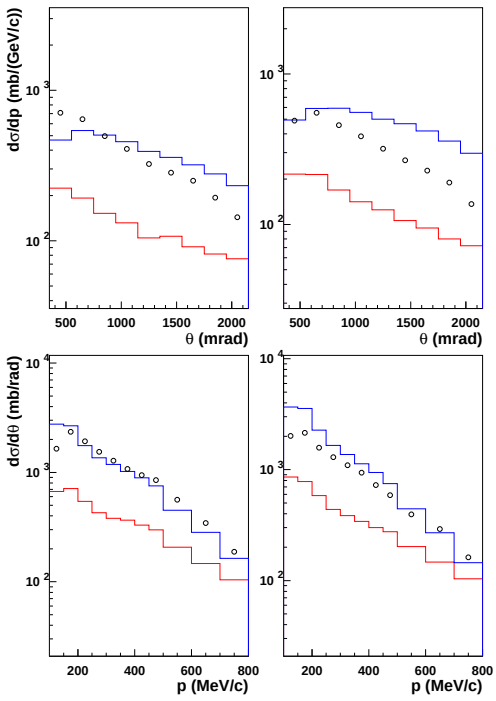

(b) p (5 GeV/c) + Pb

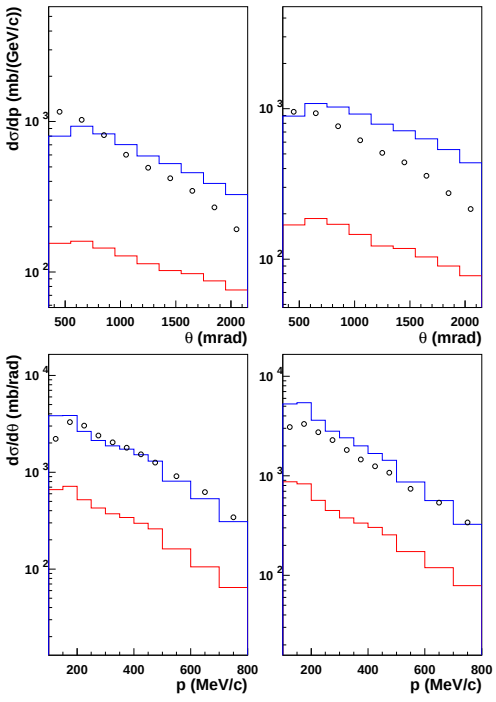

(c) p (8 GeV/c) + Pb

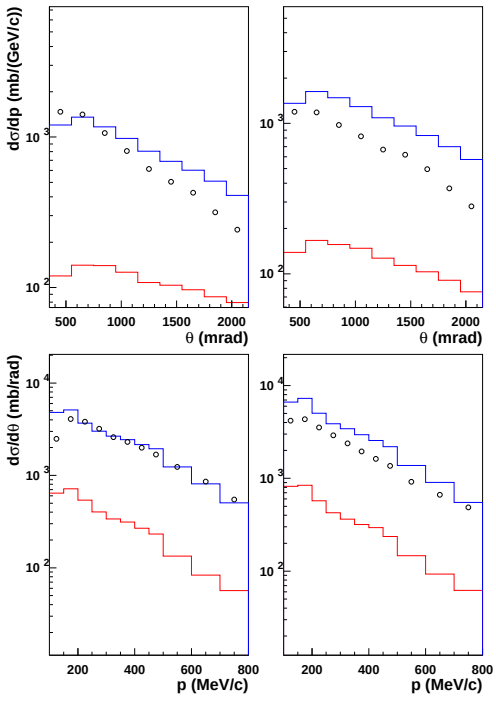

(d) p (12 GeV/c) + Pb

Figure 6.18: *Same as Figure 6.16, for a Pb target. Data are from Refs. [11, 84].*

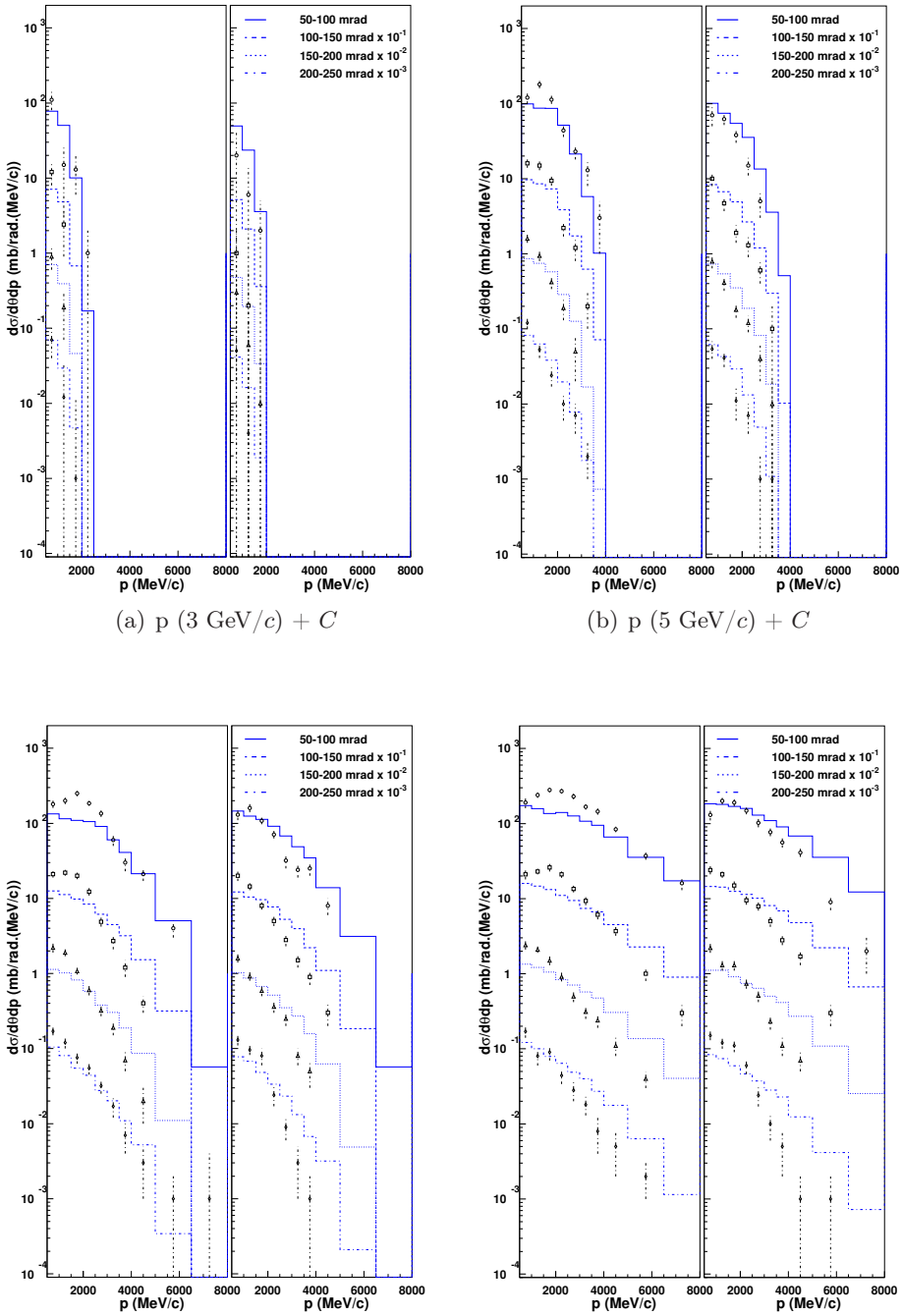

(a) p (3 GeV/c) + C (b) p (5 GeV/c) + C

(c) p (8 GeV/c) + C (d) p (12 GeV/c) + C

Figure 6.19: *Double-differential cross sections for the π^+ production (left part of each panels) and π^- production (right part of each panels) in proton-induced reactions on C target. Data (symbols) from Ref. [12] are compared with the improved version (blue lines) of INCL4. The different lines correspond to the indicated angular bins by the legend. The panels correspond to the indicated incident momenta.*

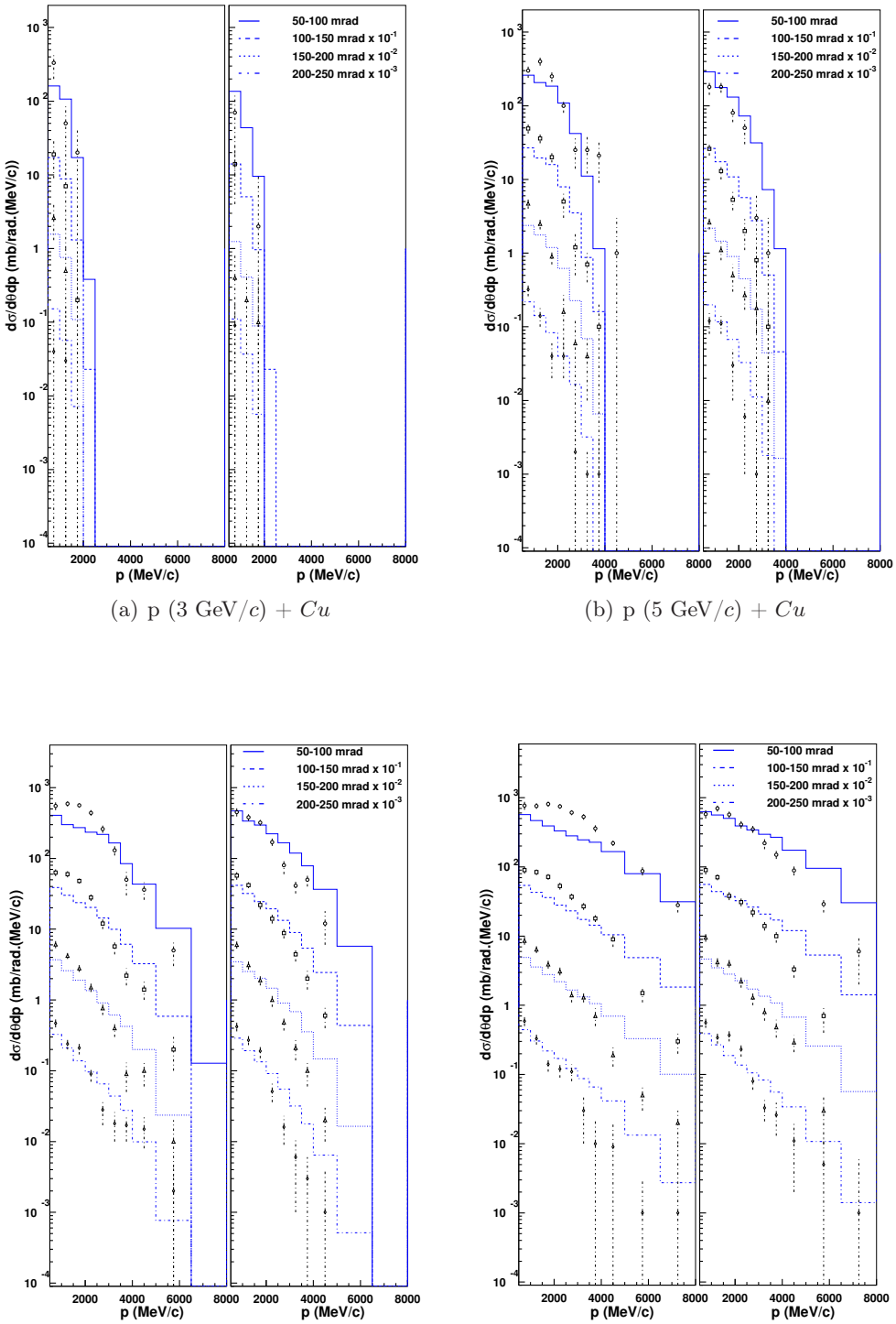

(a) p (3 GeV/c) + Cu

(b) p (5 GeV/c) + Cu

(c) p (8 GeV/c) + Cu

(d) p (12 GeV/c) + Cu

Figure 6.20: *Same as Figure 6.19 for a Cu target. Data are from Ref. [12].*

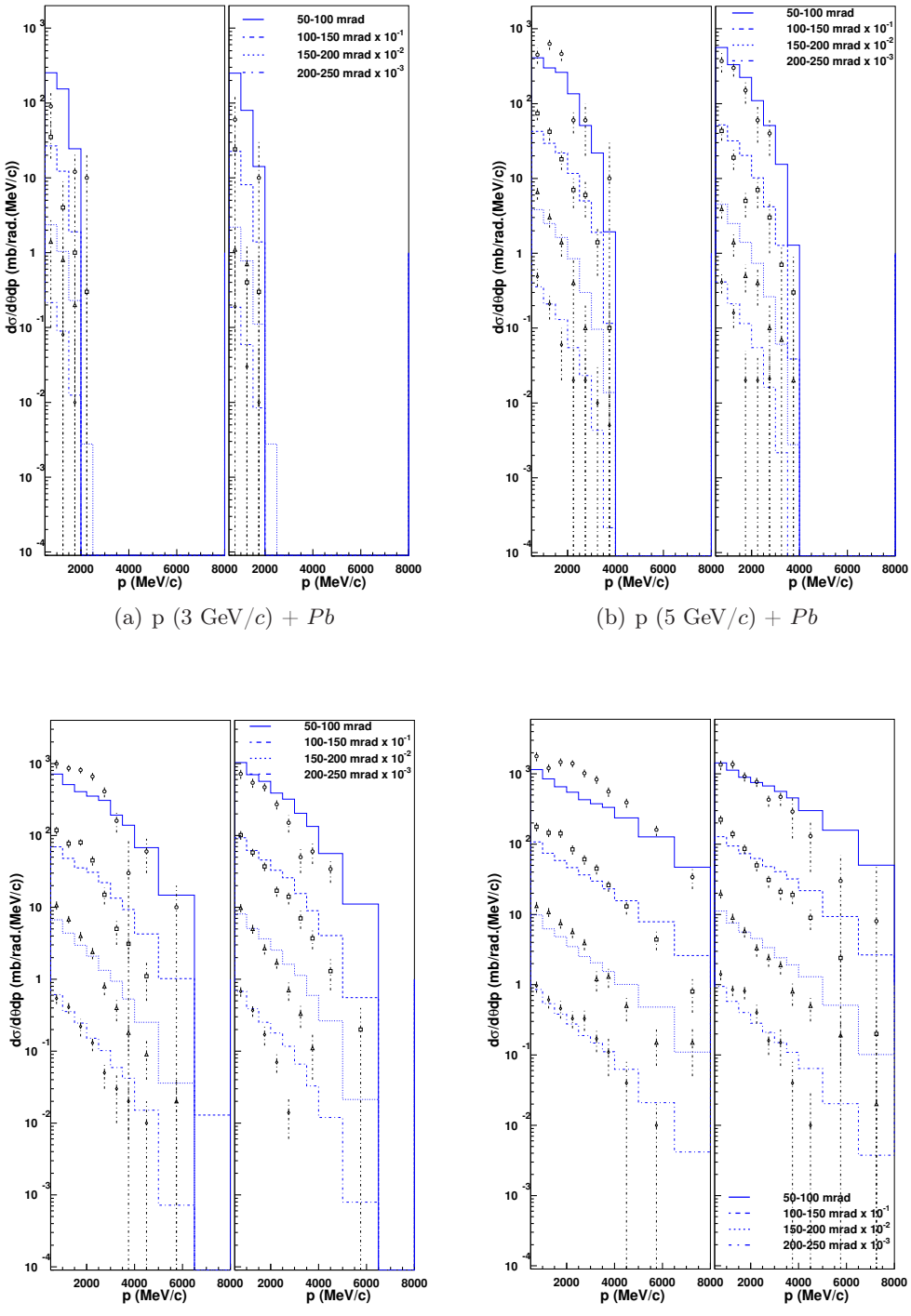

(a) p (3 GeV/c) + Pb

(b) p (5 GeV/c) + Pb

(c) p (8 GeV/c) + Pb

(d) p (12 GeV/c) + Pb

Figure 6.21: *Same as Figure 6.19 for a Pb target. Data are from Ref. [12].*

GeV and overestimated otherwise. This effect does not seem to be influenced by the mass of the target.

6.2 Charged pion-induced reactions

6.2.1 Integrated cross sections

The HARP collaboration has also performed measurements of double-differential pion production cross sections in $\pi^{\pm}$ induced reactions [13]. The targets in this experiment are the same as previously and the pions have the same incident momenta as in the proton experiments.

There were no inelastic channels in $N\pi$ collisions in the standard version of INCL4.2, simulations with this version of the code were then unable to reproduce this data and are not shown on the figures. Figure 6.22 shows the integrated double-differential cross sections over the acceptance domain of the experiment, which is the same as before and is presented in Tab. D.1.

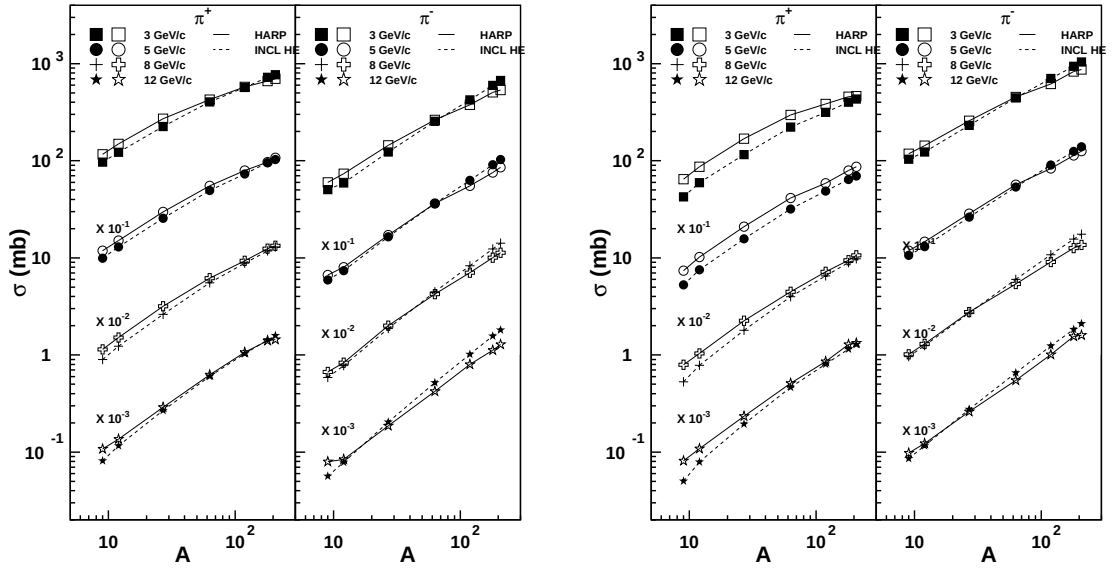

(a) π^+-induced reactions

(b) π^--induced reactions

Figure 6.22: *π^+ (left part of panels) and π^- (right part of panels) production cross sections on several targets and at different incident momenta. The projectile is a positive pion (a) and a negative pion (b). The data are obtained by integrating double-differential cross sections over the acceptance domain (in angle and momentum) of the HARP experiment, indicated in Tab. D.1. The experimental data correspond to the open symbols and our predictions correspond to the black symbols (lines are just to guide the eye). Data are from Ref. [13] and refer to Be, C, Al, Cu, Sn, Ta and Pb targets.*

One can see that the production cross sections, in pion-induced reactions, are increasing with the target mass according to a power law similar to the one observed in proton-induced reactions. The agreement with the experimental data is similar to the one achieved in proton-induced reaction case. It is slightly less good for π^+ production and slightly better for π^- production in the π^--induced reactions. The simulated cross sections are increasing with the target mass with roughly a power law $\sigma = \sigma_0 A^{\alpha}$, like it was the case for proton-induced reactions. The exponent α is slightly superior for π^- production than for π^+ production in π^+-induced reaction (and

vice versa for π^--induced reactions, see Fig. 6.22(b)). In π^+-induced reactions, the value of the exponent is slightly larger than 2/3 for the lowest incident energy and increases to ≈ 0.9 for the highest one. This indicates that the pions are directly produced in the first collision at low energy and that the secondary collisions become more important as the energy increases. One can see from the figure that the power law followed by the simulation increases too rapidly, for π^+ production cross sections (for both π^- and π^+ projectiles) it reduces the difference between the data and the simulation, and the agreement achieved for heavy targets is good; even thought it is slightly better for π^+ projectiles. For π^- production cross sections, the simulations become greater than the experimental data and the predictions overestimate the π^- production cross sections. This overestimation is less important for π^--induced reactions.

6.2.2 Double-differential pion production cross sections in π^+-induced reactions

On Figs. 6.23, 6.24 and 6.25, we compare the HARP data concerning pion production in positive-pion induced reactions on C, Cu and Pb with our predictions with our improved model. The angular domain is from 350 mrad to 2150 mrad and thus corresponds to what we called "large-angle" angular domain in Section 6.1. There is no comparison with the standard INCL4.2 model since the only inelastic πN reaction is the absorption of the pion by production of a Δ resonance, the pion production cross sections are completely underestimated. The cross sections (π^+ and π^- production) are underestimated of a factor 10 at high energy for the heaviest targets and, for the lightest targets, they are even null.

We only show the results at 5 GeV/c and 12 GeV/c, but they are illustrative of the kind of agreement that is achieved in the whole range of incident momentum. The figures for the whole set of comparisons can be found in Appendix D.

The agreement between the simulations and the data is not as good as for proton-induced reactions (compare with figures from Section 6.1.4). Nevertheless some general features are well reproduced, such as the shapes of the spectra, which are flatter than in the proton-induced case and the variations of the absolute value of the cross sections with varying angle and when going from positive pion production to negative pion production. The deficiencies observed in the proton-induced case, namely the under-prediction of pion production at small angles for all momenta and the overestimation of the cross sections at large momentum for large angles suggested by the slope of the measured cross-sections, are enhanced in the pion-induced case. The first shortcoming appears in the simple-differential cross sections (in Sec. 6.2.3), contrary to the second, which is hidden because we limited the integration to the same intervals as the data. We are inclined to attribute these shortcomings to a lack of a sufficiently forward-peaked pion production in pion-nucleon collisions. We remind that we biased the pion production in the forward direction for the first pion only, but not for the other pions in πN collisions producing several pions.

6.2.3 Simple-differential pion producing cross sections in π^+-induced reactions

Figs. 6.26 to 6.28 show the simple-differential cross sections, obtained by integrating over momentum or angle the double-differential cross sections from Section 6.2.2.

Figs. 6.26-6.28 clearly show that our results are improving as the mass of the target increases. They are in good agreement with the data for the medium target, at all energies. The agreement is also good for the heavy target, even though the pion production is overestimated at high energy (as already mentioned by the observation of integrated cross sections in Section 6.1.3).

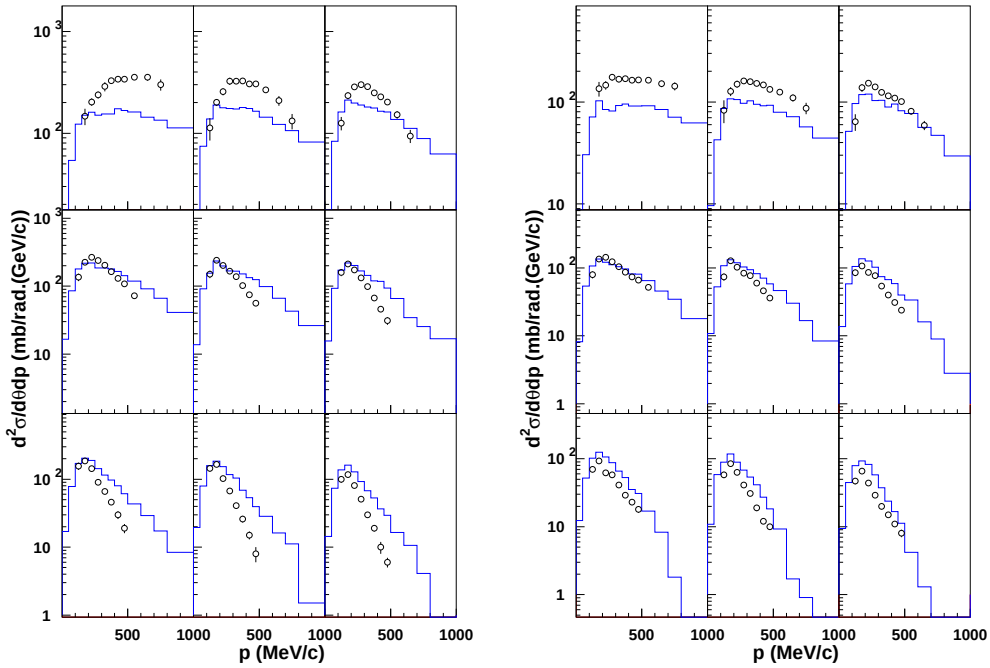

(a) π^+ (5 GeV/c) + C $\rightarrow$ π^+

(b) π^+ (5 GeV/c) + C $\rightarrow$ π^-

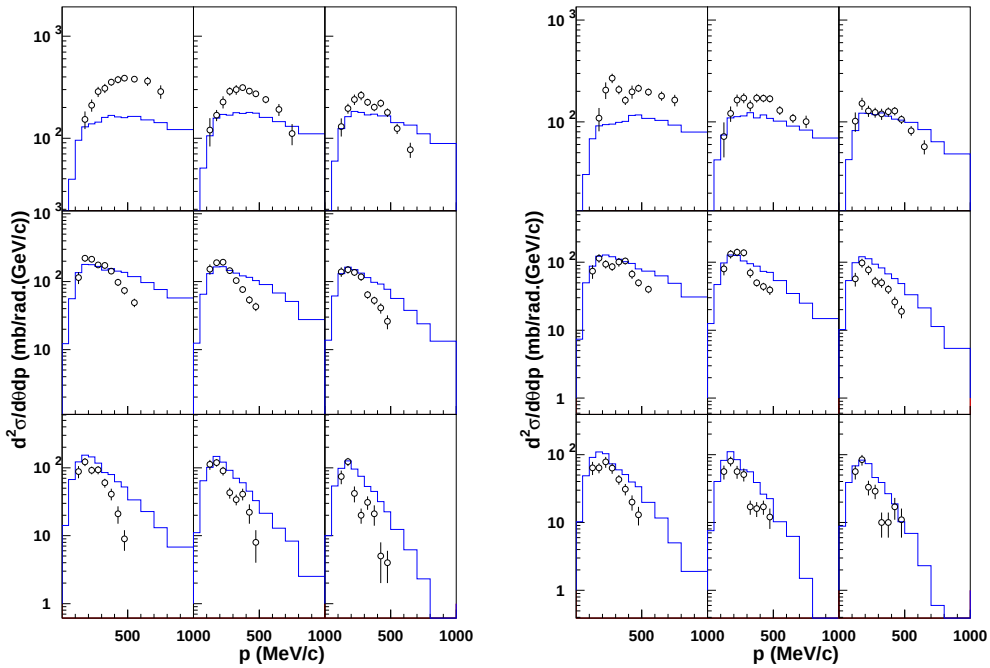

(c) π^+ (12 GeV/c) + C $\rightarrow$ π^+

(d) π^+ (12 GeV/c) + C $\rightarrow$ π^-

Figure 6.23: *Double-differential cross sections for π^+ production (a,c) and π^- production (b,d) in π^+-induced reactions on C at 5 GeV/c (a,b) and 12 GeV/c (c,d) incident momentum. Data (symbols) from Ref. [13] are compared with the improved version of the INCL4 model (blue lines). See text for detail.*

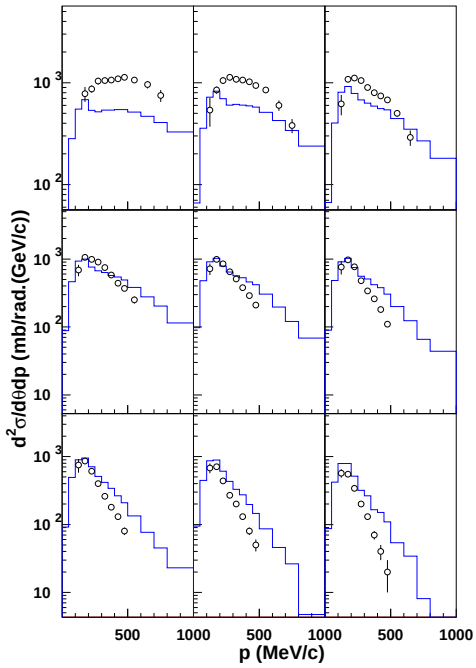

(a) π^+ (5 GeV/c) + Cu $\rightarrow$ π^+

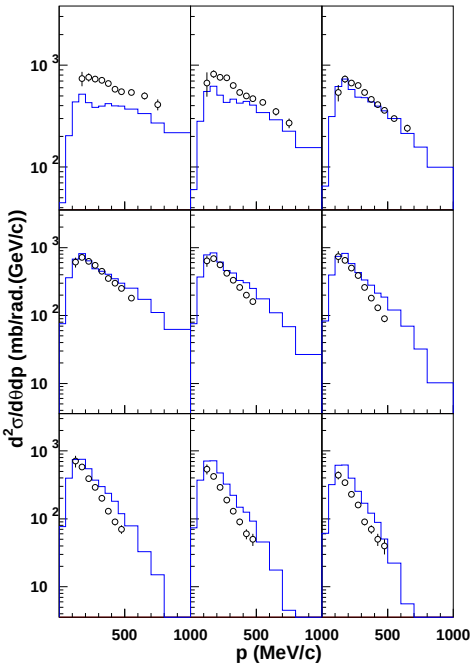

(b) π^+ (5 GeV/c) + Cu $\rightarrow$ π^-

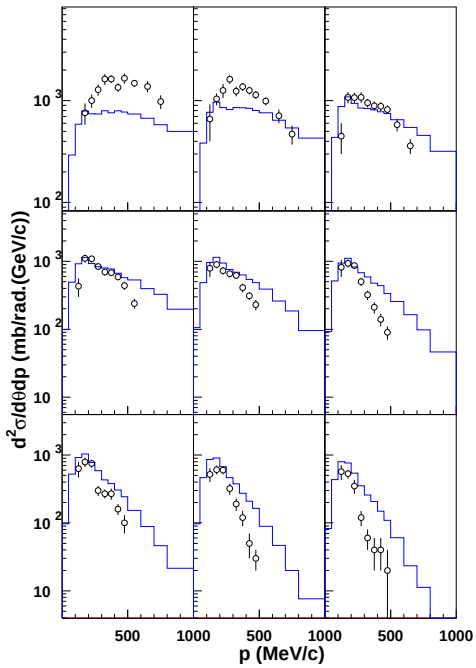

(c) π^+ (12 GeV/c) + Cu $\rightarrow$ π^+

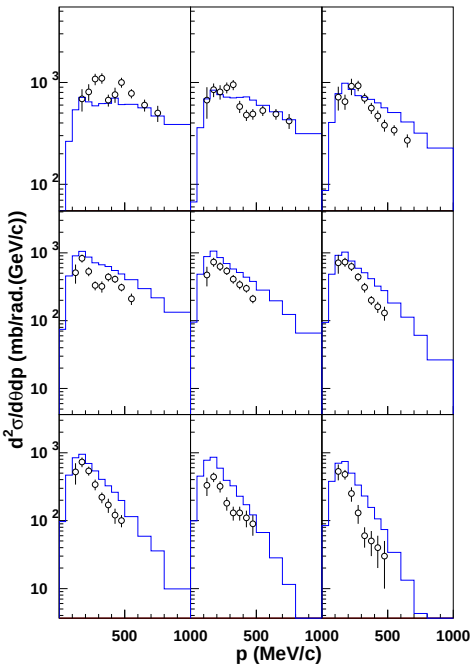

(d) π^+ (12 GeV/c) + Cu $\rightarrow$ π^-

Figure 6.24: *Same as Figure 6.23 for a Cu target. Data are from Ref. [13].*

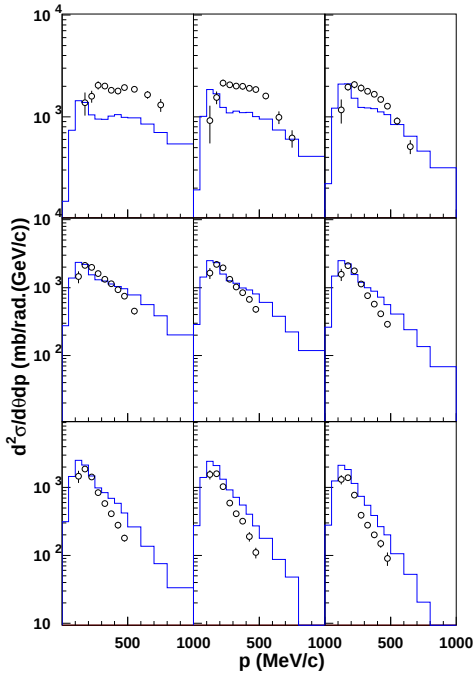

(a) π^+ (5 GeV/c) + Pb $\rightarrow$ π^+

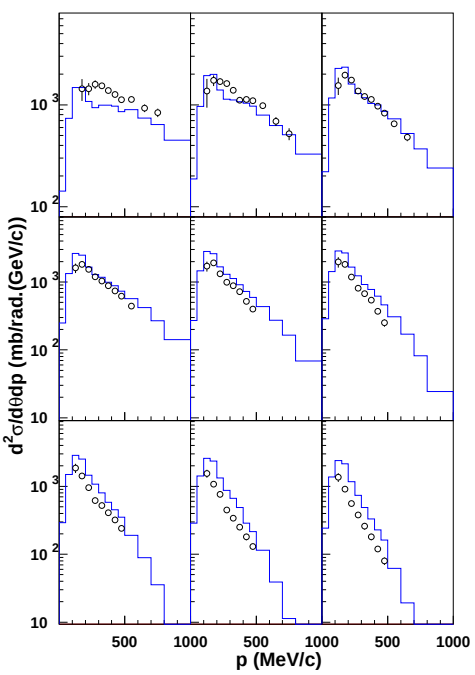

(b) π^+ (5 GeV/c) + Pb $\rightarrow$ π^-

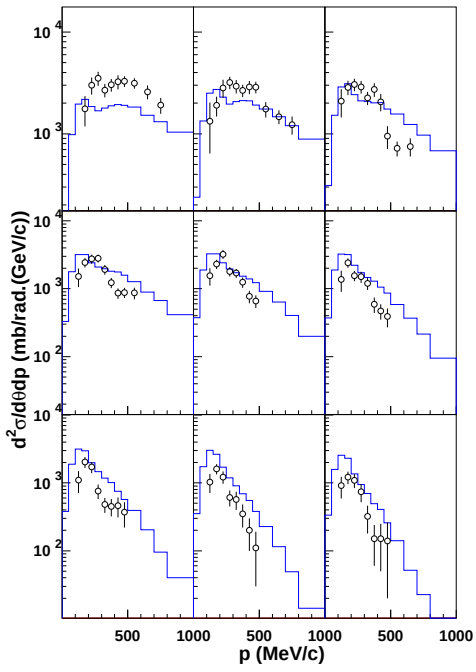

(c) π^+ (12 GeV/c) + Pb $\rightarrow$ π^+

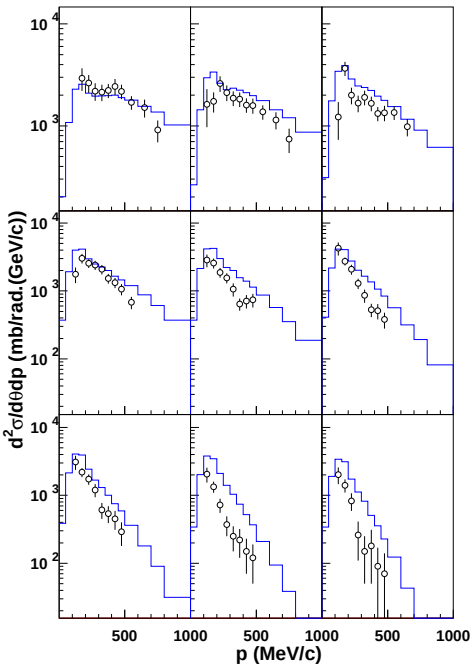

(d) π^+ (12 GeV/c) + Pb $\rightarrow$ π^-

Figure 6.25: *Same as Figure 6.23 for a Pb target. Data are from Ref. [13].*

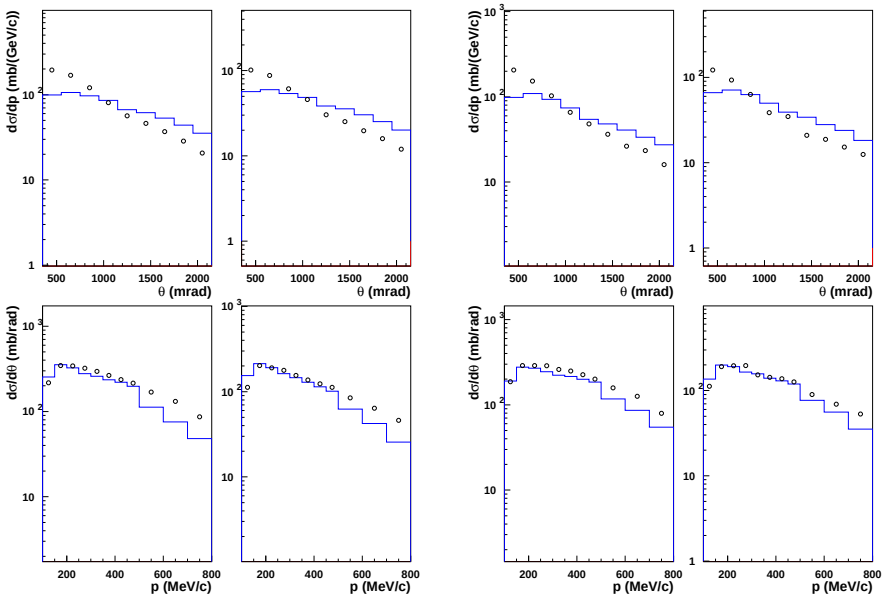

(a) π^+ (5 GeV/c) + C (b) π^+ (12 GeV/c) + C

Figure 6.26: *Simple-differential cross section in π^+-induced reactions on C target at 5 GeV/c (a) and 12 GeV/c (b) incident momentum. The data are obtained by integrating the double-differential cross sections of the HARP experiment over the angular domain or over the momentum domain (presented in Tab. D.1). Data (symbols) from Ref. [13] are compared with the improved version of INCL4 (blue lines).*

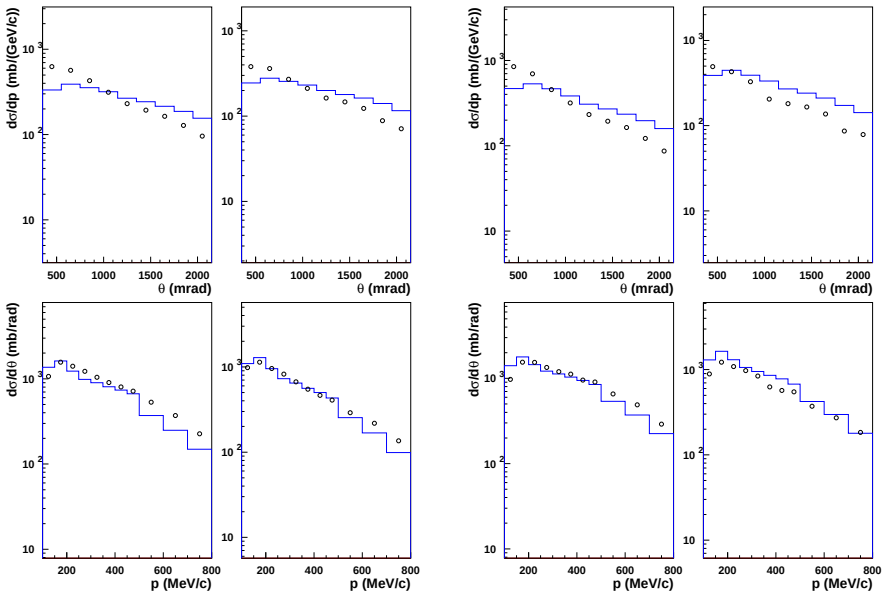

(a) π^+ (5 GeV/c) + Cu (b) π^+ (12 GeV/c) + Cu

Figure 6.27: *Same as Figure 6.26 for a Cu target. Data are from Ref. [13].*

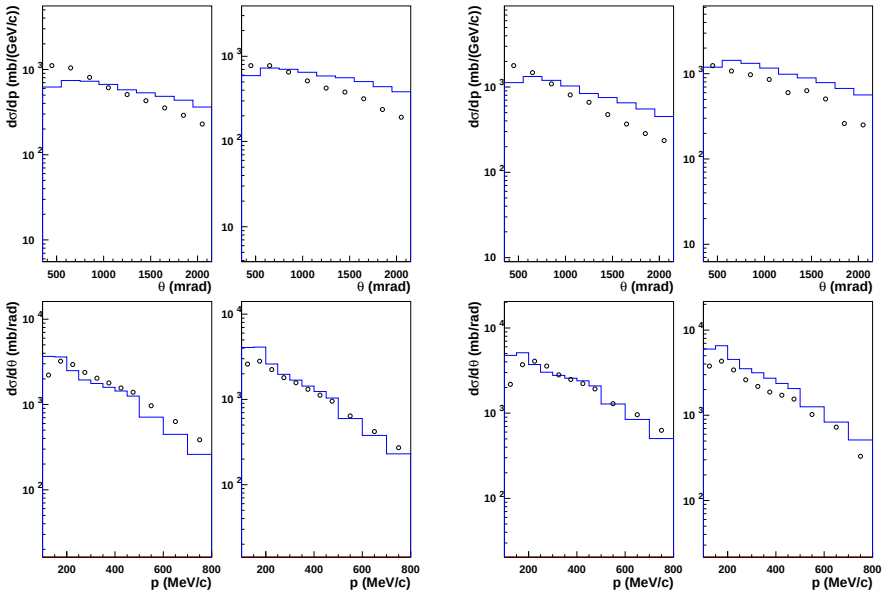

(a) π^+ (5 GeV/c) + Pb (b) π^+ (12 GeV/c) + Pb

Figure 6.28: *Same as Figure 6.26 for a Pb target. Data are from Ref. [13].*

Figs. 6.25 and 6.28, concerning the lead target, indicate that our theoretical results are clearly better for a heavy target. This is a general observation for all our results. This probably points to a limitation of the neglect of the resonance degrees of freedom, which, of course, should manifest themselves more importantly in light targets, for which the large surface/volume ratio compensates a short lifetime more easily. This may as well indicate that multiple scattering is important for heavy targets and that the results are then less sensitive to the detail of the elementary cross sections.

As it was the case for proton-induced reactions, simple-differential cross sections show that momenta spectra are well reproduced. Nevertheless, some underestimation appears at large momenta (up to 50% in the worst case, the lightest target). Both π^+ andπ^- production momenta spectra are in good agreement with the data, but the π^- one is slightly better. For the heavy target, the cross section at low momenta (for both π^+ and π^-) are overestimated, and this effect is worsened as incident momentum increases. The angular spectra are slightly better than in the proton-induced case, but INCL HE keeps on underestimating it for angles under ∼900 mrad and overestimating it for large angles.

6.2.4 Double- and simple-differential pion production cross sections in π^--induced reactions

Double-differential cross sections in π^--induced reactions were also measured by the HARP experiment. The results of this experiment are very similar to those obtained for π^+-induced reactions, with the difference that the sizes of the π^- production cross sections are larger than for π^+ production. For π^+-induced reactions, it was the opposite. This feature is reproduced by INCL HE, as it can be seen on Figs. 6.29 to 6.31, showing double-differential cross sections for pion production in π^--induced reactions.

The spectra are slightly better for π^+ production than for π^- production, the production of pions at small angles (from 350 to 950 mrad, corresponding to the first row) is underesti-

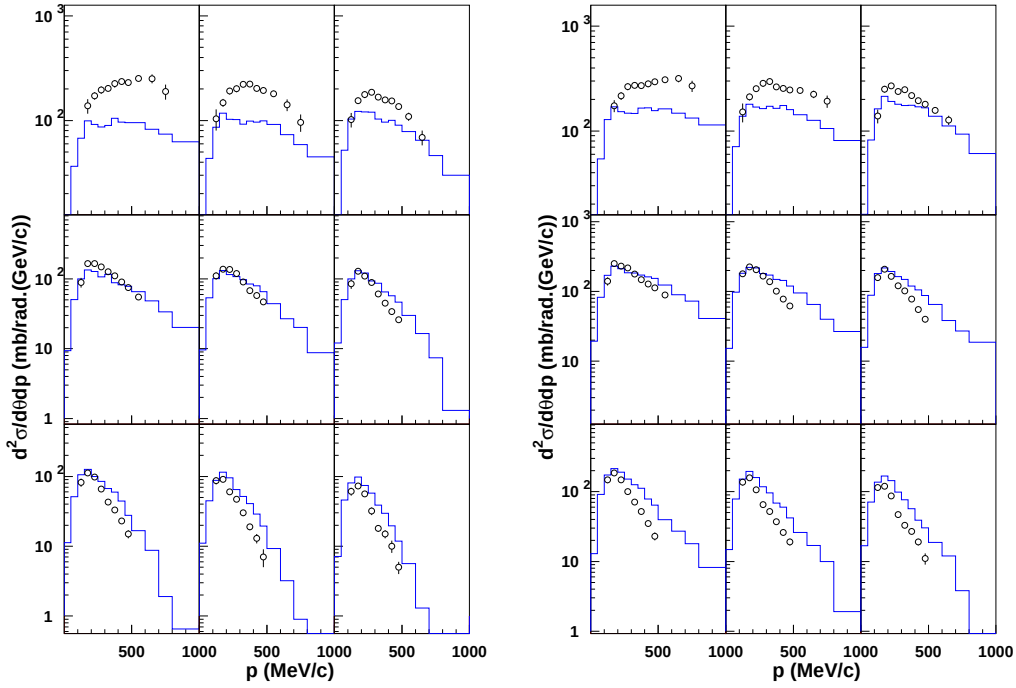

(a) π^- (5 GeV/c) + C $\rightarrow$ π^+

(b) π^- (5 GeV/c) + C $\rightarrow$ π^-

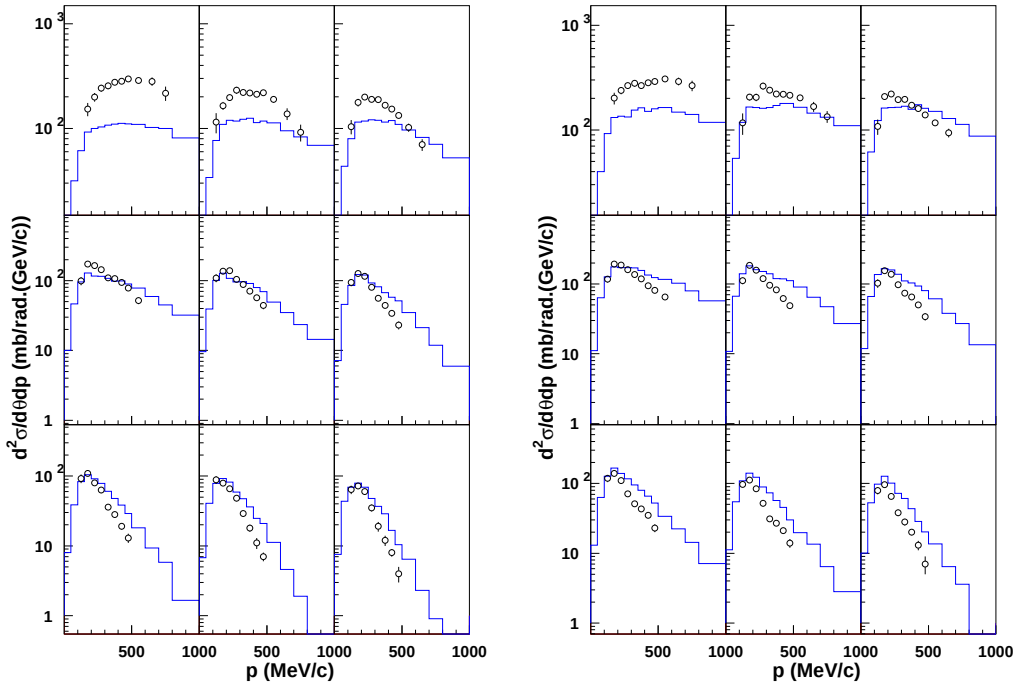

(c) π^- (12 GeV/c) + C $\rightarrow$ π^+

(d) π^- (12 GeV/c) + C $\rightarrow$ π^-

Figure 6.29: *Double-differential cross sections for π^+ production (a,c) and π^- production (b,d) in π^--induced reactions on C at 5 GeV/c (a,b) and 12 GeV/c (c,d) incident momentum. Data (symbols) from Ref. [13] are compared with the improved version of the INCL4 model (blue lines). See text for detail.*

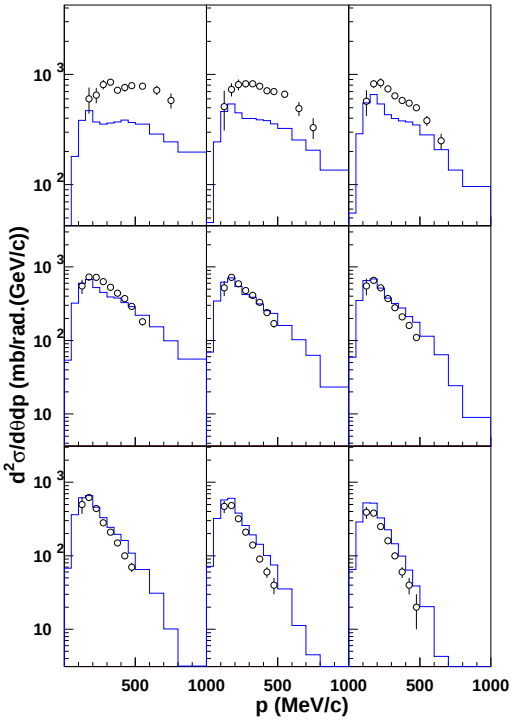

(a) π^- (5 GeV/c) + Cu $\rightarrow$ π^+

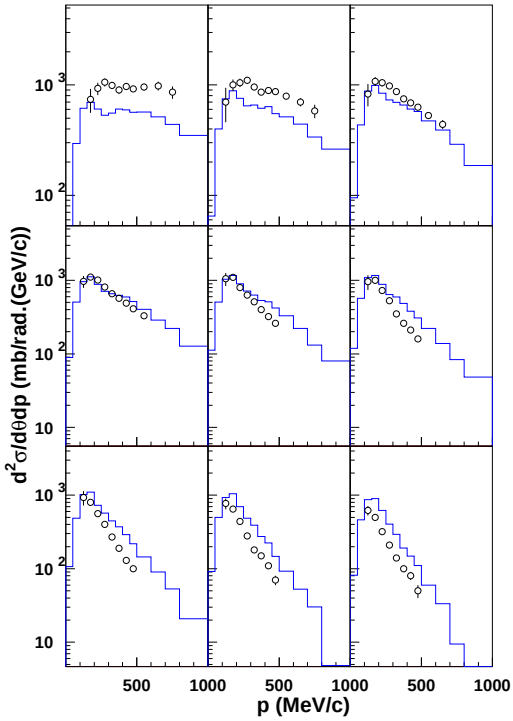

(b) π^- (5 GeV/c) + Cu $\rightarrow$ π^-

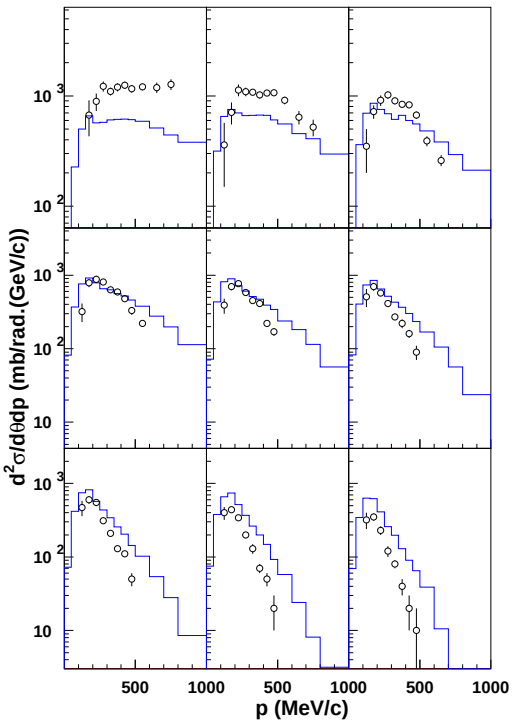

(c) π^- (12 GeV/c) + Cu $\rightarrow$ π^+

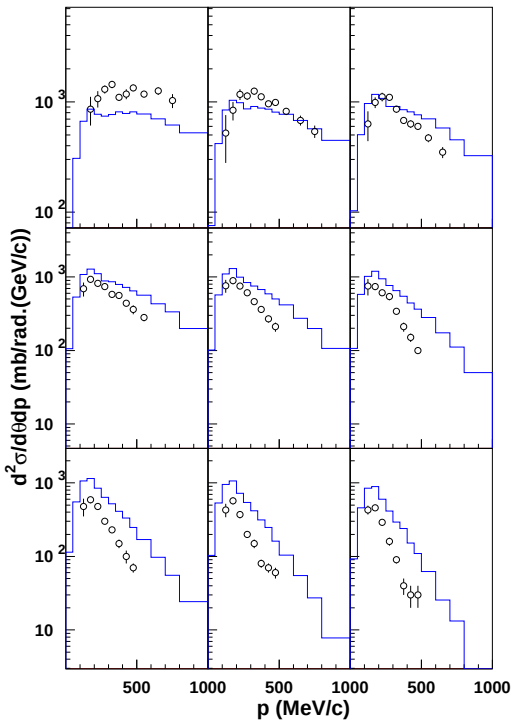

(d) π^- (12 GeV/c) + Cu $\rightarrow$ π^-

Figure 6.30: *Same as Figure 6.29 for a Cu target.*

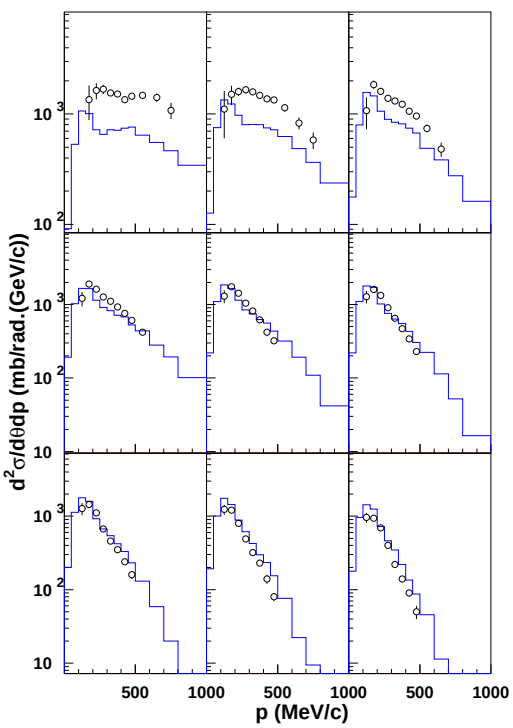

(a) π^- (5 GeV/c) + Pb $\rightarrow$ π^+

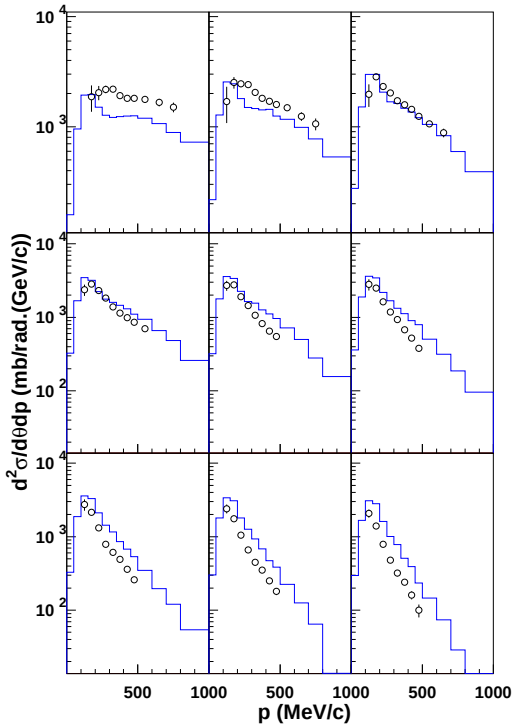

(b) π^- (5 GeV/c) + Pb $\rightarrow$ π^-

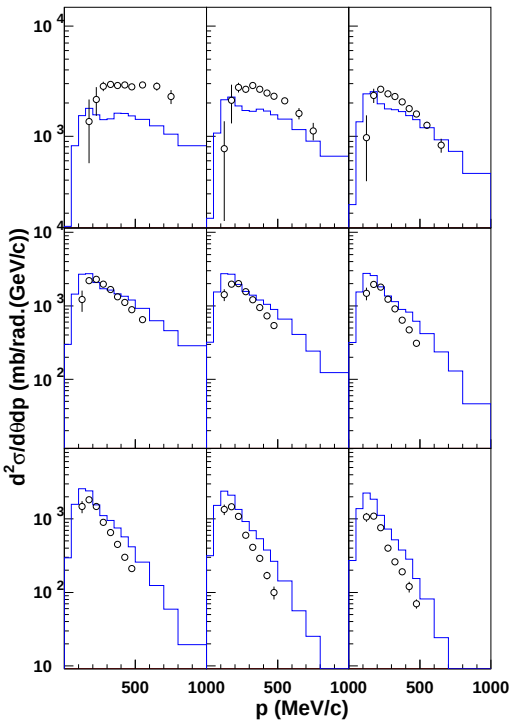

(c) π^- (12 GeV/c) + Pb $\rightarrow$ π^+

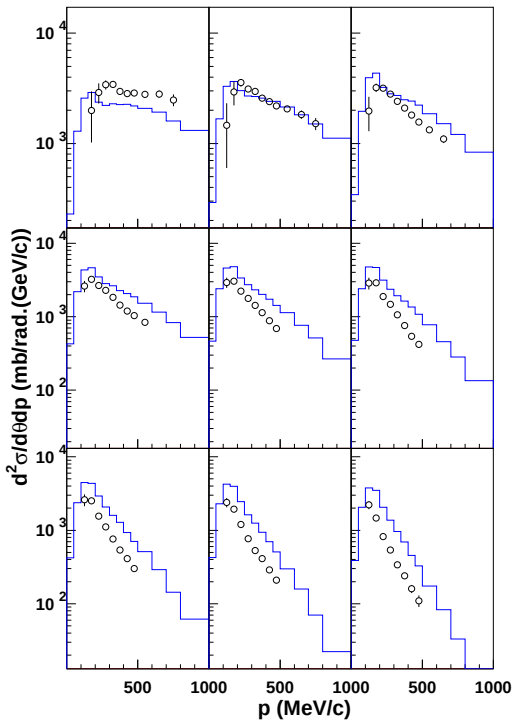

(d) π^- (12 GeV/c) + Pb $\rightarrow$ π^-

Figure 6.31: *Same as Figure 6.29 for a Pb target.*

mated, this effect is nevertheless less pronounced for π^- production and is reduced as the mass increases. For angles larger than 950 mrad (thus corresponding to the two other rows), the results are in good agreement with the experimental data, even though the π^- production is, in general, overestimated, especially as the mass of the target increases. There is also a systematic overestimation of the production of pions at large momentum.

Figs. 6.32 to 6.34 show the simple-differential cross sections, obtained by integrating over the momentum or angular domain the double-differential cross sections presented in Section 6.2.4.

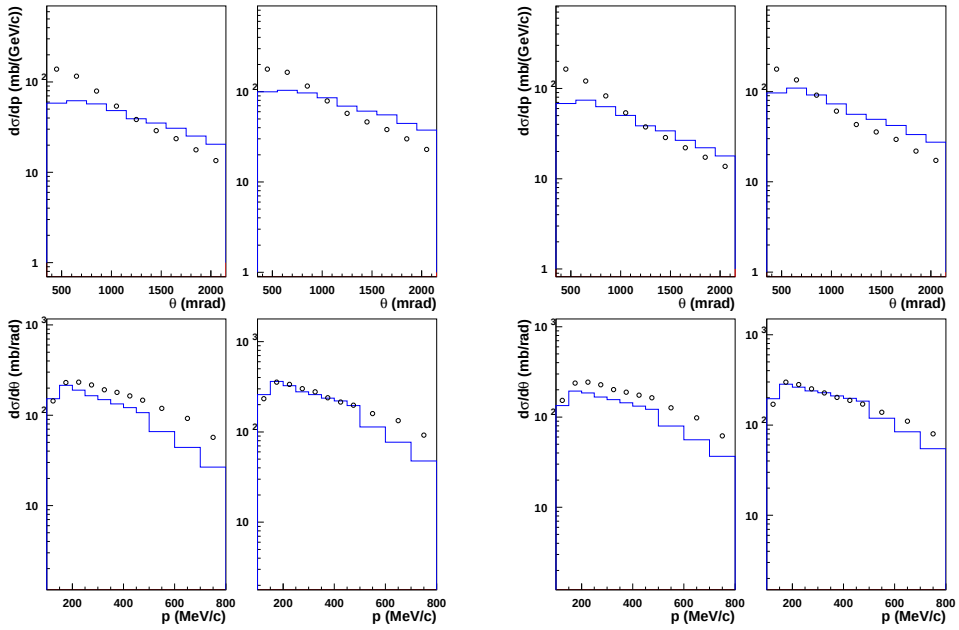

(a) π^- (5 GeV/c) + C (b) π^- (12 GeV/c) + C

Figure 6.32: *Simple-differential cross section in π^--induced reactions on C target at 5 GeV/c (a) and 12 GeV/c (b) incident momentum. Each panel is divided in four, corresponding to the integration of the π^+ production (left column of the panel) double-differential cross sections or the π^- production (right column of the panel) double-differential cross sections of the HARP experiment Ref. [13] over the momentum domain (upper part of the panel) or over the angular domain (lower part of the panel) presented in Tab. D.1. The date are represented by the circles and are compared with INCL HE (blue line).*

6.3 Discussion

The purpose of this work was to extend the INCL4.2 model to incident energies up to 10–12 GeV and to test it on systematic sets of data. The extension of the intranuclear cascade model of Liège has been realized through the introduction of multipion production both in NN and πN collisions. The total inelastic cross sections have been considered as corresponding to the sum of the multiple pion production cross sections. The multipion production cross sections have been parametrized directly, when it was possible like for $\sigma_1(NN\pi)$, some of them have been obtained from the data following the method of Ref. [68], and for those which could not be obtained by neither of these methods, they have been approximated following observations on the existing data. The cross sections are used to determine the number of particles in the outgoing state, a

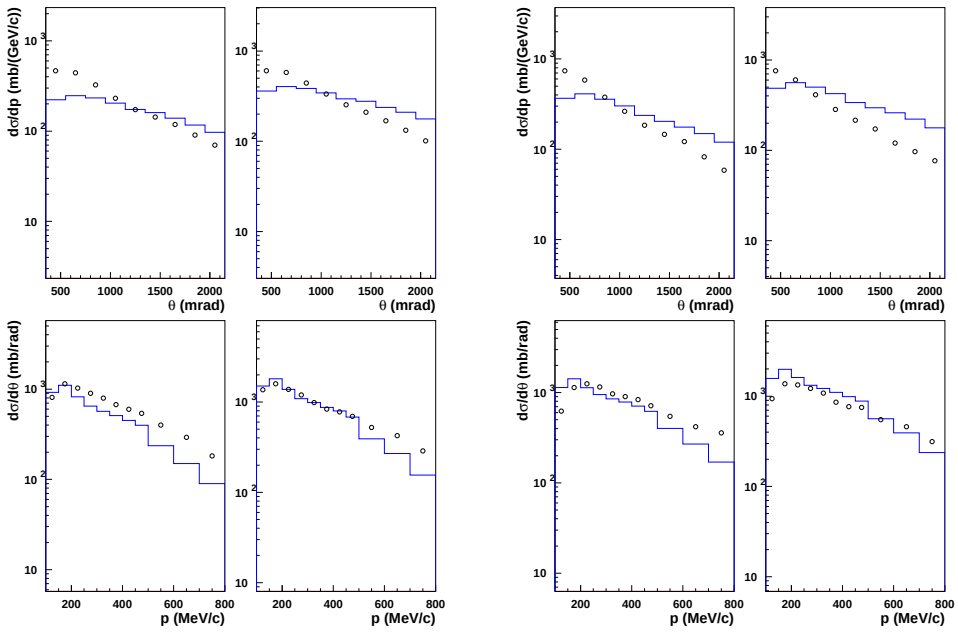

(a) π^- (5 GeV/c) + Cu (b) π^- (12 GeV/c) + Cu

Figure 6.33: *Same as Figure 6.32 for a Cu target.*

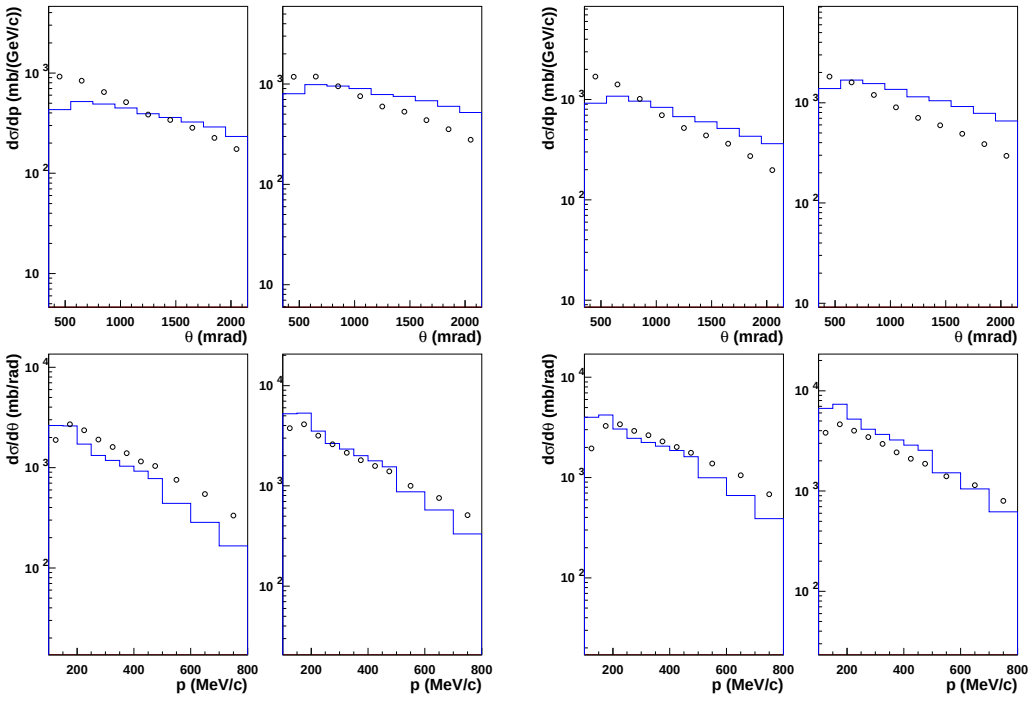

(a) π^- (5 GeV/c) + Pb (b) π^- (12 GeV/c) + Pb

Figure 6.34: *Same as Figure 6.32 for a Pb target.*

model for the generation of the charges of these particles is nevertheless needed, as we explained, and the features of this model were chosen as simple as possible. For the generation of the final energy and momentum of the particles, we considered the simplest departure from uniform phase space model, allowing forward peaking for the final direction of the incoming particles (this is also the simplest technical modification of the method of Ref. [70]).

The splitting of the inelastic cross sections in pion producing cross sections only implies that this model neglects all other inelastic channels, among which strangeness production channels. These are the most important ones but, in the energy range under consideration, the strangeness production is not expected to be important. In NN collisions, it remains at least one order of magnitude lower than non-strange channels[86]. Moreover, calculations based on QMD also indicate that, in proton-nucleus collisions and for the same energy range, strange particle cross sections are, at least, one order of magnitude smaller than non-strange particle cross sections [87, 88].

We have tested neutron and proton emissions in proton-induced reactions. Comparison for neutron and proton emissions at energies slightly above the upper limit of applicability of INCL4.2 showed that the extended version gives, as expected, better results.

We have also tested pion emission and compared results from the extended version of INCL4.2 with a large set of data provided by the HARP experiment over the past few years. These data cover three different projectiles (proton, positively and negatively charged pions), at 4 different incident momentum (3, 5, 8 and 12 GeV/c) over a set of targets from light to heavy nuclei (from Be to Pb). They have measured double-differential cross sections for the production of positive and negative pions, in two angular intervals (from 50 to 250 mrad and from 350 to 2150 mrad). This set of data has allowed us to perform systematic study on the pion production in the extended version of INCL4.2 and already led us to add multipion channels and to improve the phase space model.

The extended version of INCL4.2 reproduces reasonably well the double-differential cross sections provided by the HARP experiment. The global agreement between our model and these data, which is not perfect, gives confidence in the validity of our model or, at least in its predictive power.

Let us analyze more closely the level of agreement for proton-induced reactions. On the average, comparisons concerning total pion yield or the integrated cross sections (Section 6.1.3) showed a very good agreement with the data. It appeared that for light targets (up to Al target) the results for π^- production are better than for π^+ production: the data is reproduced within 10% for π^- production while the departure from the data can reach 20% for π^+ production. For heavier targets, secondary collisions become more important and the π^- production becomes too important, we suspect that this effect comes from the charge repartition model in πN collisions. The π^+ production is nevertheless reproduced within 15%. But the double-differential cross sections show larger disagreements. Some systematic features are revealed. Generally, the cross sections are underestimated at low pion momentum and small angle and are overestimated at large pion momentum and large angle. We want to stress the fact that the departure from uniform phase space has reduced these systematic discrepancies. We remind that the phase space repartition model only biases the final directions of the incoming particles. A biased emission of the other pions toward forward peaking, as suggested by experiment [89], would presumably improve our results. This however requires a modification of the Raubold-Lynch method to larger extent.

In general, the agreement is improved with increasing target mass and incident energy for both π^+ and π^- production (even though π^- production is overestimated for heavy targets).

We have chosen to base the extension to high energy of INCL4.2 on the direct production

of pions while this is usually based on the hadronic resonances. About this, the set of data regarding pion production provided by HARP allows us to make a few observations:

- the resonance degree of freedom does not seem to appear in the data,
- the behavior of pion spectra varies slowly with the incident energy, the mass of the target and with the considered angle.

As it has been already observed in antiproton annihilation on nuclei, which presents a similar situation and a similar average number of pions [90, 91], these spectra probably result more from the propagation of pions produced in the first collision in the target nucleus rather than from a single source (including resonance) more or less at rest. To exhibit the formation of a resonance, more exclusive measurements are probably necessary. Measurements of correlation between two particles (a nucleon and a pion, for instance) would not be useful, in all likelihood, because a peak corresponding to a resonance in the invariant mass spectrum is superposed to a huge background of uncorrelated pairs. An in depth analysis of such correlations for the Δ resonance, in proton-nucleus reactions, already showed that the signal is barely visible, only in light nuclei and in the energy range under consideration [92]. It is emphasized in Ref. [92] that the direct pion production and neglect of resonance formation in calculations can only affect pion production in light nuclei. For broader resonances, the signal should be even less visible and this conclusion presumably becomes more valid. If one considers inclusive measurements, our work seems to demonstrate that the results obtained by the multipion approach are as good as the ones given by the resonance approach (except for light nuclei). The multipion production picture thus provides a possible alternative to the conventional approach based on the hadronic resonance picture.

The HARP data have been compared at large with the MARS [80, 81, 82] and Geant4 [93] code systems [84, 11, 13, 79]. These code systems usually reach a slightly better agreement with experimental data than in our work. Comparisons have also been performed with the FLUKA code system [94, 95], and it gives very good results for the comparison with the HARP collaboration [96, 97]. But, as these code systems combine many different reaction models, the user is supposed to choose among these which ones are used. If this gives a certain flexibility to the code system it also introduces some unphysical jumps, as emphasized in Ref. [88], for instance in the excitation functions of total pion production. These jumps appear because each model has a different energy domain of validity and the code abruptly jumps from the results given by a model to the results given by the model valid in the upper energy domain. See Ref. [98] for a discussion.

6.4 Nuclear fragmentation

We want to present and comment here our results concerning the residue production. Figure 6.35 shows a comparison of the excitation energy and the masses of the remnant[3] after proton-induced reactions on a lead target for the same incident momenta as the HARP experiment (3, 5, 8 and 12 GeV/c).

First of all, one can notice that, if the results given by both versions of INCL are close to one another for the lowest incident energy curves (3 GeV/c in red), there is some kind of saturation for the excitation energies calculated with the standard version of INCL4.2, while the simulations from the extended version of INCL4.2 show excitation energy increasing with the

[3]The term "remnant" designates the target nucleus after the intranuclear stage.

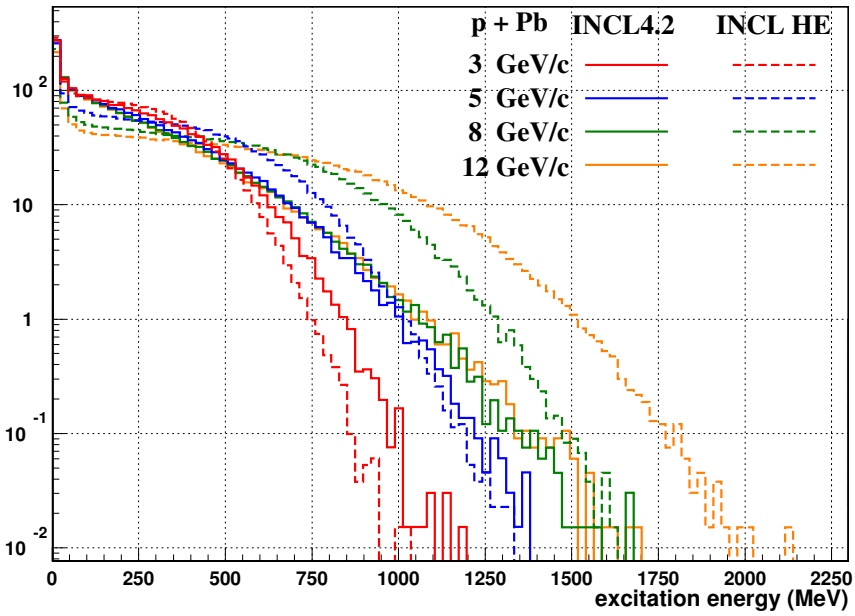

Figure 6.35: *Comparison between the excitation energy of the remnant simulated by the standard version of INCL4.2 (plain line) and its extended version, in proton-induced reactions on lead target. The colors of the lines refer to the incident momenta of the projectiles: 3 GeV/c in red, 5 GeV/c in blue, 8 GeV/c in green and 12 GeV/c in orange.*

incident momentum. Table 6.3 shows the average excitation energy computed from the curves on Fig. 6.35:

$\langle E^* \rangle$	3 GeV/c	5 GeV/c	8 GeV/c	12 GeV/c
INCL4.2	211.4	225.4	225.5	224.6
INCL HE	203.4	283.9	362	432

Table 6.3: *Average excitation energy of the remnant for the cases showed in Fig. 6.35.*

At 3 GeV/c, the excitation energy is slightly lower for the extended version of INCL4.2 than for the standard version. At such energy, only the lowest multipion channels are open and this, in all likelihood, only for the first inelastic collision. After this collision the energy is shared among two or three particles and the threshold for multipion collisions is not reached. Nevertheless this is sufficient to increase the pion production[4] and decrease the excitation energy of the remnant.

Figure 6.36 shows the mass of the remnant, after the intranuclear cascade. The saturation observed in the excitation energy also appears in this figure: the behavior of the mass of the remnant are much alike in the simulations from the standard version of INCL4.2 for the incident momentum of 8 and 12 GeV/c and they both are close to the results for an incident momentum of 5 GeV/c. The extension to high energy of INCL4.2 seems to have facilitated the emission of nucleons.

With the extension of INCL4.2 to high energy, the nucleus emits more nucleons and the remnant is left with a higher excitation energy. Nevertheless, these quantities cannot be measured experimentally and there is not much data on the isotopic distribution after a spallation reaction. Figure 6.38 shows such data for a reaction between a proton with an incident energy of 1 GeV

[4]This is already visible in comparison with pion production cross sections in Figs. 6.12(a) and 6.12(a)

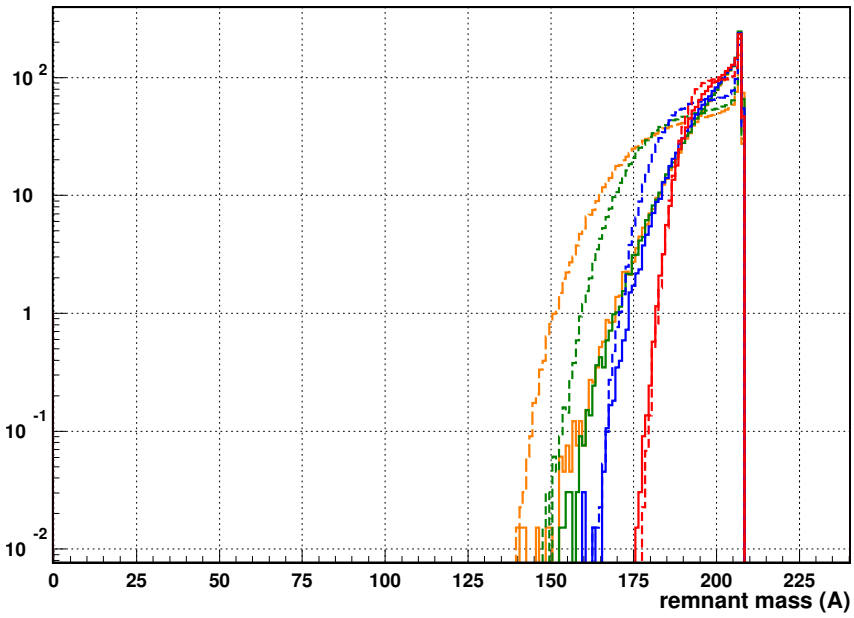

Figure 6.36: *Comparison between the masses of the remnant after the cascade, simulated by the standard version of INCL4.2 (plain line) and its extended version, in proton-induced reactions on lead target. The colors of the lines refer to the incident momenta of the projectiles: 3 GeV/c in red, 5 GeV/c in blue, 8 GeV/c in green and 12 GeV/c in orange.*

and a lead target. Even though this incident energy is right above the threshold for multipion production channels, some effect is already visible. Fig. 6.37 shows the excitation energy computed with the standard version of INCL4.2 and INCL HE. As one can suspect from Fig. 6.37, the average excitation energy of the remnant is lower in the extended version of INCL4.2.
The mean of the excitation energy calculated by the standard version of INCL4.2 is 158.1 MeV and it is calculated to be 130.6 MeV with the extended version of the model.

Figure 6.38(a) shows the residue charge spectrum of the nucleus in the upper panel, and the residue mass spectrum, in the lower panel. Data come from [99]. The lower excitation energy obviously leads to an evaporation which emits less nucleons. This explains why the extended version of INCL4.2 predicts a higher production of isotopes near the target mass, the results given by the extended version are actually better in this region. The results shown on this figure are highly dependent upon the de-excitation code. For these simulations, we used ABLA07 and it appears that it does not reproduce fission properly, which is why we have an overprediction in the $A = 75 - 110$ region and underprediction in the $A = 45 - 70$ and $A = 140 - 175$. Figures 6.38(b) to 6.38(d) show the isotopic mass distribution of the fragment for each separate element.

There has been in the past some speculation about the possible existence of a "limiting fragmentation", meaning that the mass distribution of the residues does not change any more when the incident particle energy exceeds some specific value, of the order of 1 GeV per nucleon [100, 101, 102, 103]. There are some data supporting this idea for heavy ion-heavy ion collisions [104, 101, 100, 105]. But, for proton-nucleus collisions, there is practically no measurements of residue mass yields above 2–3 GeV.

Nevertheless, the residue mass distribution seems to stay roughly the same between 1 and 3 GeV [106, 107, 108, 109], suggesting the onset of the limiting fragmentation of the target. Our results seems to contradict this statement. Indeed, the width of the mass distribution and the dependence of the remnant excitation energy with the incident energy seem to point towards the

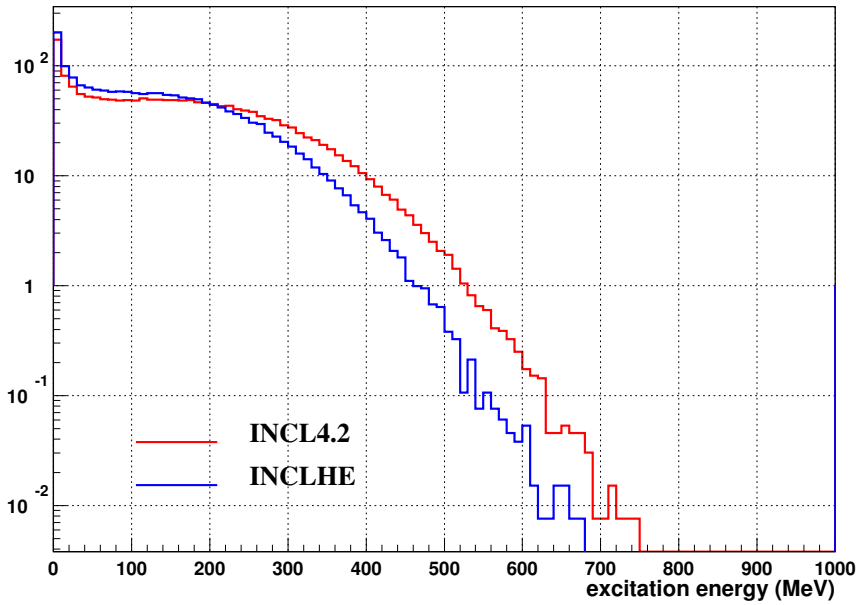

Figure 6.37: *Comparison of excitation energy of the remnant for a 1 GeV proton on lead, calculated with the standard version of INCL4.2 (in red) and the extended version of INCL (in blue).*

fragmentation of a more and more excited remnant.

Note, however, that the excitation energy of this remnant is increasing with incident energy more on a logarithmic pattern than a linear one.

6.5 Summary

We want to single out the most important results of our calculations.

Firstly, the extended version of INCL4.2 is able to reproduce the general trends of total pion production cross sections as functions of the incident energy and of the target mass numbers, and that for both incident protons and pions. One may argue that these results are largely linked with the use of realistic elementary pion cross sections ($\sigma_n(NN\pi)$ and $\sigma_n(\pi N)$) with the right multiplicity. But this result may as well be related with the basic premise of cascade model, namely the description of the whole interaction process by independent collisions, ruled by free cross sections, generating a good unfolding of multiple collisions.

Our results show also a good description of double-differential cross sections for neutrons, protons and pions productions. For the latter, the extended version of INCL4.2 reproduces fairly well the general trends: dependence upon the incident energy, target mass number, momentum of the produced pions and, to a lesser extend, upon emission angle. This is probably related with the model for multipion production in elementary collisions. Some other success can be pinned down, as the rather right ratio between π^+ and π^- production cross sections, for incident protons and incident pions. This is probably due to our charge repartition model.

Beyond the general trends, our results display some disagreement with experimental data, which are sometimes hard to analyze. However, the observation that calculated angular distributions are generally plagued with a too smooth slope whereas momentum distributions are fairly well described, shed some light on the origin of the discrepancies. This supports the idea that our phase space model is probably correct for the sharing of momentum, but is deficient as far as

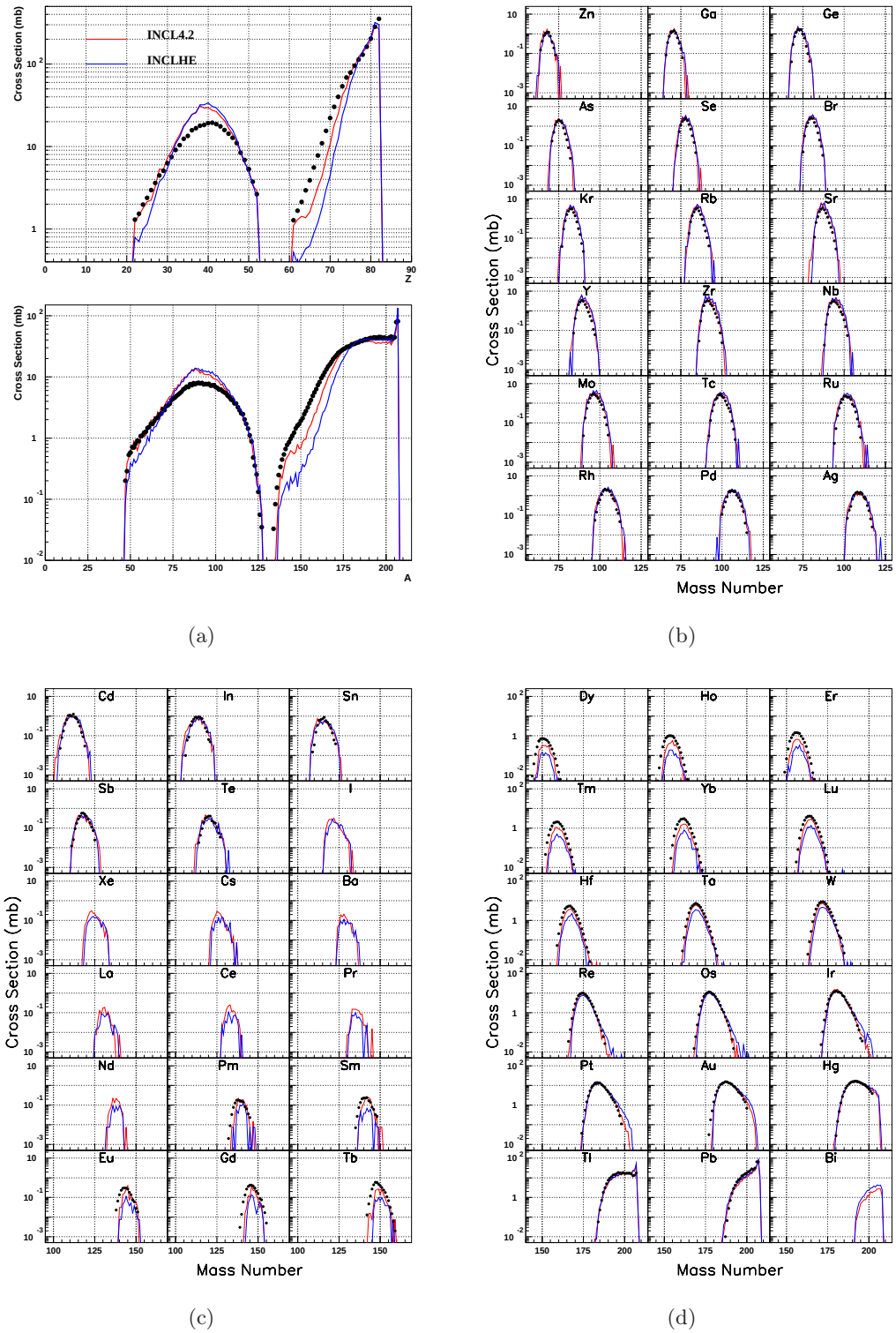

(a) (b)

(c) (d)

Figure 6.38: *Comparison between the standard version of INCL4.2 (in red) and the extended version of INCL4.2 (in blue) for the residue charge and mass production cross sections (panel (a)), and for the isotope distributions (mass distributions for given isotopes, panels (b), (c) and (d)). Data come from Ref. [99]*

the angular pattern is concerned. In all likelihood, the angular distribution should have a more marked forward-backward peaking that the one we have introduced.

Finally, we have not devoted much work to the residue production. But our results seems to indicate that limiting fragmentation does not seem to set in the energy domain of interest. Of course, a comparison with experiment is eagerly desired.

7
Conclusions, Outlook

In this thesis, we have extended the Liège intranuclear cascade model INCL4.2 to the energy domain relevant for the simulation of cosmic rays. This needed the addition of NN and πN inelastic channels opening in the 2–12 GeV energy range. They were assumed to essentially correspond to multipion production, in contrast with the usual picture of resonance production. This is the most original aspect of our work. Experimental data and isospin symmetry have been exploited in the implementation of these channels. But, we could not avoid to introduce specific models for the energy-momentum and charge repartition on the final pions. Nevertheless, the modified INCL4.2 model is able to give very reasonable results in the energy range under interest, and especially concerning the comparison with the systematic data of the HARP collaboration. The strong points of the model concerning its predictive power are summarized in section 6.5 and need not to be repeated. The weak points are dealing with the double-differential cross section for emitted pions, which is generally overestimated at small angle and small momentum and underestimated at large angle and large momentum. However, momentum spectra (which are double-differential cross sections integrated over the angular domain) are generally quite well reproduced, whereas calculated angular distributions show a decreasing shape with a too small slope. This probably comes from the momentum distribution in the multipion production, which is presumably not enough forward peaked. The situation may be a bit more complex since we have also observed that the pion double-differential cross sections are generally less well reproduced in pion-induced reactions than in proton-induced reactions.

We did not pay very much attention to the comparison with other works; The reason is that HARP data have been mostly compared with outputs of transport codes. These codes generally use different reaction models, for different energy range, sometimes the user can choose among many models. Therefore a direct comparison is meaningless. Let us stress that we have now a single model which applies now from $\sim$ 200 MeV to $\sim$ 12 GeV. A quick look at Ref. [88] which shows the results of calculation similar to ours with QMD models, based on the resonance production picture, suffices to indicate that our results are, at least, as good as theirs.

Let us discuss a little bit the implications of our results. From the physics point of view, they reveal a striking duality between the resonance production picture and the multipion production picture ; Furthermore, they seem to indicate the multipion production picture does give reasonable results around 10 GeV, in a region well above the region of identified resonances and

which is believed to be dominated by string dynamics. Let us also notice that, even if we did not devote very much time to target fragmentation, out results seem to deny the suspected onset of limiting fragmentation.

The extension to high energy, as it has been implemented in INCL4, seems to work for energies up to 12 GeV/c (a little more than 11 GeV). We did not compare the simulations from our extended version of INCL4 with experimental data above that energy. Results globally are in good agreement with experimental data. The upper limit of the energy domain of this version of INCL4 is not clearly determined. Experimental data are needed to clarify this situation: if one tries to apply our extended version of INCL4 at even higher energies, additional pion producing channels may be necessary, but the impact of these additional channels is reduced because of the multiple scattering. The amount of energy would be divided among more particles, thus reducing the pion production in following collisions. Nevertheless, inelastic channels producing strange particles should become important and these cannot be neglected at higher energy. Strangeness production channels in NN collisions, which have not been taken into account yet, remain in project for future enhancement of INCL4.

Before closing, it is interesting to discuss the remaining points to be improved and the remaining open questions. As far as applications to radiation protection in space are concerned (one of our motivation), the predictive power that are obtained is probably satisfactory. But this is true for proton- and pion-induced reactions. Cosmic rays hazards are actually coming more from ions (up to Fe). This could be handled by INCL, which can accommodate light ions, but this sector of the code has not been investigated very much, and the present model is less and less reliable as the size of the ion is increasing.

From the physics point of view, it would be interesting to improve the multipion production model. Of course, the repartition of momentum should be adjusted to reproduce experimental data in a better way. But, in addition, the multipion production model should be constrained by measurements in NN and πN systems. We have grossly checked that the model is more or less consistent with the k_T-distributions of pions, but we did not pay very much attention to this point. It would be interesting to try to discriminate between the resonance production and the multiple pion production pictures. This probably can be done only by looking at more exclusive measurements, which, if they exist, are certainly very scarce.

Appendix

A

Parametrization of the total and elastic cross sections

A.1 Nucleon–nucleon interaction

Total cross sections

If p_{lab} is the momentum of the nucleon in the laboratory frame, expressed in GeV/c, the total cross sections (in mb) are parametrized as:

$$\begin{aligned}
\sigma_{t,pp} &= 34\left(\frac{p_{lab}}{0.4}\right)^{2.104}, && p_{lab} < 0.44 \\
&= 23.5 + 1000(p_{lab} - 0.7)^4, && 0.44 < p_{lab} < 0.8 \\
&= 23.5 + \frac{24.6}{1 + \exp\left(-\frac{p_{lab}-1.2}{0.10}\right)}, && 0.8 < p_{lab} < 1.5 \\
&= 41 + 60\,(p_{lab} - 0.9)\exp(-1.2\,p_{lab}), && 1.5 < p_{lab} < 5. \qquad \text{(A.1)}
\end{aligned}$$

$$\begin{aligned}
\sigma_{t,np} &= 6.3555\,p_{lab}^{-3.2481}\exp\left(-0.377\,(\ln p_{lab})^2\right) && p_{lab} < 0.45 \\
&= 33 + 196\,|p_{lab} - 0.95|^{2.5}, && 0.45 < p_{lab} < 1 \\
&= 24.2 + 8.9 p_{lab}, && 1 < p_{lab} < 2 \\
&= 42, && 2 < p_{lab}. \qquad \text{(A.2)}
\end{aligned}$$

Elastic cross sections

$$\begin{aligned}\sigma_{el,pp} &= 34\left(\frac{p_{lab}}{0.4}\right)^{2.104}, && p_{lab} < 0.44\\ &= 23.5 + 1000(p_{lab}-0.7)^4, && 0.44 < p_{lab} < 0.8\\ &= \frac{1250}{p_{lab}+50} - 4(p_{lab}-1.3)^2, && 0.8 < p_{lab} < 2\\ &= \frac{77}{p_{lab}+1.5}, && 2 < p_{lab}.\end{aligned} \tag{A.3}$$

$$\begin{aligned}\sigma_{el,np} &= 6.3555\; p_{lab}^{-3.2481} \exp\left(-0.377\;(\ln p_{lab})^2\right) && p_{lab} < 0.45\\ &= 33 + 196\,|p_{lab}-0.95|^{2.5}, && 0.45 < p_{lab} < 0.8\\ &= \frac{31}{\sqrt{p_{lab}}}, && 0.8 < p_{lab} < 2\\ &= \frac{77}{p_{lab}+1.5}, && 2 < p_{lab}.\end{aligned} \tag{A.4}$$

Inelastic cross sections

The inelastic cross sections are given by the differences between the total and the elastic cross sections:

$$\sigma_{inel,pp} = \sigma_{t,pp} - \sigma_{el,pp} \tag{A.5}$$

$$\sigma_{inel,np} = \sigma_{t,np} - \sigma_{el,np} \tag{A.6}$$

A.2 Pion–nucleon interaction

As it has been shown in section 5.2, isospin symmetry can be used to write down relations between the various $\pi N \to \Delta$ cross section [54]. These relations are

$$\begin{aligned}\sigma(\pi^+ p \to \Delta^{++}) &= 3\sigma(\pi^+ n \to \Delta^+) = \tfrac{3}{2}\sigma(\pi^0\, p \to \Delta^+),\\ &= \tfrac{3}{2}\sigma(\pi^0\, n \to \Delta^0) = 3\sigma(\pi^- p \to \Delta^0),\\ &= \sigma(\pi^- n \to \Delta^-),\end{aligned} \tag{A.7}$$

the parametrization of $\sigma(\pi^+ p \to \Delta^{++})$ is sufficient to describe the $\pi - N \to \Delta$ interaction in this picture. The parametrization that has been used is :

$$\sigma(\pi^+ p \to \Delta^{++}) = \frac{326.5}{1 + 4\left(\frac{\sqrt{s}-1.215}{0.110}\right)^2} \frac{q^3}{q^3 + (0.18)^3}, \tag{A.8}$$

where q is the c. m. momentum

$$\begin{aligned} q &= \left[\frac{\left(s-(m_\pi+m_p)^2\right)\left(s-(m_\pi-m_p)^2\right)}{4s}\right]^{1/2}\\ &= \frac{m_p}{\sqrt{s}} p_{lab}.\end{aligned} \tag{A.9}$$

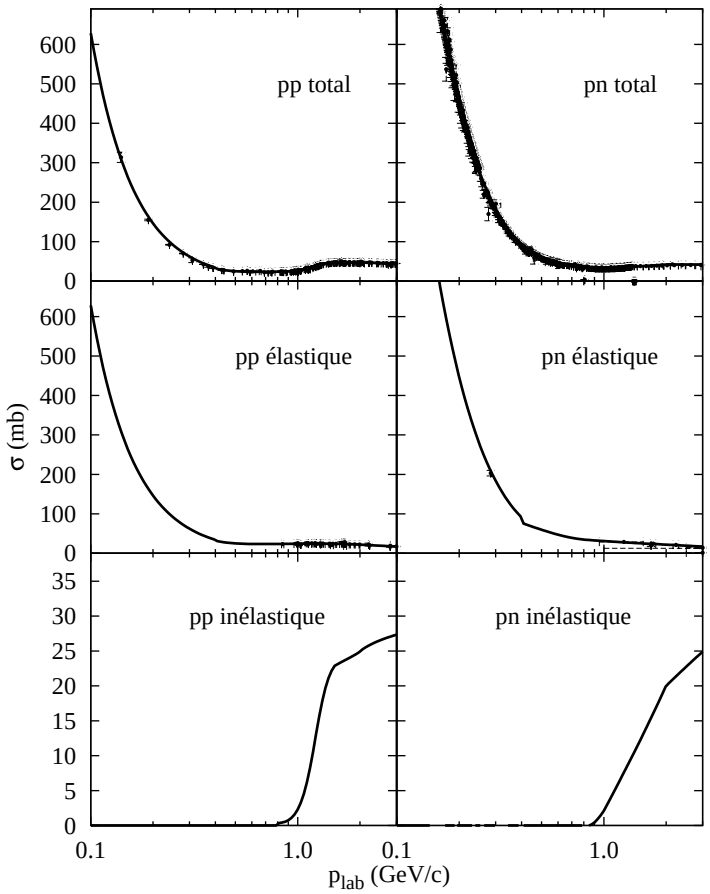

Figure A.1: *Elementary nucleon-nucleon cross sections. The line represents the parametrization used in INCL4.2 [54, 58]. Experimental data are from Ref. [69].*

Extended pion–nucleon total cross section

An extension of the total pion–nucleon cross section has been proposed in [34]. If the c. m. energy $\sqrt{s}$ is always expressed in MeV, and the cross sections in mb, the parametrization can be written:

$$\sigma_{\pi^+ p} = \begin{cases} (\sigma_{0,\pi^+} + \sigma_\Delta) & \text{if } \sqrt{s} \leq 1500 \\ (\sigma_{0,\pi^+} + \sigma_\Delta) + \frac{14420.3}{(\sqrt{s}-1675.0)^2+4085.6} & \text{if } 1500 < \sqrt{s} \leq 1790 \\ (\sigma_{0,\pi^+} + \sigma_\Delta) + \frac{54000.0}{(\sqrt{s}-1907.5)^2+4000.0} & \text{if } 1790 MeV < \sqrt{s} \leq 2370 \\ (\sigma_{0,\pi^+} + \sigma_\Delta) & \text{if } \sqrt{s} > 2370 \end{cases} \tag{A.10}$$

and

$$\sigma_{\pi^- p} = \begin{cases} (\sigma_{0,\pi^-} + \sigma_\Delta/3) & \text{if } \sqrt{s} \leq 1460 \\ (\sigma_{0,\pi^-} + \sigma_\Delta/3) + \frac{8700.0}{(\sqrt{s}-1515.0)^2+600.0} & \text{if } 1460 < \sqrt{s} \leq 1575 \\ (\sigma_{0,\pi^-} + \sigma_\Delta/3) + \frac{22000.0}{(\sqrt{s}-1675.0)^2+950.0} & \text{if } 1575 < \sqrt{s} \leq 1760 \\ (\sigma_{0,\pi^-} + \sigma_\Delta/3) & \text{if } 1760 < \sqrt{s} \leq 2050 \\ (\sigma_{0,\pi^-} + \sigma_\Delta/3) + \frac{20054.1}{(\sqrt{s}-2222.6)^2+8292.3} & \text{if } 2050 < \sqrt{s} \leq 2400 \\ (\sigma_{0,\pi^-} + \sigma_\Delta/3) & \text{if } \sqrt{s} > 2400 \end{cases} \quad \text{(A.11)}$$

In these relations σ_Δ is the parametrization introduced by equation A.8 and σ_{0,π^+} and σ_{0,π^-} give the non-Δ contributions

$$\sigma_{0,\pi^+} = \begin{cases} 0.0 & \text{if } \sqrt{s} \leq 1340 \\ 1.0441 \times 10^{-4} s - 0.2679 s^{1/2} + 171.95 & \text{if } 1340 < \sqrt{s} \leq 1750 \\ -1.129 \times 10^{-5} s + 0.057 s^{1/2} - 42.125 & \text{if } 1750 < \sqrt{s} \leq 2365 \\ 23.335 + 55.0\ exp(-8.87 \times 10^{-4} s^{1/2}) & \text{if } 2365 < \sqrt{s} \leq 7000 \\ 23.4 & \text{if } \sqrt{s} > 7000 \end{cases} \quad \text{(A.12)}$$

and

$$\sigma_{0,\pi^-} = \begin{cases} 0.0 & \text{if } \sqrt{s} \leq 1264 MeV \\ 1.55080 \times 10^{-1} s^{1/2} - 195.882 & \text{if } 1264 MeV < \sqrt{s} \leq 1463 MeV \\ 1.62786 \times 10^{-2} s^{1/2} + 7.22129 & \text{if } 1463 MeV < \sqrt{s} \leq 1780 MeV \\ 24.49 + 34.0\ exp(-6.0 \times 10^{-4} s^{1/2}) & \text{if } 1780 MeV < \sqrt{s} \leq 12000 MeV \\ 24.5 & \text{if } \sqrt{s} > 12000 MeV \end{cases} \quad \text{(A.13)}$$

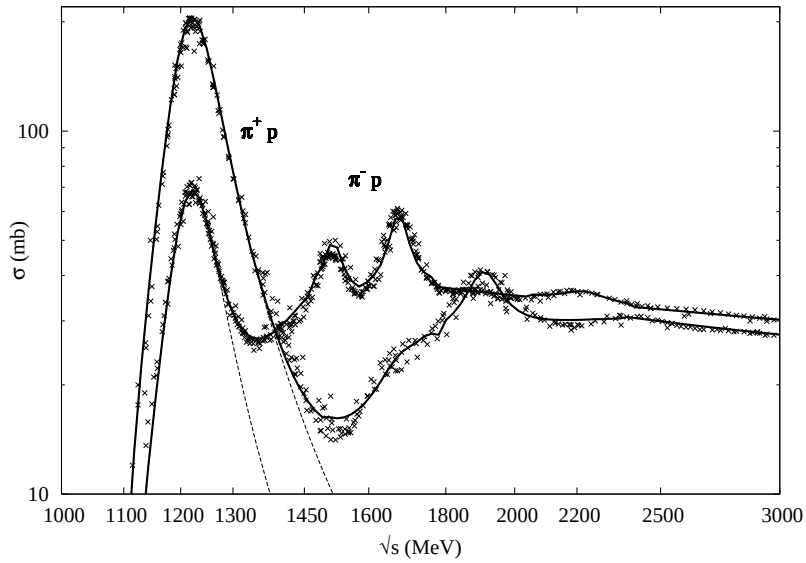

Figure A.2: *Parametrization for the $\pi^+ - p$ et $\pi^- - p$ total cross sections. The crosses represent experimental data coming from Particle Data Group [110]. Continuous lines and dotted lines respectively stand for the total reaction cross section and the Δ recombination cross section used in INCL4.2*

Inelastic cross sections

The inelastic cross sections follow the parametrizations given in [69]. Nevertheless, the parametrization for $p\pi^+$ does not account correctly for the behavior of the cross sections near

the threshold, we have thus added a low energy component of the form $A\,(p_{lab})^B$, suggested in Ref. [54], where p_{lab} is the momentum in the center of mass frame, it is always expressed in GeV/c. The cross sections, expressed in mb, are written as:

$$\sigma_{inel,p\pi^+} = \begin{cases} 0.0 & \text{if } p_{lab} \leq 0.297 \\ 17.965\ p_{lab}^{5.4606} & \text{if } 0.297 < p_{lab} \leq 0.75 \\ 24.3 - 12.3\ p_{lab}^{-1.91} + 0.324\ \left(\log(p_{lab})\right)^2 & \\ \qquad -2.81\ \log(p_{lab}) & \text{if } 0.75 < p_{lab} \end{cases} \tag{A.14}$$

$$\sigma_{inel,p\pi^-} = \begin{cases} 0.0 & \text{if } p_{lab} \leq 0.4731 \\ 26.6 - 7.18\ p_{lab}^{-1.86} + 0.327\ \left(\log(p_{lab})\right)^2 & \\ \qquad -2.81\ \log(p_{lab}) & \text{if } 0.4731 < p_{lab} \end{cases} \tag{A.15}$$

$$\sigma_{inel,p\pi^0} = \left(\sigma_{inel,p\pi^+} + \sigma_{inel,p\pi^-}\right)/2 \tag{A.16}$$

B

Isospin state of systems of particles

In this appendix, we want to define the isospin states of particles and systems composed of two particles that are used in Chapter 5 for the cross sections determination and for the calculations regarding the charge repartition of the outgoing particles.

B.1 Isospin of a system of two nucleons

The composition of two isospin states of particles ($|T_1\ m_1\rangle$ and $|T_2\ m_2\rangle$), to compute the isospin state of a system composed by two particles $|T\ m\rangle$, is obtained in the same way as the combination of angular momentum in quantum mechanics, which is

$$|(T_1T_2)Tm\rangle = \sum_{m_1=-T_1}^{T_1} \sum_{m_2=-T_2}^{T_2} |T_1 m_{T1}\rangle |T_2 m_{T2}\rangle \langle T_1 m_{T1} T_2 m_{T2}|Tm\rangle \tag{B.1}$$

The expansion coefficients $\langle T_1 m_{T1} T_2 m_{T2}|Tm\rangle$ are called *Clebsch–Gordan* coefficients. We will only consider the coupling of two nucleons, two pions and the coupling of one pion and one nucleon. The relevant Clebsch–Gordan coefficients we will use are shown on Figure B.1.

Given the coefficients in the $\frac{1}{2} \times \frac{1}{2}$ table of Figure B.1, we can compute the isospin states for two nucleons:

$$\begin{aligned}
|pp\rangle &= \left|\frac{1}{2}\ \frac{1}{2}\right\rangle \otimes \left|\frac{1}{2}\ \frac{1}{2}\right\rangle = 1\,|1\ 1\rangle\,, \\
|nn\rangle &= \left|\frac{1}{2}\ -\frac{1}{2}\right\rangle \otimes \left|\frac{1}{2}\ -\frac{1}{2}\right\rangle = 1\,|1\ -1\rangle\,, \\
|pn\rangle &= \left|\frac{1}{2}\ \frac{1}{2}\right\rangle \otimes \left|\frac{1}{2}\ -\frac{1}{2}\right\rangle = \frac{1}{\sqrt{2}}\,|1\ 0\rangle + \frac{1}{\sqrt{2}}\,|0\ 0\rangle\,, \\
|np\rangle &= \left|\frac{1}{2}\ -\frac{1}{2}\right\rangle \otimes \left|\frac{1}{2}\ \frac{1}{2}\right\rangle = \frac{1}{\sqrt{2}}\,|1\ 0\rangle - \frac{1}{\sqrt{2}}\,|0\ 0\rangle\,,
\end{aligned} \tag{B.2}$$

If the proton and the neutron are treated as two states of the same entity, we have to consider the consequences in terms of a generalized Pauli principle. If the wave-function Ψ of a system of

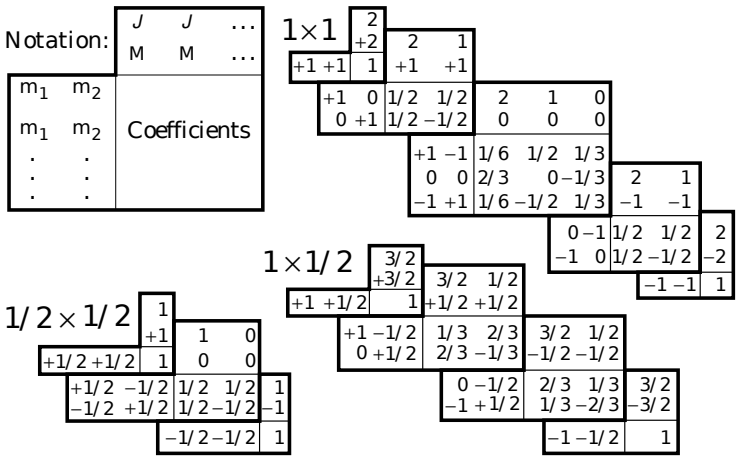

Figure B.1: *Clebsch–Gordan coefficients table for the NN, $\pi\pi$ and $N\pi$ coupling.*

nucleons factorizes as a product of space, spin and isospin components, we have

$$\Psi(\mathbf{r}_1, \mathbf{r}_2, s_1, s_2, T_1, T_2) = \psi(\mathbf{r}_1, \mathbf{r}_2)\chi(s_1, s_2), \Xi(T_1, T_2). \tag{B.3}$$

This wave-function must be anti-symmetric under the exchange of the two nucleons, that is for exchange of space, spin and isospin.

The space wave-function describes the relative motion of the two nucleons and its angular dependence (θ and ϕ) is given by a spherical harmonic function. Exchange of the nucleons corresponds to, in polar coordinates

$$\mathbf{r} = (r, \theta, \phi) \rightarrow -\mathbf{r} = (r, \pi - \theta, \pi - \phi)$$

under this transformation, the spherical harmonic function becomes

$$Y_l^m(\pi - \theta, \pi - \phi) = (-1)^l Y_l^m(\theta, \phi) \tag{B.4}$$

and the space component wave-function is symmetric for even relative orbital momentum. The spin and isospin are symmetric in triplet states antisymmetric in singlet states[1].

B.2 Isospin of a system of two pions

If we now consider a system of two pions, and consider the permutation of the two pions, a factor $(-1)^l$ appears in the Ψ wave function, due to the spherical harmonics (from Equation B.4); the isospin component Ξ becomes

$$\begin{aligned}
\Xi(T_1, T_2) &= \sum_{m_1} \sum_{m_2} (1m_1 1m_2 | \, Tm) \, \chi_1^{m_1}(1) \chi_1^{m_2}(2), \\
\Xi(T_2, T_1) &= \sum_{m_1} \sum_{m_2} (1m_1 1m_2 | \, Tm) \, \chi_1^{m_1}(2) \chi_1^{m_2}(1),
\end{aligned}$$

where we have taken into account the total isospin of pions $T_1 = T_2 = 1$ and T and m denotes the total isospin and its third component of the final state. If we write again this relation and

[1] a triplet corresponds to a total isospin $T = 1$, a singlet corresponds to a total isospin $T = 0$.

rename m_1 as m_2 and vice versa, we obtain

$$\begin{aligned}\Xi(T_2,T_1) &= \sum_{m_1}\sum_{m_2}(1m_2 1m_1|\,Tm)\,\chi_1^{m_2}(2)\chi_1^{m_1}(1)\\ &= \sum_{m_1}\sum_{m_2}(-)^{T-2}(1m_1 1m_2|\,Tm)\,\chi_1^{m_1}(1)\chi_1^{m_2}(2)\\ &= (-)^T\,\Xi_T^{M_T}(1,2)\end{aligned}$$

Finally, considering this relation and relation B.4, under the permutation of two pions, the total wave function Ψ becomes

$$\Psi(2,1) = (-)^{T+L}\Psi(1,2).$$

As long as $T+L$ remains even, the wave function remains unchanged under the permutation of two pions. As we only consider systems of 2 pions produced in very small phase space volume, it is reasonable to assume that the pion system is in the angular momentum state $L=0$. Hence the system of pions requires that isospin is even as well, and the authorized Ξ functions state are

$$\begin{aligned}\Xi_2^2 &= \pi^+\,\pi^+ = |22\rangle\,,\\ \Xi_2^1 &= \frac{1}{\sqrt{2}}\left(\pi^+\,\pi^0\;+\;\pi^0\,\pi^+\right) = |21\rangle\,,\\ \Xi_2^0 &= \frac{1}{\sqrt{6}}\pi^+\pi^- + \sqrt{\frac{2}{3}}\pi^0\pi^0 + \frac{1}{\sqrt{6}}\pi^-\pi^+ = |20\rangle\,,\\ \Xi_2^{-1} &= \frac{1}{\sqrt{2}}\left(\pi^-\,\pi^0\;+\;\pi^0\,\pi^-\right) = |2-1\rangle\,,\\ \Xi_2^{-2} &= \pi^-\,\pi^- = |2-2\rangle\,,\\ \Xi_0^0 &= \frac{1}{\sqrt{3}}\pi^+\pi^- - \frac{1}{\sqrt{3}}\pi^0\pi^0 + \frac{1}{\sqrt{3}}\pi^-\pi^+ = \frac{1}{\sqrt{3}}\,|00\rangle\,.\end{aligned} \tag{B.5}$$

These relations can be exchanged to obtain the isospin states accessible by the pions system:

$$\begin{aligned}\left|\pi^+\,\pi^+\right\rangle &= |22\rangle\,,\\ \left|\pi^0\,\pi^0\right\rangle &= \sqrt{\frac{2}{3}}\;|20\rangle\;-\;\frac{1}{\sqrt{3}}\;|00\rangle\\ \left|\pi^-\,\pi^-\right\rangle &= |2-2\rangle\\ \frac{1}{\sqrt{2}}\left(\left|\pi^+\,\pi^0\right\rangle\;+\;\left|\pi^0\,\pi^+\right\rangle\right) &= |21\rangle\\ \frac{1}{\sqrt{2}}\left(\left|\pi^+\,\pi^-\right\rangle\;+\;\left|\pi^-\,\pi^+\right\rangle\right) &= \frac{1}{\sqrt{3}}\;|20\rangle\;-\;\sqrt{\frac{2}{3}}\;|00\rangle\\ \frac{1}{\sqrt{2}}\left(\left|\pi^0\,\pi^-\right\rangle\;+\;\left|\pi^-\,\pi^0\right\rangle\right) &= |2-1\rangle\end{aligned} \tag{B.6}$$

One can see that the three last relations are symmetric. In fact, it is impossible to measure separately the production cross sections of two systems of pions in which the charges have been inverted. Hence, we have to account for the two possible states, in the following, we will use

"physical states" to denote these systems, defined by

$$\begin{aligned}
\frac{1}{\sqrt{2}}\left(\left|\pi^+\,\pi^0\right\rangle\,+\,\left|\pi^0\,\pi^+\right\rangle\right) &\Rightarrow \left|\pi^+\,\pi^0\right\rangle_\varphi \\
\frac{1}{\sqrt{2}}\left(\left|\pi^+\,\pi^-\right\rangle\,+\,\left|\pi^-\,\pi^+\right\rangle\right) &\Rightarrow \left|\pi^+\,\pi^-\right\rangle_\varphi \\
\frac{1}{\sqrt{2}}\left(\left|\pi^0\,\pi^-\right\rangle\,+\,\left|\pi^-\,\pi^0\right\rangle\right) &\Rightarrow \left|\pi^0\,\pi^-\right\rangle_\varphi
\end{aligned}$$

B.3 Isospin states of a nucleon-pion system

It is also possible to compute the isospin state of a system composed of a pion and of a nucleon, they can be written

$$\begin{aligned}
\left|\pi^+ p\right\rangle &= |11\rangle \otimes \left|\frac{1}{2}\frac{1}{2}\right\rangle = \left|\frac{3}{2}\frac{3}{2}\right\rangle \\
\left|\pi^0\, p\right\rangle &= |10\rangle \otimes \left|\frac{1}{2}\frac{1}{2}\right\rangle = \sqrt{\frac{2}{3}}\left|\frac{3}{2}\frac{1}{2}\right\rangle - \frac{1}{\sqrt{3}}\left|\frac{1}{2}\frac{1}{2}\right\rangle \\
\left|\pi^- p\right\rangle &= |1\,{-1}\rangle \otimes \left|\frac{1}{2}\frac{1}{2}\right\rangle = \left|\frac{3}{2}\,{-\frac{3}{2}}\right\rangle \\
\left|\pi^+ n\right\rangle &= |11\rangle \otimes \left|\frac{1}{2}\,{-\frac{1}{2}}\right\rangle = \left|\frac{3}{2}\frac{3}{2}\right\rangle \\
\left|\pi^0\, n\right\rangle &= |10\rangle \otimes \left|\frac{1}{2}\,{-\frac{1}{2}}\right\rangle = \frac{1}{\sqrt{3}}\left|\frac{3}{2}\,{-\frac{1}{2}}\right\rangle - \sqrt{\frac{2}{3}}\left|\frac{1}{2}\,{-\frac{1}{2}}\right\rangle \\
\left|\pi^- n\right\rangle &= |1\,{-1}\rangle \otimes \left|\frac{1}{2}\,{-\frac{1}{2}}\right\rangle = \left|\frac{3}{2}\,{-\frac{3}{2}}\right\rangle
\end{aligned} \tag{B.7}$$

C

Phase space Considerations

The "phase space integral" R_n contains all the information about the kinematics of a reaction [71]. Expressed in terms of momentum, this phase space integral corresponds to an hyper surface containing the possible sets of variables. Generating the probabilities distribution of a random variable on that hypersurface turns out to be difficult and thus, for practical reasons, it is necessary to change variables in such way that the probability distribution in terms of these variables is defined on a finite volume in a space of lower dimensionality. This is realized using the invariant masses and angles (of the direction of the momenta) as variables. We will show how to rewrite the phase space factor in terms of invariant masses in Section C.2.

C.1 Phase space integral

The uniform phase space integral, for a system of n particles with momenta p_i, $i = 1, \ldots, n$, is defined by [71]

$$R_n(P; m_1, ..., m_n) = \int ... \int \prod_{i=1}^{n} \left[d^4 p_i \delta(p_i^2 - m_i^2) \theta_H(p_i^0) \right] \delta^4(\sum_{j=1}^{n} p_j - P), \tag{C.1}$$

P is the total 4-momentum vector of the system and where $\theta_H(x)$ is the Heaviside function (1 for $x > 0$, 0 otherwise), the presence of these functions ensures that only positive energy solutions are accepted. R_n is Lorentz invariant, even if it is written in terms of the 4-vector P, it depends only upon $s = P^2$ (and upon the masses, of course). It is proportional to the number of states of a system of n non-interacting bodies with masses $m_1, m_2, ..., m_n$ with a total 4-momentum P (in the continuous limit[1]).

In the center of mass frame, the total 4-momentum reduces to $P = (E, \vec{0})$ and the uniform phase space integral becomes

$$R_n(E, m_1, m_2, \ldots, m_n) = \int \ldots \int \prod_{i=1}^{n} \frac{d^3 p_i}{2\sqrt{\vec{p_i}^2 + m_i^2}} \delta^3(\sum_{i=1}^{n} \vec{p_i}) \delta(\sum_{i=1}^{n} \sqrt{\vec{p_i}^2 + m_i^2} - E). \tag{C.2}$$

[1]The term "phase space" is thus slightly misleading, since configuration space is disregarded.

We can write R_n in the simplest case $n = 1$, which gives

$$\begin{aligned} R_1(E;m) &= \int d^3\vec{p} \int dp_0 \delta((p^2 - m^2)\theta_H(p_0)\delta^3(\vec{p})\delta((p_0 - E) \\ &= \int d^3\vec{p}\delta^3(\vec{p}) \int_0^\infty dp_0 \frac{\delta(p_0 - \sqrt{(}p^2 + m^2)}{2\sqrt{(}p^2 + m^2)}\delta((p_0 - E) \\ &= \frac{\delta(E - m)}{2m}. \end{aligned} \tag{C.3}$$

We can also write R_n in the case $n = 2$:

$$R_2(\sqrt{s}; m_1, m_2) = \frac{\pi}{\sqrt{s}} p^*(\sqrt{s}, m_1, m_2), \tag{C.4}$$

where p^* is the c. m. momentum[2]. Indeed, one has necessarily

$$\begin{aligned} R_2(\sqrt{s}; m_1, m_2) &= \int d^4p_1 \int d^4p_2 \delta(p_1^2 - m_1^2)\delta(p_2^2 - m_2^2)\theta_H(p_1^0)\theta_H(p_2^0) \\ &\quad \times\delta^3(\vec{p_1} + \vec{p_2})\delta(p_1^0 + p_2^0 - \sqrt{s}) \\ &= \int d^3p_1 \int d^3p_2 \frac{1}{2\varepsilon_1}\frac{1}{2\varepsilon_2}\delta^3(\vec{p_1} + \vec{p_2})\delta(\varepsilon_1 + \varepsilon_2 - \sqrt{s}) \\ &= \int d^3p_1 \frac{1}{4\varepsilon_1\varepsilon_2}\delta(\sqrt{p_1^2 + m_1^2} + \sqrt{p_1^2 + m_2^2} - \sqrt{s}) \\ &= \pi \int_0^\infty p_1^2 dp_1 \frac{1}{\varepsilon_1\varepsilon_2}\delta(\sqrt{p_1^2 + m_1^2} + \sqrt{p_1^2 + m_2^2} - \sqrt{s}) \\ &= \pi(p^*)^2 \frac{1}{\varepsilon_1^*\varepsilon_2^*}(\frac{p^*}{\varepsilon_1^*} + \frac{p^*}{\varepsilon_2^*})^{-1} \\ &= \pi\frac{p^*}{\sqrt{s}}, \end{aligned} \tag{C.5}$$

where one has introduced $\varepsilon_i = \sqrt{p_i^2 + m_i^2}$ and $\varepsilon_i^* = \sqrt{(p^*)^2 + m_i^2}$.

By integrating Eq. C.1 over p_n^0, it is possible to define the recurrence formula

$$R_n(P; m_1, ..., m_n) = \int \frac{d^3\vec{p_n}}{2E_n} R_{n-1}(P - (E_n, \vec{p_n}); m_1, m_2, ..., m_{n-1}), \tag{C.6}$$

where $E = \sqrt{\vec{p}^2 + m^2}$.

The following relation, whose proof follows, can also be obtained

$$R_n(P; m_1, ..., m_n) = \int dM^2 R_{n-1}(P; M, m_3, ..., m_n) R_2(M; m_1, m_2). \tag{C.7}$$

[2]The c. m. momentum of a system of two particles with masses m_1 and m_2 is defined as

$$p_{cm}(s) = \frac{1}{2}\sqrt{\frac{(s - (m_1 + m_2)^2)\,(s - (m_1 - m_2)^2)}{s}},$$

where s corresponds to the square of the sum of the 4-momenta of the particles.

The r.h.s. of the equation can be rewritten as

$$\begin{aligned}\int dM^2 R_{n-1}(P;M,m_3,...,m_n)R_2(M;m_1,m_2) = \\ \int dM^2 \int d^4p_2' \int d^4p_3 ... \int d^4p_n \delta((p_2')^2 - M^2)\theta_H((p_2')^0) \\ \times \prod_{i=3}^{n}\{\delta(p_i^2 - m_i^2)\theta_H(p_i^0)\}\delta^4(p_2' + \sum_{j=3}^{n} p_j - P) \\ \times \int d^4p_1 \int d^4p_2 \delta(p_1^2 - m_1^2)\delta(p_2^2 - m_2^2)\theta_H(p_1^0)\theta_H(p_2^0)\delta^4(p_1 + p_2 - p'),\end{aligned} \tag{C.8}$$

with $p'^2 = M^2$. R_2 (the last double integral) being an invariant, we can evaluate it in the frame where $\vec{p'} = \vec{p_2'}$. The integration over the variable M^2 makes the delta function involving M^2 to disappear and the 4-vector p' equal to p_2'. The condition over the positivity of $(p_2')^0$ is automatically satisfied (since the integration runs over M^2, and not M) and one recovers Eq. C.7.

C.2 Writing the phase space integral in terms of invariant masses

The factor $\delta^4(\sum_{j=1}^{n} p_j - P)$ in the definition of R_n (Eq. C.1) indicates that R_n corresponds to an hyper surface in the phase space of the system of n particles. Because of this factor, using a random generator to obtain a set of coordinates that belongs to R_n will not be effective, the probability to reject the generated event being very high. That is why another set of coordinates is used: the invariant masses M_i of the subsystems composed with the i first particles, and the angles that define the direction of the momenta of the outgoing particles. They automatically account for the constraints imposed by these delta functions and the quantity R_n is associated with a finite domain of variation of these variables.

An expression of R_n in these coordinates may be obtained by iterating Eq. C.7. We introduce the notation M_2 as the invariant mass of the system composed of m_1 and m_2, M_3 as the invariant mass of the system composed of M_2 and m_3, M_3 corresponds to the invariant mass of the first three particles, M_4 as the invariant mass of the system composed of M_3 and m_4 and so on. The last invariant mass is equal to the center of mass energy ($M_n = \sqrt{s}$). From the recurrence formula C.7 and the definition of R_2 by Eq. C.4, and by replacing M by M_2, one gets

$$\begin{aligned}R_n(\sqrt{s};m_1,\ldots,m_n) &= \int dM_2^2 R_{n-1}(\sqrt{s};M_2,m_3,\ldots,m_n)\pi\frac{p^*(M_2,m_1,m_2)}{M_2} \\ &= 2\pi\int dM_2 R_{n-1}(\sqrt{s};M_2,m_3,\ldots,m_n)p^*(M_2,m_1,m_2).\end{aligned} \tag{C.9}$$

The second equality was obtained by simplifying with $dM_2^2 = 2M_2dM_2$. The second iteration will give

$$\begin{aligned}R_n(\sqrt{s};m_1,\ldots,m_n) \\ &= 2\pi^2\int dM_2 \int dM_3^2 R_{n-2}(\sqrt{s};M_3,m_4,\ldots,m_n)\frac{p^*(M_3,M_2,m_3)}{M_3}p^*(M_2,m_1,m_2) \\ &= (2\pi)^2\int dM_2 \int dM_3 R_{n-2}(\sqrt{s};M_3,m_4,\ldots,m_n)p^*(M_3,M_2,m_3)p^*(M_2,m_1,m_2),\end{aligned}$$

and after $n-2$ iterations, one obtain

$$R_n(\sqrt{s}; m_1, \ldots, m_n) = (2\pi)^{n-1} \int dM_2 \int dM_3 \ \ldots \int dM_{n-1} \times p^*(M_2, m_1, m_2) p^*(M_3, M_2, m_3) \ldots p^*(\sqrt{s}, M_{n-1}, m_n). \tag{C.10}$$

One can see that the integration over M_2 is limited as follows

$$m_1 + m_2 \leq M_2 \leq (\sqrt{s} - \sum_{j=1}^{n} m_j) + m_1 + m_2. \tag{C.11}$$

The lower bound is obvious. The upper bound is reached when the particles 3 to n have zero kinetic energy. The bounds for the other invariant masses are thus given by

$$\begin{aligned} m_3 + M_2 \leq \quad & M_3 \quad && \leq (\sqrt{s} - \sum_{j=1}^{n} m_j) + m_1 + m_2 + m_3 \\ & \ldots \\ m_{n-1} + M_{n-2} \leq \quad & M_{n-1} \quad && \leq (\sqrt{s} - \sum_{j=1}^{n} m_j) + m_1 + m_2 + m_3 + \ldots + m_{n-1} \\ & && = \sqrt{s} - m_n. \end{aligned} \tag{C.12}$$

One can notice that the expression C.1 is an integral over $3n-4$ variables ($4n$ minus n, coming from the onshell conditions, minus 4, from energy-momentum conservation) and after iterations, we ended with the expression C.10, which is an integral over $n-2$ variables, the invariant masses. The remaining $2n-2$ variables are angles corresponding to the directions of the momenta.

What the calculations actually show is that going from the original variables $\vec{p}_i$ to the variables M_i plus the angles, the integrand does not depend upon these angles. In other words, the density of uniform phase space, which is equal to the delta functions in the original variables, turns into a density which only depends on the invariant masses M_i in the final variables.

D

The HARP experiment

D.1 Description of the Harp experiment

The knowledge of hadron-production is useful for the design of experiments and facilities, it can also be used to improve or validate hadron production models, which play an important role in the design and the interpretation of particle physics experiment. The HARP experiment, located at CERN, has the goal to provide a large angular and momentum coverage of charged particles production, and more specifically charged pion production, with beams of pions and protons hitting a large set of targets. The three motivations for the measurements realized in this experiment are: first they are necessary for a quantitative and economic design of a future neutrino factory. Second, an improved knowledge of the interaction of pions and protons with the Earth's atmosphere can reduce the uncertainties on the neutrino fluxes and their oscillation. Finally, precise measurements, such as the ones realized in the HARP experiment, are needed as input for simulations of interaction of hadrons [111].

A complete description of the experiment can be found in Ref. [111]. The experimental setup comprises two spectrometers; a forward spectrometer that covers the angular region up to 250 mrad and a large angle spectrometer which has an angular acceptance of 0.35 rad $\leq \theta \leq$ 2.15 rad. The data we have used to make comparison with INCL4.2 and our extended version of INCL comprise charged pion production data for beryllium, carbon, aluminum, copper, tin, tantalum and lead targets with incident proton or charged pions with momenta 3 GeV/c, 5 GeV/c, 8 GeV/c, 12 GeV/c at large angle and at forward angle (for proton only).

The large angle detector is composed of a cylindrical time projection chamber (TPC), placed inside a solenoidal magnet. The TPC was designed for tracking, momentum determination and energy deposition in the 0.25–2.5 rad with respect to the beam axis. The target is placed in the inner field cage of the TPC in such a way that both forward and backward tracks can be measured. After the data-taking, it appeared that a relatively large number of pads of the TPC were dead or noisy and,that the reconstructed trajectories suffered from static and dynamic distortions. These shortfalls have been solved in the analysis as presented in [12, 11, 111], with the consequence that all the data could not be used for the analysis. Finally, the percentage of reliable data varies between 44% to 98%, as specified in the papers. A set of resistive plate chambers, surrounding the time projection chamber and inside the magnet is used to measure arrival time of secondary

particles and perform time-of-flight measurement for additional particles identification.

The beam is generated in CERN PS. The composition of the positively charged particles beam depends upon the energy; it is mainly composed of protons, but also contains positrons, pions and a few kaons and deuterons, depending upon the energy. As an example, the proportion of protons varies from 35% at 3 GeV/c to 92% at 12 GeV/c; the momentum precision of the beam is of the order of 1%. The negatively-charged particle beam contains mainly pions, with a background of muons and electrons. The projectiles are selected before they reach the target, the techniques used for the projectile selection are described in [112]. The purity of the selection of protons is higher than 99.9 %. For the selection of pions, a contamination with electrons occurs for the low momentum beams and the ratio e/π was measured to be 1% for a 3 GeV/c beam, at 5 GeV/c it has been found to be smaller than 10^{-3}; it has been assumed negligible for the higher momenta beams.

Finally, the statistic for the measurements is generally good at large angles: the relative statistical error on the number of measured pions varies between 0.2% to 2.2% for all projectiles. It improves with the momenta of the projectiles and is slightly better for protons and π^- than for π^+. The statistics is not so good for forward angle measurements, especially at low momentum where the relative statistical error on the number of measured pions is comprised between 5 and 10% for π^+ production and varies between 11.8% and 18 % for π^- produced with a 3 GeV/c proton at forward angle.

D.2 Double-differential cross sections pion production in proton-induced reactions

The HARP collaboration has measured double-differential cross section for the production of a particle of type a. In the laboratory frame, if p_i and θ_j are the momentum and the polar angle of the produced particle, the double-differential cross section is expressed as

$$\frac{d^2\sigma_a}{dp_i d\theta_i} = \frac{1}{N_{\text{pot}}} \frac{A}{N_A \rho t} \frac{1}{\Delta p_i \Delta\theta_j} \sum_{i',j',a'} M^{-1}_{ija i'j'a'} . N^{a'}_{i'j'}, \tag{D.1}$$

where N_{pot} is the number of proton hitting the target; the factor $\frac{A}{N_A \rho t}$ is the inverse number of target nuclei per unit area (A is the target mass number, N_A is the Avogadro number, ρ is the target density and t is its thickness); Δp_i is the bin size in momentum and $\Delta\theta_j$ is the bin size in angle; the matrix $M^{-1}_{ija i'j'a'}$ corrects for the efficiency and resolution of the detector and $N^{a'}_{i'j'}$ is the number of particles of type a' in bins of reconstructed momentum p'_i and angle θ'_j.

D.2.1 Large angle

The measurements at large angle are realized in an angular domain spreading from 350 to 2150 mrad, separated in 9 bins of 200 mrad each. The momentum acceptance is not the same for each of these bin; they are summarized in Tab. D.1.

The momentum bins are of two different sizes:

$$\Delta p_j = \begin{cases} 0.05\text{GeV}/c & \text{if } p \leq 0.5 \text{ GeV}/c \\ 0.1\text{GeV}/c & \text{if } p < 0.5 \text{ GeV}/c \end{cases} \tag{D.2}$$

Figures D.1 to D.3 show the comparison between data from the HARP experiment (symbols) and simulations realized with INCL4.2 (red lines) and its extended version (blue lines) for a Be target with 4 projectile momentum (3 GeV/c, 5 GeV/c, 8 GeV/c and 12 GeV/c). The following

Polar Angle domain (mrad)	Momentum domain (MeV/c)
350–550	150–800
550–750	100–800
750–950	100–700
950–1150	100–600
1150–1350	100–500
1350–1550	
1550–1750	
1750–1950	
1950–2150	

Table D.1: *Acceptance domain for the double-differential cross-sections at large angle, for incident protons in the HARP experiment [11].*

figures show the same comparison for different targets: aluminium target (Figs. D.4 to D.6), tin target (Figs. D.7 to D.9) and tantalum target (Figs. D.10 to D.12). For each target, the two first figures show comparisons for double-differential cross section for π^+ production and π^- production, respectively, and the third figure shows the simple-differential cross sections after integration over the momentum domain (first row) and the angular domain (second row) for π^+ production (first column) and π^- production (second column).

Each figure is divided in four panels, one for each incident momentum of the proton (3 GeV/c in panel (a), 5 GeV/c in panel (b), 8 GeV/c in panel (c) and 12 GeV/c in panel (d)). In turn, each panel is divided in nine parts, each of them corresponding to a different angular bin in the experiments. The values of these angular bins are always the same and are arranged as in Table 6.2 in Chapter 6. For convenience, this Table has been reproduced here:

350–550 mrad	550–750 mrad	750–950 mrad
950–1150 mrad	1150–1350 mrad	1350–1550 mrad
1550–1750 mrad	1750–1950 mrad	1950–2150 mrad

Table D.2: *Angular bins of each panels on figures showing comparison between simulations and double-differential cross section data from HARP experiment.*

The comparisons concerning C, Cu and Pb targets have been presented in Chapter 6.

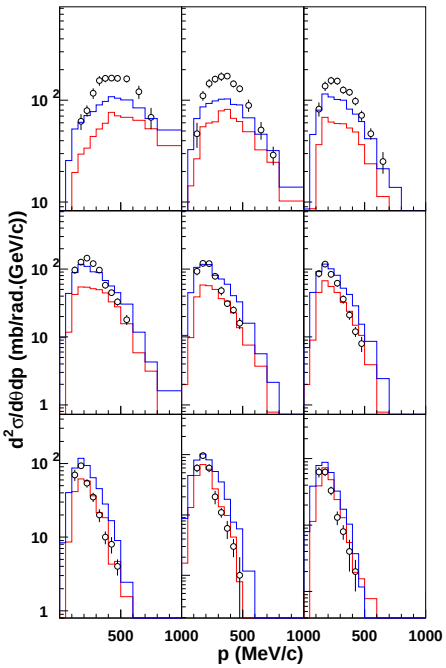

(a) p (3 GeV/c) + Be $\rightarrow$ π^+

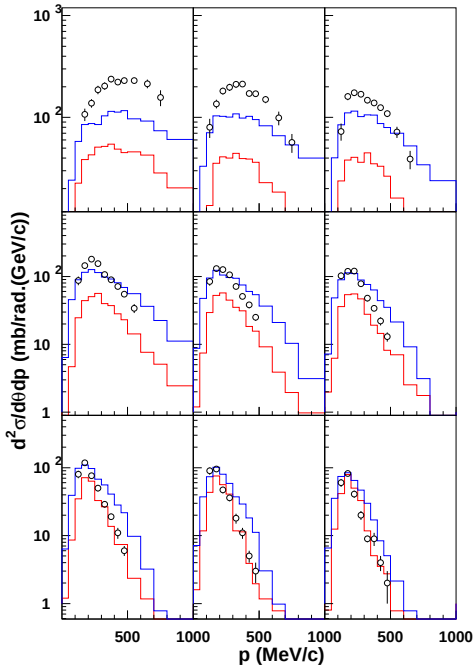

(b) p (5 GeV/c) + Be $\rightarrow$ π^+

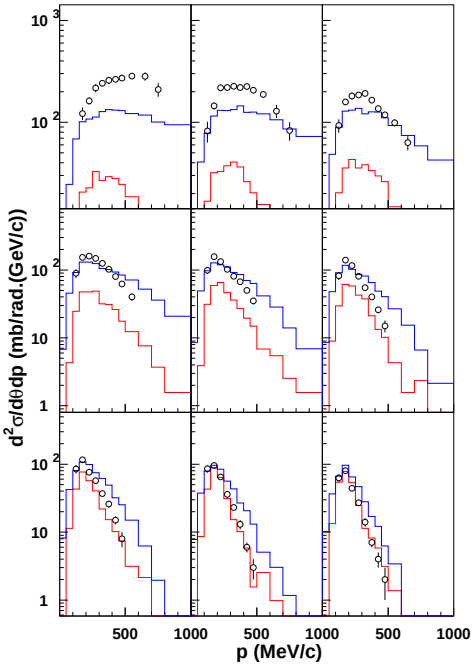

(c) p (8 GeV/c) + Be $\rightarrow$ π^+

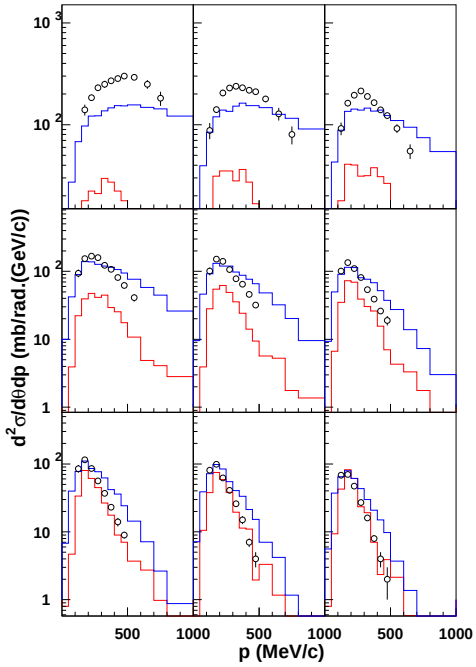

(d) p (12 GeV/c) + Be $\rightarrow$ π^+

Figure D.1: *Double-differential cross sections for π^+ production in proton-induced reactions on Be at 3 GeV/c (a), 5 GeV/c (b), 8 GeV/c (c) and 12 GeV/c (d) incident momentum. Data (symbols) from Refs. [11, 84] are compared with the standard version (red lines) and the improved version (blue lines) of the INCL4 model (standard INCL4.2 version plus implementation of direct multipion production).*

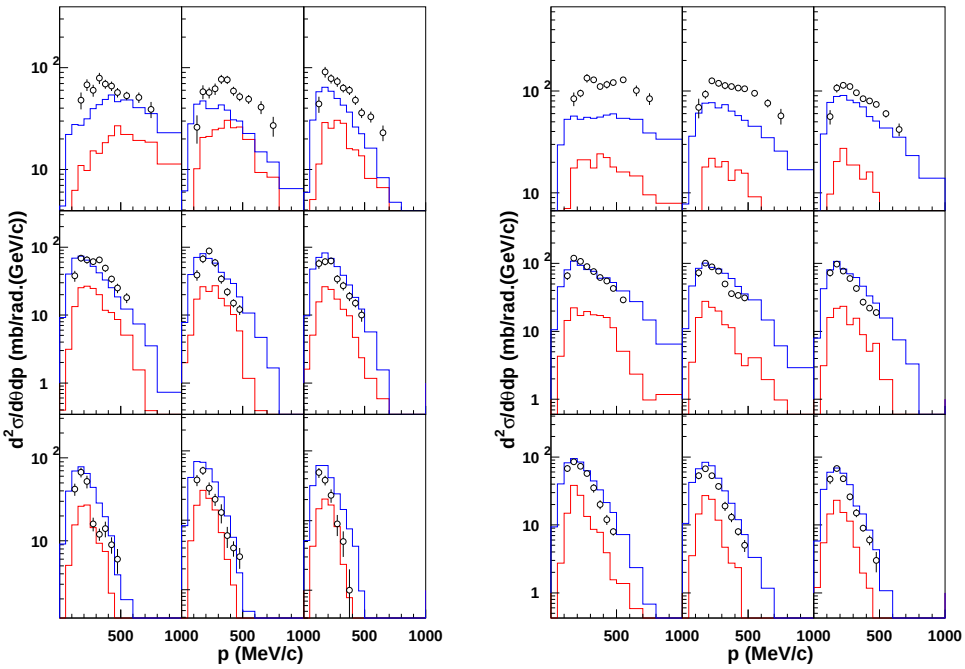

(a) p (3 GeV/c) + Be $\rightarrow$ π^-

(b) p (5 GeV/c) + Be $\rightarrow$ π^-

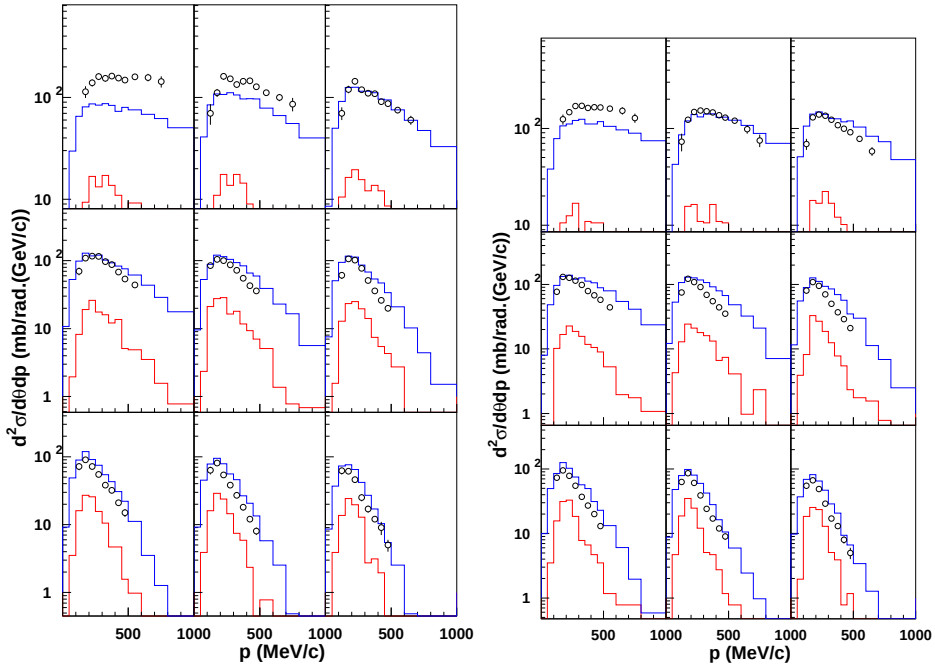

(c) p (8 GeV/c) + Be $\rightarrow$ π^-

(d) p (12 GeV/c) + Be $\rightarrow$ π^-

Figure D.2: *Double-differential cross sections for π^- production in proton-induced reactions on Be at 3 GeV/c (a), 5 GeV/c (b), 8 GeV/c (c) and 12 GeV/c (d) incident momentum. Data (symbols) from Refs. [11, 84] are compared with the standard version (red lines) and the improved version (blue lines) of the INCL4 model (standard INCL4.2 version plus implementation of direct multipion production).*

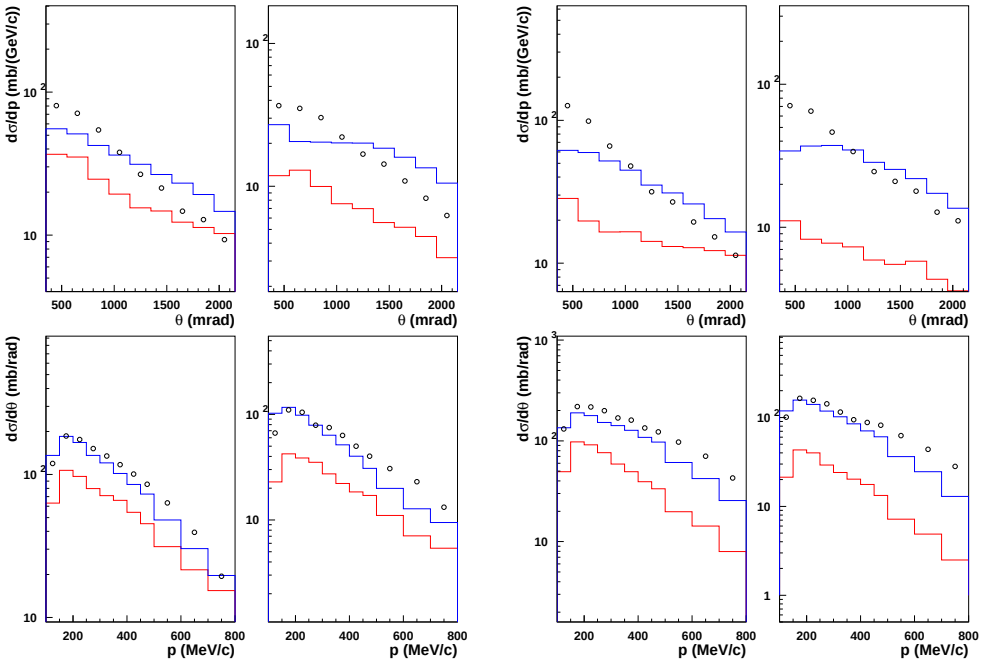

(a) p (3 GeV/c) + Be

(b) p (5 GeV/c) + Be

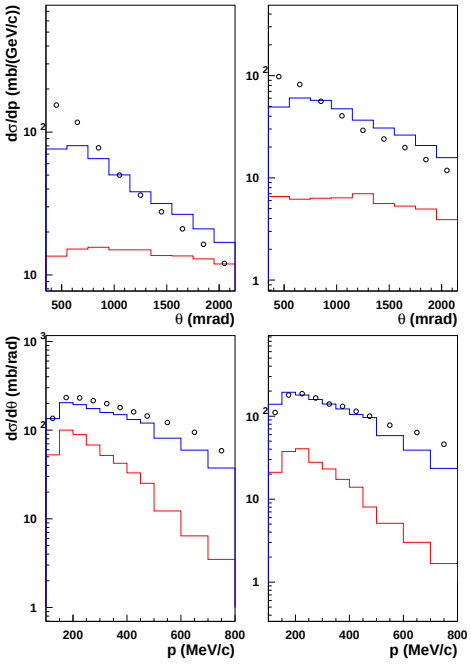

(c) p (8 GeV/c) + Be

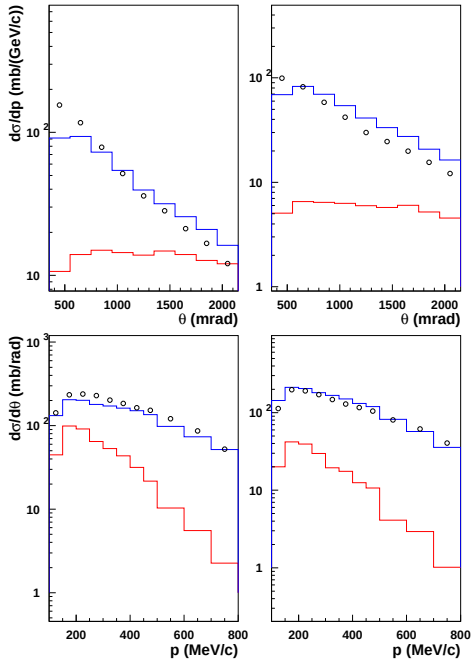

(d) p (12 GeV/c) + Be

Figure D.3: *Simple-differential cross section in proton-induced reactions on Be target at 3 GeV/c (a), 5 GeV/c (b), 8 GeV/c (c) and 12 GeV/c (d) incident momentum. Each panel is divided in four, corresponding to the integration of the π^+ production (left column of the panel) double-differential cross sections or the π^- production (right column of the panel) double-differential cross sections of the HARP experiment Ref. [11, 84] over the momentum domain (upper part of the panel) or over the angular domain (lower part of the panel) presented in Tab. D.1. The date are represented by the circles and are compared with INCL HE (blue line).*

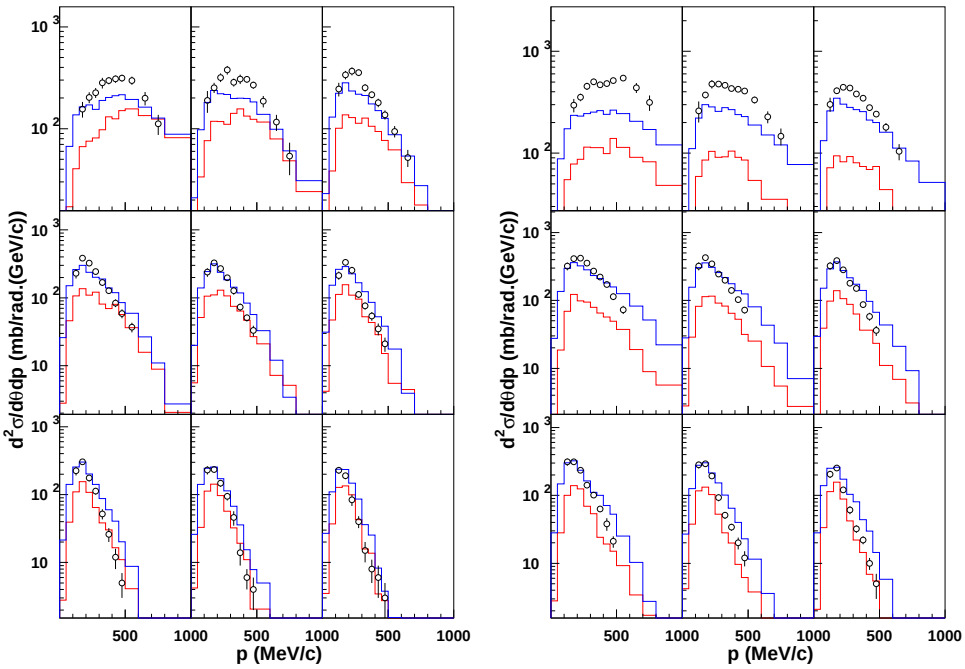

(a) p (3 GeV/c) + Al $\rightarrow$ π^+

(b) p (5 GeV/c) + Al $\rightarrow$ π^+

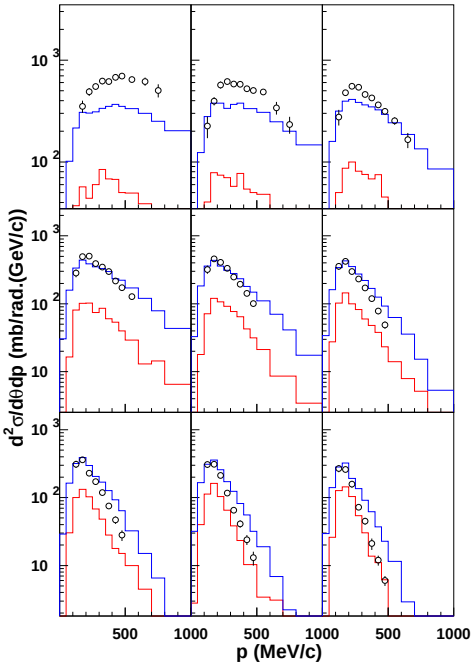

(c) p (8 GeV/c) + Al $\rightarrow$ π^+

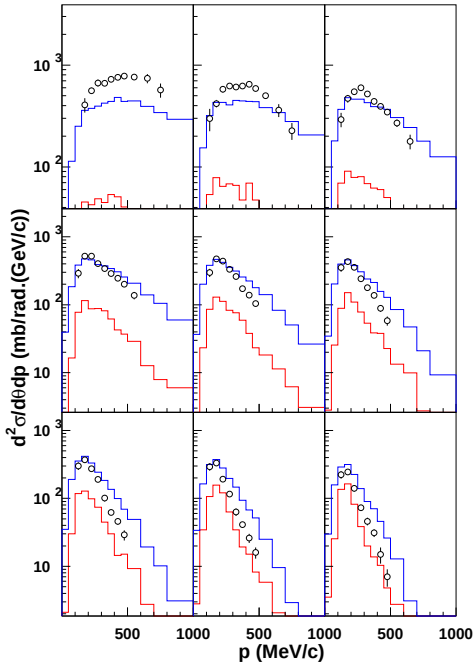

(d) p (12 GeV/c) + Al $\rightarrow$ π^+

Figure D.4: *Double-differential cross sections for π^+ production in proton-induced reactions on Al at 3 GeV/c (a), 5 GeV/c (b), 8 GeV/c (c) and 12 GeV/c (d) incident momentum. Data (symbols) from Refs. [11, 84] are compared with the standard version (red lines) and the improved version (blue lines) of the INCL4 model (standard INCL4.2 version plus implementation of direct multipion production).*

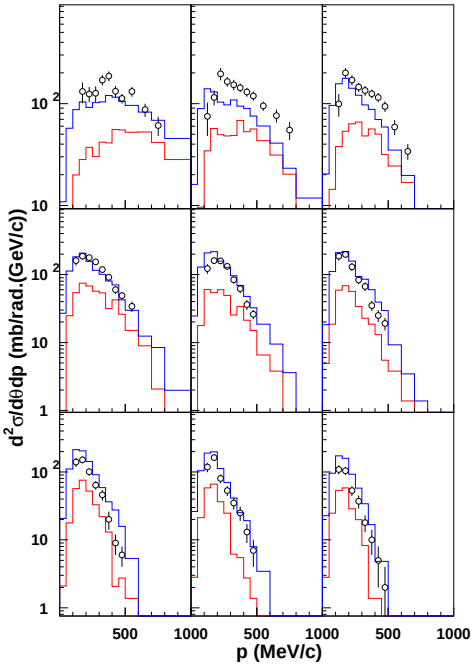

(a) p (3 GeV/c) + Al $\rightarrow$ π^-

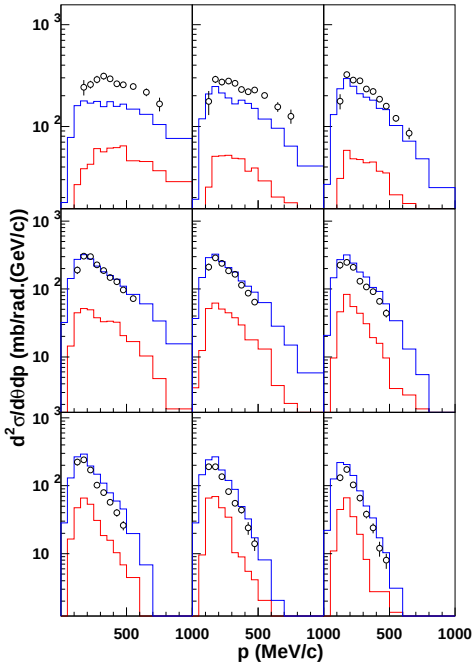

(b) p (5 GeV/c) + Al $\rightarrow$ π^-

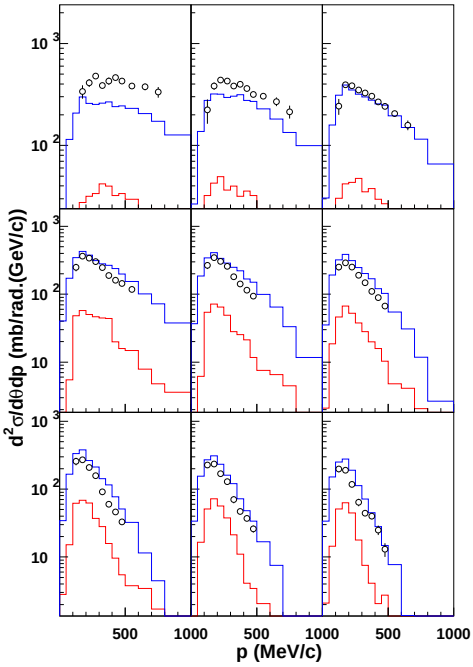

(c) p (8 GeV/c) + Al $\rightarrow$ π^-

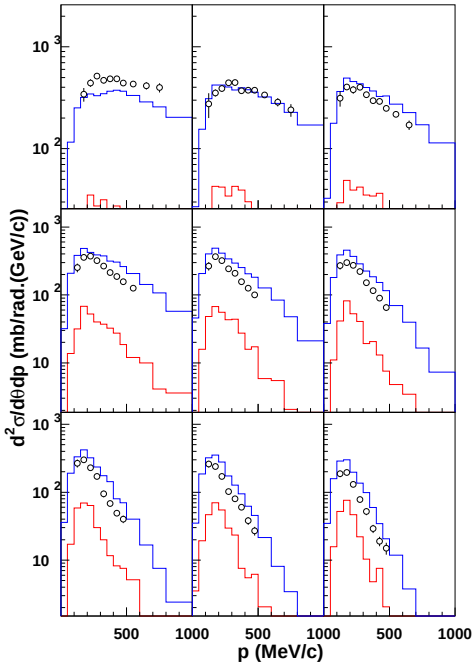

(d) p (12 GeV/c) + Al $\rightarrow$ π^-

Figure D.5: *Double-differential cross sections for π^- production in proton-induced reactions on Al at 3 GeV/c (a), 5 GeV/c (b), 8 GeV/c (c) and 12 GeV/c (d) incident momentum. Data (symbols) from Refs. [11, 84] are compared with the standard version (red lines) and the improved version (blue lines) of the INCL4 model (standard INCL4.2 version plus implementation of direct multipion production).*

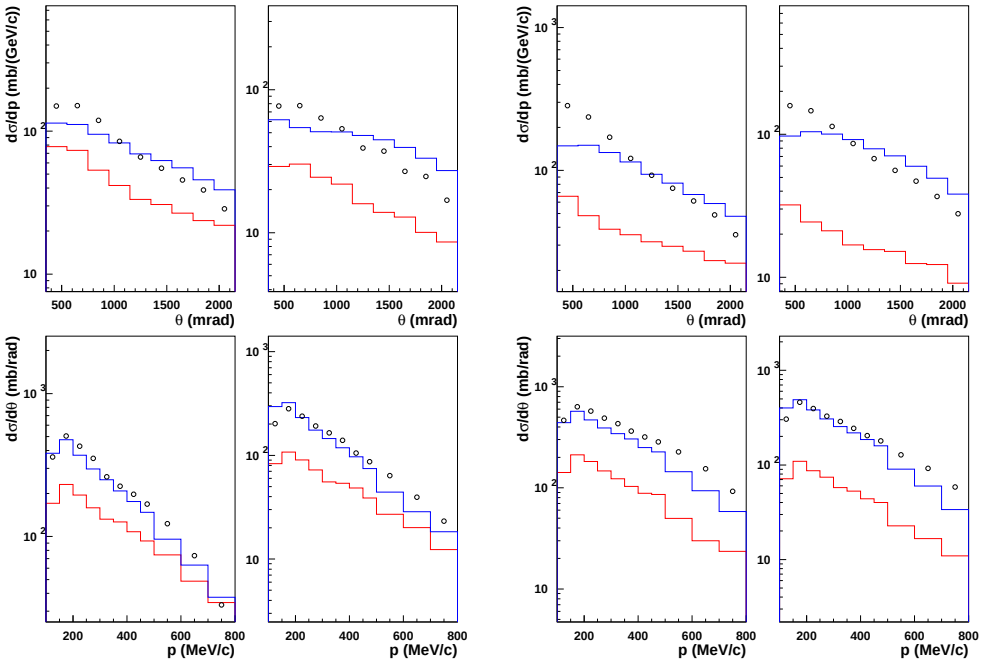

(a) p (3 GeV/c) + Al (b) p (5 GeV/c) + Al

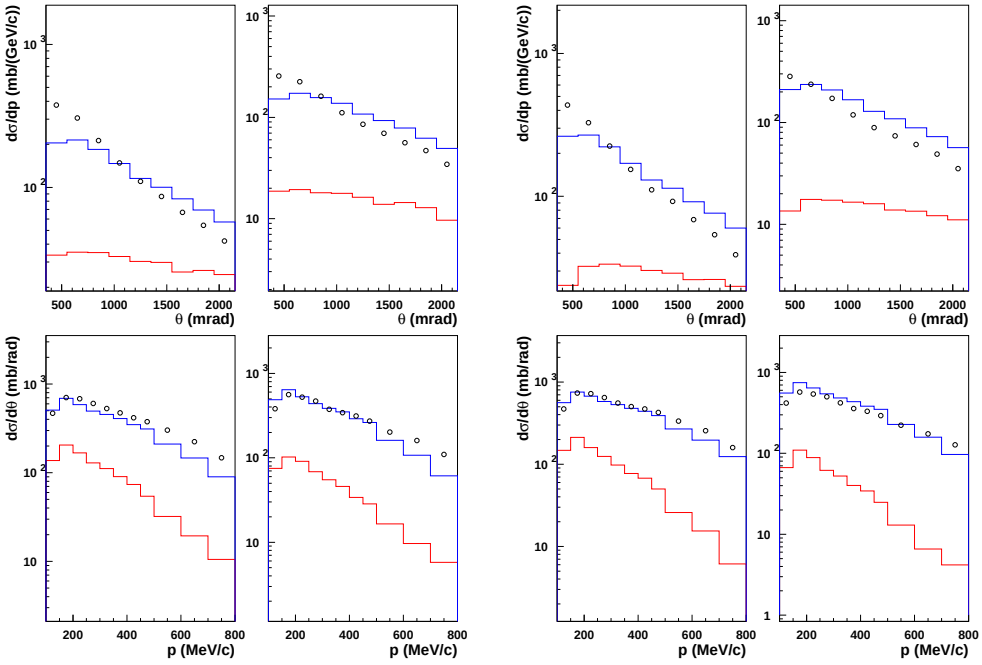

(c) p (8 GeV/c) + Al (d) p (12 GeV/c) + Al

Figure D.6: *Simple-differential cross section in proton-induced reactions on Al target at 3 GeV/c (a), 5 GeV/c (b), 8 GeV/c (c) and 12 GeV/c (d) incident momentum. Each panel is divided in four, corresponding to the integration of the π^+ production (left column of the panel) double-differential cross sections or the π^- production (right column of the panel) double-differential cross sections of the HARP experiment Ref. [11, 84] over the momentum domain (upper part of the panel) or over the angular domain (lower part of the panel) presented in Tab. D.1. The date are represented by the circles and are compared with INCL HE (blue line).*

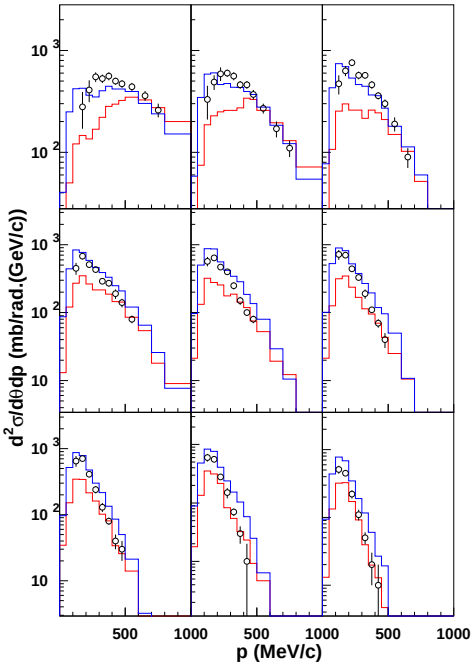

(a) p (3 GeV/c) + Sn $\rightarrow$ π^+

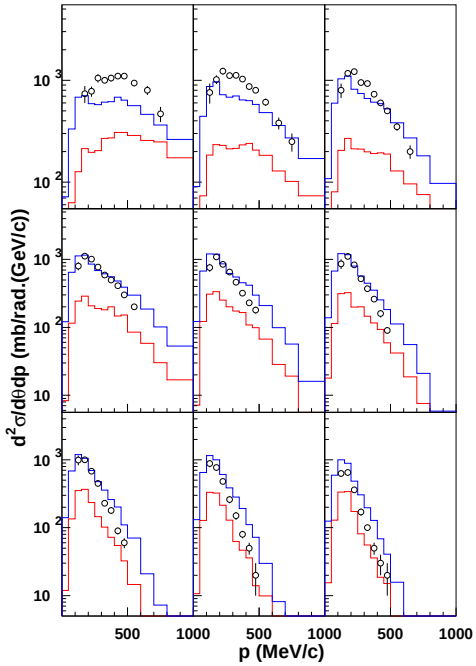

(b) p (5 GeV/c) + Sn $\rightarrow$ π^+

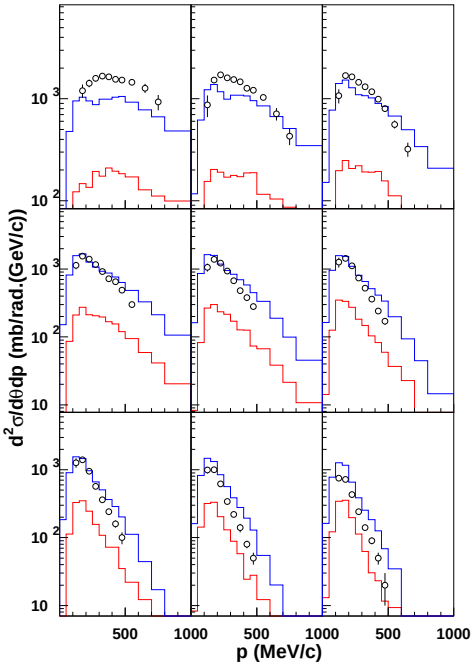

(c) p (8 GeV/c) + Sn $\rightarrow$ π^+

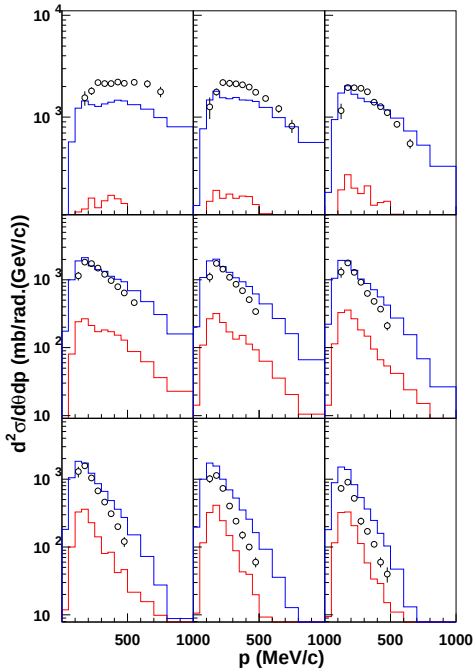

(d) p (12 GeV/c) + Sn $\rightarrow$ π^+

Figure D.7: *Double-differential cross sections for π^+ production in proton-induced reactions on Sn at 3 GeV/c (a), 5 GeV/c (b), 8 GeV/c (c) and 12 GeV/c (d) incident momentum. Data (symbols) from Refs. [11, 85] are compared with the standard version (red lines) and the improved version (blue lines) of the INCL4 model (standard INCL4.2 version plus implementation of direct multipion production).*

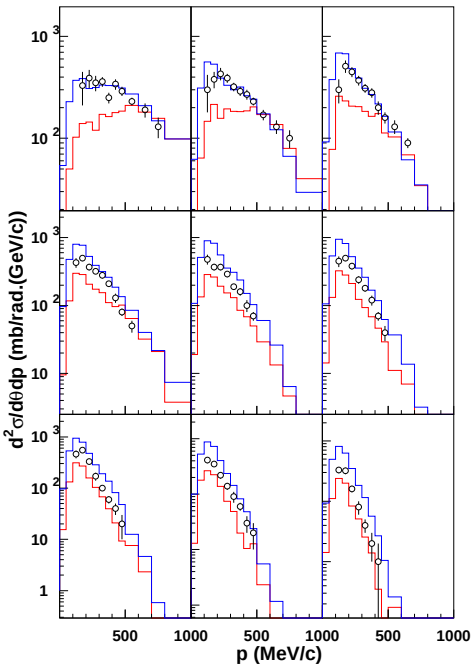

(a) p (3 GeV/c) + Sn $\rightarrow$ π^-

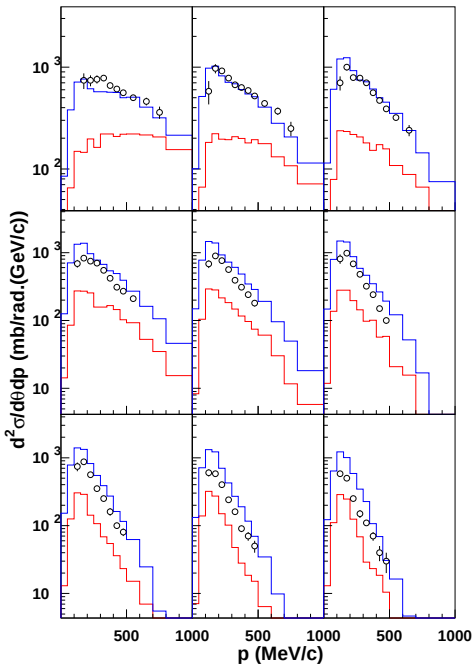

(b) p (5 GeV/c) + Sn $\rightarrow$ π^-

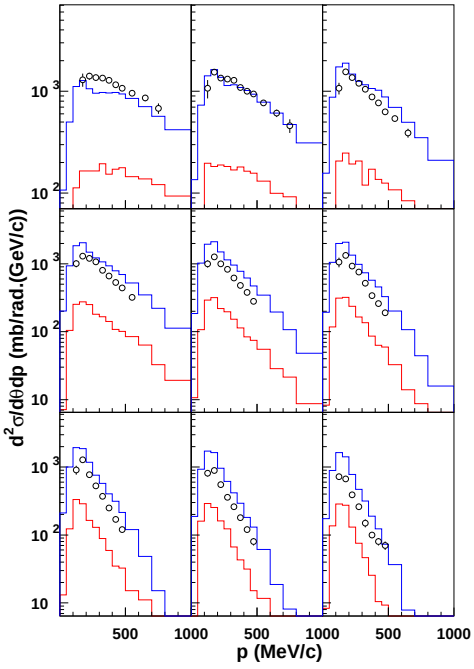

(c) p (8 GeV/c) + Sn $\rightarrow$ π^-

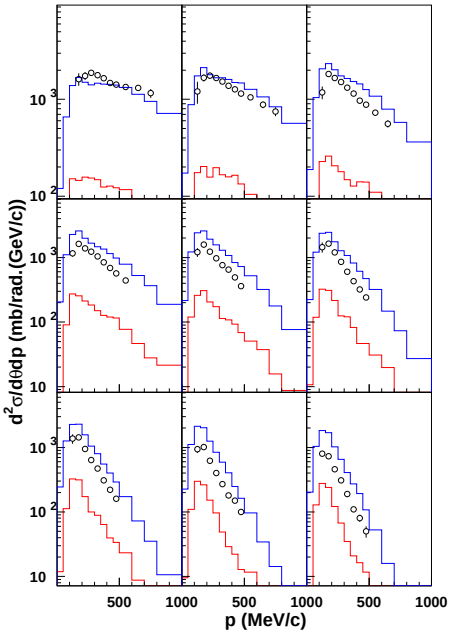

(d) p (12 GeV/c) + Sn $\rightarrow$ π^-

Figure D.8: *Double-differential cross sections for π^- production in proton-induced reactions on Sn at 3 GeV/c (a), 5 GeV/c (b), 8 GeV/c (c) and 12 GeV/c (d) incident momentum. Data (symbols) from Refs. [11, 85] are compared with the standard version (red lines) and the improved version (blue lines) of the INCL4 model (standard INCL4.2 version plus implementation of direct multipion production).*

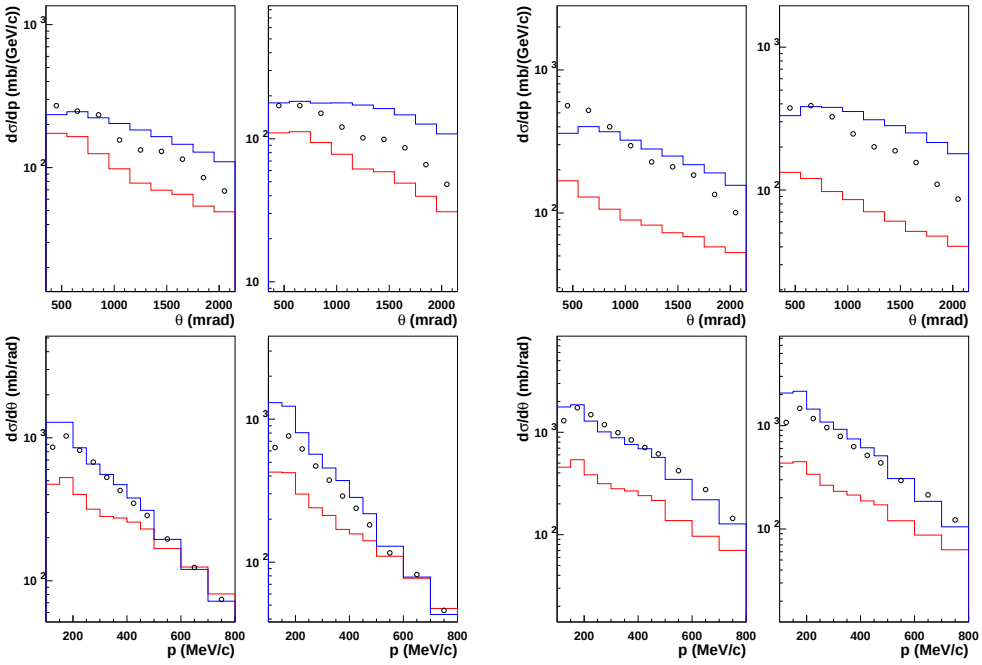

(a) p (3 GeV/c) + Sn (b) p (5 GeV/c) + Sn

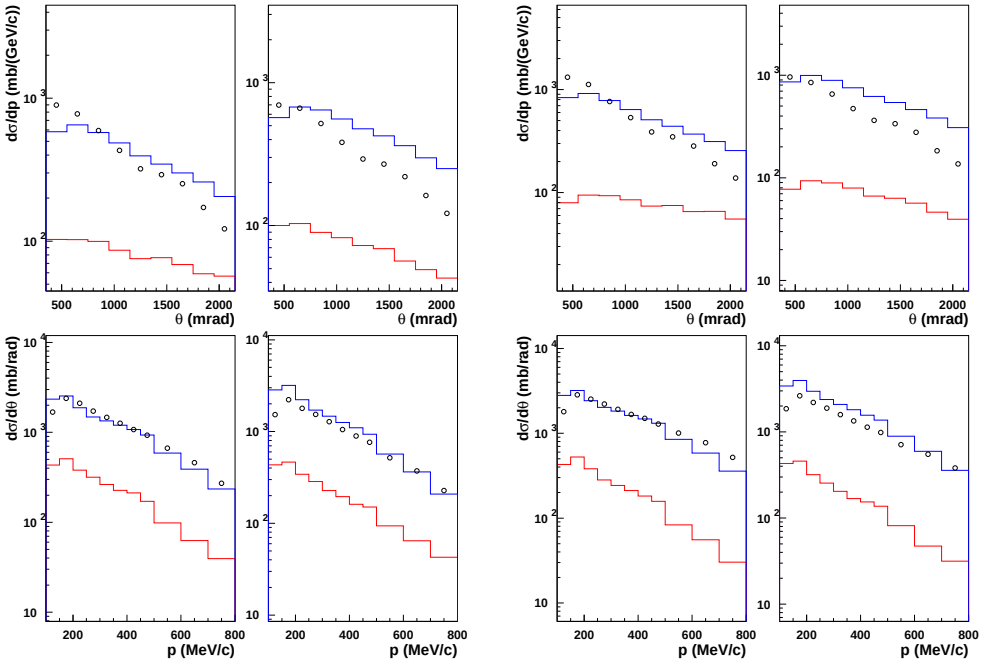

(c) p (8 GeV/c) + Sn (d) p (12 GeV/c) + Sn

Figure D.9: *Simple-differential cross section in proton-induced reactions on Sn target at 3 GeV/c (a), 5 GeV/c (b), 8 GeV/c (c) and 12 GeV/c (d) incident momentum. Each panel is divided in four, corresponding to the integration of the π^+ production (left column of the panel) double-differential cross sections or the π^- production (right column of the panel) double-differential cross sections of the HARP experiment Ref. [11, 85] over the momentum domain (upper part of the panel) or over the angular domain (lower part of the panel) presented in Tab. D.1. The date are represented by the circles and are compared with INCL HE (blue line).*

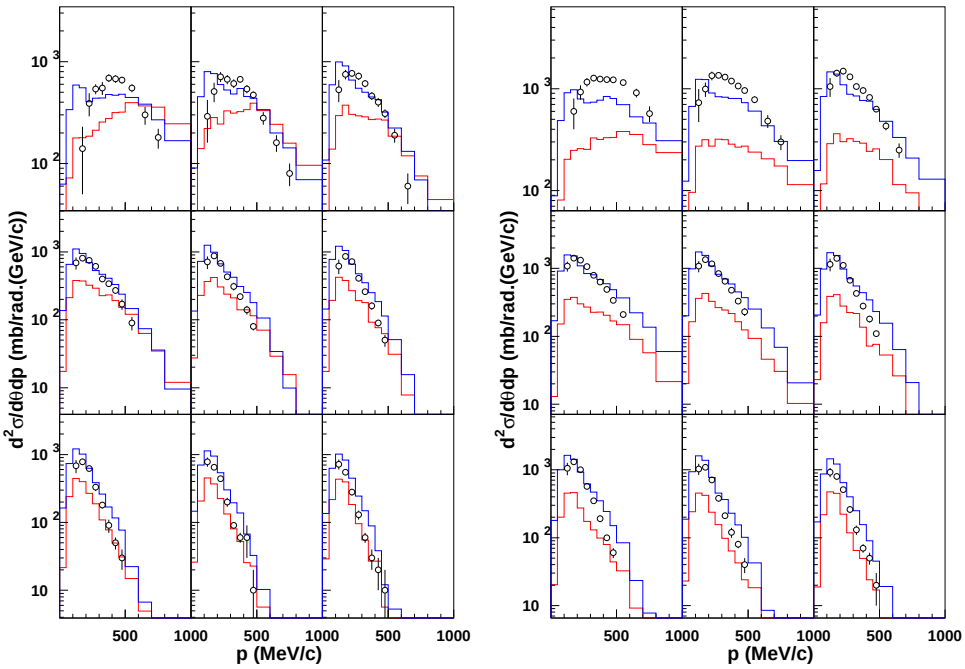

(a) p (3 GeV/c) + Ta $\rightarrow$ π^+

(b) p (5 GeV/c) + Ta $\rightarrow$ π^+

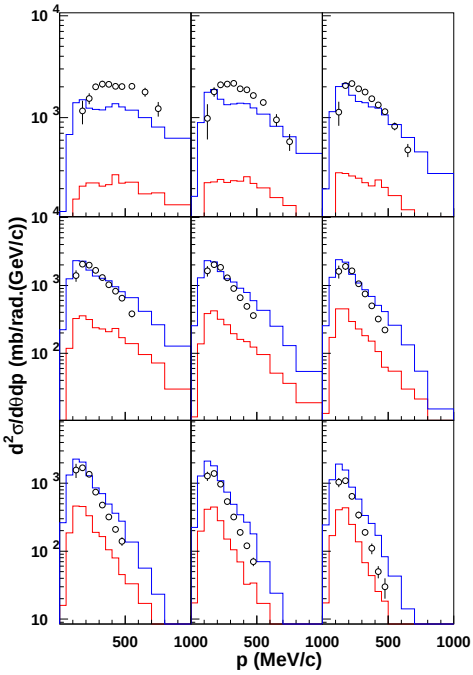

(c) p (8 GeV/c) + Ta $\rightarrow$ π^+

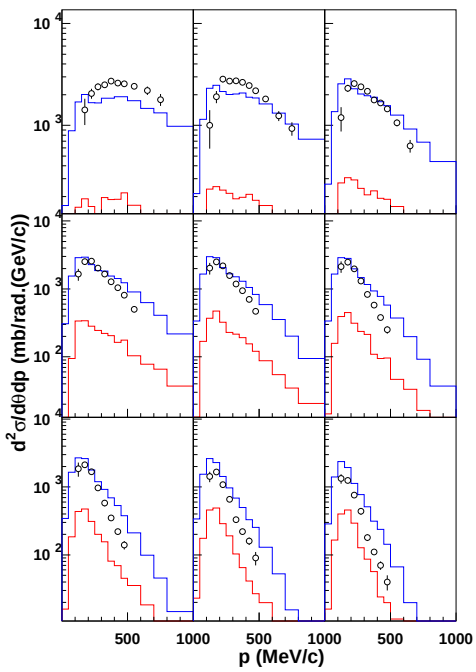

(d) p (12 GeV/c) + Ta $\rightarrow$ π^+

Figure D.10: *Double-differential cross sections for π^+ production in proton-induced reactions on Ta at 3 GeV/c (a), 5 GeV/c (b), 8 GeV/c (c) and 12 GeV/c (d) incident momentum. Data (symbols) from Refs. [11, 83] are compared with the standard version (red lines) and the improved version (blue lines) of the INCL4 model (standard INCL4.2 version plus implementation of direct multipion production).*

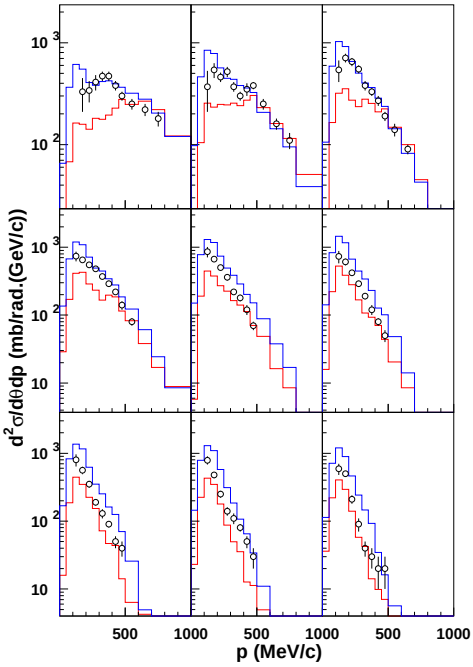

(a) p (3 GeV/c) + Ta $\rightarrow$ π^-

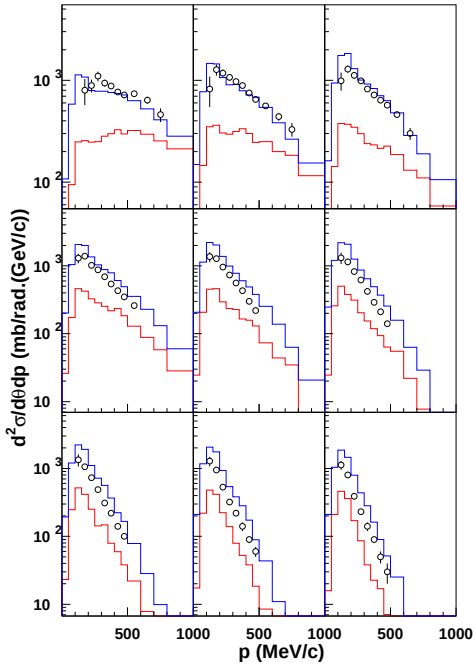

(b) p (5 GeV/c) + Ta $\rightarrow$ π^-

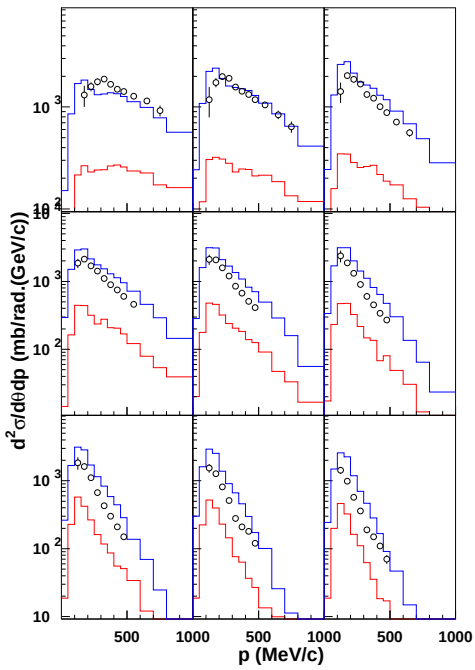

(c) p (8 GeV/c) + Ta $\rightarrow$ π^-

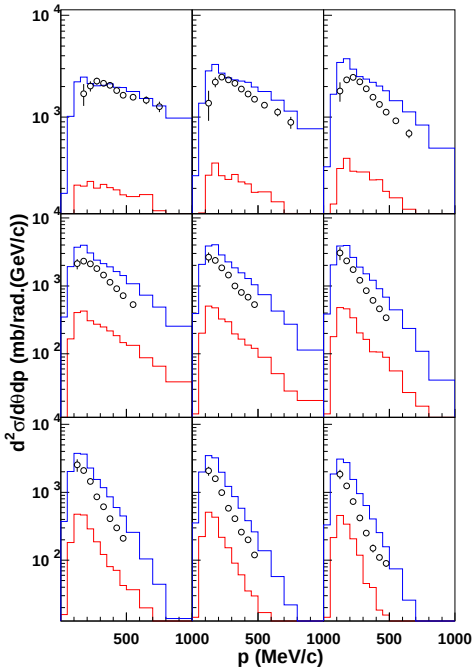

(d) p (12 GeV/c) + Ta $\rightarrow$ π^-

Figure D.11: *Double-differential cross sections for π^- production in proton-induced reactions on Ta at 3 GeV/c (a), 5 GeV/c (b), 8 GeV/c (c) and 12 GeV/c (d) incident momentum. Data (symbols) from Refs. [11, 83] are compared with the standard version (red lines) and the improved version (blue lines) of the INCL4 model (standard INCL4.2 version plus implementation of direct multipion production).*

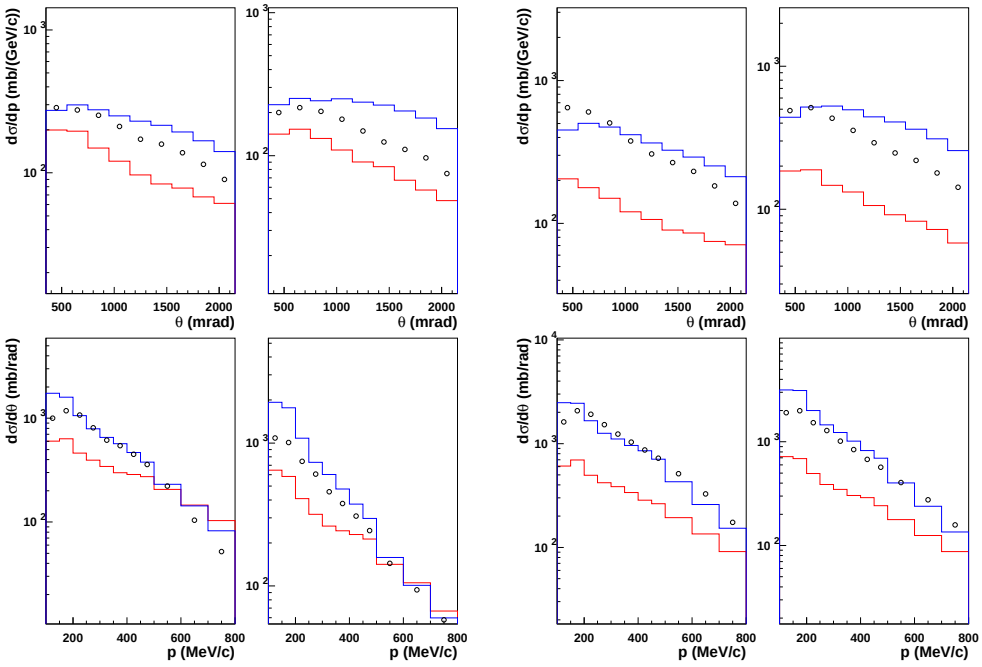

(a) p (3 GeV/c) + Ta (b) p (5 GeV/c) + Ta

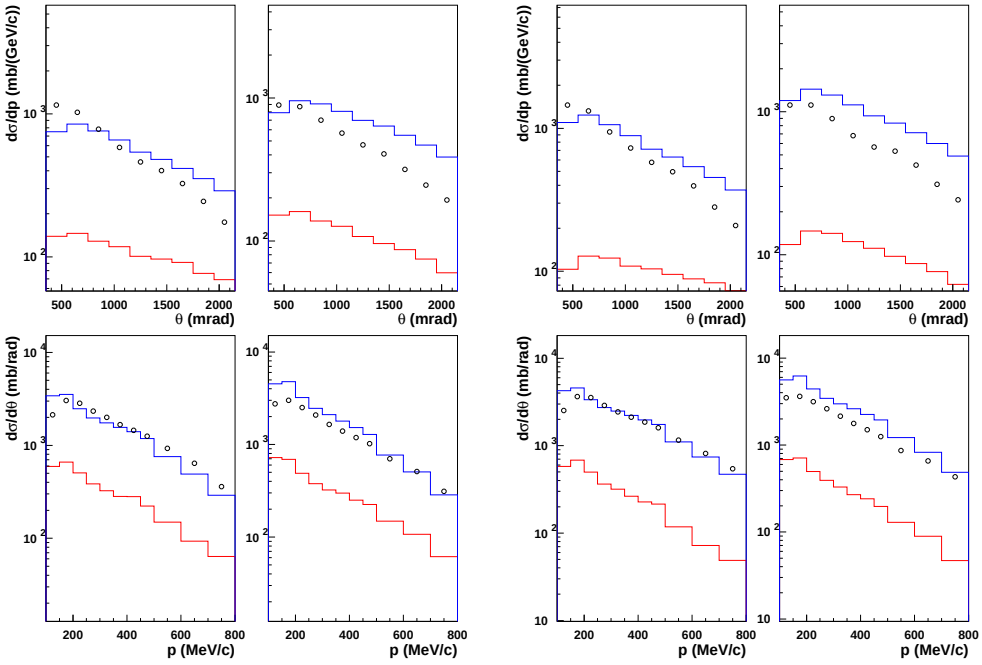

(c) p (8 GeV/c) + Ta (d) p (12 GeV/c) + Ta

Figure D.12: *Simple-differential cross section in proton-induced reactions on Ta target at 3 GeV/c (a), 5 GeV/c (b), 8 GeV/c (c) and 12 GeV/c (d) incident momentum. Each panel is divided in four, corresponding to the integration of the π^+ production (left column of the panel) double-differential cross sections or the π^- production (right column of the panel) double-differential cross sections of the HARP experiment Ref. [11, 83] over the momentum domain (upper part of the panel) or over the angular domain (lower part of the panel) presented in Tab. D.1. The date are represented by the circles and are compared with INCL HE (blue line).*

D.2.2 Forward angle double-differential cross sections

The angular domain for the measurements realized at forward angle spreads from 50 to 250 mrad, decomposed in 4 bins of 50 mrad each. The momentum acceptance spreads from 0.5 GeV/c to 8 GeV/c. The momentum bin sizes are:

$$\Delta p_j = \begin{cases} 0.5 \text{ GeV}/c & \text{if } 0.5 < p < 4 \text{ GeV}/c \\ 1 \text{ GeV}/c & \text{if } 4 < p < 5 \text{ GeV}/c \\ 1.5 \text{ GeV}/c & \text{if } 5 < p < 8 \text{ GeV}/c \end{cases} \tag{D.3}$$

Figures D.13 to D.16 show the comparison between data from the HARP experiment (symbols) and simulations realized with the extended version of INCL4.2 (red lines) for a Be target, an Al target, a Sn target and a Ta target, respectively.

Each figure stands for a single target and is decomposed in four panels. Each panel corresponds to a separate incident momentum of the proton (3 GeV/c in panel (a), 5 GeV/c in panel (b), 8 GeV/c in panel (c) and 12 GeV/c in panel (d)). Each panel has two separate part, one for the π^+ production (left part) and one for the π^- production (right part). Finally, the different type of lines corresponds to the different angular bins:

- solid lines corresponds to 50–100 mrad,
- dashed lines corresponds to 100–150 mrad,
- dotted lines corresponds to 150–200 mrad,
- dash-dotted lines corresponds to 200–250 mrad.

The comparisons concerning C, Cu and Pb targets have been presented in Chapter 6.

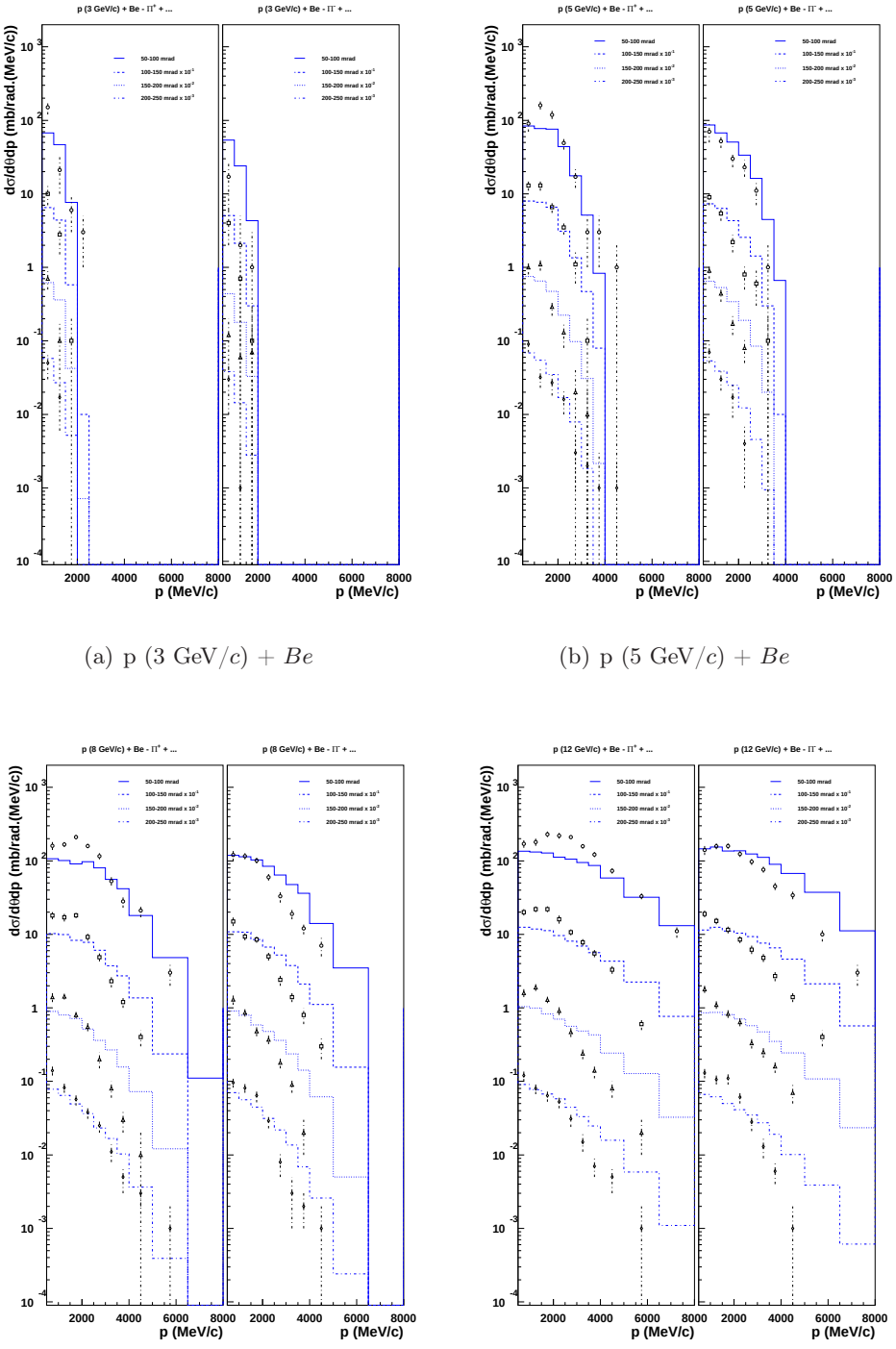

(a) p (3 GeV/c) + Be

(b) p (5 GeV/c) + Be

(c) p (8 GeV/c) + Be

(d) p (12 GeV/c) + Be

Figure D.13: *Double-differential cross sections for the π^+ production π^+ (left part of each panels) and π^- (right part of each panels) in proton-induced reactions on Be target. Data (symbols) from Ref. [12] are compared with the improved version (blue lines) of INCL4. The different lines correspond to the indicated angular bins by the legend. The panels correspond to the indicated incident momenta.*

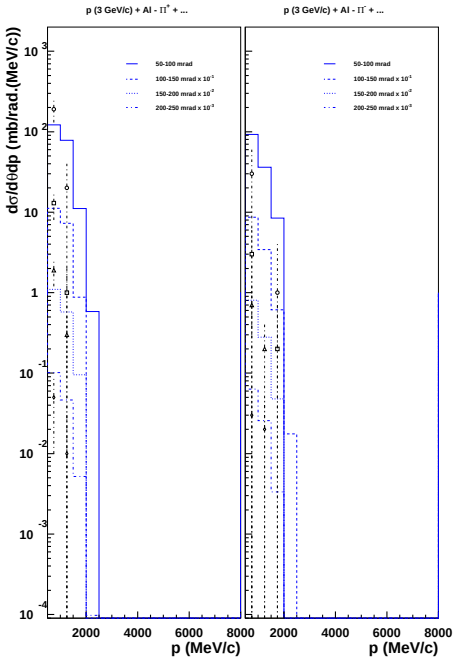

(a) p (3 GeV/c) + Al

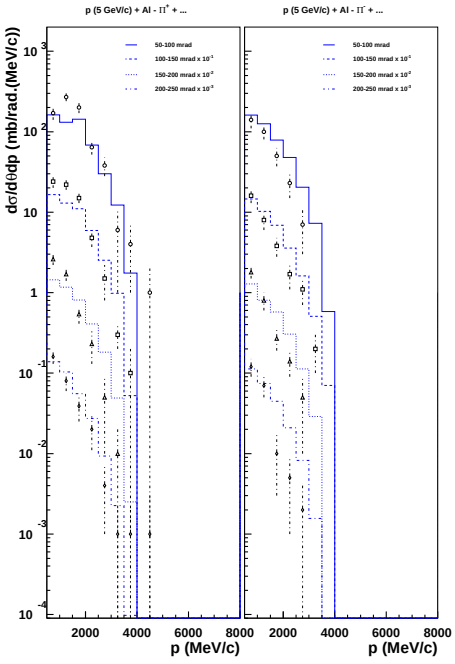

(b) p (5 GeV/c) + Al

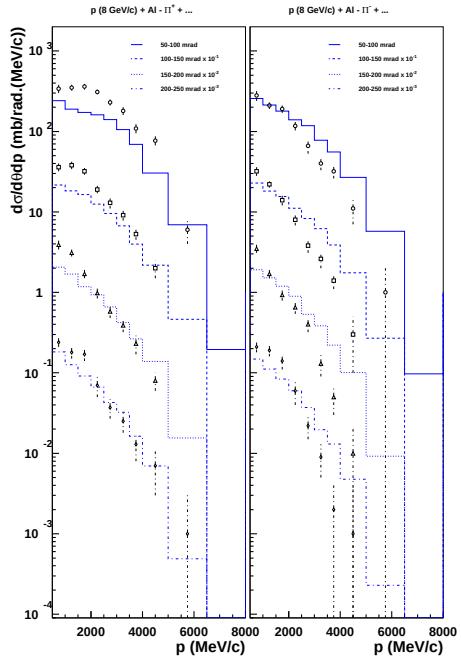

(c) p (8 GeV/c) + Al

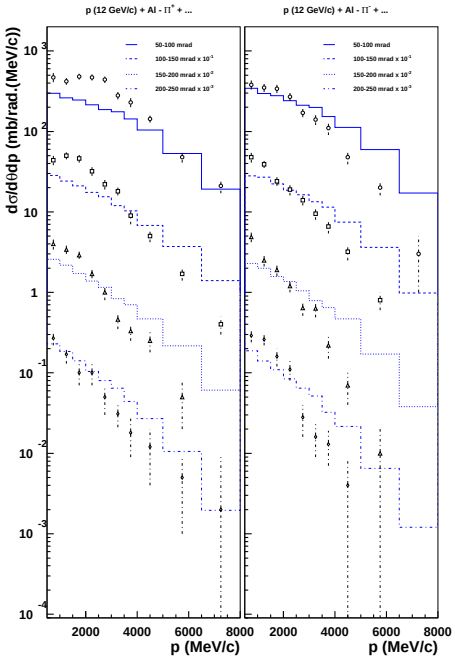

(d) p (12 GeV/c) + Al

Figure D.14: *Same as Figure D.13 for an Al target. Data are from Ref. [12].*

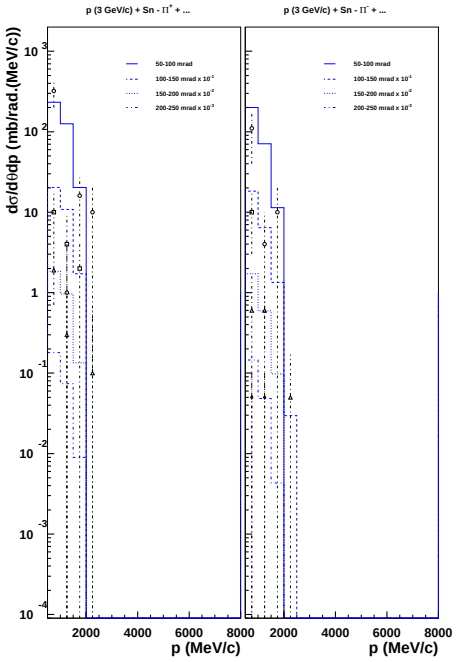

(a) p (3 GeV/c) + Sn

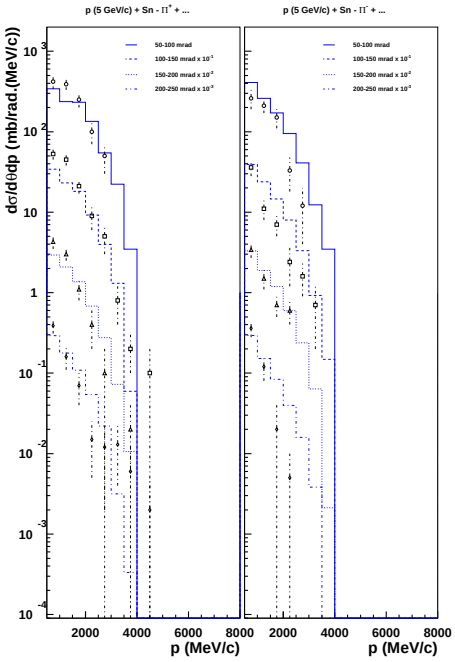

(b) p (5 GeV/c) + Sn

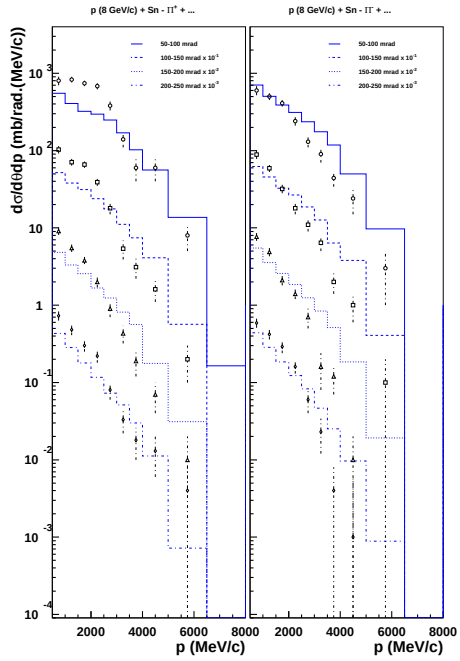

(c) p (8 GeV/c) + Sn

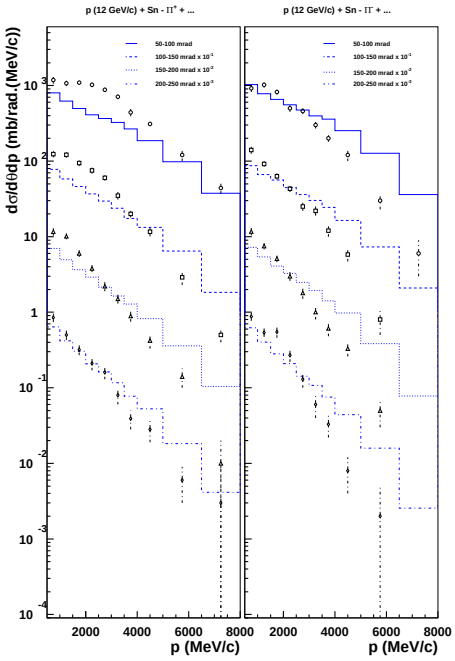

(d) p (12 GeV/c) + Sn

Figure D.15: *Same as Figure D.13 for a Sn target. Data are from Ref. [12].*

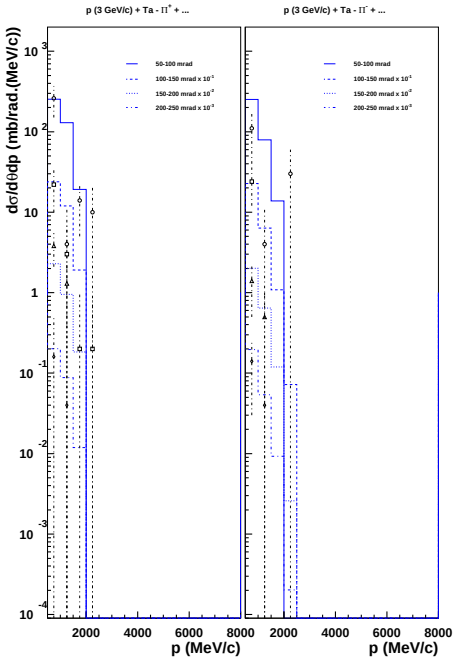

(a) p (3 GeV/c) + Ta

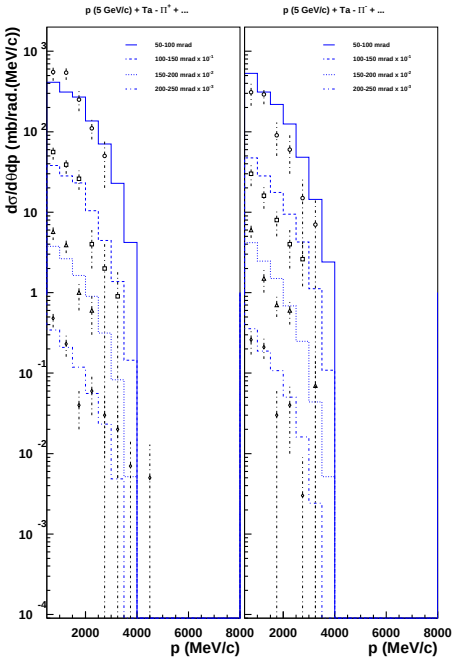

(b) p (5 GeV/c) + Ta

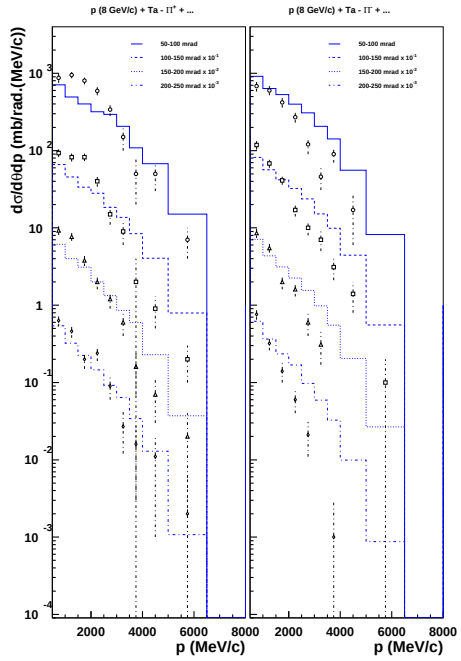

(c) p (8 GeV/c) + Ta

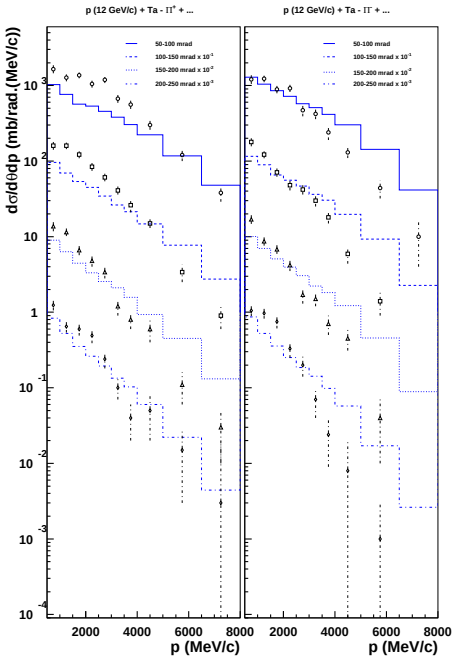

(d) p (12 GeV/c) + Ta

Figure D.16: *Same as Figure D.13 for a Ta target. Data are from Ref. [12].*

D.3 Double-differential cross sections for large-angle pion production in charged pion-induced reactions

The measures at large angle are realized in an angular domain spreading from 350 to 2150 mrad, decomposed in 9 bins of 200 mrad each. The momentum acceptance and the momentum bin size is the same as for proton-induced reactions; they are summarized in Tab. D.1 and Eq. D.2.

The figures are organized exactly as for proton-induced reaction: each figure is divided in four panels, one for each incident momentum of the proton (3 GeV/c in panel (a), 5 GeV/c in panel (b), 8 GeV/c in panel (c) and 12 GeV/c in panel (d)). In turn, each panel is divided in nine parts, each of them corresponding to a different angular bin in the experiments. The values of these angular bins are the same as for proton-induced reactions and are summarized in Table 6.2.

D.3.1 Positively charged pion as projectile

Figures D.17 to D.19 show the comparison between data from the HARP experiment (symbols) and simulations realized with the extended version of INCL4.2 (blue lines) for a Be target with four positively charged pion projectile momentum (3 GeV/c, 5 GeV/c, 8 GeV/c and 12 GeV/c). The following figures show the same comparison for different targets: carbon (Figs. D.20 to D.21), aluminium (Figs. D.22 to D.24), copper (Figs. D.25 to D.26), tin (Figs. D.27 to D.29), tantalum (Figs. D.30 to D.32) and lead (Figs. D.33 to D.34).

For each target, comparisons for π^+ and π^- production double-differential cross section and simple-differential cross sections after integration over the angular domain and the momentum domain are shown.

In the case of the C, Cu and Pb targets, only two values of the projectile incident momentum are considered here (3 and 8 GeV/c), the figures for other values of the projectile momentum have been presented in Chapter 6.

D.3.2 Negatively charged pion as projectile

Figures D.35 to D.37 show the comparison between data from the HARP experiment (symbols) and simulations realized with the extended version of INCL4.2 (blue lines) for a Be target with four π^- projectile momentum (3 GeV/c, 5 GeV/c, 8 GeV/c and 12 GeV/c). The following figures show the same comparison for different targets: carbon (Figs. D.38 to D.39), aluminium (Figs. D.40 to D.42), copper (Figs. D.43 to D.44), tin (Figs. D.45 to D.47), tantalum (Figs. D.48 to D.50) and lead (Figs. D.51 to D.52).

For each target, comparisons for double-differential cross section for positive pion production and negative pion production and simple-differential cross sections after integration over the angular domain and the momentum domain are shown.

In the case of the C, Cu and Pb targets, only two values of the projectile incident momentum are considered here (3 and 8 GeV/c), the figures for other values of the projectile momentum have been presented in Chapter 6.

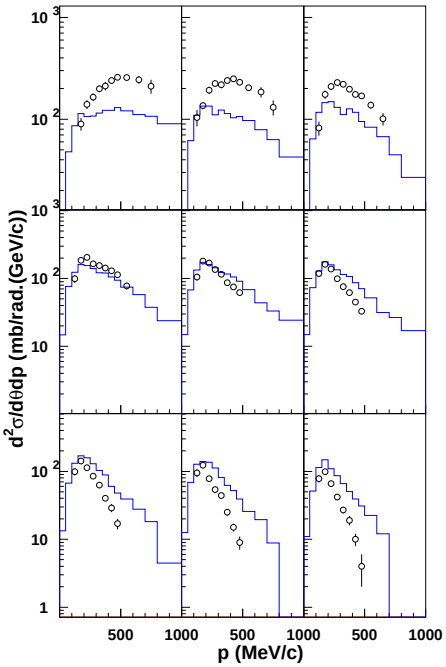

(a) π^+ (3 GeV/c) + Be $\rightarrow$ π^+

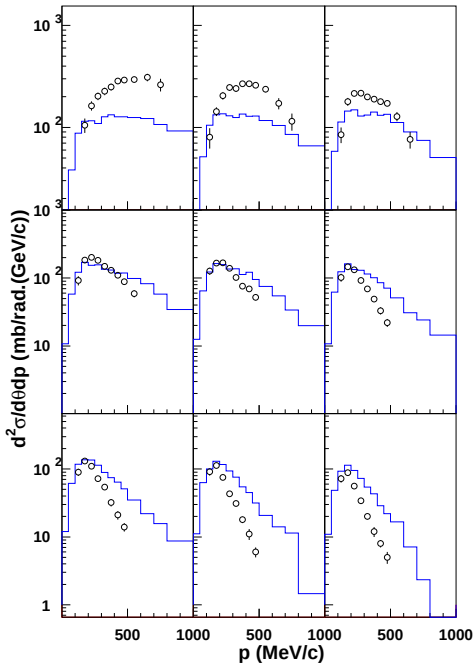

(b) π^+ (5 GeV/c) + Be $\rightarrow$ π^+

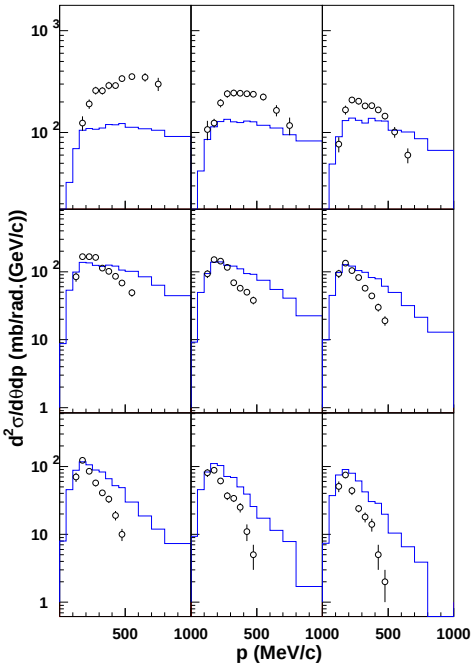

(c) π^+ (8 GeV/c) + Be $\rightarrow$ π^+

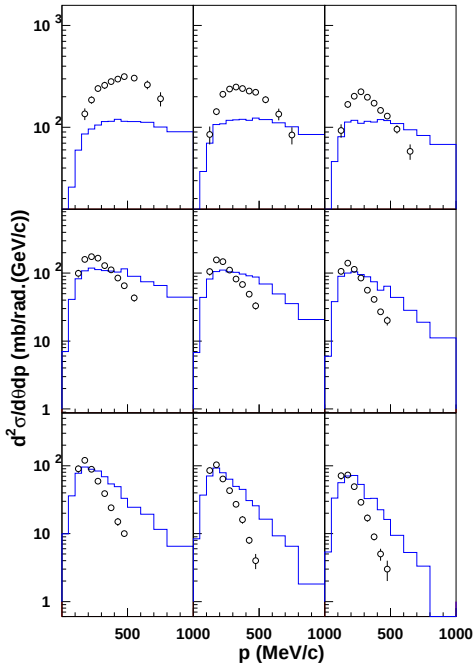

(d) π^+ (12 GeV/c) + Be $\rightarrow$ π^+

Figure D.17: *Double-differential cross sections for the π^+ production in π^+-induced reactions on Be at 3 GeV/c (a), 5 GeV/c (b), 8 GeV/c (c) and 12 GeV/c (d) incident momentum. Data (symbols) from Refs. [13] are compared with the improved version of INCL4.2 (blue lines).*

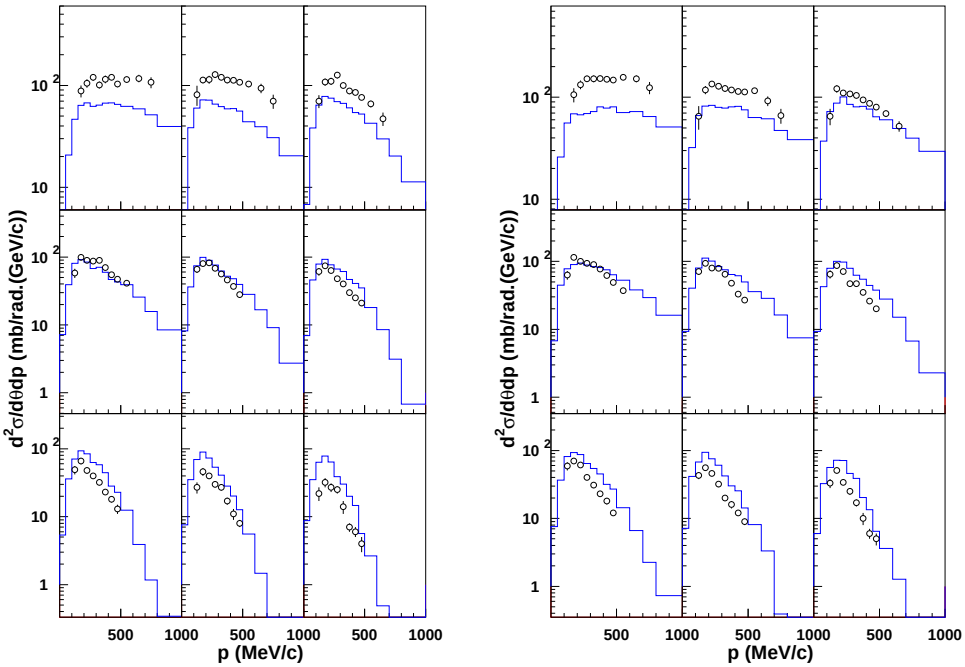

(a) π^+ (3 GeV/c) + Be $\rightarrow$ π^- (b) π^+ (5 GeV/c) + Be $\rightarrow$ π^-

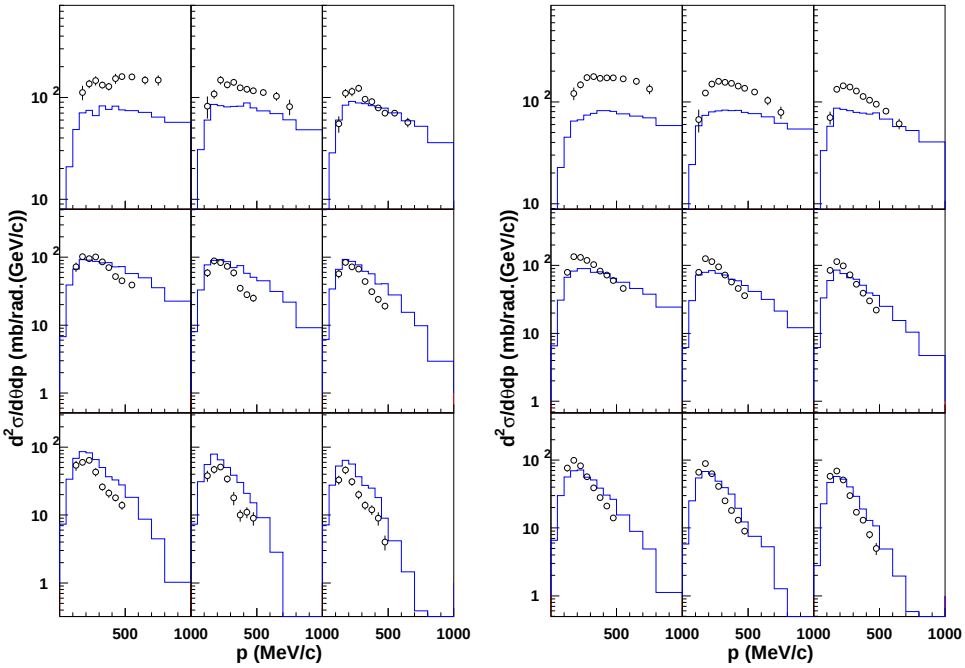

(c) π^+ (8 GeV/c) + Be $\rightarrow$ π^- (d) π^+ (12 GeV/c) + Be $\rightarrow$ π^-

Figure D.18: *Double-differential cross sections for the π^- production in π^+-induced reactions on Be at 3 GeV/c (a), 5 GeV/c (b), 8 GeV/c (c) and 12 GeV/c (d) incident momentum. Data (symbols) from Refs. [13] are compared with the improved version of INCL4.2 (blue lines).*

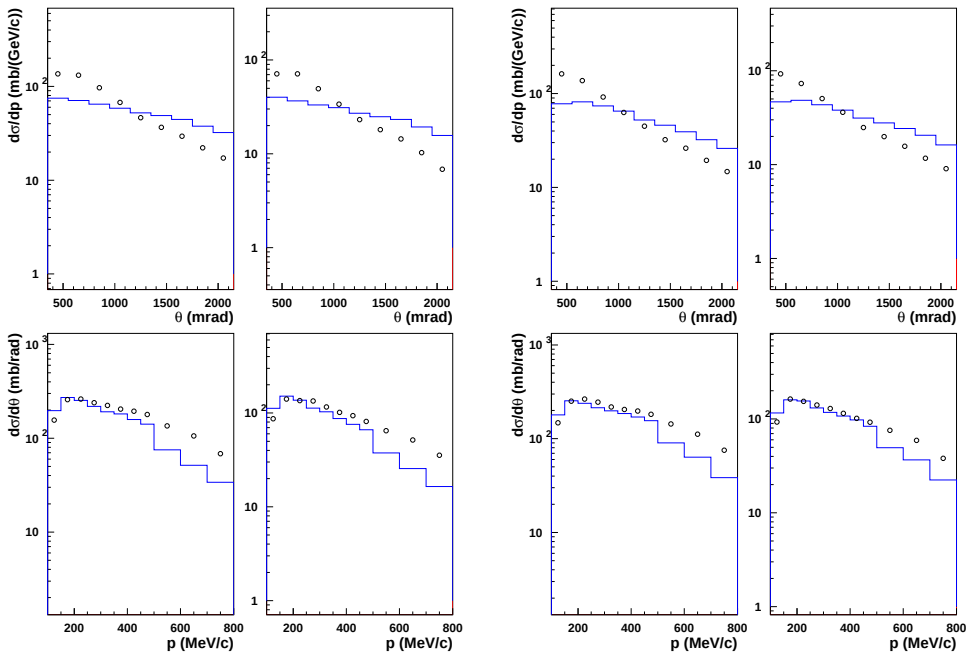

(a) π^+ (3 GeV/c) + Be (b) π^+ (5 GeV/c) + Be

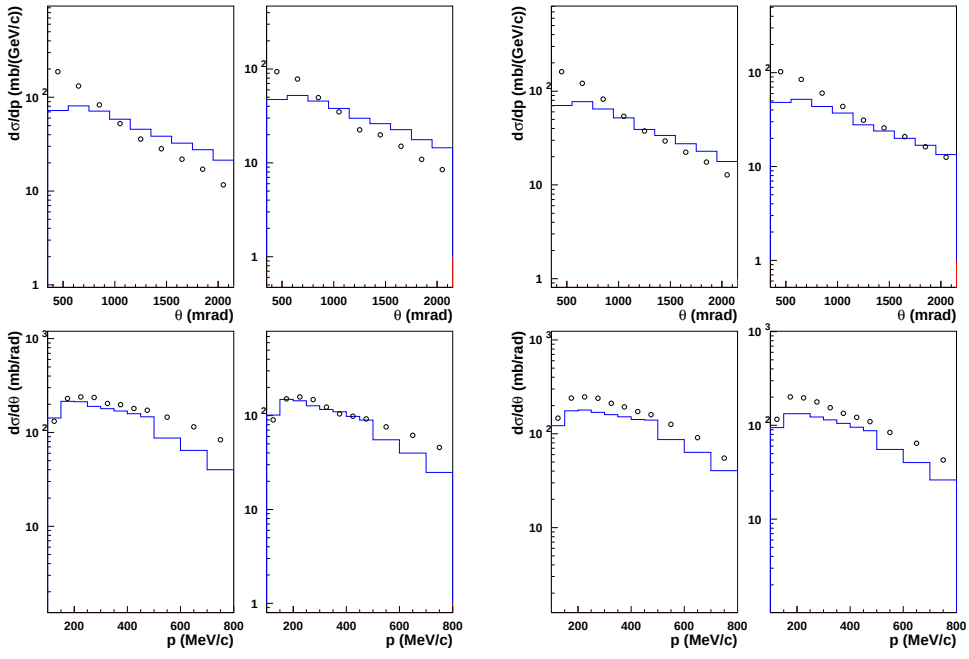

(c) π^+ (8 GeV/c) + Be (d) π^+ (12 GeV/c) + Be

Figure D.19: *Simple-differential cross section in π^+-induced reactions on Be target at 3 GeV/c (a), 5 GeV/c (b), 8 GeV/c (c) and 12 GeV/c (d) incident momentum. Each panel is divided in four, corresponding to the integration of the π^+ production (left column of the panel) double-differential cross sections or the π^- production (right column of the panel) double-differential cross sections of the HARP experiment Ref. [13] over the momentum domain (upper part of the panel) or over the angular domain (lower part of the panel) presented in Tab. D.1. The data (symbols) are compared with the improved version of the INCL4 model (blue lines).*

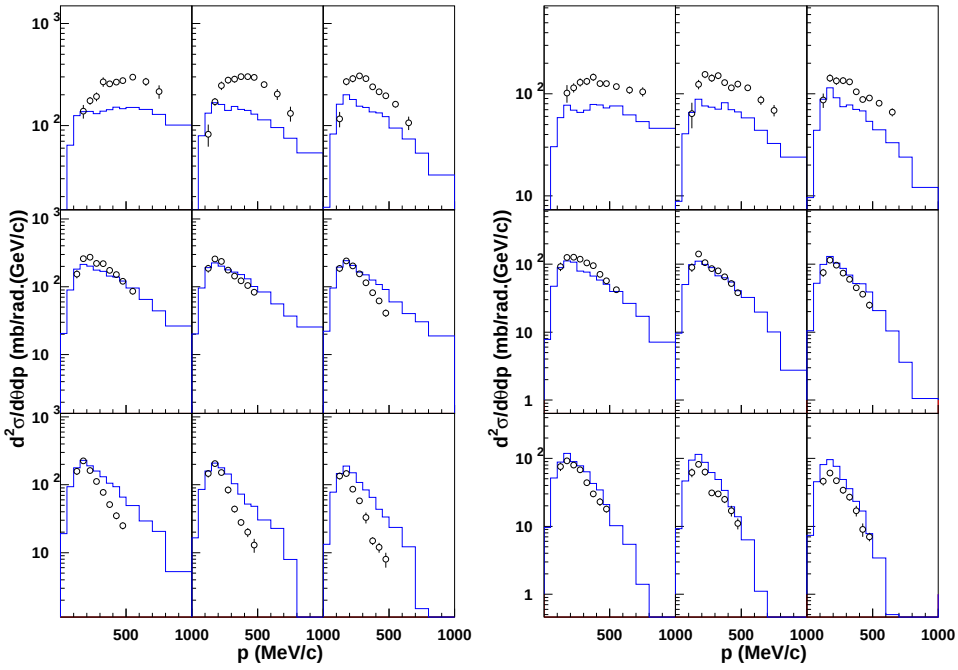

(a) π^+ (3 GeV/c) + C $\rightarrow$ π^+ (b) π^+ (3 GeV/c) + C $\rightarrow$ π^-

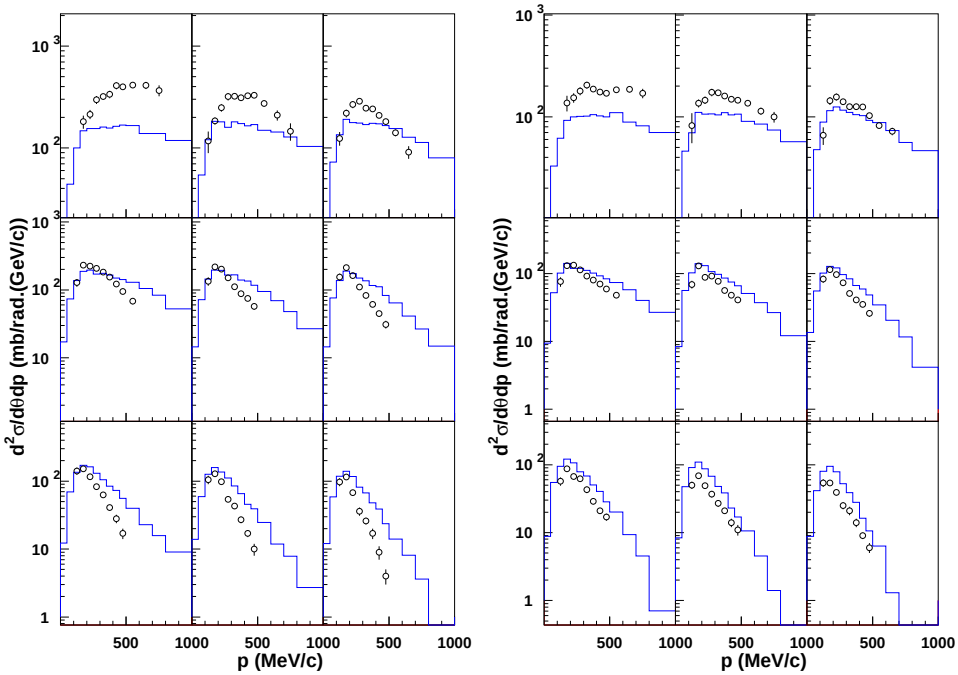

(c) π^+ (8 GeV/c) + C $\rightarrow$ π^+ (d) π^+ (8 GeV/c) + C $\rightarrow$ π^-

Figure D.20: *Double-differential cross sections for π^+ production (a,c) and π^- production (b,d) in π^+-induced reactions on C at 3 GeV/c (a,b) and 8 GeV/c (c,d) incident momentum. Data (symbols) from Ref. [13] are compared with the improved version of the INCL4 model (blue lines).*

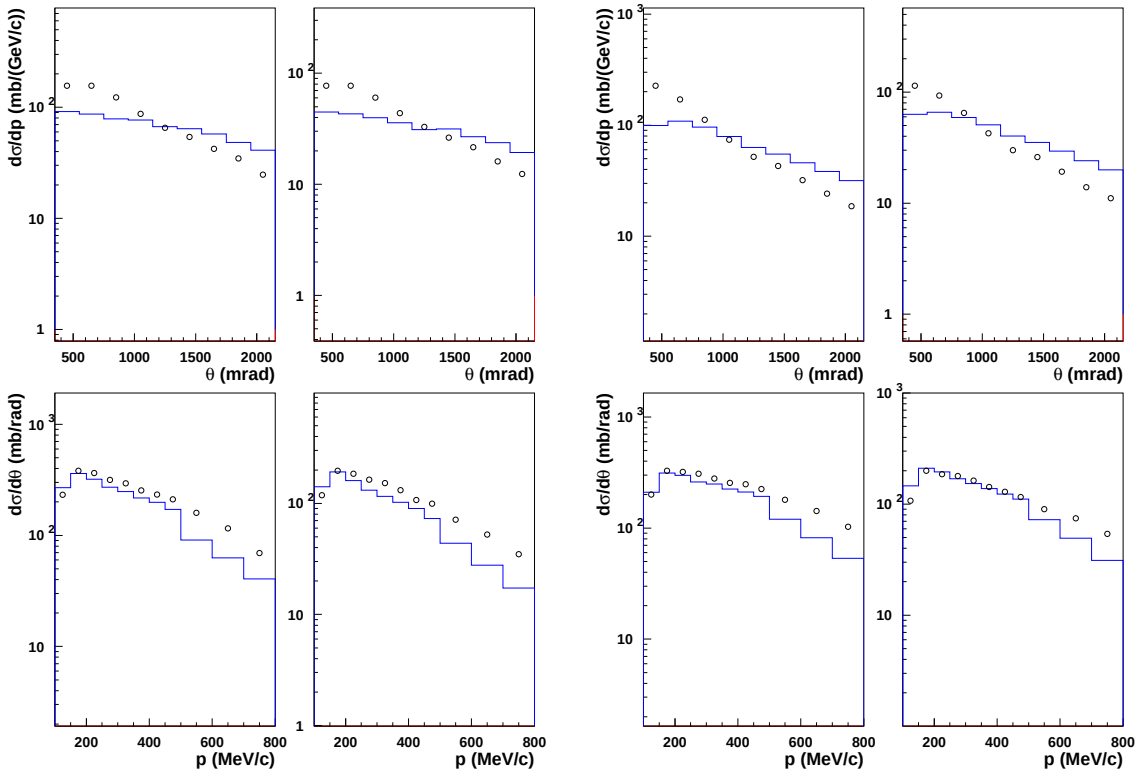

(a) π^+ (3 GeV/c) + C (b) π^+ (8 GeV/c) + C

Figure D.21: *Simple-differential cross section in π^+-induced reactions on C target at 3 GeV/c (a) and 8 GeV/c (b) incident momentum. The data are obtained by integrating the double-differential cross sections of the HARP experiment over the angular domain or over the momentum domain (presented in Tab. D.1). Data (symbols) from Ref. [13] are compared with the improved version of INCL4 (blue lines).*

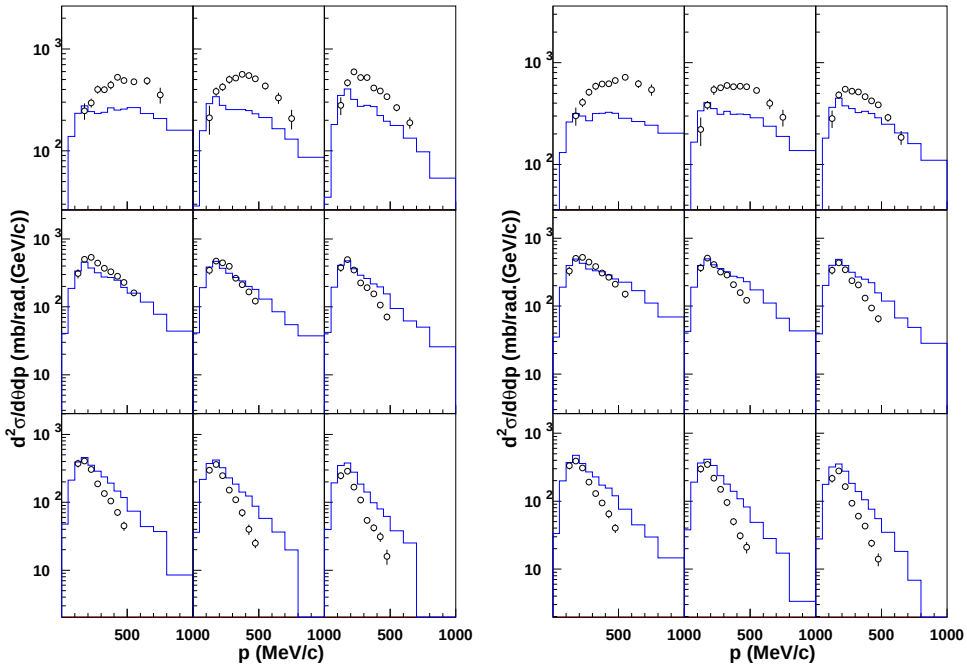

(a) π^+ (3 GeV/c) + Al $\rightarrow$ π^+

(b) π^+ (5 GeV/c) + Al $\rightarrow$ π^+

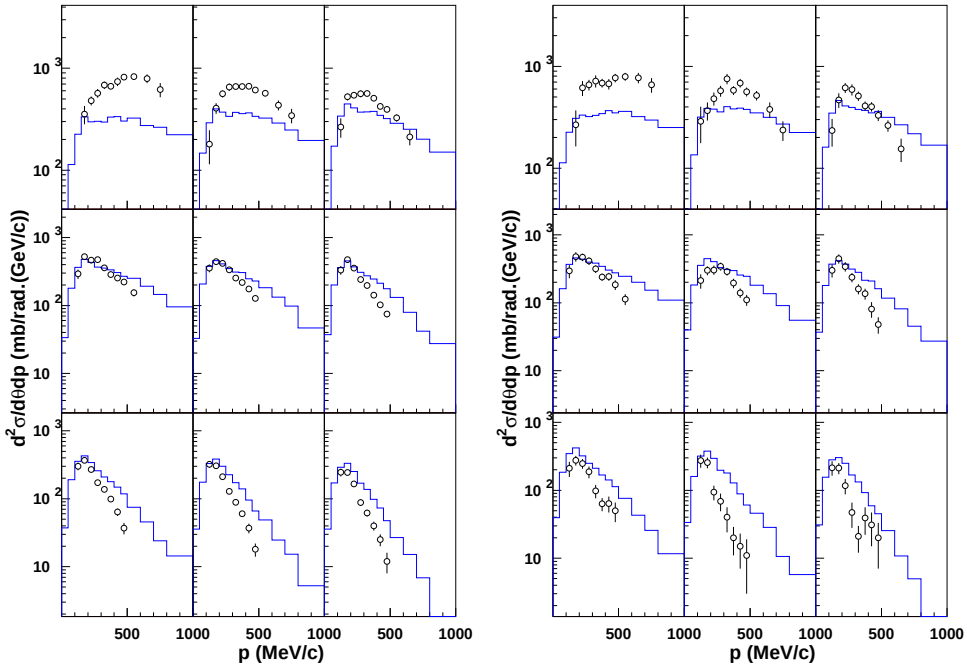

(c) π^+ (8 GeV/c) + Al $\rightarrow$ π^+

(d) π^+ (12 GeV/c) + Al $\rightarrow$ π^+

Figure D.22: *Double-differential cross sections for the π^+ production in π^+-induced reactions on Al at 3 GeV/c (a), 5 GeV/c (b), 8 GeV/c (c) and 12 GeV/c (d) incident momentum. Data (symbols) from Refs. [13] are compared with the improved version of INCL4.2 (blue lines).*

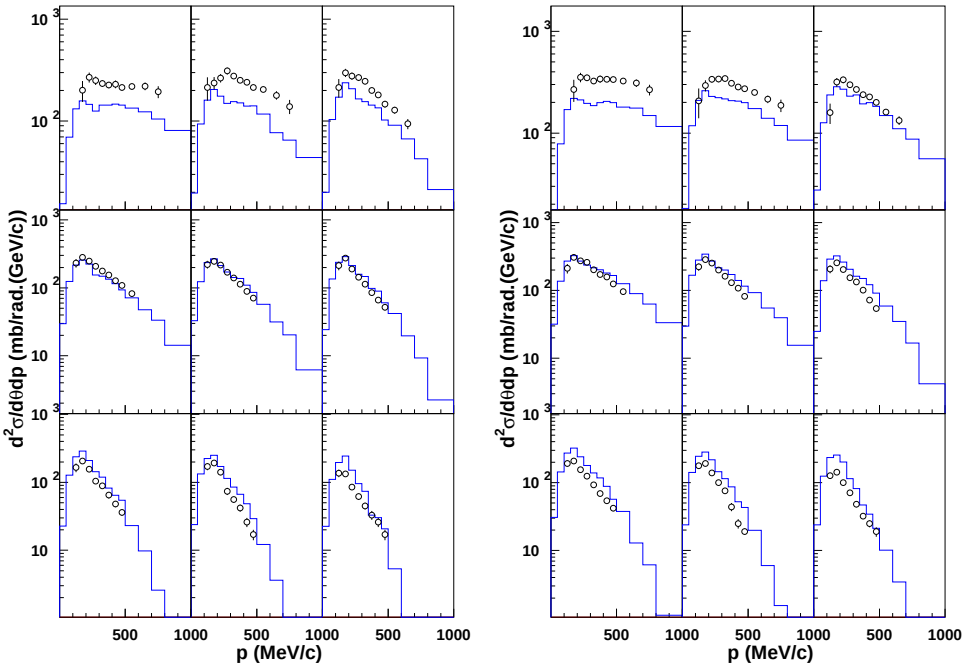

(a) π^+ (3 GeV/c) + Al $\rightarrow$ π^-

(b) π^+ (5 GeV/c) + Al $\rightarrow$ π^-

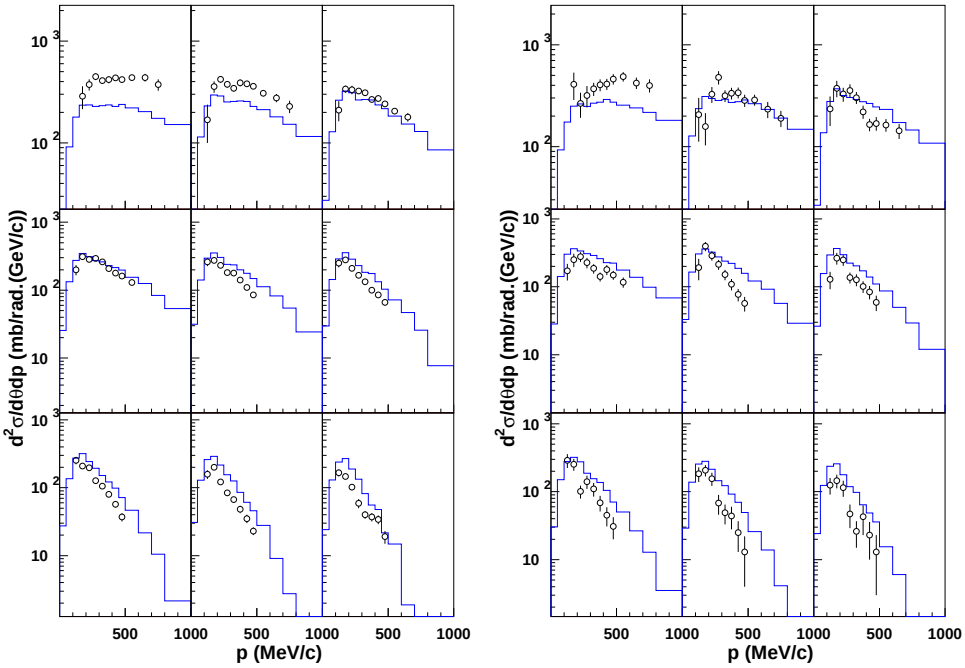

(c) π^+ (8 GeV/c) + Al $\rightarrow$ π^-

(d) π^+ (12 GeV/c) + Al $\rightarrow$ π^-

Figure D.23: *Double-differential cross sections for the π^- production in π^+-induced reactions on Al at 3 GeV/c (a), 5 GeV/c (b), 8 GeV/c (c) and 12 GeV/c (d) incident momentum. Data (symbols) from Refs. [13] are compared with the improved version of INCL4.2 (blue lines).*

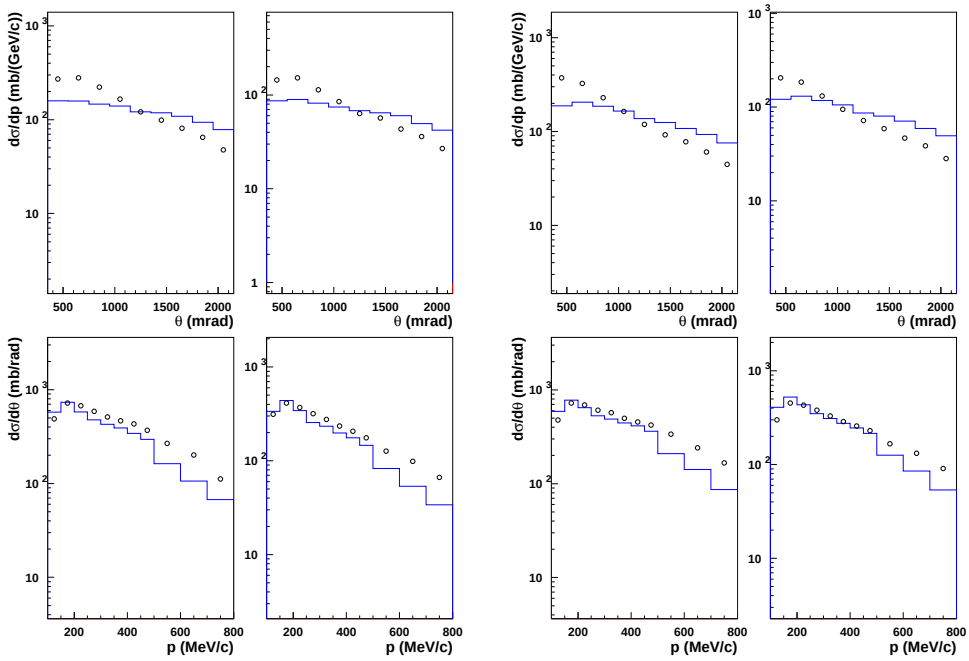

(a) π^+ (3 GeV/c) + Al (b) π^+ (5 GeV/c) + Al

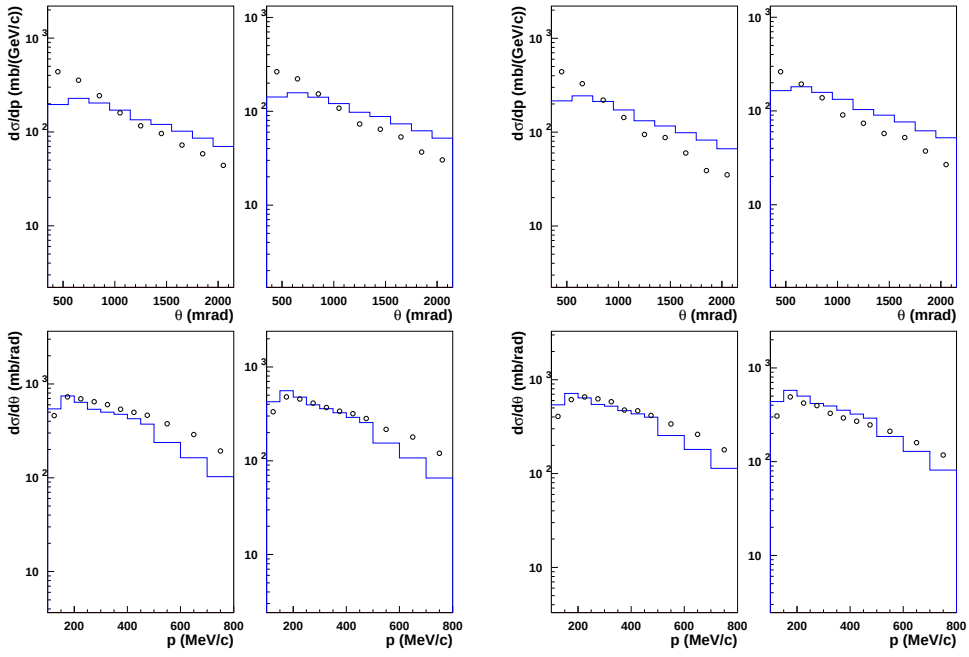

(c) π^+ (8 GeV/c) + Al (d) π^+ (12 GeV/c) + Al

Figure D.24: *Simple-differential cross section in π^+-induced reactions on Al target at 3 GeV/c (a), 5 GeV/c (b), 8 GeV/c (c) and 12 GeV/c (d) incident momentum. Each panel is divided in four, corresponding to the integration of the π^+ production (left column of the panel) double-differential cross sections or the π^- production (right column of the panel) double-differential cross sections of the HARP experiment Ref. [13] over the momentum domain (upper part of the panel) or over the angular domain (lower part of the panel) presented in Tab. D.1. The data (symbols) are compared with the improved version of the INCL4 model (blue lines).*

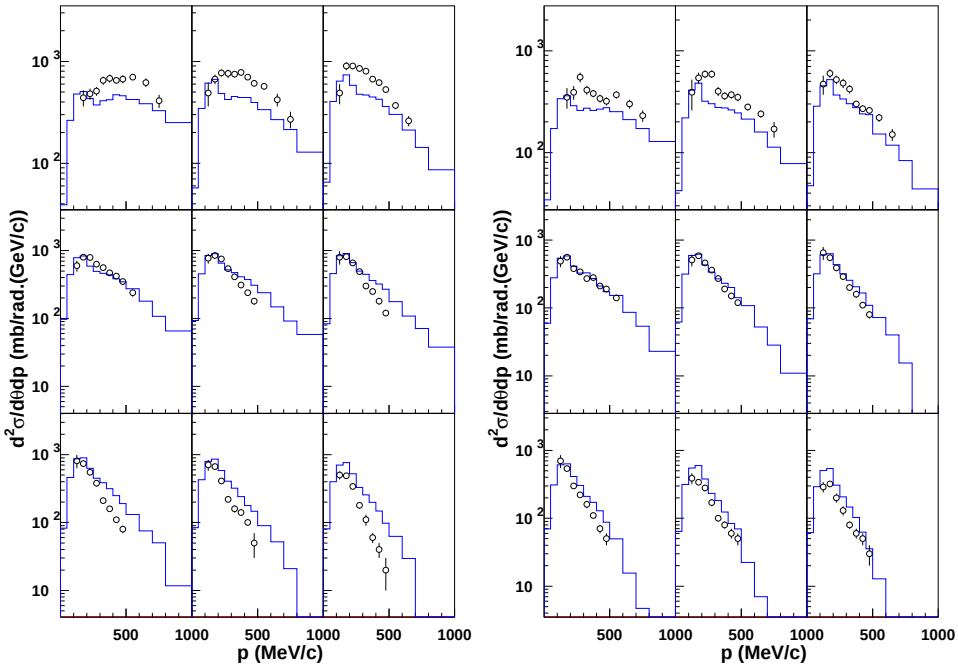

(a) π^+ (3 GeV/c) + Cu $\rightarrow$ π^+

(b) π^+ (5 GeV/c) + Cu $\rightarrow$ π^-

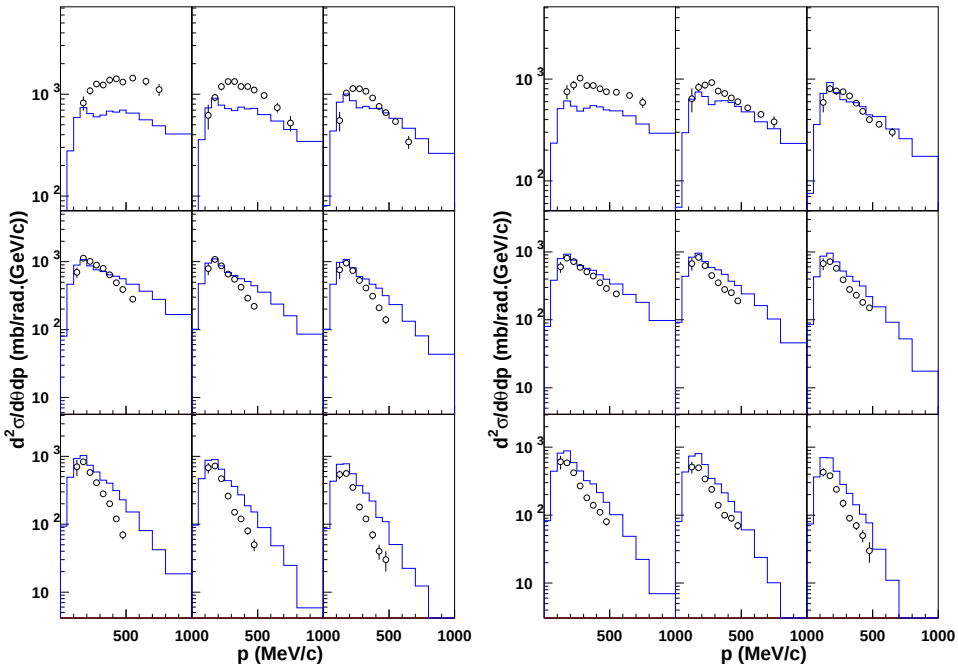

(c) π^+ (8 GeV/c) + Cu $\rightarrow$ π^+

(d) π^+ (12 GeV/c) + Cu $\rightarrow$ π^-

Figure D.25: *Double-differential cross sections for π^+ production (a,c) and π^- production (b,d) in π^+-induced reactions on Cu at 3 GeV/c (a,b) and 8 GeV/c (c,d) incident momentum. Data (symbols) from Ref. [13] are compared with the improved version of the INCL4 model (blue lines).*

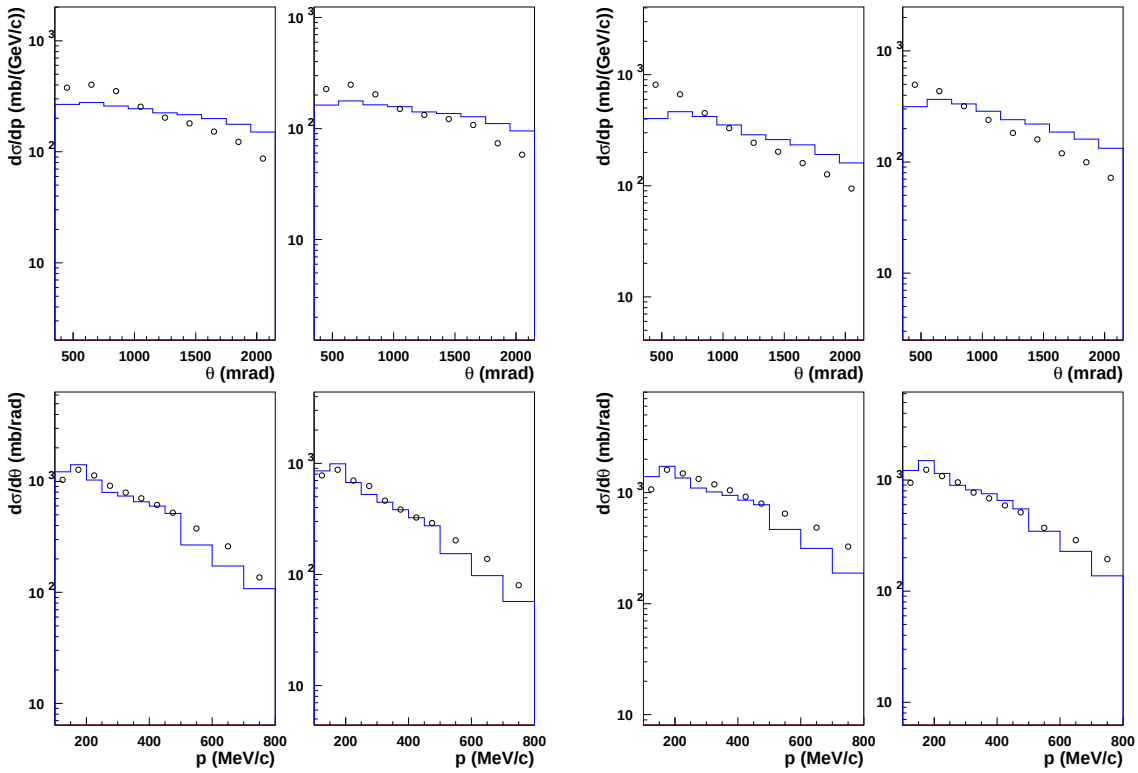

(a) π^+ (3 GeV/c) + Cu (b) π^+ (8 GeV/c) + Cu

Figure D.26: *Simple-differential cross section in π^+-induced reactions on Cu target at 3 GeV/c (a) and 8 GeV/c (b) incident momentum. The data are obtained by integrating the double-differential cross sections of the HARP experiment over the angular domain or over the momentum domain (presented in Tab. D.1). Data (symbols) from Ref. [13] are compared with the improved version of INCL4 (blue lines).*

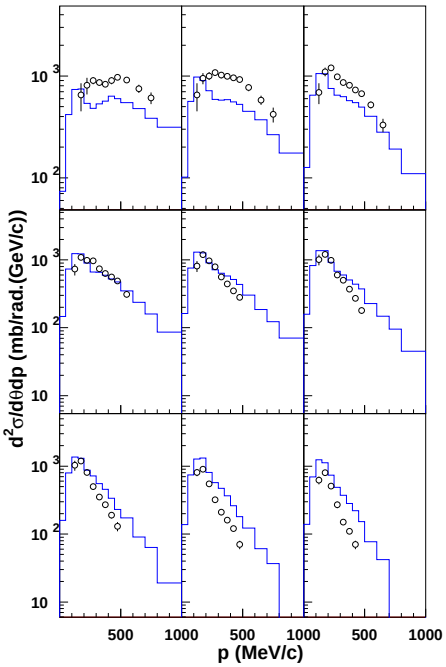

(a) π^+ (3 GeV/c) + Sn $\rightarrow$ π^+

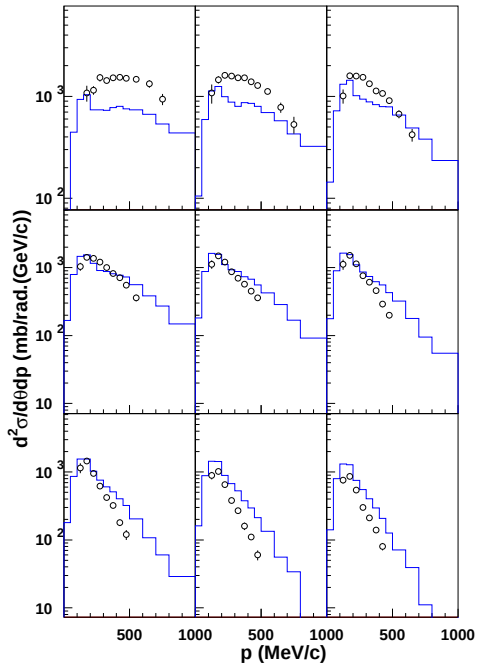

(b) π^+ (5 GeV/c) + Sn $\rightarrow$ π^+

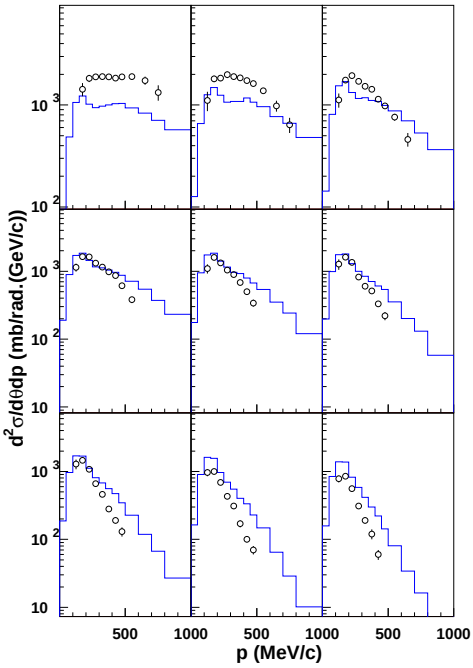

(c) π^+ (8 GeV/c) + Sn $\rightarrow$ π^+

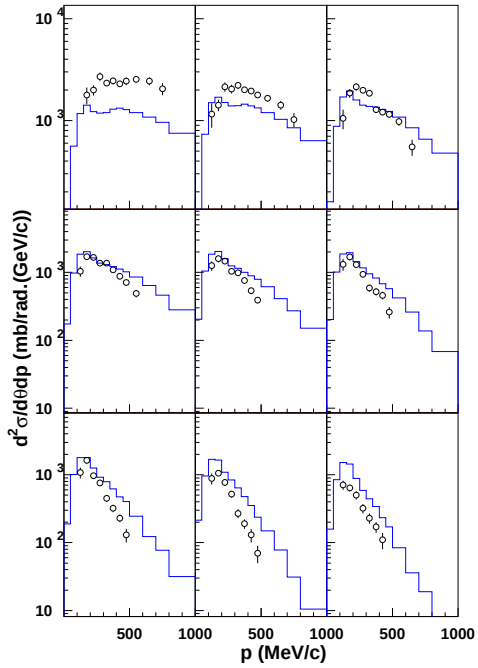

(d) π^+ (12 GeV/c) + Sn $\rightarrow$ π^+

Figure D.27: *Double-differential cross sections for the π^+ production in π^+-induced reactions on Sn at 3 GeV/c (a), 5 GeV/c (b), 8 GeV/c (c) and 12 GeV/c (d) incident momentum. Data (symbols) from Refs. [13] are compared with the improved version of INCL4.2 (blue lines).*

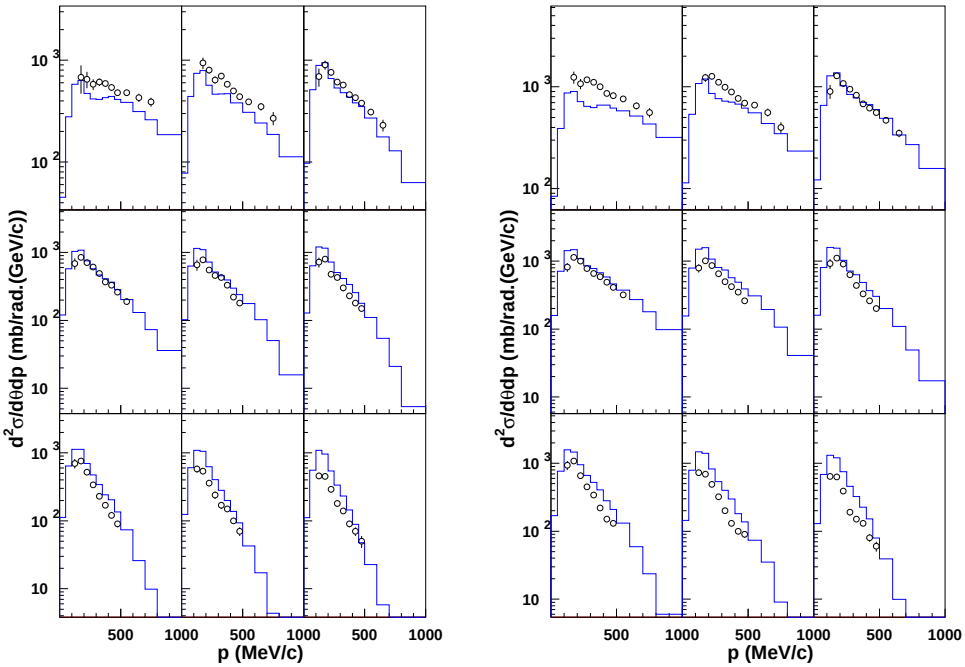

(a) π^+ (3 GeV/c) + Sn $\rightarrow$ π^-

(b) π^+ (5 GeV/c) + Sn $\rightarrow$ π^-

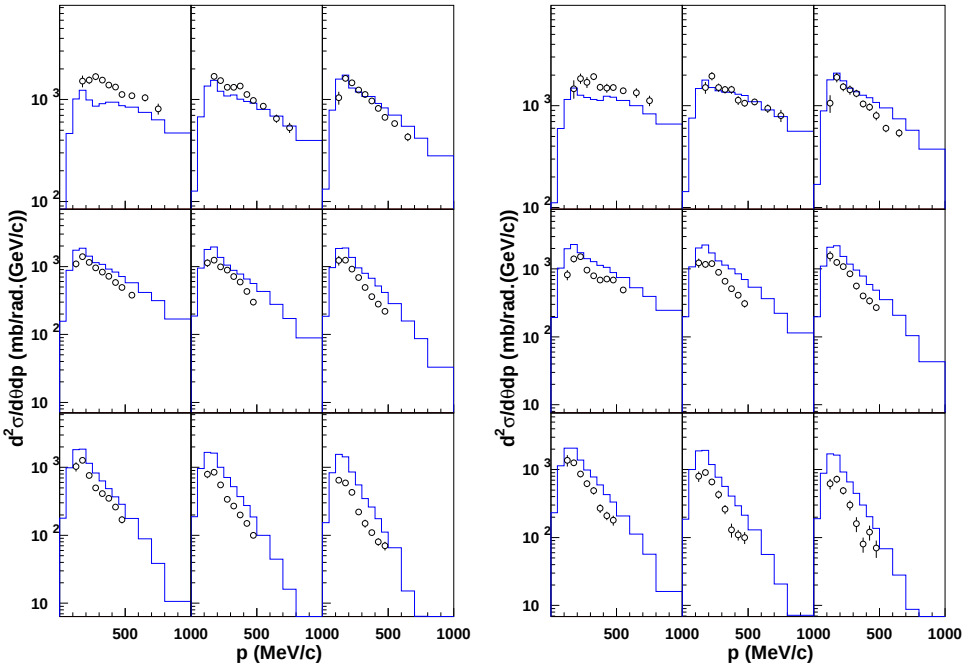

(c) π^+ (8 GeV/c) + Sn $\rightarrow$ π^-

(d) π^+ (12 GeV/c) + Sn $\rightarrow$ π^-

Figure D.28: *Double-differential cross sections for the π^- production in π^+-induced reactions on Sn at 3 GeV/c (a), 5 GeV/c (b), 8 GeV/c (c) and 12 GeV/c (d) incident momentum. Data (symbols) from Refs. [13] are compared with the improved version of INCL4.2 (blue lines).*

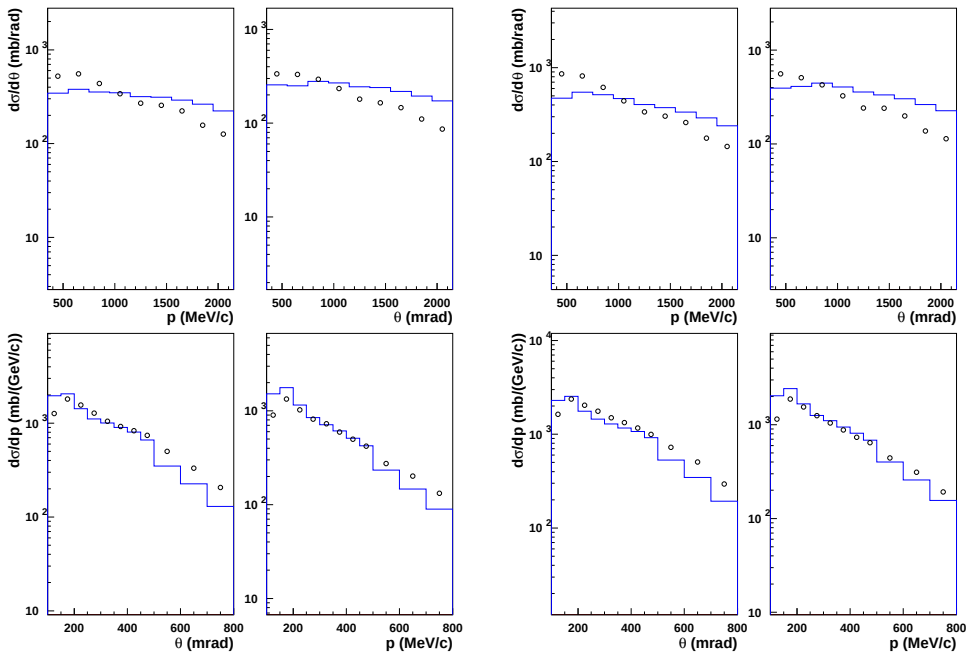

(a) π^+ (3 GeV/c) + Sn (b) π^+ (5 GeV/c) + Sn

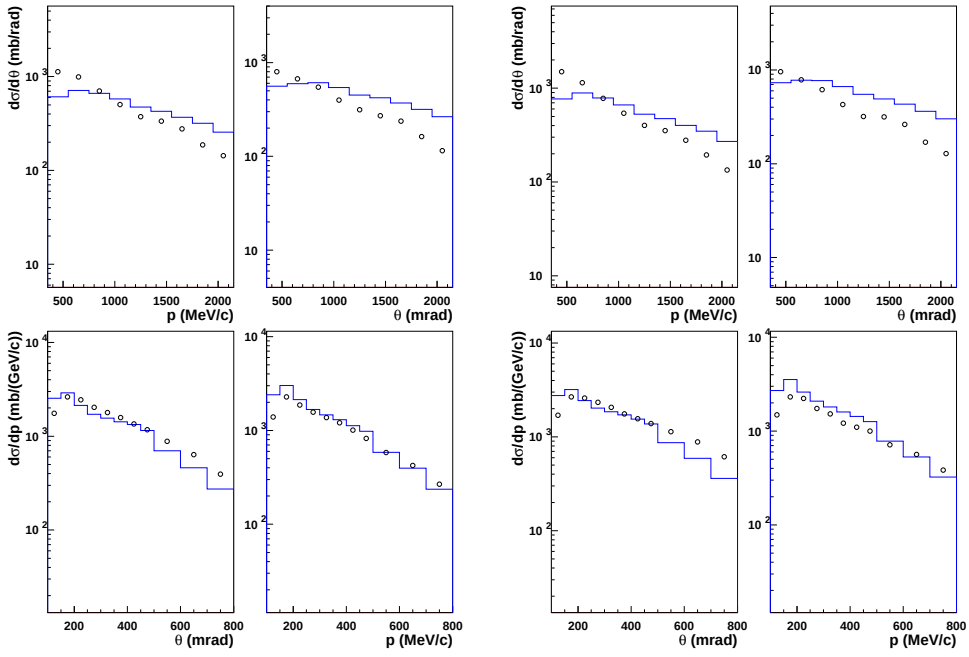

(c) π^+ (8 GeV/c) + Sn (d) π^+ (12 GeV/c) + Sn

Figure D.29: *Simple-differential cross section in π^+-induced reactions on Sn target at 3 GeV/c (a), 5 GeV/c (b), 8 GeV/c (c) and 12 GeV/c (d) incident momentum. Each panel is divided in four, corresponding to the integration of the π^+ production (left column of the panel) double-differential cross sections or the π^- production (right column of the panel) double-differential cross sections of the HARP experiment Ref. [13] over the momentum domain (upper part of the panel) or over the angular domain (lower part of the panel) presented in Tab. D.1. The data (symbols) are compared with the improved version of the INCL4 model (blue lines).*

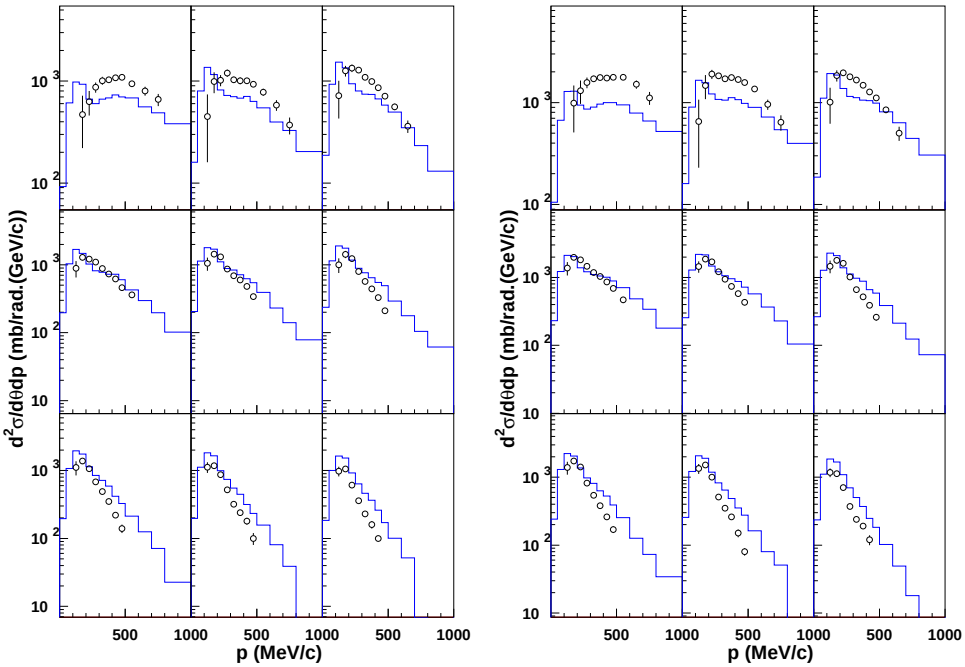

(a) π^+ (3 GeV/c) + Ta $\rightarrow$ π^+

(b) π^+ (5 GeV/c) + Ta $\rightarrow$ π^+

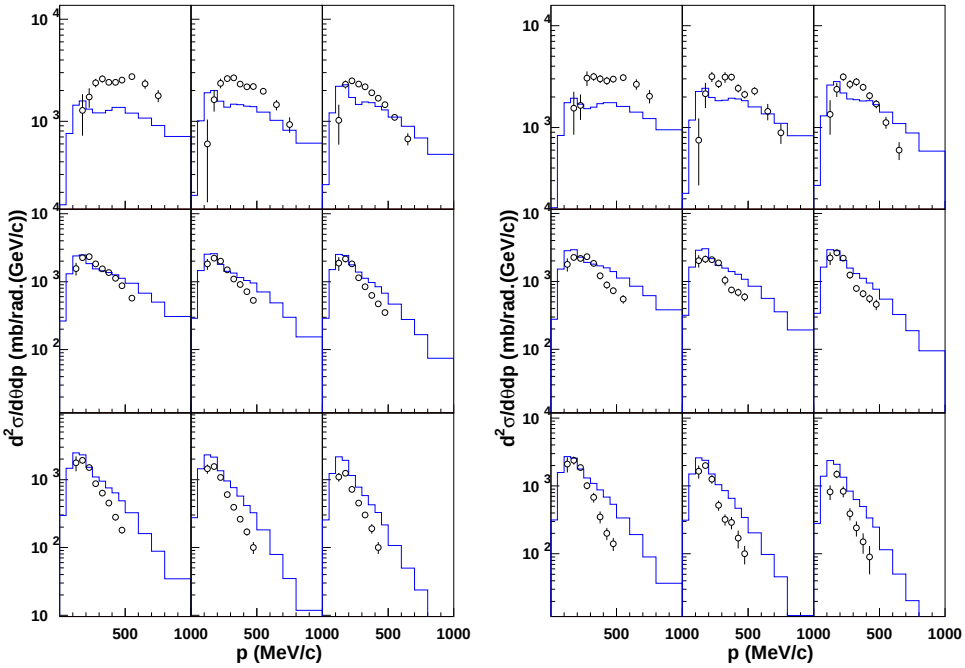

(c) π^+ (8 GeV/c) + Ta $\rightarrow$ π^+

(d) π^+ (12 GeV/c) + Ta $\rightarrow$ π^+

Figure D.30: *Double-differential cross sections for the π^+ production in π^+-induced reactions on Ta at 3 GeV/c (a), 5 GeV/c (b), 8 GeV/c (c) and 12 GeV/c (d) incident momentum. Data (symbols) from Refs. [13] are compared with the improved version of INCL4.2 (blue lines).*

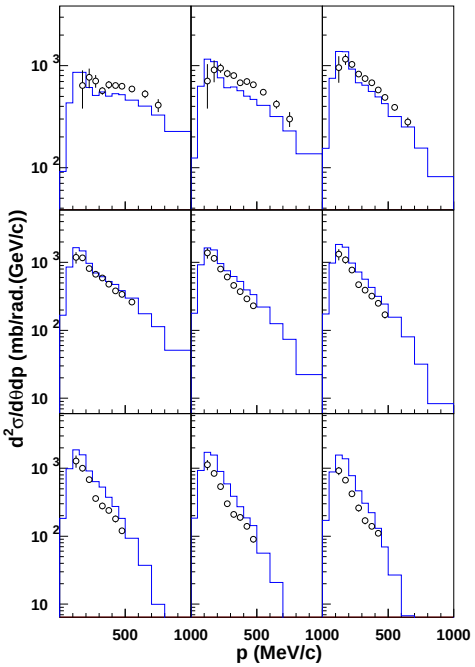

(a) π^+ (3 GeV/c) + Ta $\rightarrow$ π^-

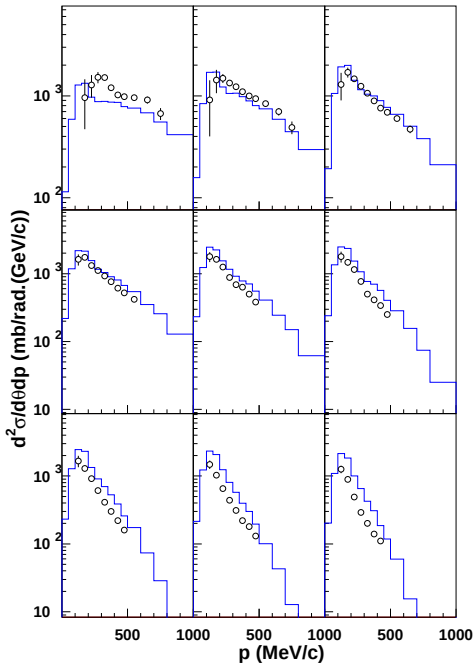

(b) π^+ (5 GeV/c) + Ta $\rightarrow$ π^-

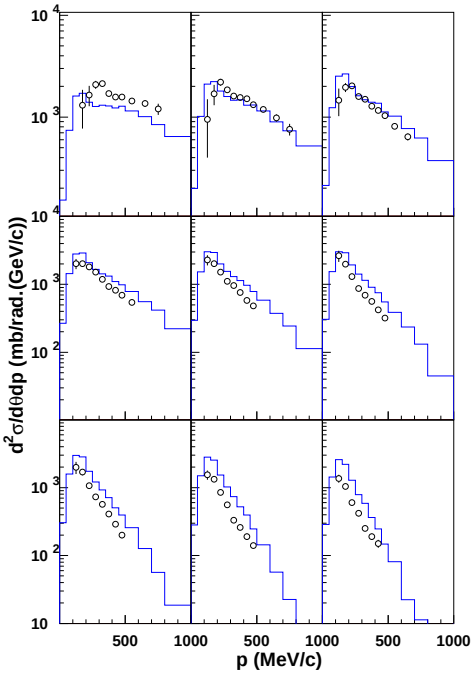

(c) π^+ (8 GeV/c) + Ta $\rightarrow$ π^-

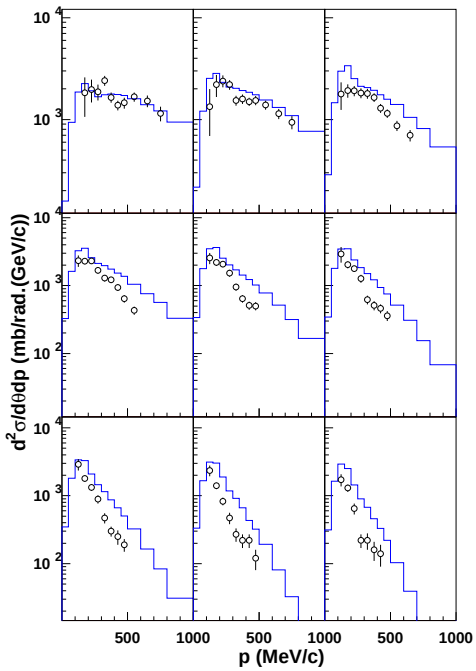

(d) π^+ (12 GeV/c) + Ta $\rightarrow$ π^-

Figure D.31: *Double-differential cross sections for the π^- production in π^+-induced reactions on Ta at 3 GeV/c (a), 5 GeV/c (b), 8 GeV/c (c) and 12 GeV/c (d) incident momentum. Data (symbols) from Refs. [13] are compared with the improved version of INCL4.2 (blue lines).*

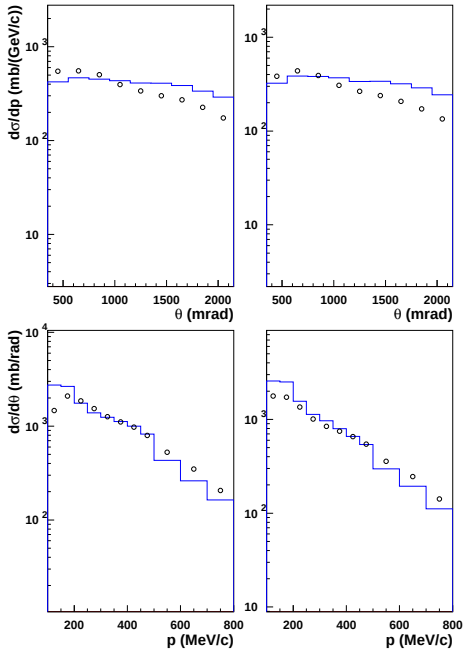

(a) π^+ (3 GeV/c) + Ta

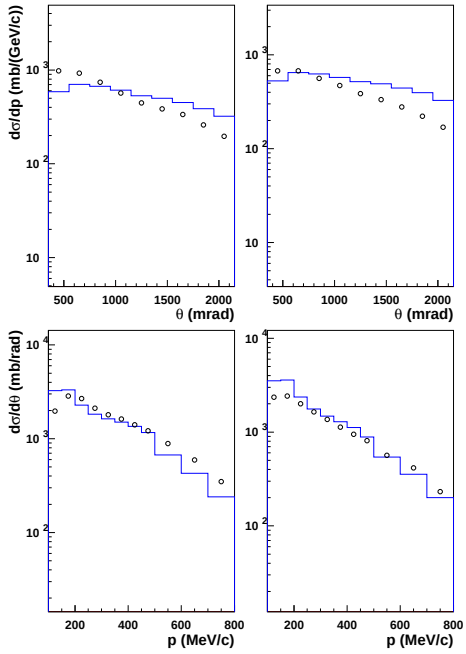

(b) π^+ (5 GeV/c) + Ta

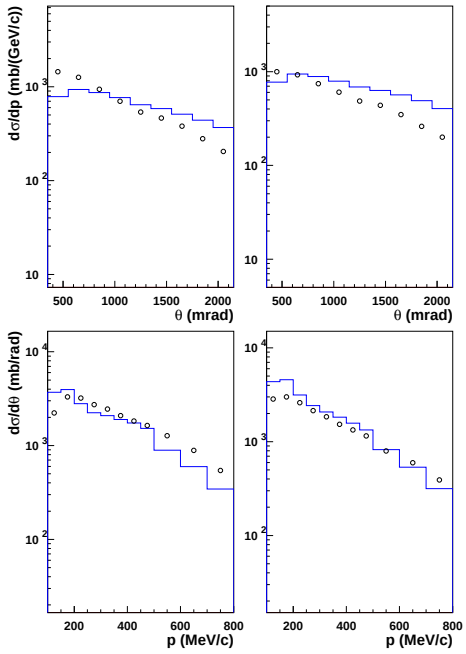

(c) π^+ (8 GeV/c) + Ta

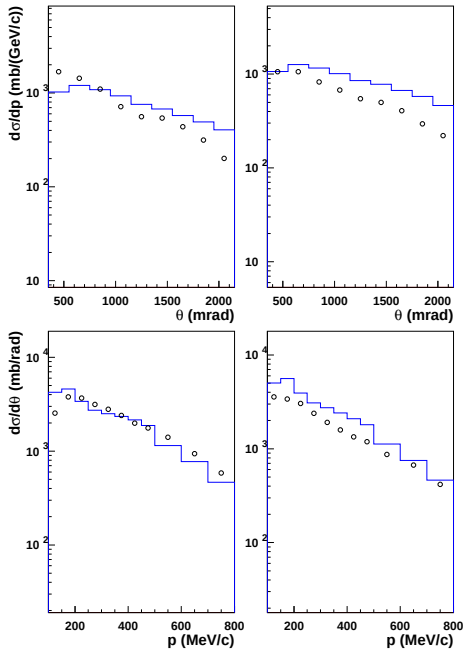

(d) π^+ (12 GeV/c) + Ta

Figure D.32: *Simple-differential cross section in π^+-induced reactions on Ta target at 3 GeV/c (a), 5 GeV/c (b), 8 GeV/c (c) and 12 GeV/c (d) incident momentum. Each panel is divided in four, corresponding to the integration of the π^+ production (left column of the panel) double-differential cross sections or the π^- production (right column of the panel) double-differential cross sections of the HARP experiment Ref. [13] over the momentum domain (upper part of the panel) or over the angular domain (lower part of the panel) presented in Tab. D.1. The data (symbols) are compared with the improved version of the INCL4 model (blue lines).*

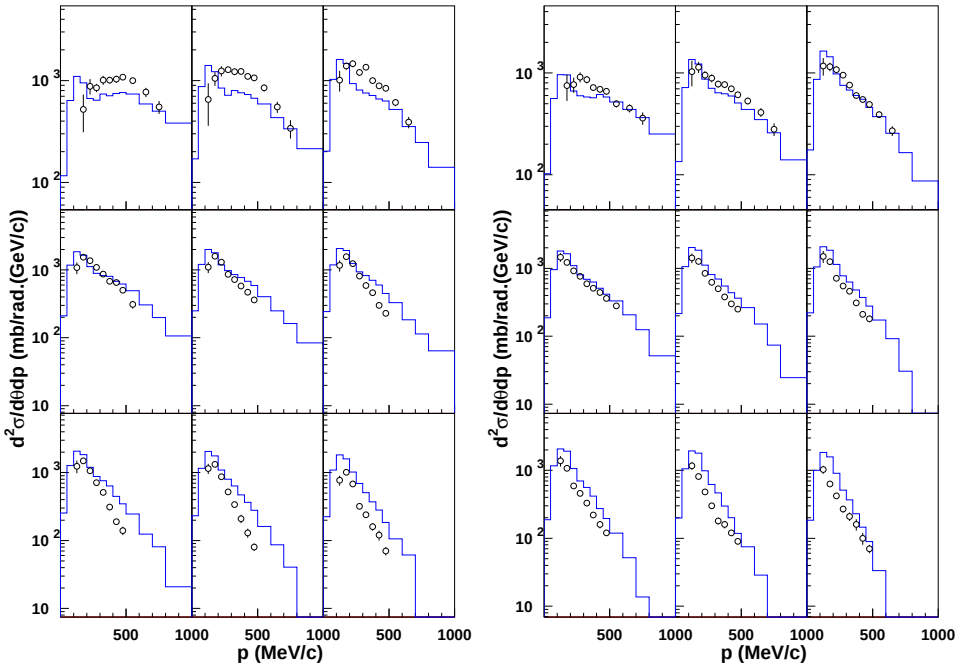

(a) π^+ (3 GeV/c) + Pb $\rightarrow$ π^+ (b) π^+ (3 GeV/c) + Pb $\rightarrow$ π^-

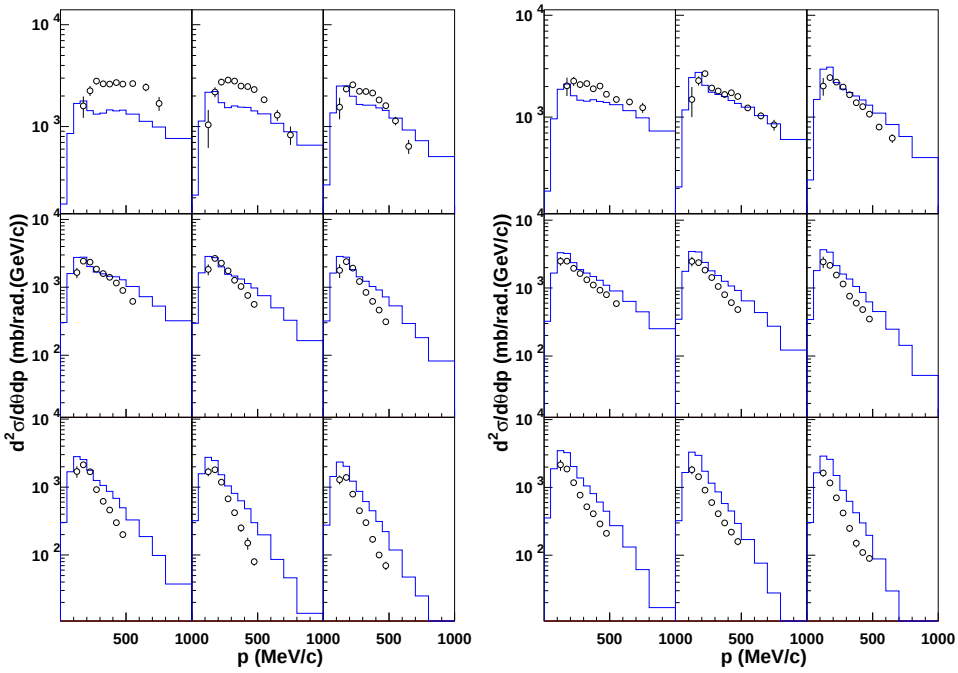

(c) π^+ (8 GeV/c) + Pb $\rightarrow$ π^+ (d) π^+ (8 GeV/c) + Pb $\rightarrow$ π^-

Figure D.33: *Double-differential cross sections for π^+ production (a,c) and π^- production (b,d) in π^+-induced reactions on Pb at 3 GeV/c (a,b) and 8 GeV/c (c,d) incident momentum. Data (symbols) from Ref. [13] are compared with the improved version of the INCL4 model (blue lines).*

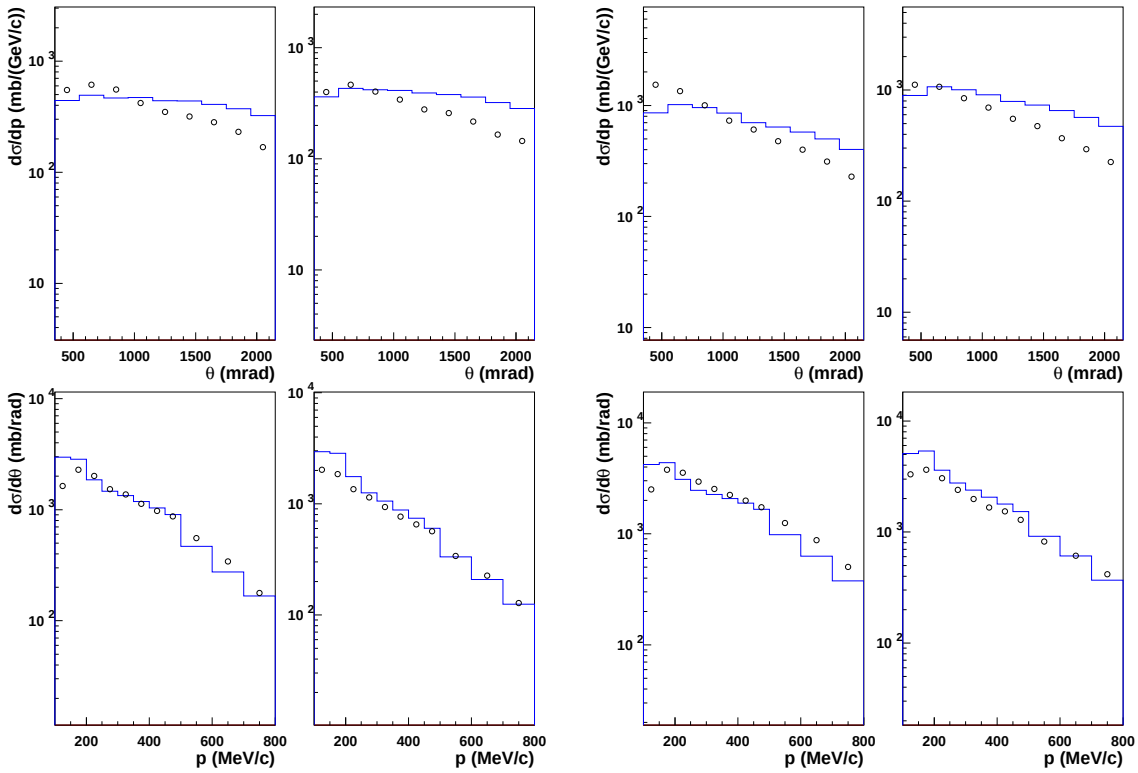

(a) π^+ (3 GeV/c) + Pb (b) π^+ (8 GeV/c) + Pb

Figure D.34: *Simple-differential cross section in π^+-induced reactions on Pb target at 3 GeV/c (a) and 8 GeV/c (b) incident momentum. The data are obtained by integrating the double-differential cross sections of the HARP experiment over the angular domain or over the momentum domain (presented in Tab. D.1). Data (symbols) from Ref. [13] are compared with the improved version of INCL4 (blue lines).*

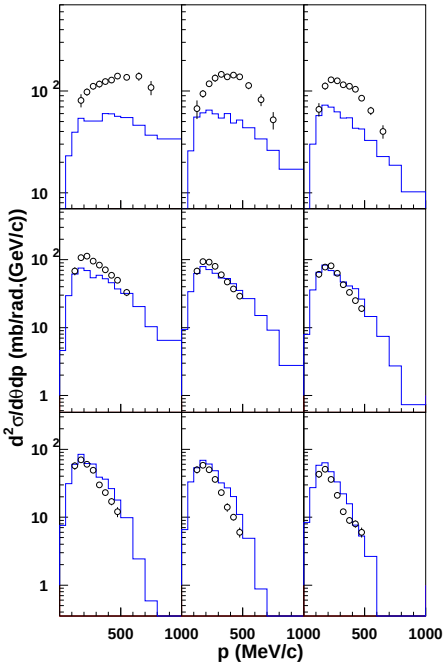

(a) π^- (3 GeV/c) + Be $\rightarrow$ π^+

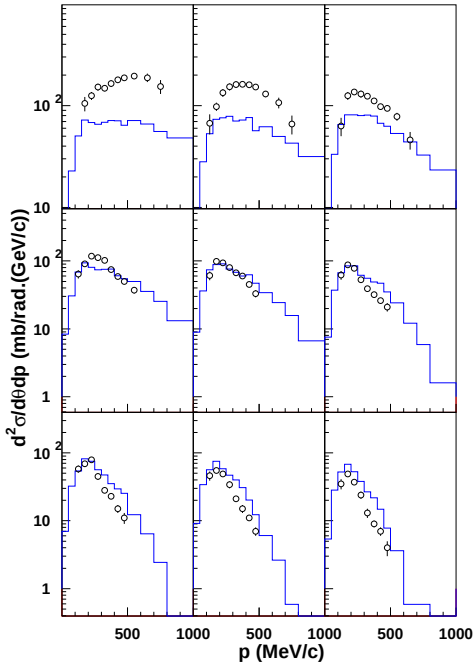

(b) π^- (5 GeV/c) + Be $\rightarrow$ π^+

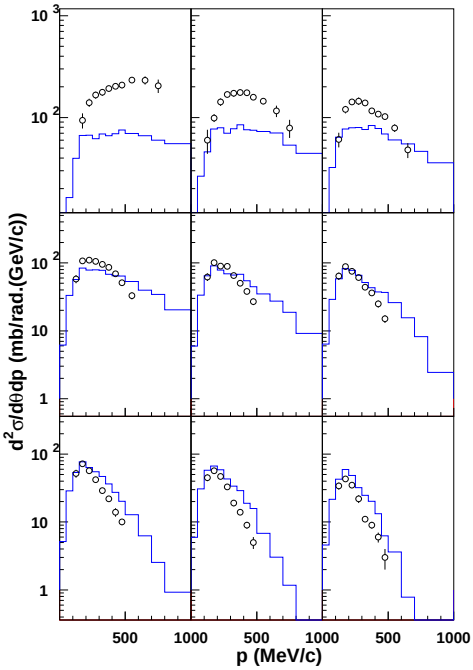

(c) π^- (8 GeV/c) + Be $\rightarrow$ π^+

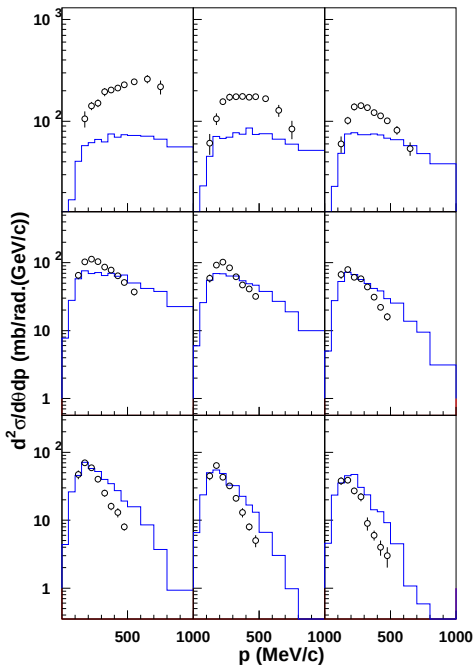

(d) π^- (12 GeV/c) + Be $\rightarrow$ π^+

Figure D.35: *Double-differential cross sections for the π^+ production in π^--induced reactions on Be at 3 GeV/c (a), 5 GeV/c (b), 8 GeV/c (c) and 12 GeV/c (d) incident momentum. Data (symbols) from Refs. [13] are compared with the improved version of INCL4.2 (blue lines).*

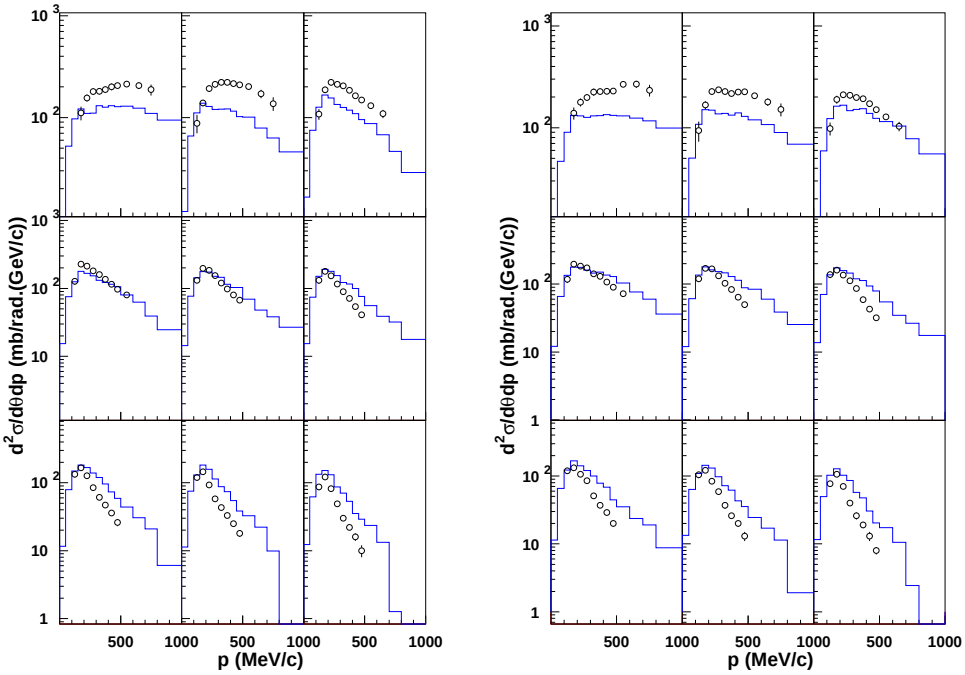

(a) π^- (3 GeV/c) + Be $\rightarrow$ π^-

(b) π^- (5 GeV/c) + Be $\rightarrow$ π^-

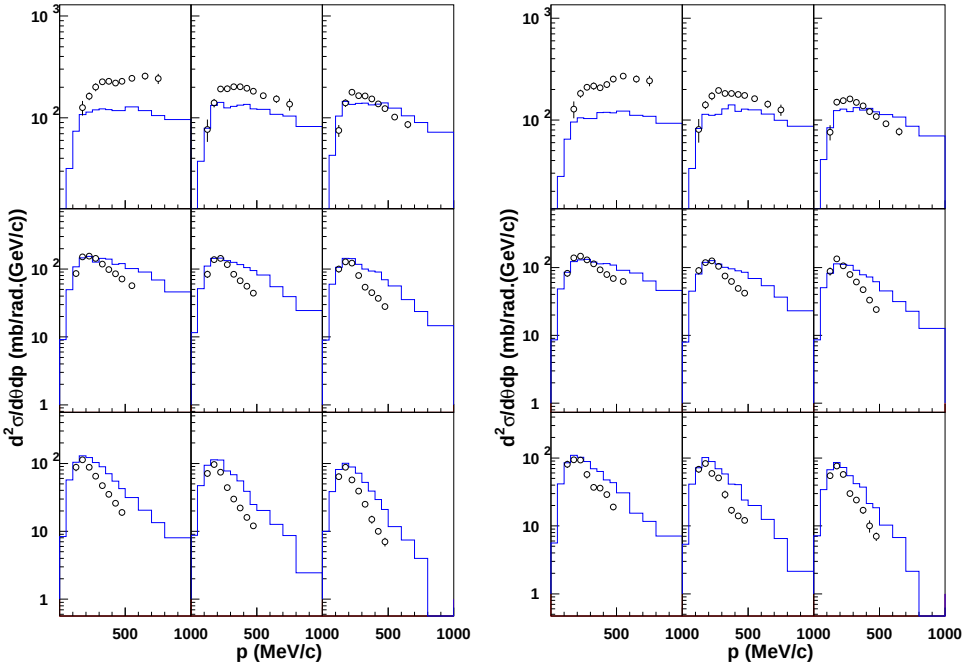

(c) π^- (8 GeV/c) + Be $\rightarrow$ π^-

(d) π^- (12 GeV/c) + Be $\rightarrow$ π^-

Figure D.36: *Double-differential cross sections for the π^- production in π^--induced reactions on Be at 3 GeV/c (a), 5 GeV/c (b), 8 GeV/c (c) and 12 GeV/c (d) incident momentum. Data (symbols) from Refs. [13] are compared with the improved version of INCL4.2 (blue lines).*

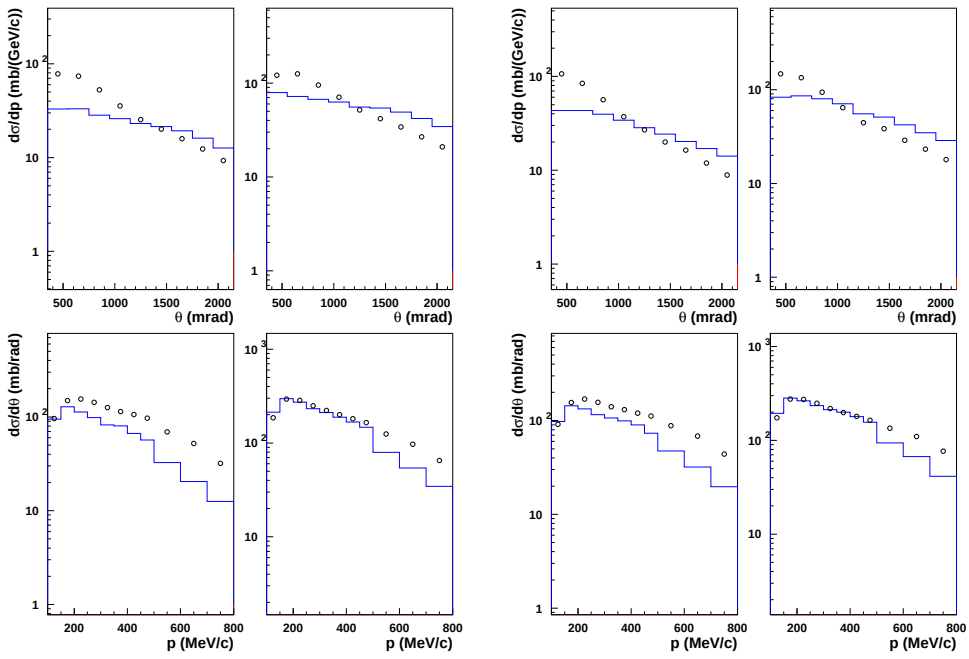

(a) π^- (3 GeV/c) + Be (b) π^- (5 GeV/c) + Be

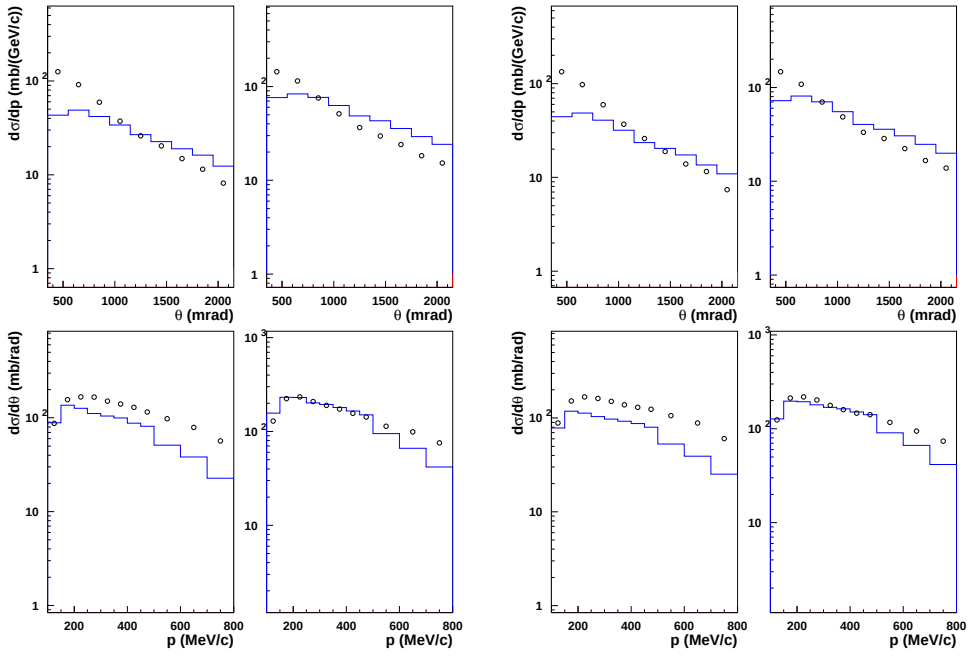

(c) π^- (8 GeV/c) + Be (d) π^- (12 GeV/c) + Be

Figure D.37: *Simple-differential cross section in π^--induced reactions on Be target at 3 GeV/c (a), 5 GeV/c (b), 8 GeV/c (c) and 12 GeV/c (d) incident momentum. Each panel is divided in four, corresponding to the integration of the π^+ production (left column of the panel) double-differential cross sections or the π^- production (right column of the panel) double-differential cross sections of the HARP experiment Ref. [13] over the momentum domain (upper part of the panel) or over the angular domain (lower part of the panel) presented in Tab. D.1. The data (symbols) are compared with the improved version of the INCL4 model (blue lines).*

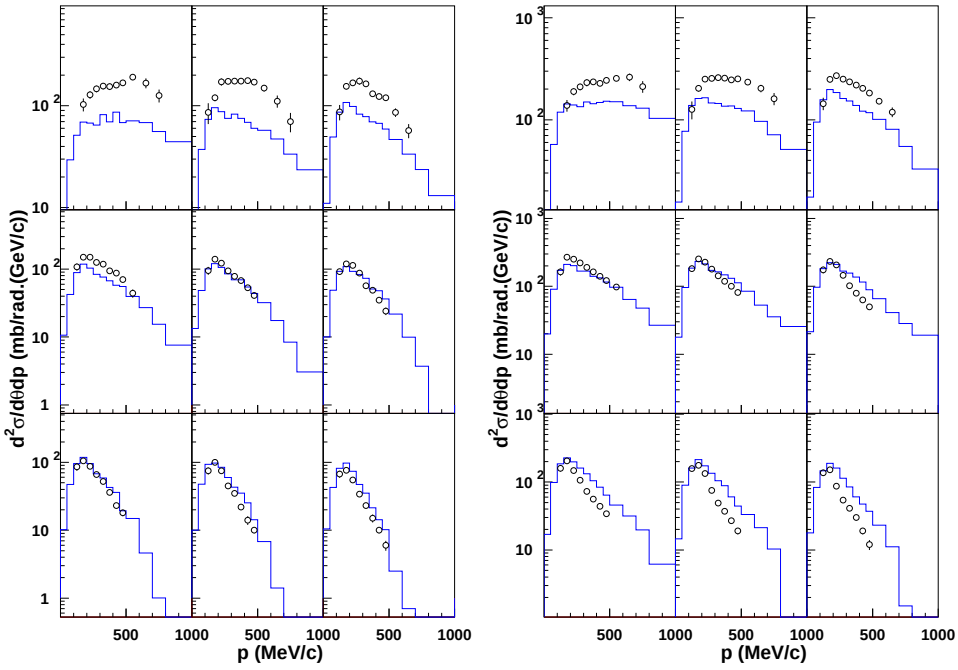

(a) π^- (3 GeV/c) + C $\rightarrow$ π^+ (b) π^- (3 GeV/c) + C $\rightarrow$ π^-

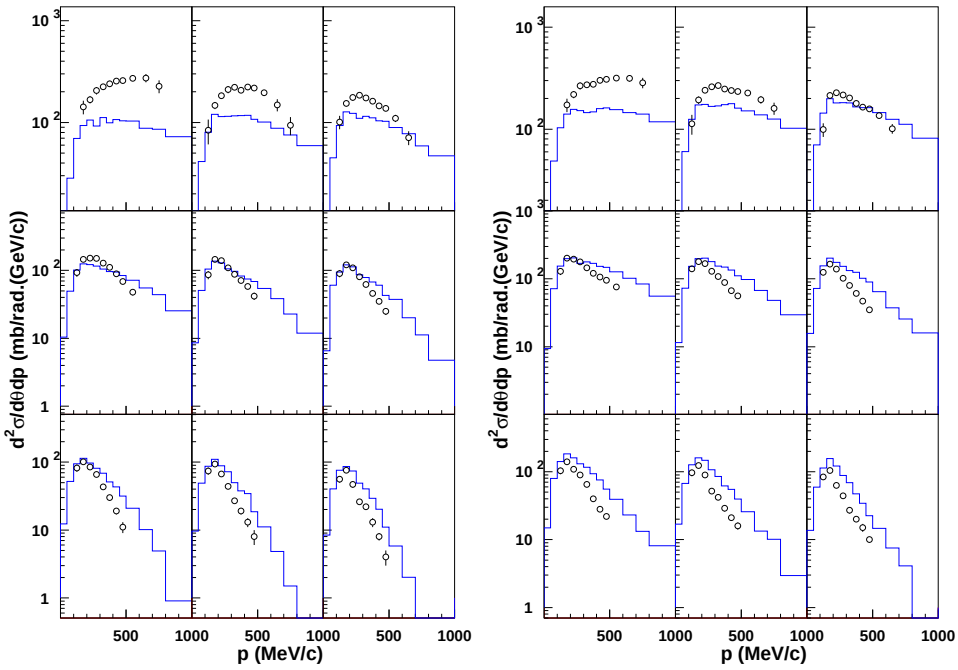

(c) π^- (8 GeV/c) + C $\rightarrow$ π^+ (d) π^- (8 GeV/c) + C $\rightarrow$ π^-

Figure D.38: *Double-differential cross sections for π^- production (a,c) and π^- production (b,d) in π^+-induced reactions on C at 3 GeV/c (a,b) and 8 GeV/c (c,d) incident momentum. Data (symbols) from Ref. [13] are compared with the improved version of the INCL4 model (blue lines).*

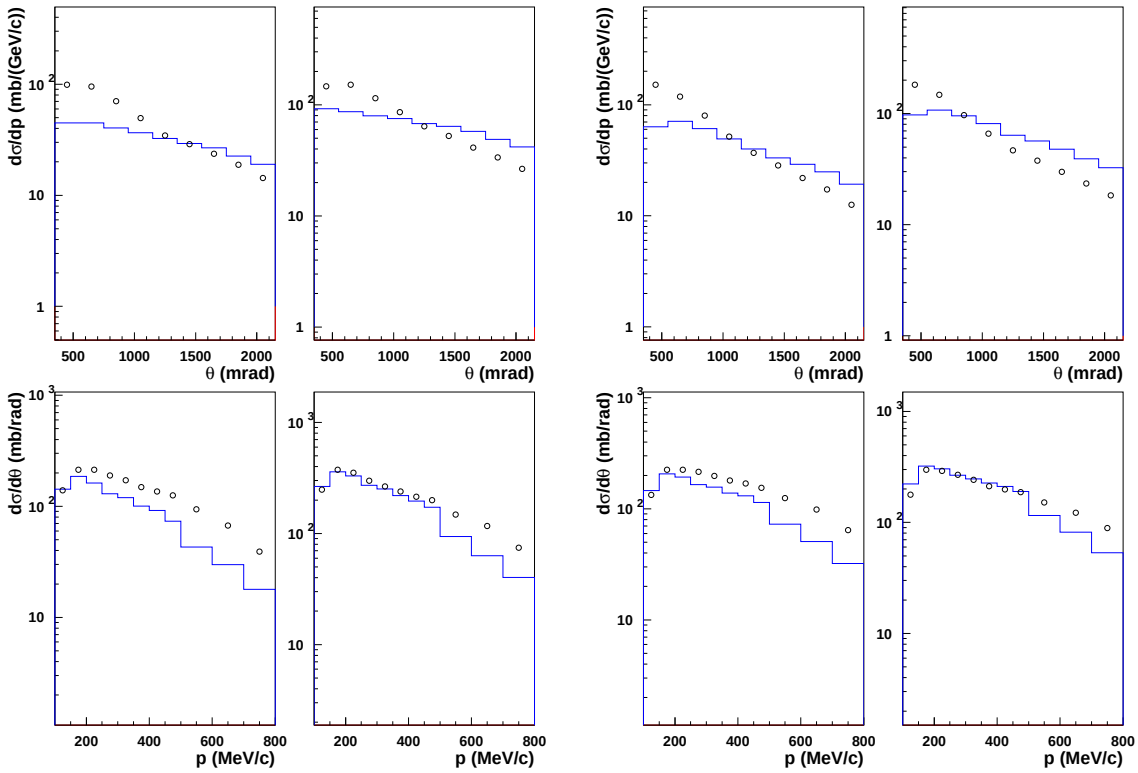

(a) π^- (3 GeV/c) + C (b) π^- (8 GeV/c) + C

Figure D.39: *Simple-differential cross section in π^--induced reactions on C target at 3 GeV/c (a) and 8 GeV/c (b) incident momentum. The data are obtained by integrating the double-differential cross sections of the HARP experiment over the angular domain or over the momentum domain (presented in Tab. D.1). Data (symbols) from Ref. [13] are compared with the improved version of INCL4 (blue lines).*

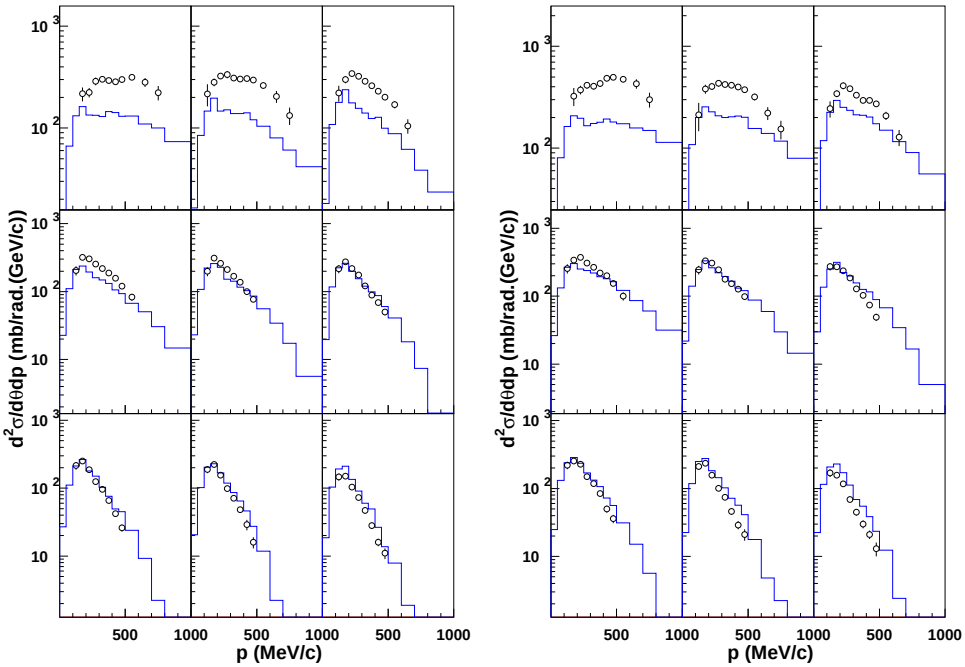

(a) π^- (3 GeV/c) + Al $\rightarrow$ π^+

(b) π^- (5 GeV/c) + Al $\rightarrow$ π^+

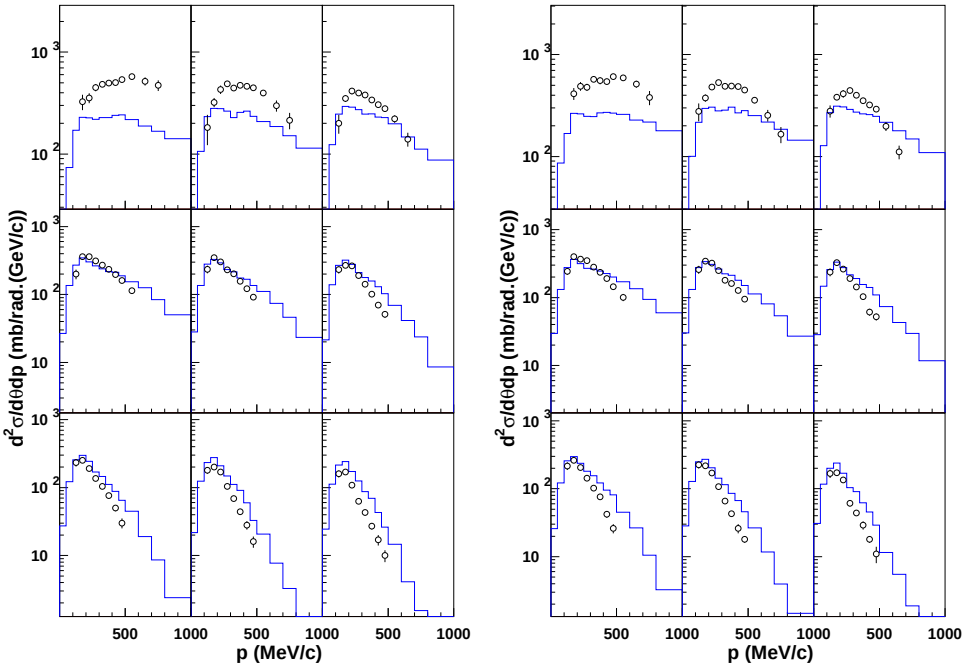

(c) π^- (8 GeV/c) + Al $\rightarrow$ π^+

(d) π^- (12 GeV/c) + Al $\rightarrow$ π^+

Figure D.40: *Double-differential cross sections for the π^+ production in π^--induced reactions on Al at 3 GeV/c (a), 5 GeV/c (b), 8 GeV/c (c) and 12 GeV/c (d) incident momentum. Data (symbols) from Refs. [13] are compared with the improved version of INCL4.2 (blue lines).*

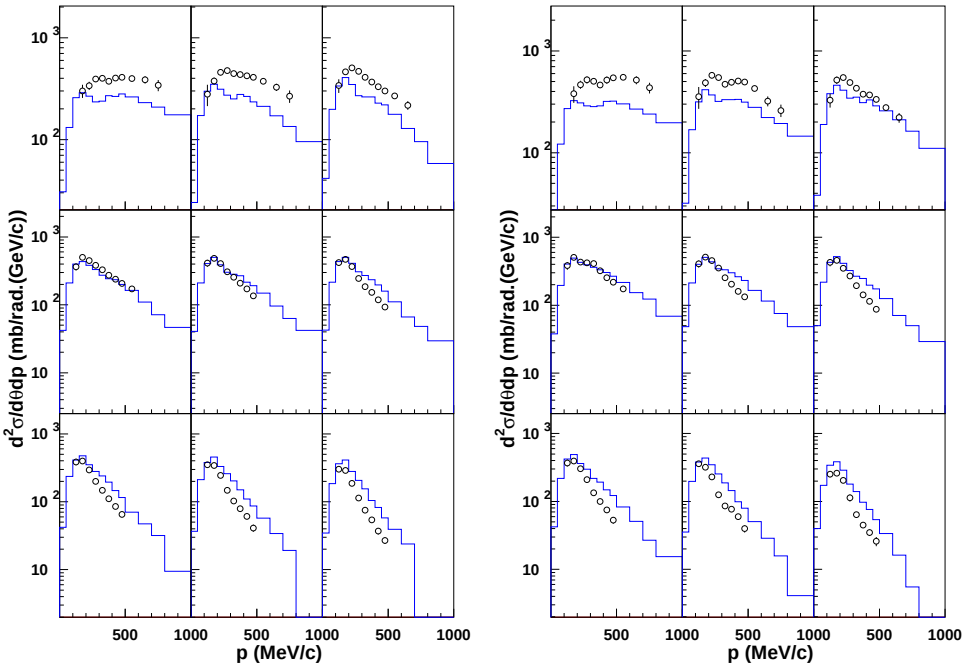

(a) π^- (3 GeV/c) + Al $\rightarrow$ π^- (b) π^- (5 GeV/c) + Al $\rightarrow$ π^-

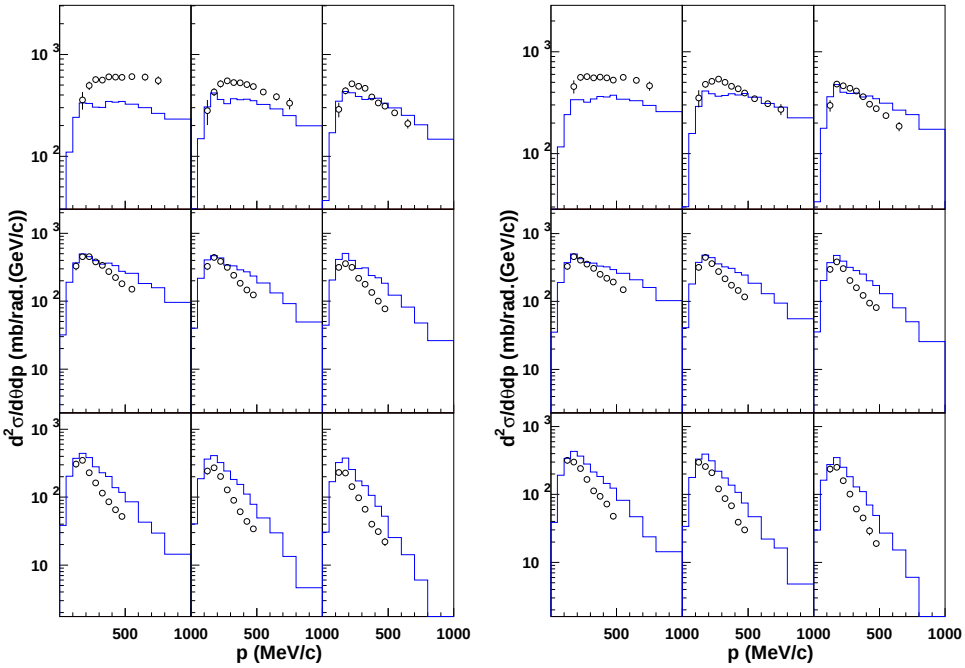

(c) π^- (8 GeV/c) + Al $\rightarrow$ π^- (d) π^- (12 GeV/c) + Al $\rightarrow$ π^-

Figure D.41: *Double-differential cross sections for the π^- production in π^--induced reactions on Al at 3 GeV/c (a), 5 GeV/c (b), 8 GeV/c (c) and 12 GeV/c (d) incident momentum. Data (symbols) from Refs. [13] are compared with the improved version of INCL4.2 (blue lines).*

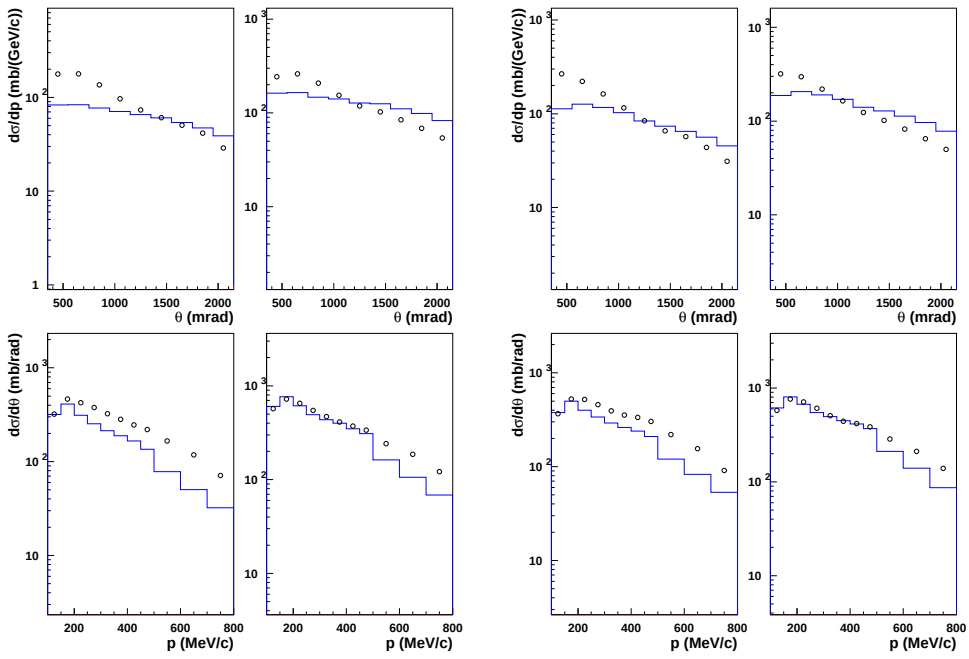

(a) π^- (3 GeV/c) + *Al*

(b) π^- (5 GeV/c) + *Al*

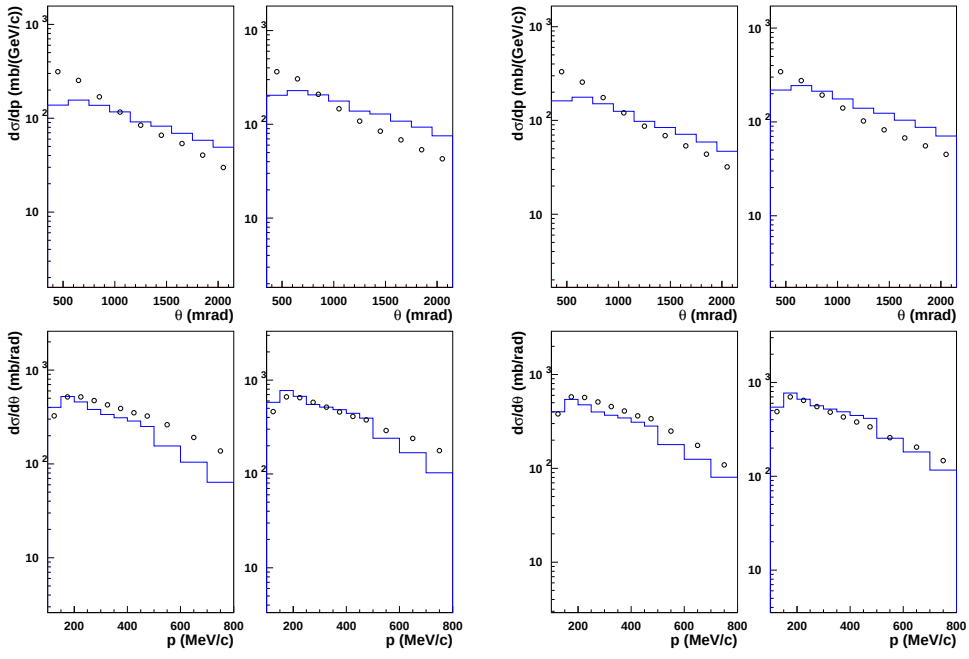

(c) π^- (8 GeV/c) + *Al*

(d) π^- (12 GeV/c) + *Al*

Figure D.42: *Simple-differential cross section in π^--induced reactions on Al target at 3 GeV/c (a), 5 GeV/c (b), 8 GeV/c (c) and 12 GeV/c (d) incident momentum. Each panel is divided in four, corresponding to the integration of the π^+ production (left column of the panel) double-differential cross sections or the π^- production (right column of the panel) double-differential cross sections of the HARP experiment Ref. [13] over the momentum domain (upper part of the panel) or over the angular domain (lower part of the panel) presented in Tab. D.1. The data (symbols) are compared with the improved version of the INCL4 model (blue lines).*

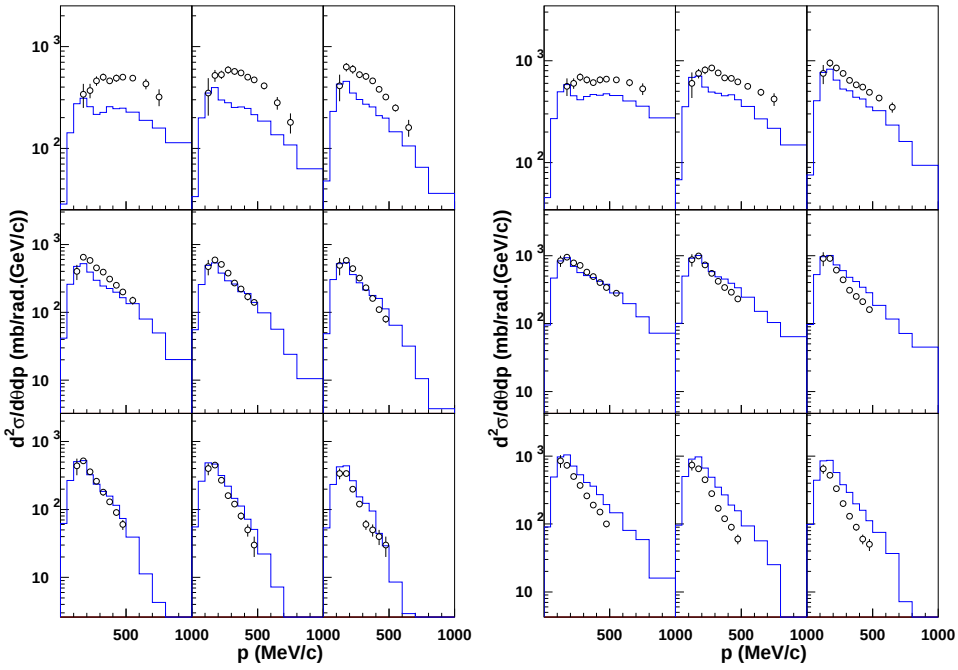

(a) π^- (3 GeV/c) + Cu $\rightarrow$ π^+

(b) π^- (5 GeV/c) + Cu $\rightarrow$ π^-

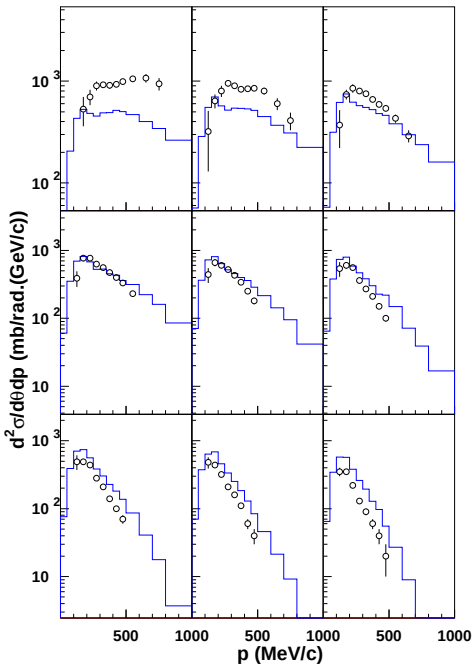

(c) π^- (8 GeV/c) + Cu $\rightarrow$ π^+

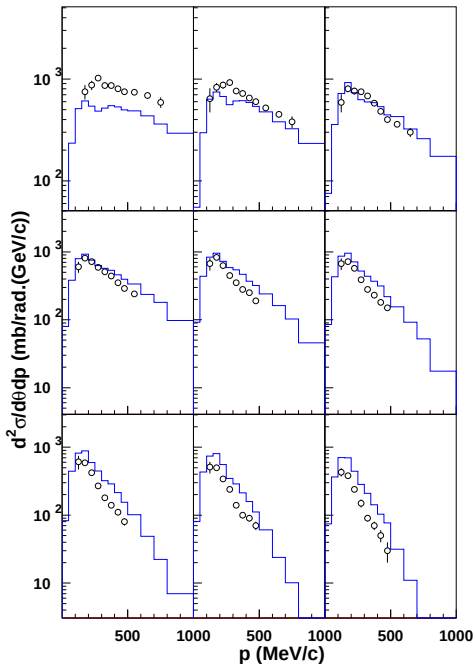

(d) π^- (12 GeV/c) + Cu $\rightarrow$ π^-

Figure D.43: *Double-differential cross sections for π^- production (a,c) and π^- production (b,d) in π^+-induced reactions on Cu at 3 GeV/c (a,b) and 8 GeV/c (c,d) incident momentum. Data (symbols) from Ref. [13] are compared with the improved version of the INCL4 model (blue lines).*

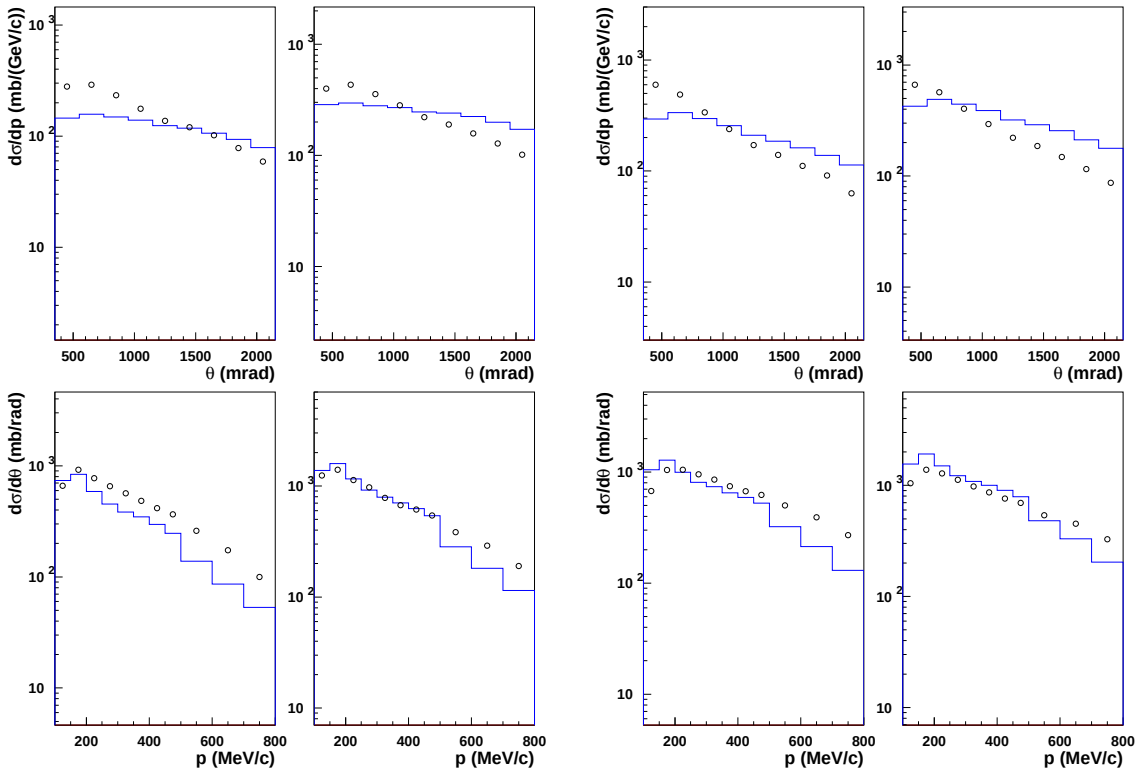

(a) π^- (3 GeV/c) + Cu (b) π^- (8 GeV/c) + Cu

Figure D.44: *Simple-differential cross section in π^--induced reactions on Cu target at 3 GeV/c (a) and 8 GeV/c (b) incident momentum. The data are obtained by integrating the double-differential cross sections of the HARP experiment over the angular domain or over the momentum domain (presented in Tab. D.1). Data (symbols) from Ref. [13] are compared with the improved version of INCL4 (blue lines).*

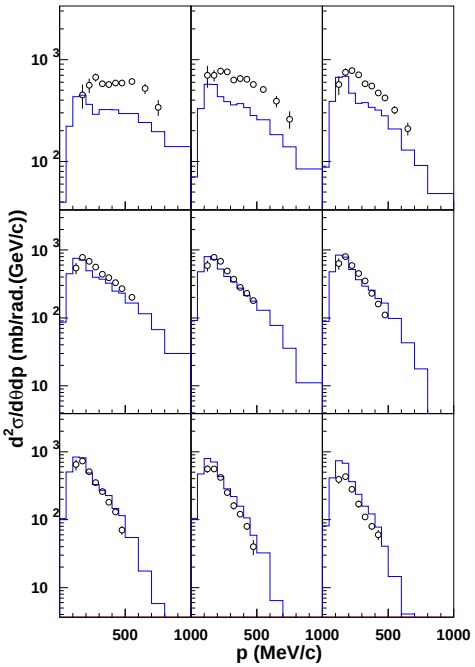

(a) π^- (3 GeV/c) + Sn $\rightarrow$ π^+

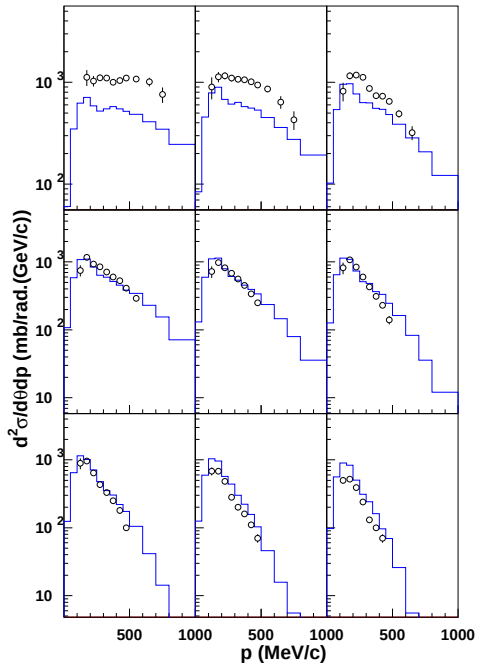

(b) π^- (5 GeV/c) + Sn $\rightarrow$ π^+

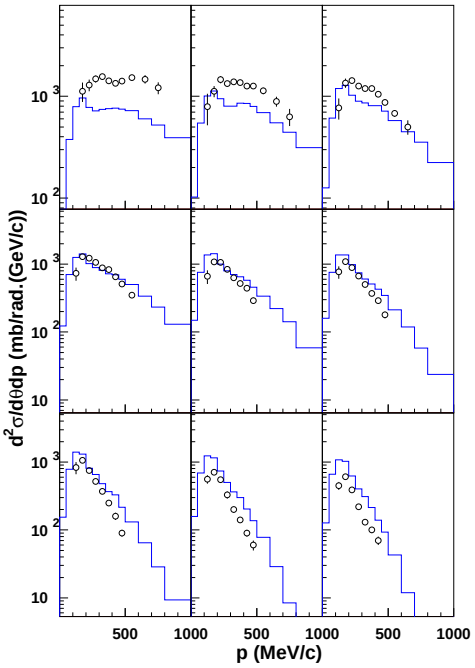

(c) π^- (8 GeV/c) + Sn $\rightarrow$ π^+

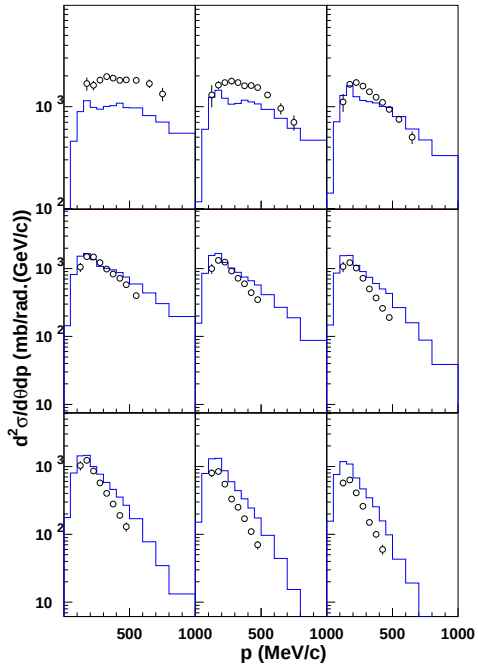

(d) π^- (12 GeV/c) + Sn $\rightarrow$ π^+

Figure D.45: *Double-differential cross sections for the π^+ production in π^--induced reactions on Sn at 3 GeV/c (a), 5 GeV/c (b), 8 GeV/c (c) and 12 GeV/c (d) incident momentum. Data (symbols) from Refs. [13] are compared with the improved version of INCL4.2 (blue lines).*

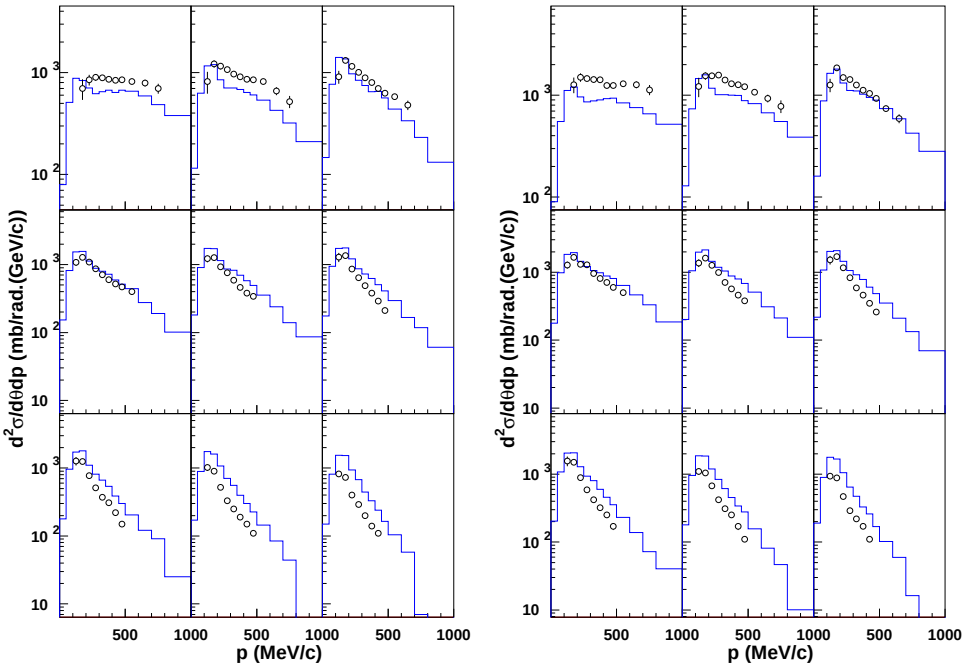

(a) π^- (3 GeV/c) + Sn $\rightarrow$ π^-

(b) π^- (5 GeV/c) + Sn $\rightarrow$ π^-

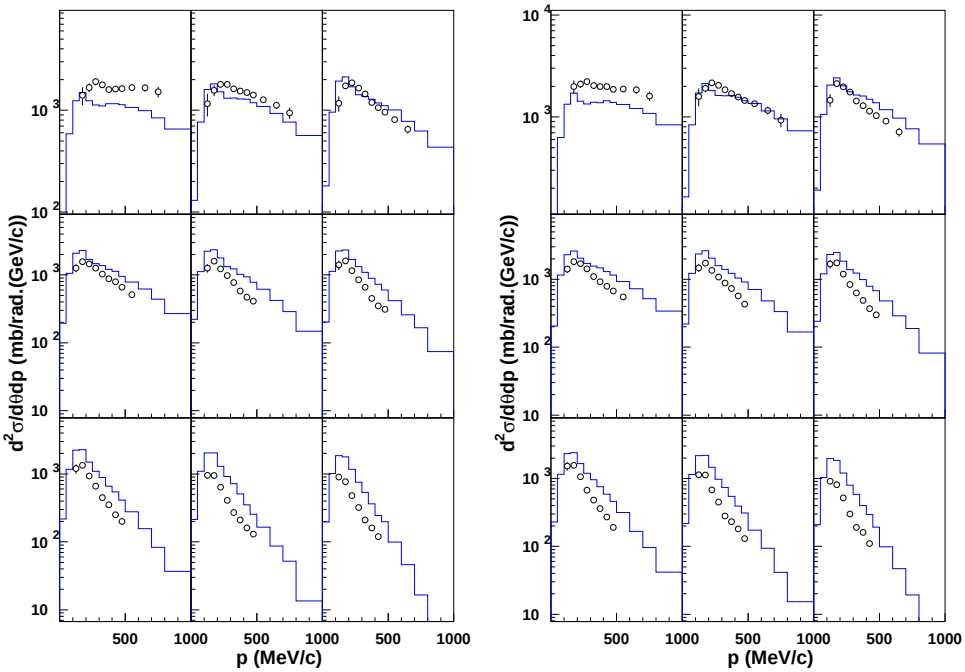

(c) π^- (8 GeV/c) + Sn $\rightarrow$ π^-

(d) π^- (12 GeV/c) + Sn $\rightarrow$ π^-

Figure D.46: *Double-differential cross sections for the π^- production in π^--induced reactions on Sn at 3 GeV/c (a), 5 GeV/c (b), 8 GeV/c (c) and 12 GeV/c (d) incident momentum. Data (symbols) from Refs. [13] are compared with the improved version of INCL4.2 (blue lines).*

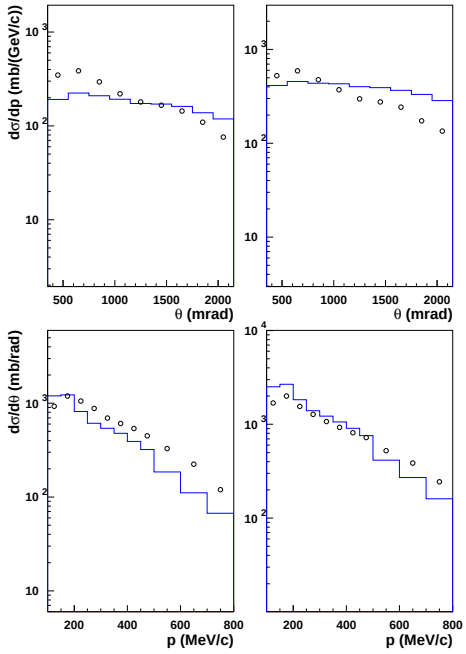

(a) π^- (3 GeV/c) + Sn

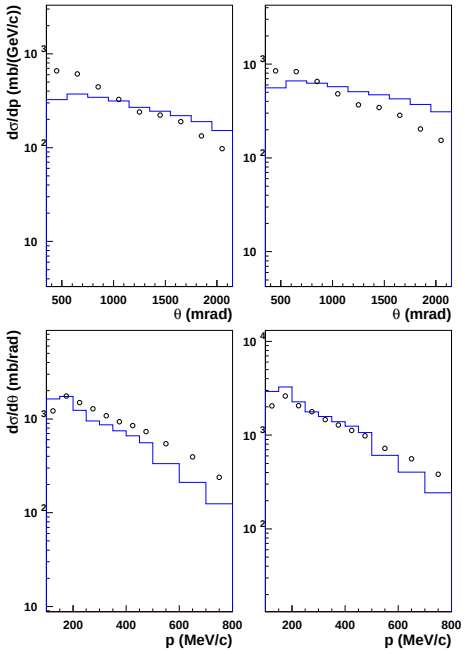

(b) π^- (5 GeV/c) + Sn

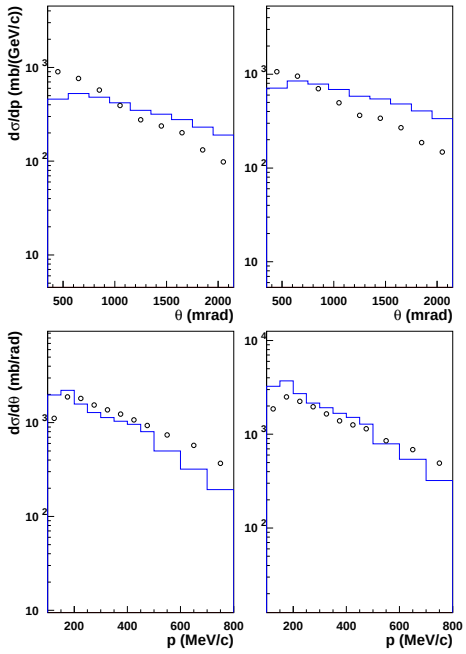

(c) π^- (8 GeV/c) + Sn

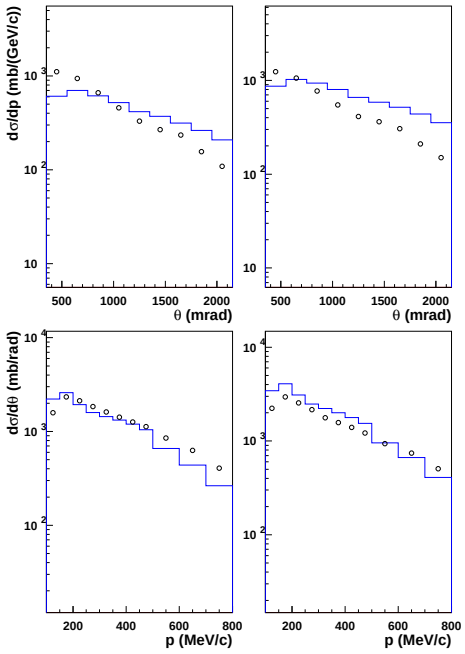

(d) π^- (12 GeV/c) + Sn

Figure D.47: *Simple-differential cross section in π^--induced reactions on Sn target at 3 GeV/c (a), 5 GeV/c (b), 8 GeV/c (c) and 12 GeV/c (d) incident momentum. Each panel is divided in four, corresponding to the integration of the π^+ production (left column of the panel) double-differential cross sections or the π^- production (right column of the panel) double-differential cross sections of the HARP experiment Ref. [13] over the momentum domain (upper part of the panel) or over the angular domain (lower part of the panel) presented in Tab. D.1. The data (symbols) are compared with the improved version of the INCL4 model (blue lines).*

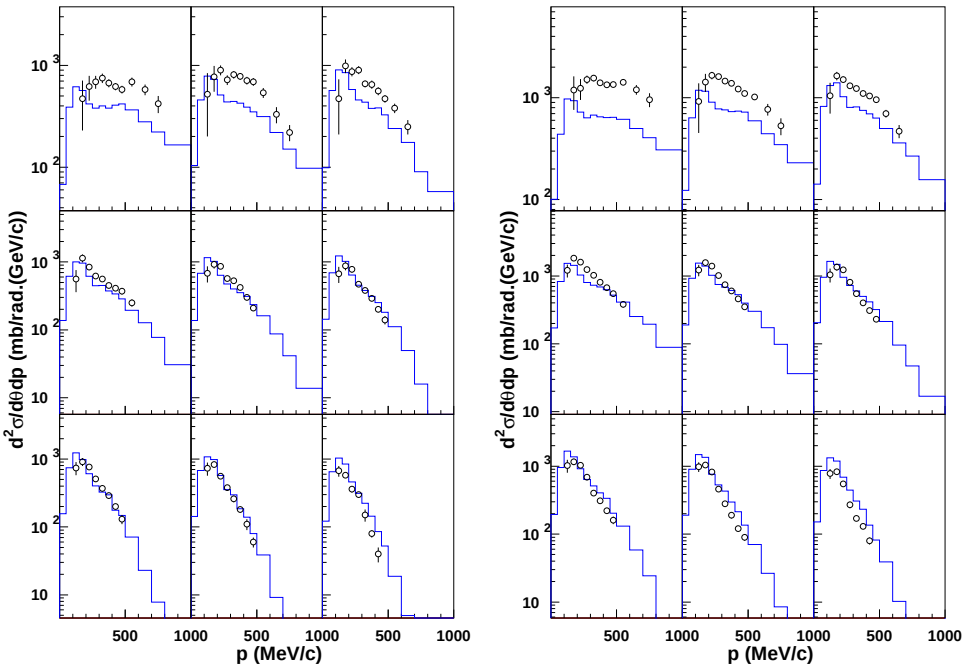

(a) π^- (3 GeV/c) + Ta $\rightarrow$ π^+

(b) π^- (5 GeV/c) + Ta $\rightarrow$ π^+

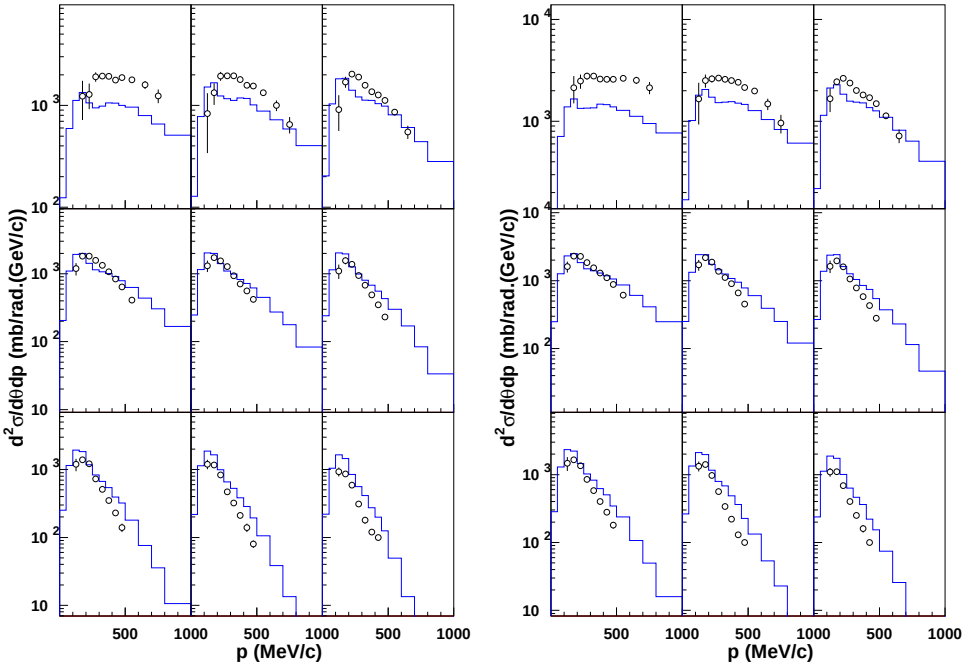

(c) π^- (8 GeV/c) + Ta $\rightarrow$ π^+

(d) π^- (12 GeV/c) + Ta $\rightarrow$ π^+

Figure D.48: *Double-differential cross sections for the production of positive pions in negative pion-induced reactions on Ta at 3 GeV/c (a), 5 GeV/c (b), 8 GeV/c (c) and 12 GeV/c (d) incident momentum. Data (symbols) from Refs. [13] are compared with the standard version (red lines) and the improved version (blue lines) of the INCL4 model (standard INCL4.2 version plus implementation of direct multipion production).*

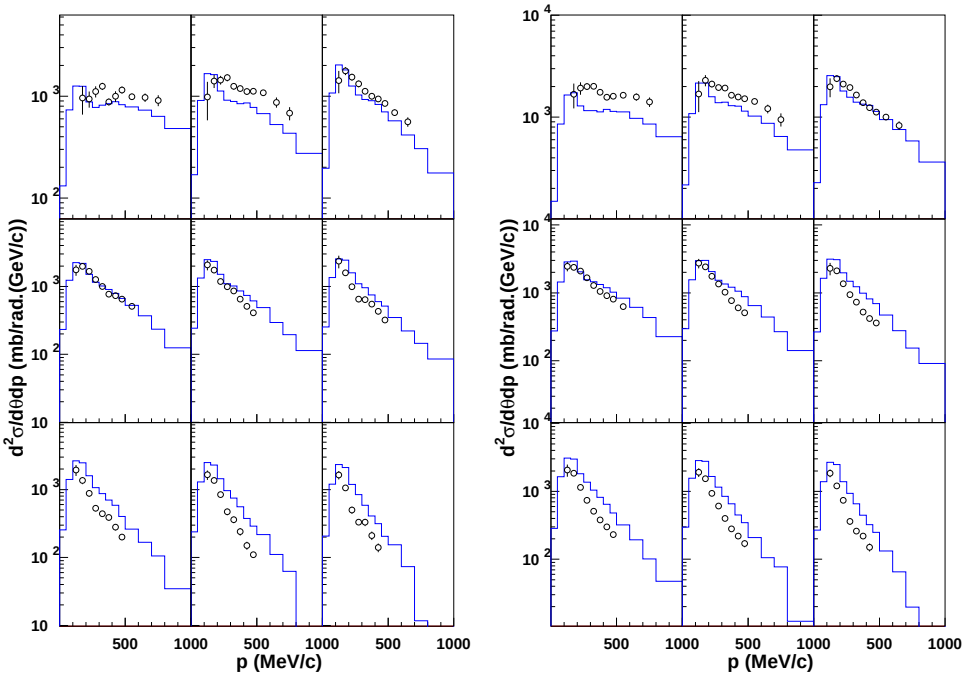

(a) π^- (3 GeV/c) + Ta $\rightarrow$ π^-

(b) π^- (5 GeV/c) + Ta $\rightarrow$ π^-

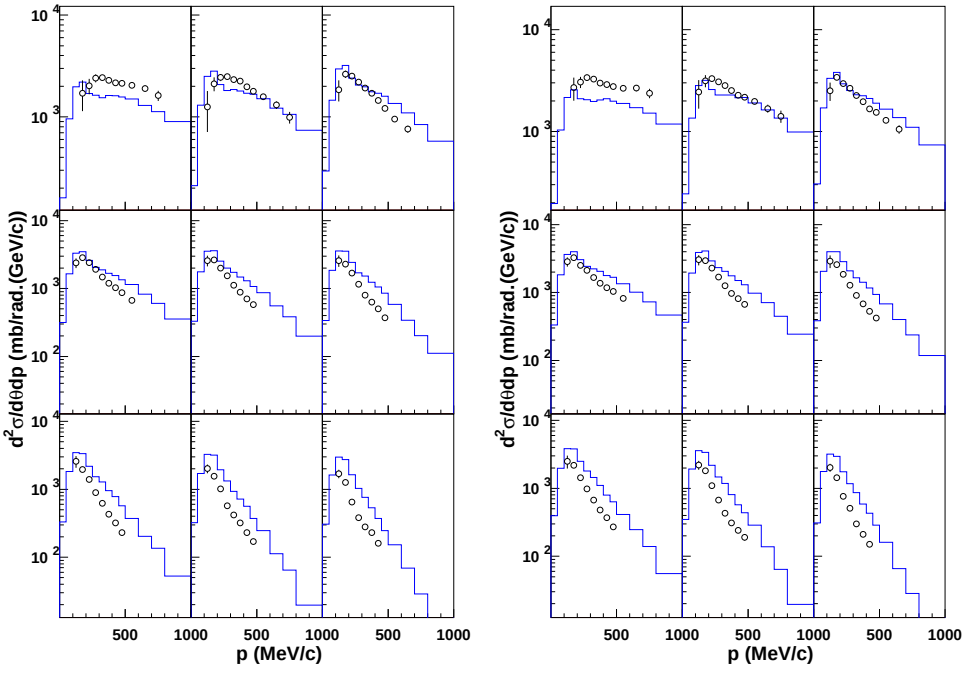

(c) π^- (8 GeV/c) + Ta $\rightarrow$ π^-

(d) π^- (12 GeV/c) + Ta $\rightarrow$ π^-

Figure D.49: *Double-differential cross sections for the π^+ production in π^--induced reactions on Ta at 3 GeV/c (a), 5 GeV/c (b), 8 GeV/c (c) and 12 GeV/c (d) incident momentum. Data (symbols) from Refs. [13] are compared with the improved version of INCL4.2 (blue lines).*

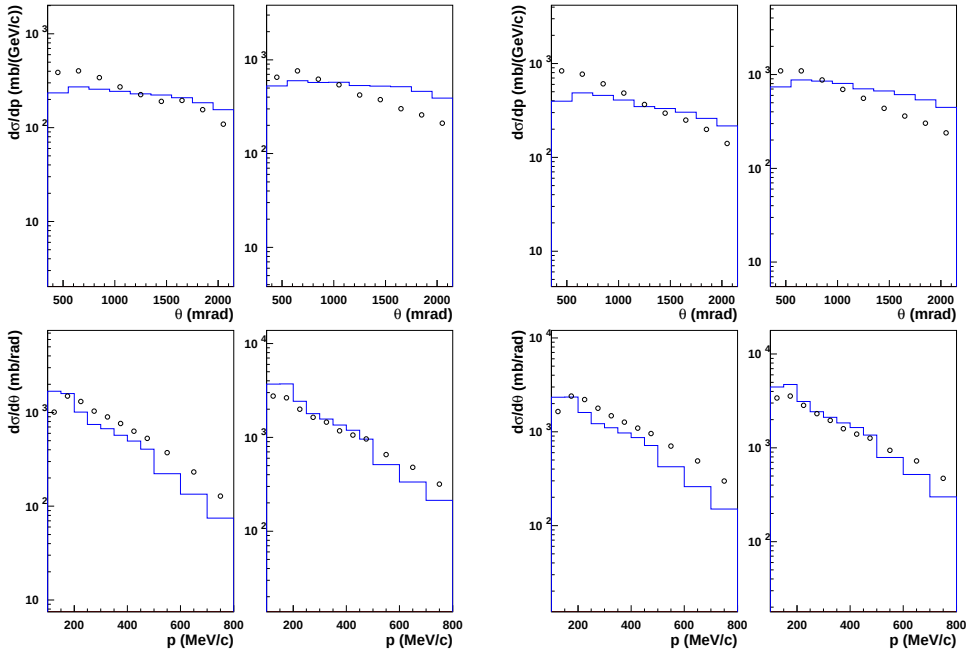

(a) π^- (3 GeV/c) + Ta (b) π^- (5 GeV/c) + Ta

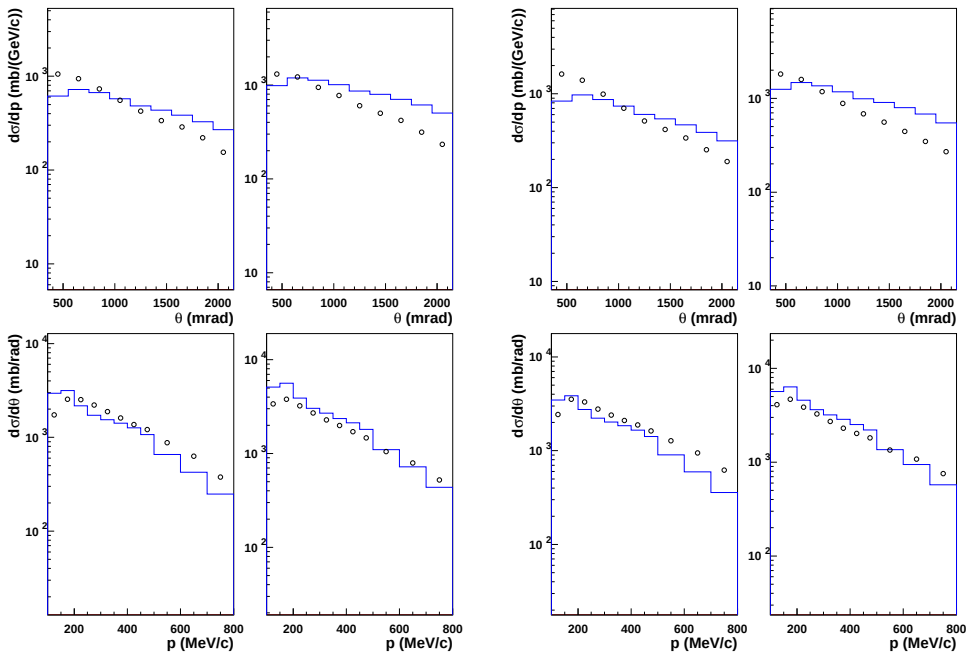

(c) π^- (8 GeV/c) + Ta (d) π^- (12 GeV/c) + Ta

Figure D.50: *Double-differential cross sections for the π^- production in π^--induced reactions on Ta at 3 GeV/c (a), 5 GeV/c (b), 8 GeV/c (c) and 12 GeV/c (d) incident momentum. Data (symbols) from Refs. [13] are compared with the improved version of INCL4.2 (blue lines).*

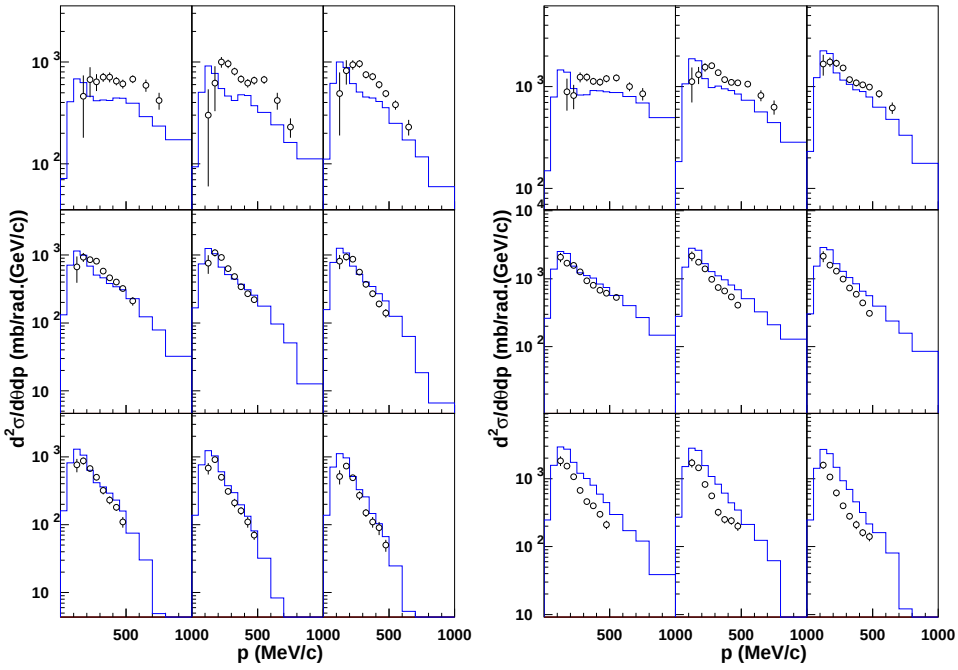

(a) π^- (3 GeV/c) + Pb $\rightarrow$ π^+ (b) π^- (5 GeV/c) + Pb $\rightarrow$ π^-

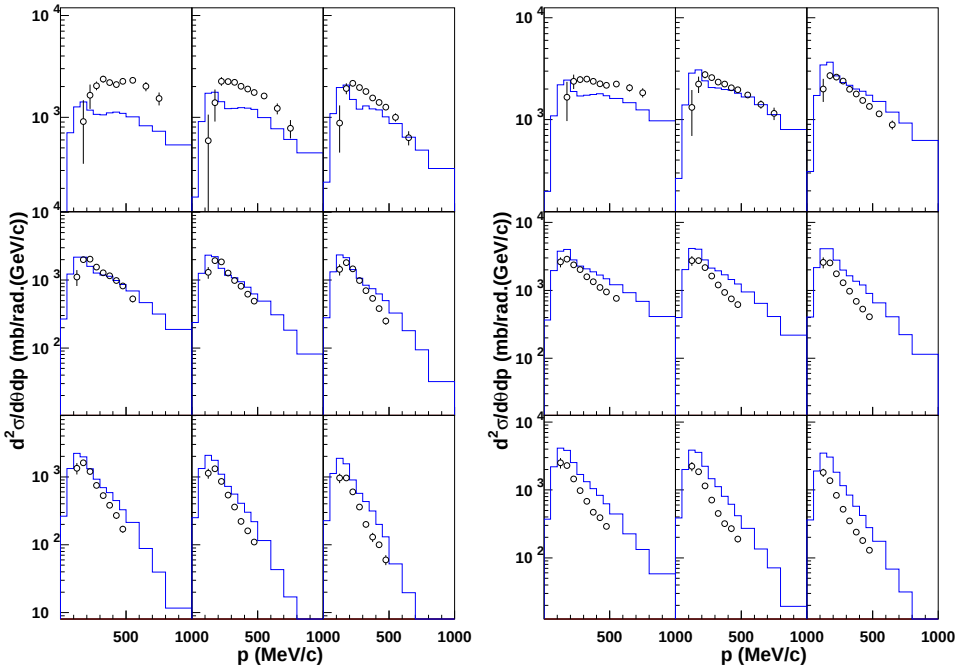

(c) π^- (8 GeV/c) + Pb $\rightarrow$ π^+ (d) π^- (12 GeV/c) + Pb $\rightarrow$ π^-

Figure D.51: *Double-differential cross sections for π^- production (a,c) and π^- production (b,d) in π^+-induced reactions on Cu at 3 GeV/c (a,b) and 8 GeV/c (c,d) incident momentum. Data (symbols) from Ref. [13] are compared with the improved version of the INCL4 model (blue lines).*

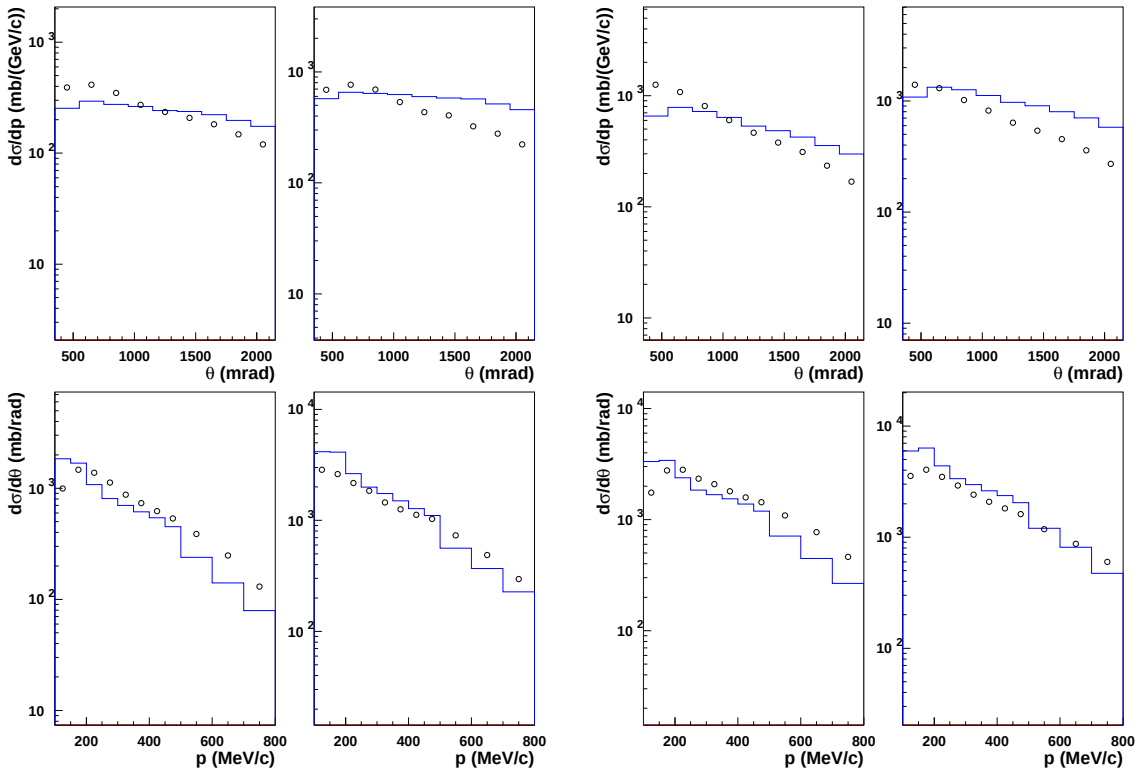

(a) π^- (3 GeV/c) + Pb (b) π^- (8 GeV/c) + Pb

Figure D.52: *Simple-differential cross section in π^--induced reactions on Pb target at 3 GeV/c (a) and 8 GeV/c (b) incident momentum. The data are obtained by integrating the double-differential cross sections of the HARP experiment over the angular domain or over the momentum domain (presented in Tab. D.1). Data (symbols) from Ref. [13] are compared with the improved version of INCL4 (blue lines).*

Bibliography

[1] J.-P. Meulders *et al.* HINDAS EU Contract FIKW-CT-2000-00031, Final report. *to be published.*

[2] EUROTRANS/NUDATRA project. EU contract F16W-CT-2004-516529. `http://nuklear-server.ka.fzk.de/Eurotrans/`.

[3] R. Serber. Nuclear Reactions at High Energies. *Phys. Rev.*, 72(11):1114, 1947.

[4] AIEA. `http://nds121.iaea.org/alberto/mediawiki-1.6.10/index.php`.

[5] J. Cugnon, A. Boudard, S. Leray, and D. Mancusi. Results with INCL4. In *Proceedings to the Satellite Meeting on Nuclear Spallation Reactions, International Topical Meeting on Nuclear Research Applications and Utilization of Accelerators*, Vienna, Austria, 2009. IAEA.

[6] S. Pedoux. Extension du modèle de Cascade Intranucléaire de Liège aux énergies comprises entre 2 et 10 GeV. Master's thesis, University of Liège, 2005–2006.

[7] J. Cugnon, Th. Aoust, A. Boudard, J.-C. David, S. Pedoux, S. Leray, and Y. Yariv. The INCL model for spallation reactions below 10 GeV. *Adv. Sp. Res.*, 40(9):1332, 2007.

[8] S. Pedoux, J. Cugnon, A. Boudard, J.-C. David, and S. Leray. Extension of INCL4 between 2 and 15 GeV. *Adv. Sp. Res.*, 44(8):926, 2009.

[9] S. Pedoux, A. Boudard, J. Cugnon, J.-C. David, S. Leray, and D. Mancusi. The extension of the INCL model for simulation of shielding in space. *Adv. Sp. Res.*, 48(2):383, 2011.

[10] S. Pedoux and J. Cugnon. Extension of the Liège intranuclear cascade model at incident energies between 2 and 12 GeV. Aspects of pion production. *Nucl. Phys. A*, In Press, Corrected Proof, 2011.

[11] M.G. Catanesi *et al.* Large-angle production of charged pions with 3–12.9 GeV/c incident protons on nuclear targets. *Phys. Rev. C*, 77(5):055207, 2008.

[12] M. Apollonio *et al.* Forward production of charged pions with incident protons on nuclear targets at the CERN Proton Synchrotron. *Phys. Rev. C*, 80(3):035208, 2009.

[13] M. Apollonio *et al.* Large-angle production of charged pions with incident pion beams on nuclear targets. *Phys. Rev. C*, 80(6):065207, 2009.

[14] IEA. `http://www.iea.org/stats`.

[15] US Census Bureau. `http://2010.census.gov/2010census/data/`.

[16] H. Abderrahim, P. Baeten, D. De Bruyn, J. Heyse, P. Schuurmans, and J. Wagemans. MYRRHA, a Multipurpose Hybrid Research Reactor for High-end Applications. *Nucl. Phys. News*, 1(20):24, 2010.

[17] I. S. K. Gardner. A Review of Spallation Neutron Source Accelerators. In S. Myers, editor, *EPAC98: Proceedings*, page 98. IOP Publishing, 1998.

[18] G. Kraft. Heavy Ion Tumor Therapy: From the Scientific Principles to the Clinical Routine. *Nucl. Phys. News*, 17:24, 2007.

[19] E. Parker. Shielding space explorers from cosmic rays. *Space Weather*, 3(S08004), 2005.

[20] M. Durante. Radiation protection in space. *Riv. Nuovo Cimento*, 25(8):1, 2002.

[21] Y. Yariv and Z. Fraenkel. Intranuclear cascade calculation of high-energy heavy-ion interactions. *Phys. Rev. C*, 20(6):2227, 1979.

[22] J. Cugnon, S. Leray, E. Martinez, Y. Patin, and S. Vuillier. New constraints on the delta production cross section. *Phys. Rev. C*, 56(5):2431, 1997.

[23] J.-J. Gaimard and K.-H. Schmidt. A reexamination of the abrasion-ablation model for the description of the nuclear fragmentation reaction. *Nucl. Phys. A*, 531(3-4):709, 1991.

[24] A. Kelić, M. V. Ricciardi, and K.-H. Schmidt. ABLA07: Towards a complete description of the decay channels of a nuclear system from spontaneous fission to multifragmentation. In *Joint ICTP-IAEA Advanced Workshop on Model Codes for Spallation Reactions*, page 181, Trieste, Italy, 2008. IAEA. Report INDC(NDC)-0530.

[25] R. J. Charity. GEMINI: a code to simulate the decay of a compound nucleus by a series of binary decays. In *Joint ICTP-IAEA Advanced Workshop on Model Codes for Spallation Reactions*, page 139, Trieste, Italy, 2008. IAEA. Report INDC(NDC)-0530.

[26] J. P. Bondorf, A. S. Botvina, and A. S. Iljinov et al. Statistical multifragmentation of nuclei. *Phys. Rep.*, 257(3):133, 1995.

[27] A. Letourneau *et al.* Neutron production in bombardments of thin and thick W, Hg, Pb targets by 0.4, 0.8, 1.2, 1.8 and 2.5 GeV protons. *Nucl. Instrum. Meth. B*, 170(3-4):299, 2000.

[28] SCK-CEN. `http://myrrha.sckcen.be/en/MYRRHA/ADS`.

[29] E. Hernãndez and E. Oset. Pion spectra after annihilation in nuclei. *Nucl. Phys. A*, 455(4):584, 1986.

[30] L.L. Salcedo, E. Oset, M.J. Vicente-Vacas, and C. Garcia-Recio. Computer simulation of inclusive pion nuclear reactions. *Nucl. Phys. A*, 484(3-4):557, 1988.

[31] Swordy S.P. The energy spectra and anisotropies of cosmic rays. *Space Science Reviews*, 99(1-4):85, 2001.

[32] N. Bohr. Neutron Capture and Nuclear Constitution. *Nature*, 137:344, 1936.

[33] A. J. Koning, S. Hilaire, and M. Duijvestijn. *TALYS-0.64 A nuclear reaction program*, 2004. NRG Report 21297/04.62841/PFAI/AK/AK.

[34] Th. Aoust. *Amelioration du modèle de cascade intranucleaire de Liège en vue de l'étude de cibles de spallation pour les systèmes hybrides*. PhD thesis, University of Liege, 2006-2007.

[35] E. Segrè. *Nuclei and particles*. W. A. Benjamin, Inc., 1977. Second edition.

[36] P. E. Hodgson, E. Gadioli, and E. E. Gadioli. *Introductory Nuclear Physics*. Clarendon Press, Oxford, 1997.

[37] J.-P. Jeukenne, A. Lejeune, and C. Mahaux. Optical-model potential in finite nuclei from Reid's hard core interaction. *Phys. Rev. C*, 16(1):80, 1977.

[38] D. F. Jackson. *Nuclear Reaction*. Methuen and CO LTD, 1970.

[39] V. F. Weisskopf and D. H. Ewing. On the yield of nuclear reactions with heavy elements. *Phys. Rev.*, 57(6):472, 1940.

[40] W. Hauser and H. Feshbach. The inelastic scattering of neutrons. *Phys. Rev.*, 87(2):366, 1952.

[41] J. J. Griffin. Statistical model of intermediate structure. *Phys. Rev. Lett.*, 17(9):478, 1966.

[42] E. Gadioli and P. E. Hodgson. *Pre-Equilibrium Nuclear Reactions*. Clarendon Press, Oxford, 1992.

[43] C. K. Cline and M. Blann. The pre-equilibrium statistical model: Description of the nuclear equilibration process and parameterization of the model. *Nucl. Phys. A*, 172(2):225, 1971.

[44] I. Ribaňský and P. Obložinský and E. Běták. Pre-equilibrium decay and the exciton model. *Nucl. Phys. A*, 205(3):545, 1973.

[45] K. K. Gudima, S. G. Mashnik, and V. D. Toneev. Cascade-exciton model of nuclear reactions. *Nucl. Phys. A*, 401(2):329, 1983.

[46] J. Cugnon and P. Henrotte. Nuclear Reaction Mechanisms: From Compound Nucleus to Multiple Scattering. `http://www.theo.phys.ulg.ac.be/wiki/index.php/Cugnon-Joseph`, 2002. Lectures delivered at the University of Louvain-la-Neuve.

[47] W. Botermans and R. Malfliet. Quantum transport theory of nuclear matter. *Phys. Rep.*, 198(3):115, 1990.

[48] V. E. Bunakov and G. V. Matvejev. The physical and mathematical foundations of the intranuclear cascade model algorithm. *Z. Phys. A*, 322:511, 1985.

[49] J. Cugnon. Dynamics of the relativistic heavy ion collisions. In P. Bonche, M. Lévy, P. Quentin, and D. Vautherin, editors, *Heavy ion collisions: Cargese 1984 : proceedings*, page 209, New-York, 1986. Plenum Press.

[50] P. Henrotte. *Extension du modèle de cascade intranucléaire pour les réactions de spallation*. PhD thesis, University of Liège, 2005.

[51] J. Cugnon, T. Mizutani, and J. Vandermeulen. Equilibration in relativistic nuclear collisions. a monte carlo calculation. *Nucl. Phys. A*, 352(3):505, 1981.

[52] J. Cugnon. Proton-nucleus interaction at high energy. *Nucl. Phys. A*, 462(4):751, 1987.

[53] J. Cugnon and M.-C. Lemaire. Medium effects in pion production. *Nucl. Phys. A*, 489(4):781, 1988.

[54] J. Cugnon, D. L'Hôte, and J. Vandermeulen. Simple parametrization of cross-sections for nuclear transport studies up to the GeV range. *Nucl. Instrum. Meth. B*, 111(3-4):215, 1996.

[55] J. Cugnon and J. Vandermeulen. Transfer of energy following on nuclei. *Nuclear Physics A*, 445(4):717, 1985.

[56] J. Cugnon, C. Volant, and S. Vuillier. Improved intranuclear cascade model for nucleon-nucleus interactions. *Nucl. Phys. A*, 620(4):475, 1997.

[57] J. Cugnon, C. Volant, and S. Vuillier. Nucleon and deuteron-induced spallation reactions. *Nucl. Phys. A*, 625(4):729, 1997.

[58] A. Boudard, J. Cugnon, S. Leray, and C. Volant. Intranuclear cascade model for a comprehensive description of spallation reaction data. *Phys. Rev. C*, 66(4):044615, 2002.

[59] A. R. Junghans, M. de Jong, H.-G. Clerc, A. V. Ignatyukb, G. A. Kudyaevb, and K.-H. Schmidt. Projectile-fragment yields as a probe for the collective enhancement in the nuclear level density. *Nucl. Phys. A*, 629(3-4):635, 1998.

[60] J. Cugnon and P. Henrotte. The liege intranuclear cascade model. In D. Filges, F. Goldenbaum, and Y. Yariv, editors, *Proceedings of the Fifth Workshop on SImulating Accelerator Radiation Environments (SARE-5)*, page 65, Jülich, Germany, 2001. Jülich Publications.

[61] J. D. Bowman, W. J. Świątecki, and C. F. Tsang. Abrasion and ablation of heavy ions. Lawrence Berkeley Laboratory Report LBL-2908, University of California, 1973.

[62] J. Benlliure, A. Grewe, M. de Jong, K.-H. Schmidt, and S. Zhdanov. Calculated nuclide production yields in relativistic collisions of fissile nuclei. *Nucl. Phys. A*, 628(3):458, 1998.

[63] K. Kruglov *et al.* Yields of neutron-rich isotopes around Z = 28 produced in 30 MeV proton-induced fission of ^{238}U. *Eur. Phys. J. A*, 14:365, 2002.

[64] J. Cugnon, A.Boudard, S. Leray, and D. Mancusi. New features of the INCL4 model for spallation reactions. In *Proc. of the Int. Conf. On Nuclear data for Science and Technology*. IAEA, 2010. to be published.

[65] A. Boudard, J. Cugnon, S. Leray, and C. Volant. A new model for production of fast light clusters in spallation reactions. *Nucl. Phys. A*, 740(1-2):195, 2004.

[66] Th. Aoust and J. Cugnon. Effects of isospin and energy dependences of the nuclear mean field in spallation reactions. *Eur. Phys. J. A*, 21:79, 2004.

[67] Th. Aoust and J. Cugnon. Pion physics in the Liège intranuclear cascade model. *Phys. Rev. C*, 74(6):064607, 2006.

[68] J. Bystricky, P. La France, F. Lehar, F. Perrot, T. Siemiarczuk, and P. Winternitz. Energy dependence of nucleon-nucleon inelastic total cross-sections. *J. Phys. France*, 48(11):1901, 1987.

[69] A. Baldini, V. Flaminio, W.G. Moorhead, and D.R.O. Morrison. *Landolt-Bornstein, Numerical data and functional relationships in science and technology*, volume 12. Springer-Verlag Berlin Heidelberg, 1988. New series Group 1.

[70] F. James. E. raubold and g. r. lynch. their event generator has not been published by the authors; it has been described inMonte-Carlo phase space. CERN-68-15, 1968,.

[71] R. Hagedorn. *Relativistic Kinematics*. Benjamin, 1963. New York.

[72] A. Baldini, V. Flaminio, W.G. Moorhead, and D.R.O. Morrison. *Landolt-Bornstein, Numerical data and functional relationships in science and technology*, volume 7. Springer-Verlag Berlin Heidelberg, 1988. New series Group 1.

[73] X. Ledoux *et al.* Spallation Neutron Production by 0.8, 1.2, and 1.6 GeV Protons on Pb Targets. *Phys. Rev. Lett.*, 82(22):4412, 1999.

[74] K. Ishibashi *et al.* Measurement of Neutron-Production Double-Differential Cross Sections for Nuclear Spallation Reaction Induced by 0.8, 1.5 and 3.0 GeV Protons. *J. Nucl. Sci. Technol.*, 34(6):529, 1997.

[75] A. Letourneau *et al.* Composite-particle emission in the reaction p+Au at 2.5 GeV. *Nucl. Phys. A*, 712(1-2):133, 2002.

[76] A. Bubak *et al.* Non-equilibrium emission of complex fragments from $p + au$ collisions at 2.5 gev proton beam energy. *Phys. Rev. C*, 76(1):014618, 2007.

[77] Yu. D. Bayukov *et al.* Angular dependence of inclusive production of nucleons in nuclear reactions at high energies and separation of the contributions of quasifree and deep inelastic nuclear processes. *Yad. Fiz.*, 42:185, 1985.

[78] Yu D. Bayukov. `http://hepdata.cedar.ac.uk/view/p6926/prev`.

[79] J. Collot, H. G. Kirk, and N. V. Mokhov. Pion production models and neutrino factories. *Nucl. Instrum. Meth. A*, 451:327, 2000.

[80] N. V. Mokhov. The MARS code system user guide. *Fermilab*, FN-628, 1995. Version 13.

[81] N. V. Mokhov, S. I. Striganov, A. Van Ginneken, S. G. Mashnik, A. J. Sierk, and J. Ranft. MARS code developments. *LANL Report*, LA-UR-98-5716, 1998. nucl-th/9812038 v2.

[82] S. G. Mashnik and A. J. Sierk. Improved Cascade-Exciton Model of Nuclear Reactions. In T. A. Gabriel, editor, *Proceedings of the Fourth Workshop on Simulating Accelerator Radiation Environments (SARE4)*, page 29, 1999. ORNL.

[83] M.G. Catanesi *et al.* Measurement of the production of charged pions by protons on a tantalum target. *Eur. Phys. J. C*, 51:787, 2007.

[84] M.G. Catanesi *et al.* Large-angle production of charged pions by 3–12.9 GeV/c protons on beryllium, aluminium and lead targets. *Eur. Phys. J. C*, 54:37, 2008.

[85] M.G. Catanesi *et al.* Large-angle production of charged pions by 3 GeV/c–12 GeV/c protons on carbon, copper and tin targets. *Eur. Phys. J. C*, 53:177, 2008.

[86] Z. Chen. Hadron production in p+A reactions at AGS energies: a review. *Int. J. Modern Phys. E*, 2:285, 1993.

[87] J. Aichelin. "Quantum" molecular dynamics–a dynamical microscopic n-body approach to investigate fragment formation and the nuclear equation of state in heavy ion collisions. *Phys. Rep.*, 202(5-6):233, 1991.

[88] K. Gallmeister and U. Mosel. Production of charged pions off nuclei with 3-30 GeV incident protons and pions. *Nucl. Phys.* **A**, 826(1–2):151, 2009.

[89] V. Blobel *et al.* Multiplicities, topological cross sections, and single particle inclusive distributions from pp interactions at 12 and 24 GeV/c. *Nucl. Phys. B*, 69(3):454, 1974.

[90] J. Cugnon. Anti-proton - nucleus annihilation. In J.-M. Richard, E. Aslanidès, and N. Boccara, editors, *The Elementary Structure of Matter*, page 211, Berlin, 1988. Springer-Verlag.

[91] J. Cugnon, P. Jasselette, and J. Vandermeulen. Dynamics of the anti-p nucleus annihilation. In C. Amsler et al., editor, *Physics at LEAR with Low-Energy Antiprotons*, page 775, Chur, 1988. Harwood Ac. Publ.

[92] M. Trzaska *et al.* Excitation of the delta-resonance in proton-nucleus collisions. *Z. Phys. A*, 340:325, 1991.

[93] S. Agostinelli *et al.* GEANT4–a simulation toolkit. *Nucl. Instrum. Meth. A*, 506(3):250, 2003.

[94] A. Fassò, A. Ferrari, J. Ranft, and P. R. Sala. FLUKA: a multi-particle transport code. *CERN-2005-10*, 2005. INFN/TC-05/11, SLAC-R-773.

[95] G. Battistoni, F. Cerutti, A. Fassò, A. Ferrari, S. Muraro, J. Ranft, S. Roesler, and P. R. Sala. Proceedings of the hadronic shower simulation workshop 2006, fermilab 6–8, september, 2006. volume 896, page 31, 2007.

[96] F. Ballarini *et al.* Nuclear models in fluka: Present capabilities, open problems, and future improvements. *AIP Conference Proceedings*, 769(1):1197, 2005.

[97] G. Battistoni *et al.* Recent developments in the fluka nuclear reaction models. In *Proc. 11th Int. Conf. on nuclear reaction mechanisms*, 2006. Varenna (Italy), June 12-16.

[98] A. Bolshakova *et al.* HARP-CDP hadroproduction data: comparison with FLUKA and GEANT4 simulations. *Eur. Phys. J. C*, 70:543, 2010.

[99] T. Enqvist *et al.* Isotopic yields and kinetic energies of primary residues in 1 A GeV 208Pb+p reactions. *Nucl. Phys. A*, 686(1-4):481, 2001.

[100] A. I. Warwick *et al.* Breakup of spectator residues in relativistic nuclear collisions. *Phys. Rev. C*, 27(3):1083, 1983.

[101] N. T. Porile, G. D. Cole, and C. R. Rudy. Nuclear reactions of silver with 25.2 GeV ^{12}C ions and 300 GeV protons. *Phys. Rev. C*, 19(6):2288, 1979.

[102] A. M. Poskanzer, G. W. Butler, and E. K. Hyde. Fragment production in the interaction of 5.5-GeV protons with uranium. *Phys. Rev. C*, 3(2):882, 1971.

[103] P. B. Price, J. Stevenson, and K. Frankel. Universal fragment-momentum distribution in high-energy nucleus-nucleus collisions. *Phys. Rev. Lett.*, 39(4):177, 1977.

[104] J. Stevenson, P. B. Price, and K. Frankel. Evidence for slowly moving, highly excited nuclear matter produced in high-energy nucleus-nucleus collisions. *Phys. Rev. Lett.*, 38(20):1125, 1977.

[105] X. Campi, J. Desbois, and E. Lipparini. in "heavy ion conference". 1984.

[106] R. Michel *et al. Nucl. Sci. Tech.*, Suppl. 2:242, 2002.

[107] Y. E. Titarenko *et al.* Excitation functions of product nuclei from 40 to 2600 MeV proton-irradiated 206, 207, 208, nat Pb and 209Bi. *Nucl. Instr. Meth. A*, 562(2):801, 2006.

[108] M. Gloris, R. Michel, F. Sudbrock, U. Herpers, P. Malmborg, and B. Holmqvist. Proton-induced production of residual radionuclides in lead at intermediate energies. *Nucl. Instr. Meth. A*, 463(3):593, 2001.

[109] I. Leya, R. Wieler, J.-C. David, S. Leray, L. Donadille, J. Cugnon, and R. Michel. Production of noble gas isotopes by proton-induced reactions on lead. *Nucl. Instr. Meth. B*, 229(1):1, 2005.

[110] K. Hagiwara *et al.* Review of particle properties. *Phys. Rev. D*, 66(1):10001, 2002.

[111] M.G. Catanesi *et al.* The HARP detector at the CERN PS. *Nucl. Instrum. Meth. A*, 571(3):527, 2007.

[112] M.G. Catanesi *et al.* Measurement of the production cross-section of positive pions in p-Al collisions at 12.9 GeV/c. *Nucl. Phys. B*, 732(1-2):1, 2006.